University of Nevada, Reno

Paragenetic Evolution of the Robertson Deposit: Eocene Intrusion Related Gold Deposit in the Northern Shoshone Range, Nevada

A thesis submitted in partial fulfillment of the requirements for the degree of Master of Science in Geology

by

Neal E. Mankins

Dr. John L. Muntean/Thesis Advisor

May, 2022

THE GRADUATE SCHOOL

We recommend that the thesis

prepared under our supervision by

Neal E. Mankins

Entitled

Paragenetic Evolution of the Robertson Deposit:

Eocene Intrusion Related Gold Deposit in the

Northern Shoshone Range, Nevada

be accepted in partial fulfillment of the

requirements for the degree of

Master of Science

John Muntean, PhD.

Advisor

Matthieu Harlaux, PhD.

Co-advisor

Scott Bassett, PhD

Graduate School Representative

David W. Zeh, Ph.D., Dean

Graduate School

May 2022

ABSTRACT

The Robertson deposit, formerly known as Tenabo, is an Eocene intrusion-related gold deposit 5 km north of Pipeline, which is a 20 Moz+ Carlin-type gold deposit in the northern Shoshone Range, Nevada. Carlin-type gold deposits have been the focus of many studies as they represent the second largest accumulation of gold in the world, and a growing body of scientific literature indicates that the source for this gold may be related to Eocene magmatism. The presence of an Eocene intrusion-related gold deposit within 5 km of a Carlin-type deposit begs the question of whether the two deposits are genetically related, however detailed characterized of Robertson deposit is needed before this link can be examined.

Most of the previously defined gold mineralization at Robertson occurred near the contacts of intrusions and hosted by hornfels in the overlying lithologies. Ongoing exploration has discovered significant free visible gold both within the stock and in distal settings within metasedimentary host rocks. Here, gold mineralization is spatially and temporally related to an intrusive complex referred to as the Tenabo stock, and based on petrographic and geochemical analysis, is composed of successive intrusive phases including an early ilmenite-bearing diorite, andesite dikes, hypabyssal dacitic porphyry dikes, composite ilmenite-bearing granodiorite, granitic porphyry dikes (formerly called feldspar porphyry dikes), pebble dikes, and subvolcanic rhyolitic dikes.

The purpose of this study is to characterize gold mineralization as it relates to intrusive phases, alteration styles, and structural controls by combining fieldwork, petrography, geochemistry and geochronology. This study is the first in depth examination of Robertson focusing on gold mineralization within intrusive phases and in distal settings, presenting six new

U/Pb LA-ICP-MS ages of intrusive phases, one molybdenite Re/Os age, and one hydrothermal orthoclase $^{40}Ar/^{39}Ar$ age, conservatively constraining gold mineralization to 39.65-35.77 Ma.

Emplacement of the Tenabo stock resulted in contact metamorphism of the host siliciclastic lithologies yielding quartz, biotite, and calc-silicate hornfels, which formed an aureole up to 1 km from the stock. Subsequent hydrothermal alteration followed, including endo/exoskarn, potassic alteration, sericitic alteration, and chloritic alteration. Petrographic observations of veins at Robertson indicate the succession of three main stages referred as 1) pre-gold, 2) syn-gold, and 3) post-gold. The pre-gold stage includes barren quartz veins, potassic alteration veins comprised of biotite veinlets and quartz-K-feldspar, quartz – arsenopyrite, quartz – chalcopyrite, and quartz – molybdenite veins. The syn-gold stage is composed of quartz – gold ± Bi-Te-Se-Pb-Ag-S sulfosalt veins, consisting of native gold seen as single grains in quartz gangue and/or on the surface of pyrrhotite, arsenopyrite, chalcopyrite, and loellingite grains. The post-gold veins encompass pyrite ± quartz, quartz – calcite – polymetallic sulfide veins with Pb-Zn-Sb-Ag-Sn base metal sulfides, bull quartz veins, and calcite veins.

Cross-cutting relationships along with geochronological data indicate that gold mineralization resulted from the emplacement of upper Eocene (40.99-37.38 Ma) reduced ilmenite-bearing intrusive phases that intruded into Ordovician-Devonian siliciclastic sedimentary lithologies, forming a high-tonnage, low-grade gold deposit characterized by a Au-As-Bi-Te-Cu metal association, similar to reduced intrusion related gold deposits and gold skarns described globally. Based on petrographic and geochemical evidence, it is concluded that mineralizing conditions for gold precipitation were under relatively low sulfur fugacity and oxidation state, leading to preferential formation of minerals such as native Bi, arsenopyrite, pyrrhotite, and loellingite, typical of low-sulfidation assemblages. Under such conditions it is possible to transport gold to

lower temperatures <300°C, where native gold is commonly associated with Bi-bearing minerals or to even lower temperatures (~150-200°C) where it remains within the lattice of sulfides as invisible gold, typifying Carlin-type deposits.

ACKNOWLEDGEMENTS

I first would like to thank Nevada Gold Mines for their financial support and guidance of this study. The Robertson team including Matthew Mann, John Muir, Meredith Baker, Casey Fletcher, Gonzalo Mercado, Jeff Blackman, Jay Olcott and countless others for their continued support in the field, the core shed, and virtually. Geotechnical services at the Pipeline core shed for hunting old holes, cutting core, and setting up benches for site visits.

To my advisor Dr. John Muntean, I appreciate you taking a chance on me when I approached you in regards to a masters during your Epithermal Short Course (trip sponsored by VR Resources). Without this opportunity, I am not sure where I would be today. Thank you, Paul Dobak, who initially interviewed me for the Robertson project, got me up to speed, and continued to support me to the very end, lending me much life advice. To my committee members, Dr. Matthieu Harlaux and Dr. Scott Bassett, I cannot thank you enough for the time you dedicated to answer the countless questions I had regarding intrusion related gold systems and beyond. Without the guidance on figures, writing, and interpretation of observations, this work would have not been complete. Dr. Matthieu Harlaux, your mentorship on Raman Spectroscopy and expertise in ioGas was invaluable and I will carry these skills beyond University of Nevada, Reno. Dr. John McCormack, if you hadn't gotten me up to speed with ore petrography, I know that this study would have not been possible and for that I am truly grateful. I will surely continue to use this knowledge and the "lost art of petrography" to further my understanding of geology in the years to come. Dr. Joel DesOrmeau, I thank you for lending your help and expertise with geochronology and SED-EDS analysis, often leading into the late hours of the night. To Dr. John Dilles, thank you for introducing me to the world of economic geology during my undergraduate and continuing to stay in contact, even through my masters, lending your own personal time to do site visits.

Countless others, including Curtis Johnson, Justin Daley, Mike Gunning, Scott Berdahl, Michael Sepp, Michael Hutchinson, Nansen Olsen, Laurence Pryer et al., who inspire me to not only be the best geologist I can but the best version of myself.

I would like to thank the Ralph J. Roberts Center for Research in Economic Geology (CREG) and especially Dawn Snell for your support over the last couple years. Dawn, without your emotional support and personal advice, I am not sure I would have made it to the end. You have shown me that there is a lot more that goes on "behind the scenes," and for that I thank you. I thank the numerous conferences including Society of Economic Geologist (SEG), American Exploration and Mining Association (AEMA), Association for Mineral Exploration (AME Roundup), Geologic Society of Nevada (GSN), for allowing me to network and further my career. Without the opportunity to present and discuss geologic concepts in this manner I would have not met the countless geologist I continue to work with today. A special thanks to the Geologic Society of Nevada (Elko Chapter), for the generous scholarships and BBQ events, where I got to enjoy the company of fellow geologists both young and old outside of the mine setting. I want to thank the CREG students for donating their time in the office, field, or lab. The discussions we had about geology and beyond will be missed, but surely not forgotten. These discussions took us around the world, physically leading us to volcanoes of Iceland and skarn deposits of Sweden. These are memories, experiences, and most importantly rocks, that I will hold onto forever.

Finally, I would like to thank my parents Richard and Teri for their unwavering support of my pursuits in geology. My mom, Teri Rae Mankins, lost her battle with cancer during the writing of this thesis, but before she passed, she told me, "Finish your masters and follow your passion." From that day forward, I did everything in my power in order to do so. I will continue to live each day to fulfill those words and in writing this, I can only wish that you were here to see me do it.

TABLE OF CONTENTS

Page #

LIST OF TABLES

LIST OF FIGURES

Abbreviations: Act = actinolite, Ant = Anatase, Ap = apatite, Apy = Arsenopyrite, Au = gold, Bab = Babkinite, Bi = native bismuth, Bt = biotite, Cal = calcite, Ccp = chalcopyrite, Chl = chlorite, Elc = Electrum, Ep = epidote, Fb = freibergite, Gn = galena, Hbl = hornblende, Kaw = Kawazulite, Ksp = K-feldspar, Lo = loellingite, Mol = molybdenite, Mrc = marcasite, Ms = muscovite, Non = Nontronite, Pl = plagioclase, Po = pyrrhotite, Py = pyrite, Qz = quartz, Rt = rutile, Ser = sericite, Sp = sphalerite, Sb = Stibnite, Tet = Tetradymite, Ttn = Titanite, Ttr = tetrahedrite, Vrm = vermiculite, Ves = vesuvianite, Zeo = Zeolite, Zo = zoisite

Chemical Formulas: Babkinite = $Pb_2Bi_2(Se,S)_3$, Bismuthinite = Bi_2S_3, Boulangerite = $Pb_5Sb_4S_{11}$, Canfieldite = Ag_8SnS_6, Cosalite = $Pb_2Bi_2S_5$, Electrum = AuAg, Freibergite = $(Ag, Cu, Fe)_{12}(Sb, As)_4S_{13}$, Hedleyite = Bi_7Te_3, Hessite = Ag_2Te, Ikunolite = $Bi_4(Se,S)_3$, Kawazulite = $Pb_2Bi_2S_5$, Loellingite = FeAs, Native Bismuth = Bi, Naumannite = Ag_2Se, Pavonite $AgBi_3S_5$, Pilsenite = Bi4Te3, Protojoseite Bi_2TeS_2, Stannite Cu_2FeSnS_4, Tellurobismuthite = Bi2Te3, Tetradymite = Bi_2Te_2S, Tetrahedrite $(Cu,Fe)_{12}Sb_4S_{13}$

1. INTRODUCTION

The Robertson deposit is located within the Battle Mountain-Eureka trend along the eastern flank of the northern Shoshone Range, Nevada. Early geologic descriptions (King, 1876; Spurr, 1903; Emmons, 1910; Lee et al., 1916) of the northern Shoshone Range were largely reconnaissance in nature, with later comprehensive studies completed by Gilluly and Gates (1965) and Stewart and McKee (1977). The Battle Mountain-Eureka trend and subsequent districts, including the Tenabo subdistrict, host a variety of precious metal deposit types and are described in detail by Kelson, (2008), Colgan, (2014), Henry et al., (2020), Muntean, (2020), Muntean and Cline, (2018), Fithian et al., (2018), Ressel, (2006), Johnson, (2020), Ahmed, (2010), Reid, (2010), Maroun et al., (2017), Holley, (2019). Carlin-style gold deposits have been the focus of many of these studies, as these deposits dominate in regards to gold endowment in north-central Nevada, and along with the Carlin Trend, represent the largest accumulation of gold in the Northern Hemisphere (Holley et al., 2022).

Previous research has been done where Carlin-style mineralization is related to Eocene intrusive activity on the Battle Mountain-Eureka trend, Johnston et al., (2008), Muntean et al., (2017), Henry et al., (2020), Mercer, (2021), however, there is little research where intrusion-related gold mineralization is both spatially and temporally related to Carlin-type mineralization. Exploring the link between Carlin-style gold deposits and intrusion-related gold deposits is critical in the assessment of whether or not Carlin-style deposits formed from magmatic hydrothermal fluids and the understanding of the mechanisms associated with gold transport in the upper continental crust. Before this can be done however, detailed characterization of the Tenabo stock and subsequent hydrothermal events is necessary.

There is little published work on Robertson, limited to a Geological Society of Nevada Field Trip Guidebook paper by McCusker in 1996, district scale studies by Kelson et al., (2008), and technical reports, with two unpublished petrographic and scanning electron microscope (SEM) studies by Russ Honea in 1996 and Annick Chouinard in 2017 and 2019. This study builds on these earlier regional studies and unpublished investigations conducted while Robertson was being explored and developed. The purpose is to characterize the timing and relationships of hydrothermal alteration and mineralization related to the emplacement of the Tenabo stock, in order to better understand a lesser-known deposit type in a well-known world class mining district. Here, the presence of a low-grade high tonnage gold deposit with low oxidation and sulfidation state mineral assemblages is documented, giving us insights into Eocene intrusion-related gold systems in north-central Nevada. The link between Robertson and other reduced intrusion-related gold deposits on a global scale is examined, in an attempt to better understand the relationship between deposit types, associated intrusions, and metal suites, allowing us to put Robertson into a regional and global framework. With this framework established, the link between Carlin-style gold deposits and intrusion related gold deposits may be examined and this work may serve as a foundation for future studies.

2. EXPLORATION AND MINING HISTORY

The earliest recorded gold discovery in the Tenabo area was made by Charles Montgomery in 1905 from fault hosted quartz-arsenopyrite veins near the head of Mill Gulch (McCusker, 1996). Following this discovery, the Gold Quartz underground mine, produced ~10,000 oz gold from 1906-1912 and was the principal producer in the area. Other gold producers included Phoenix, Gylding, Gold Pan, and Little Gem mines. In 1916, A.J. Raleigh discovered placer gold in the area and in 1937 the Mill Gulch Placer Mining Company operated a small dragline dredge and washing

plant until 1939 (Johnson, 1973). Although gold was the primary commodity, the Little Gem mine was one of the leading producers of copper in Nevada until 1960 (Stager, 1977).

In the late 1960s, a number of companies, including Bear Creek and Superior Oil explored the district for porphyry copper mineralization but quickly lost interest. They were soon followed by a number of Canada-based junior mining companies, including Placer Development (1974-75), Teck Corporation (1977), E & B Exploration Ltd. (1980-81), and Aaron Mining Ltd. (1975-86), all of whom sporadically explored the Tenabo area with limited success (McCusker, 2004). Aaron Mining Ltd. did however open pit mine and heap leach a total 48,443 metric tons of ore, recovering 980 oz Au from 1974-1980 (Sampson, 1988).

In 1986, Coral Gold Corp. acquired the Tenabo property from Aaron Mining and began to expand the land package, soon to be called Robertson. During the period 1986 through 1989, Coral completed approximately 380 reverse circulation (RC) holes and 7 diamond drill holes (DDH), totaling about 33,338 m. Coral Gold commenced mining in 1988 having reported reserves of 9.9 Mt at 0.048 ounces per metric ton (opt) (Nevada Bureau of Mines, 1989), but shut down a year later due to low gold prices. During the operating life of the Robertson mine, approximately 317,000 metric tons of low-grade material was placed on leach pads, from which about 6,800 ounces of gold were recovered (McCusker, 2004).

Amax Gold optioned the property from 1990-1996, and drilled 338 RC holes and 62 DDH holes totaling over 53,644 m (Sampson, 1997). Of these holes, 3 were designed to test for the presence of lower plate carbonates, none of which intercepted. In a 1994 feasibility study, AMAX outlined approximately 1.2 Moz. of Au within 5 zones with much of their exploration effort focusing on the porphyry zone, containing ~718,000 oz Au (Tarnocai, 1998). This however, did not reach the heap leach target AMAX was interested in and AMAX subsequently returned the property. In 1998

Cortez Gold Mines optioned the property, drilling 46 RVC drill holes and a single mud rotary hole, totaling 17,373 m, outlined in a report by Tarnocai in 1998. After drilling, Cortez declared its interest in renegotiating the terms of the Option Agreement, but when Coral declined, Cortez subsequently terminated the agreement and did not earn an interest in the property (McCusker, 2004).

From 2004-2010 Coral Gold completed 8 drill programs consisting of 126 RC holes and 14 DDH holes totaling 31,373 m outlined in a preliminary economic assessment by Beacon Hill in 2012. Of these drilling programs, in 2007 Coral Gold drilled two deep RC holes totaling 1962 m in which one hole was able to reach the lower plate of the RMT at 939 m returning a 60.96 m thick interval of weakly to strongly anomalous gold values ranging from 0.031 to 2.190 ppm gold, hosted by altered lower plate carbonates rocks (McCusker, 2004). In 2017, Barrick Gold bought the Robertson property from Coral Gold and continued a drill program up to the joint venture (JV) with Newmont in 2019. The JV with Newmont known as, Nevada Gold Mines (NGM), has carried out a drill program at Robertson since the merger.

3. GEOLOGIC BACKGROUND

3.1. Regional Geology

The Robertson property lies along the far eastern flank of the northern Shoshone Range in northcentral Nevada within the Basin and Range physiographic province of western North America (Fig. 1A). The region lies at or very near a rifted margin of continental crust which was subjected to periodic contractual deformation starting in middle Paleozoic and continuing until Late Cretaceous (Stewart, 1980, Oldow, 1984). The geology of this region is dominated by a

complex set of branching, low-angle faults that are part of the Roberts Mountains thrust (RMT) which formed as a result of the Antler Orogeny. Forming the upper plate of this regionally

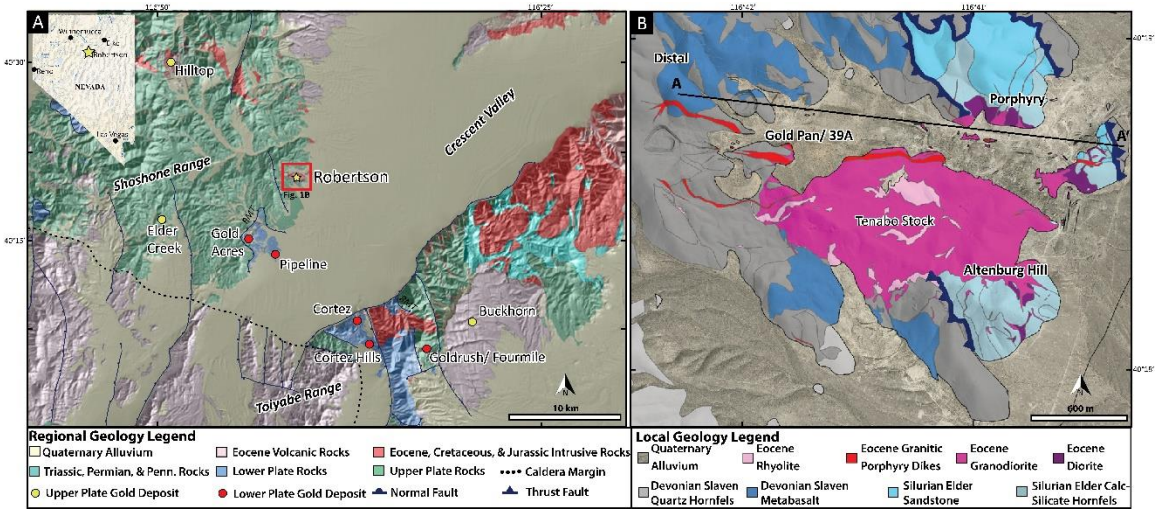

Fig. 1. Simplified geologic map of the Northern Shone Range and Cortez district. Modified from Colgan et al. (2014) using data from Gilluly and Gates (1956). (A) Regional geologic map of the Shoshone and Cortez range with Caetano caldera outlined, Nevada state inset map, and labeled lower plate Carlin Type and upper plate gold deposits. (B) Local geology inset map of the Robertson deposit with Gold Pan, 39A, Porphyry, Distal, and Altenburg Hill resource zones shown. Cross section line shown from A-A' can be seen in figure 3

significant structure, are a series of thick, vertically stacked nappes, predominately of distal slope facies, characterized by dark-gray, fine-grained siliceous sedimentary and lesser volcanic rocks of early to middle Paleozoic age. During latest Devonian or earliest Mississippian time, these rocks are postulated to have been transported eastward along segments of the RMT and structurally emplaced over carbonate sequence of similar age that comprises the lower plate (Roberts, 1964).

Subduction-related calc-alkaline magmatism began as early as Middle Jurassic and continued through early Miocene time (Stewart, 1980). Beginning in the late Eocene, an important episode of magmatism gradually swept from northeast to southwest across northern Nevada which was accompanied by extensional deformation (Christiansen and Yeats, 1992). Many of the region's largest gold deposits, including those situated along the Carlin and Battle Mountain-Eureka

trends, are both spatially and temporally related to this period of calc-alkaline Eocene magmatism and extensional tectonics (Ressel and Henry, 2006). Starting ~17 Ma, regional extensional block faulting, accompanied by rift-related bimodal basalt-rhyolite volcanism, further modified the region resulting in the characteristic basin and range topography encountered in Nevada (Dickinson, 2002).

3.2. Local Geology

Paleozoic and Cenozoic rocks underlie the northern Shoshone Range, with the oldest and most abundant lithologies at Robertson being siliceous and/or siliciclastic sedimentary and volcanic rocks of the Ordovician Valmy Formation, Silurian Elder Formation, and Devonian Slaven Formation. These rocks are a part of Roberts Mountains allochthon, which is emplaced as a series of both small and large-scale thrust slices along segments of the RMT, and generally form an out of-sequence tectono-stratigraphic succession of mappable units (Colgan et al., 2014) (Fig. 2). On the west side of the property, the Valmy Formation

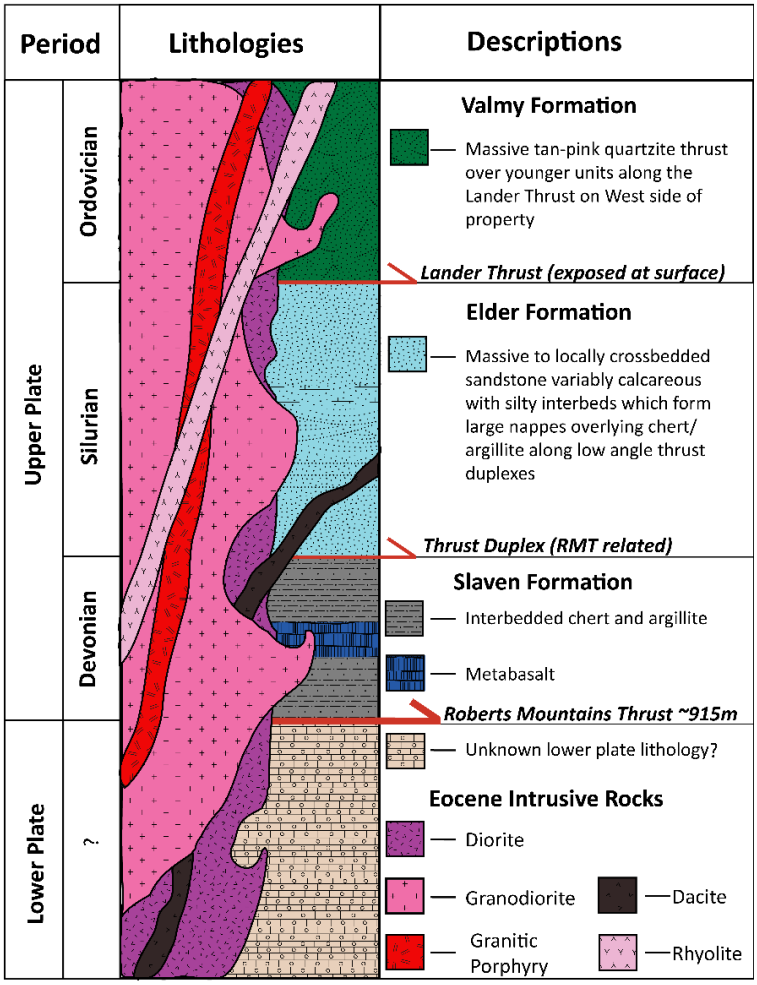

Fig. 2. Generalized tectono-stratigraphic column of Robertson. Robertson mountains thrust depth estimated from USGS drill hole #1 in 1968 and drill hole TV07-02 by Coral Gold in 2007, which reached the lower plate at depths of 2,938 ft (895 m) and 3,080 ft (938 m)

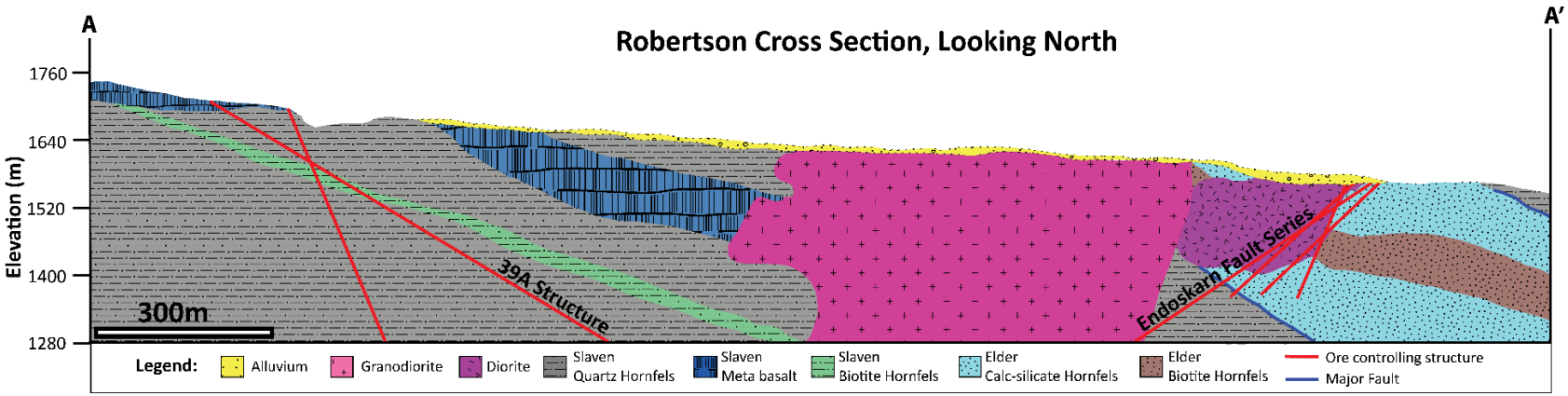

Fig. 3. Generalized geologic cross section of the Robertson deposit looking North (section line shown on fig. 1B). Lithology textures do not reflect dip angle or internal deformation complexities.

structurally overlies the rest of the sequence along the Lander thrust, and is typically observed as a fine-grained siliciclastic orthoquartzite locally capped by a thin green colored chert of early Silurian age called the Cherry Springs Formation. More commonly observed at Robertson, are the Slaven and Elder Formations. Along the north and east side of the property, the Silurian Elder Formation forms two large nappes composed of fine-grained interbedded-cross bedded sandstones/siltstones that are variably calcareous. Both nappes dip shallowly ~20-30° to the NE, with the western package being ~210 m thick and the eastern package being ~105 m thick, separated by a thick sequence of similarly NE dipping Slaven Formation (Fig. 3). A majority of the upper plate package at Robertson is the Devonian Slaven Formation, which includes highly folded thinly bedded chert, argillite, and a single package of submarine basalts/ greenstone. This formation is well exposed on the west side of the property and although internally folded, dips gently to the east similar to the Elder Formation. Within the Slaven, is a single basalt/greenstone package which varies in thickness from ~88-143 m and is exposed on surface on the west side of the property. Surface mapping and drilling indicate that this layer dips shallowly to the east similar to the rest of the Slaven and extends to depth to the east.

Intruding the upper plate sequence at Robertson is the Tenabo stock and related dikes/sills which were emplaced along a west-northwest trend through the northern Shoshone Range and are located both proximal and distal to mineralized areas (Gilluly and Gates, 1965; Stager, 1977; Kelson et al., 2000, 2005). The intrusive complex consists of an elliptical-shaped composite stock or laccolith that varies in composition from diorite, which forms scattered bodies mainly along the northern and eastern stock margins, to granodiorite. In its longest dimension, the stock is exposed at surface for ~1670 m E-W and ~730 m N-S. The overall orientation of the stock is W-

NW following a similar orientation to other Eocene stocks in the northern Shoshone Range including Granite Mountain and Hilltop (Fig. 1A).

The earliest intrusive rocks are medium to dark gray, phaneritic diorite, which forms > 125 m sill-like bodies along the east and north margins of the stock (McCusker, written communication). At the surface, the diorite has steep contacts with other units, but appears to flatten out at depth. Spatially associated with the diorite, are several narrow and discontinuous andesite dikes with amphibole and pyroxene phenocrysts; however, these dikes are volumetrically poor and are not well exposed on surface. Cutting the diorite, are a series of dark brown dacitic porphyry dikes, ~0.5-1.5 m thick, containing 30-40 vol% phenocrysts in an aphanitic biotite rich groundmass. Forming the bulk of the composite stock, is a multiphase medium to coarse grained equigranular granodiorite that is locally porphyritic (Fig. 1B). The granodiorite stock is essentially a N-NW oriented ellipsoid, which, unlike the diorite, is sill-like near the surface and more plug-like to depth plunging steeply toward the NW. Previous K-Ar dating by Silberman and McKee (1975) and $^{40}Ar/^{39}Ar$ by Kelson et al., (2005), provide age constraints of the granodiorite. Recalculated K-Ar methods on igneous hornblende (M-123) yielded an age of 39.13 ± 0.80 Ma and K-Ar methods on igneous biotite (M-123, M-124) yielded an age range of 39.11-37.38 Ma with ± 2 sigma included. $^{40}Ar/^{39}Ar$ methods by Kelson et al., (2005) on igneous biotite (T99413-570) in the granodiorite returned a similar 8-step plateau age of 39.55 ± 0.10 Ma. A previously published Re/Os age for molybdenite (T99413-560) cutting the granodiorite stock by Kelson et al. (2005) yields a Re/Os age of 39.0 ± 1.4 Ma.

E-W striking, south-dipping ~55°, feldspar porphyry dikes cut the granodiorite and diorite and are well exposed on surface in the NW section of the property. These dikes can be up to 22 m thick and are laterally continuous for 2,042 m (Fig. 1B). Pebble dikes extend northward from the

northern contact of the stock and contain a variety of rounded and hydrothermally altered igneous and sedimentary rocks that are sometimes weakly mineralized (McCusker, written communication). Cutting all earlier intrusive rocks are a series of SE-striking subvolcanic feldspar-quartz-biotite porphyritic rhyolite dikes which typically dip ~35° to the SW and are laterally continuous for 875 m (Fig. 2). Previous K-Ar ages by Silberman and McKee (1975), of biotite (M-125) and sanidine (M-125) within the rhyolite, show similar ages at 35.68 ± 0.70 Ma and 35.59 ± 0.70 Ma. More precise weighted mean ages, by Henry (written communication), via $^{40}Ar/^{39}Ar$ methods on sanidine (H10-21, H10-22, Table 5) of the rhyolite indicate the same age at 35.83 ± 0.08 Ma, n = 12 and 35.84 ± 0.07 Ma, n = 15.

3.3. Gold Mineralized Zones

As a result of previous and current drilling, five main mineralized zones have been identified, each having distinct lithologic and structural controls (McCusker, 2004). The resource combining the Porphyry, Altenburg Hill, Gold Pan, and 39A zones is 2.03 Moz of gold at 0.53 g/t. (Barrick Q2 Report 2021). The Porphyry and Altenburg Hill zones occur within or along the contact of the Tenabo stock, the Gold Pan and 39A zones occur outside in the siliciclastic host rocks, and the Distal zone occurs ~500 m from the nearest exposed stock contact. The proximal zones are spatially associated with, and partly host by, the diorite and granodiorite margin phases of the stock, have a lower overall gold grade, and significantly higher copper than the more distal zones. The outboard zones are hosted in siliciclastic units, predominantly in the Slaven Formation, and exhibit higher silver, antimony, lead, and arsenic values (Fig. 1B). Here gold mineralization is strongly controlled by structures, lithologic contacts, and bedding planes. The entirety of defined gold mineralization is confined to the upper plate and to date there have only been two drill holes

at Robertson to reach the lower plate, one by the USGS in 1968 and one by Coral Gold in 2007, which reached the lower plate at depths of 896 m and 939 m, respectively.

3.4. Structural Setting

Within the Shoshone Range, rocks of the area are cut by low-angle thrust faults associated with the emplacement of the Roberts Mountain allochthon. A younger Mesozoic thrusting event, documented by Leonardson et al., (2011), exhibits a Cretaceous episode of east-directed thrusting that displaces the Roberts Mountains thrust and upper and lower plates around the Pipeline deposit known as the Abyss fault. This S-SW dipping fault is thought to represent a fault duplex, with imbricate thrusts linking the Roberts Mountains thrust and Abyss fault. At Robertson, these intra-allochthon thrusts range from the Lander thrust, which locally emplaces the Ordovician Valmy Formation over younger Elder and Slaven Formations, to thrust duplexes within Elder and Slaven (Fig. 3). Paleozoic rocks of the district are locally folded into small-scale isoclinal folds that typically plunge 5-15° to the N-NE. This fold orientation is largely confined to the Devonian Slaven Chert (Tarnocai, 1998). Larger district scale folds have been proposed Richardson, (2019); McCusker, (written communication); Chapin, (written communication); however, the merits of these larger scale features are not addressed in this study.

The intrusion of the Tenabo plutonic complex and related gold mineralization are controlled by a series of low-high angle faults and related fracture zones (McCusker, 2004). Previous logging and geophysics, has shown that this body was emplaced upward E-SE from the W-NW at depth. This event deformed the local lithologies in a brittle manner, resulting in a series of fracture networks and thrust faults, which strike ~N-S and dip moderately west. NW-striking high angle faults occur along the north side of the granodiorite and at least in part control the emplacement of feldspar porphyry dikes. According to Humphery (1945), a low-angle fault dipping 20° south

and filled by a porphyritic rhyolite dike cuts the Tenabo stock. A second rhyolite body, located 600 m to the east, forms a flat-lying sill-like dike, that is emplaced along a low-angle fault that also cuts the stock. These relationships indicate that, at least in the Tenabo area, Eocene-age low-angle faults younger than 39.55 Ma cut the Tenabo stock and are filled by 35.8 Ma rhyolite dikes (McCusker, written communication).

Magmatism appears to have ceased by ~33 Ma and after which, the area appears to have been tectonically quiescent until the onset of basin and range extension and northern Nevada rift volcanism in the middle Miocene (Colgan et al., 2014). Major extension in the Cortez region began ~16-17 Ma, as part of regional extension across much of the Basin and Range Province of western North America (Colgan and Henry, 2009). As a result of late Tertiary basin and range block faulting, rocks along the east side of the northern Shoshone Range, including the Tenabo area, have been tilted as much as 15° to 25° to the east (Gilluly and Gates, 1965). Henry and John, (2013) and Colgan et al., (2014) similarly found outcrops in the Shoshone Range supporting post-Eocene tilting and faulting, with outcrops of the 25.4 Ma Nine Hill Tuff dipping ~10-23° East, similar to overlying 16.5 to 15 Ma mafic lava flows of the northern Nevada rift (John et al., 2000). The overall structural style of extensional faulting in the northern Shoshone Range is similar to that documented within the Caetano caldera (Colgan et al., 2008, 2011), with closely spaced, west-dipping faults bounding east-tilted, “domino-style” fault blocks (Colgan et al., 2014). Miocene extension resulted in 22 ± 3 km of extension within the Caetano caldera oriented ~280° (Colgan et al., 2008). Following large-magnitude middle Miocene extension, post-10 to 12 Ma faulting in north-central Nevada took place on widely spaced, high-angle normal faults that cut both extended and unextended Miocene domains and formed the modern basins and ranges that now dominate the landscape (Colgan and Henry, 2009).

4. MATERIALS AND METHODS

4.1. Fieldwork and Sampling

Detailed field mapping in conjunction with trench and high wall sampling were primarily focused on vein and structural orientations. The goal of this work was to help delineate observations seen in drill core to the surface, in order to expand the geologic model. A handheld GPS was used to record observation locations to which were later input into the database with a total of 59 samples taken for geochemical analysis. Surface mapping at 1:5,000 scale was focused on areas with limited geologic knowledge, including Distal and west Altenburg Hill. A total of 6,131 m of core was logged at 0.30 m intervals from 30 drill holes with 137 samples taken and described using a binocular microscope. Emphasis while logging was focused on cross-cutting relationships, alteration styles, and vein paragenesis in order to guide sample collection. Visual estimates using a hand lens and a petrographic microscope were conducted to determine relative mineral abundances.

4.2. Petrography

119, 30-micron polished thin sections were described and annotated by standard transmitted and reflected light microscopy. Raman spectroscopy using a Horiba LabRAM HR Evolution Confocal Raman microscope instrument was used to identify accessory minerals in further detail. Analytical spectral device (ASD) analysis using a Terraspec mineral spectrometer was used to help identify clay minerals. Scanning Electron Microscope (SEM) analyses were conducted at the University of Nevada, Reno on a JEOL 6010^{TM} W-filament SEM equipped with a semiquantitative energy dispersive spectrometer (EDS); secondary electron and backscattered electron imaging were completed with an operating voltage of 20 kV, minimum spot size of ~1 µm, and a working

distance of 10 mm. A subset of 40 samples were analyzed using SEM-EDS to further understand mineral assemblages on the microscopic scale. A JEOL JSM-7100FT™ Field Emission Scanning Electron Microscope (FE-SEM) equipped with a cathodoluminescence (CL) detector was used to examine quartz generations in 5 auriferous vein samples.

4.3. Geochemistry

Drill core was sampled on 1.5 m intervals (23,731 samples total) by Nevada Gold Mines and analyzed by ALS Minerals Ltd. using ME-MS61L methods including four acid digestion and inductively coupled plasma-mass spectrometry (ICP-MS) for 48 elements. Geochemical indicators were combined from 161 drill holes into a comprehensive database owned by Nevada Gold Mines. Results were plotted and evaluated using ioGAS and LeapFrog software, creating a variety of classification diagrams including, total alkali vs silica plots (TAS), alumina saturation indices, Shand's peraluminosity index, various element ratio plots, and ternary diagrams (Middlemost, 1994); (Debon & Le Fort, 1988); (Maniar and Piccoli, 1989); (McMillan, 1995). Altered samples were sorted and grouped by separating anomalous values based on several classification diagrams. For petrologic classification, SiO_2 was estimated by normalizing major oxide data to 100% and subtracted from this. In doing this calculation, the wt. % for lost on ignition elements (LOI) is assumed to be zero. Given that many samples are hydrothermally altered, there most likely is some LOI component which SiO_2 fills in for in the calculation thus artificially increasing the SiO_2 values. Spearman rank correlation matrices were used to correlate elements for various mineralized zones in order to recognize geochemical patterns and determine if field groupings matched statistical classifications.

4.4. Geochronology

As a part of this study 8 samples were selected for geochronologic studies including, six new U/Pb LA-ICP-MS ages of intrusive phases, one molybdenite Re/Os age, and one hydrothermal orthoclase $^{40}Ar/^{39}Ar$ age. Ages from previous studies including Silberman and McKee (1971), Kelson et al. (2005, 2008), and Henry (pers. comm.) were compiled and select samples were recalculated in accordance with modern decay constants (Steiger and Jaeger, 1977). Recalculated ages were done so using the Fish Canyon sanidine (Min et al., 2000) (Kuiper et al., 2008).

All U/Pb analyses were completed at University of Nevada Reno (UNR). Zircon grains from 6 samples were extracted using standard mineral-separation techniques through sieving of material <500 µm. The sieved fine material was then run through a Jasper Canyon Research zircon concentrating table and grains were pulled directly from the top row of the table for picking for each sample. Zircon grains (~40-150 um in diameter) were subsequently placed on Kapton double-sided tape and mounted in Streuers epoxy and allowed to set for 24 hours. The mount was then polished using 5 µm SiC lapping film to expose the grains followed by 6, 3, 1, and 0.25 µm diamond suspension on low nap nylon and silk cloth pads. CL images of the zircon grains were collected using the FE-SEM at UNR. Zircon CL images were used to identify zoning and potential inherited portions within grains and to assist with laser-ablation spot placements. Zircon U-Th-Pb isotopic compositions were measured on an Agilent 7700x quadrupole ICP-MS with a Resonetics RESOlution M50 cell equipped with an ATL 193 nm excimer laser at UNR. Geostar version 10.12 and MassHunter 4.5 software were used to run the laser and mass spectrometer, respectively. Zircons were analyzed with a laser fluence of 3.0 J/cm^2, repetition rate of 7 Hz, and a spot size of 33 µm. The robustness of the 'dry' plasma was monitored by tuning the mass spectrometer in raster mode across glass reference material NIST 610 (5um/s transit speed, 3.0 J/cm^2, 10 Hz repetition rate, 33 µm spot) to obtain maximum sensitivity and minimum oxide production (U/Th

ratio of ~1.0 ; ThO/Th < 0.3%). Pulse analog (PA) factors were measured for masses $Pb^{204,6,7,8}$, Th^{232}, and U^{238} by adjusting the spot size of the NIST 610 tuning line described above from 33 to 75 um. Unknown measurements were bracketed every 8–10 measurements with 91500 (1062 Ma, Wiedenbeck et al., 1995) as the primary calibration reference material and Plešovice (337 Ma, Sláma et al., 2008), Temora2 (417 Ma, Black et al., 2004), and GHR1 (48 Ma, Eddy et al., 2020) as validation reference materials. Data were reduced using Iolite v4 (Paton et al., 2010) and all data was plotted in ET_Redux (Bowring et al., 2011; McLean et al., 2011). All uncertainties are reported with 2σ absolute uncertainty.

One sample was selected for Re/Os age determinations at the University of Alberta. Methods utilized are described in detail by Selby and Creaser (2004). The ^{187}Re and ^{187}Os concentrations in molybdenite were determined by isotope dilution mass spectrometry using Carius-tube, solvent extraction, anion chromatography and negative thermal ionization mass spectrometry techniques. For this work, a mixed double spike containing known amounts of isotopically enriched ^{185}Re, ^{190}Os, and ^{188}Os analysis was used (Markey et al., 2007). Isotopic analysis used a ThermoScientific Triton™ multicollector mass spectrometer equipped with Faraday collector. Total procedural blanks for Re and Os are less than <3 picograms and 2 picograms, respectively, which are insignificant in comparison to the Re and Os concentrations in molybdenite. The Reference Material 8599 Henderson molybdenite (Markey et al., 2007) is routinely analyzed as a standard, and during the past 6 years returned an average Re/Os date of 27.78 ± 0.07 Ma (n=31), indistinguishable from the Reference Age Value of 27.66 ± 0.1 Ma (Wise and Watters, 2011). The ^{187}Re decay constant used is 1.666e-11.a-1 (Smoliar et al, 1996).

One sample was submitted to the New Mexico Geochronology Research Laboratory for $^{40}Ar/^{39}Ar$ age determination. Here a Helix MC Plus™ Multicollector Noble Gas Mass Spectrometer

was used to determine isotope concentrations. The obtained integrated age was calculated by summing isotopic measurements of all steps and the error calculated by quadratically combining errors of isotopic measurements of all steps. The Fish Canyon Tuff sanidine (FC-2) with assigned age = 28.201 Ma (Kuiper et al., 2008) was used in calculating ages. Decay constants after Min et al. (2000); ltotal = 5.463 x 10-10 yr-1. Isotopic abundances after Steiger and Jäger (1977).

5. RESULTS

5.1. Geology and Geochemistry of Host Rocks

5.1.a Petrography

Upper plate siliciclastic lithologies of the RMT are locally represented at Robertson by the Ordovician Valmy Formation, Silurian Elder Formation, and Devonian Slaven Formation. Fine grained massive siliciclastic quartzites of the Valmy Formation are exposed on the west side of the Robertson area. In hand sample and thin section, the Valmy appears as a hard, non-foliated quartz rich siliciclastic orthoquartzite, with fine grained subrounded quartz grains 0.2-0.7 mm. Quartzite of the Valmy and Vinini Formations differs from that of the Osgood Mountain and Prospect Mountain Quartzites in its smaller maximum grain size, much better sorting, greater purity, association with bedded chert, absence of sedimentary structures, and occurrence as relatively thick beds (Ketner, 2013). The younger Elder Formation is exposed on the north and east side of the Robertson property, and is observed locally as fine-grained well bedded-cross bedded sandstones with interbedded siltstones, mudstones, and minor limestone lenses. Trace crinoids have been observed in hand samples, and previous studies, (Gilluly & Gates, 1965), indicate the presence of graptolites indicating a Silurian age assignment. Predominantly in core near the Tenabo stock, massive sandstones, which are variable calcareous, are observed due to

extensive alteration which has overprinted bedding features. Dark grey-black, platy, thin-bedded argillite and chert of the Slaven Formation display highly contorted beds at the outcrop scale and in hand sample constitute siliceous interbeds often with cleated layers where deformed. Deformation related to the RMT can be observed in thin section as stretching lineations, riedel shears, and static quartz recrystallization. Where there is contact metamorphism, these interbedded layers form biotite, calc-silicate, and quartz hornfels. Within the Slaven Formation, a package of massive grey non-magnetic metabasalt is present (Fig. 3). Locally the metabasalt displays flow banding, pillows, and vesicular textures often filled as amygdules with actinolite, quartz, or calcite. Optically, skeletal ilmenite is seen throughout the metabasalt and can be used as a geochemical identifier where less altered.

Five types of intrusive rocks are identifiable petrographically at Robertson based on features summarized in Table 1 and Figure 4. Diorite, dacite, granodiorite, rhyolite, and feldspar porphyry dikes are classification terms used in previous studies. Volumetrically minor units include andesite dikes and pebble dikes, which due to lack of field observations and drill intercepts, were not

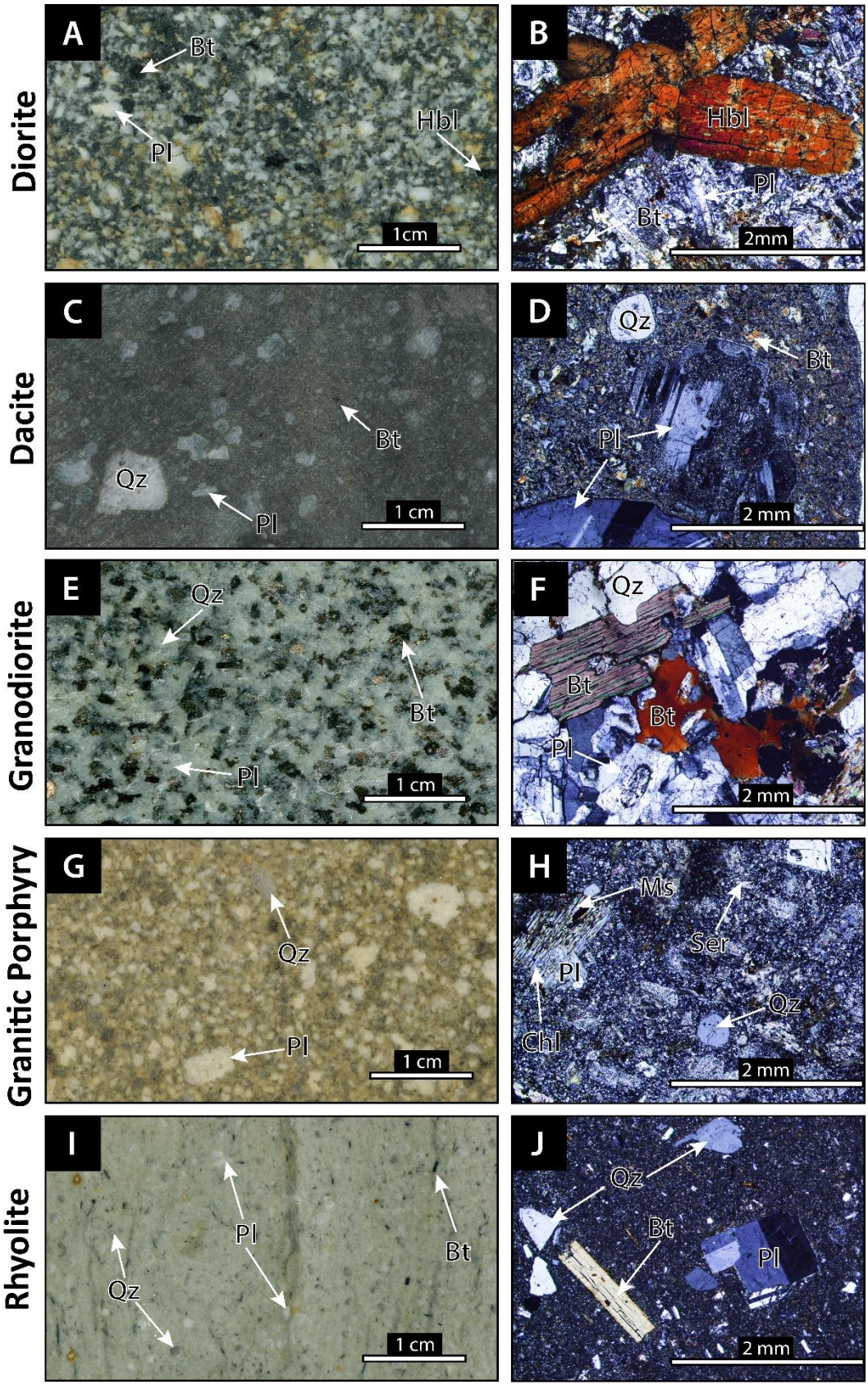
Diorite
A
Bt
Pl
Hbl
1cm
B
Hbl
Pl
Bt
2mm
Dacite
C
Bt
Qz
Pl
1 cm
D
Qz
Bt
Pl
2 mm
Granodiorite
E
Qz
Bt
Pl
1 cm
F
Qz
Bt
Bt
Pl
2 mm
Granitic Porphyry
G
Qz
Pl
1 cm
H
Ms
Ser
Pl
Qz
Chl
2 mm
Rhyolite
I
Pl
Bt
Qz
1 cm
J
Qz
Bt
Pl
2 mm

Fig. 4. Examples of intrusive rocks at Robertson Deposit represented by the rock slab photos on the left and cross-polarized photomicrographs on the right. (A-B) Equigranular diorite with intergrown K-feldspar, plagioclase, biotite, hornblende, and minor quartz (C-D) Porphyritic dacite with 30-40 vol% phenocrysts of quartz (0.5-15mm), plagioclase (0.1-4mm), and lesser biotite and K-feldspar (E-F) Equigranular granodiorite (medium grained phase) with interstitial quartz, plagioclase, K-feldspar, and biotite (G-H) Granitic porphyry dikes with 30-40 vol% phenocrysts of plagioclase (1-9mm), quartz (0.1-6mm), and lesser biotite and K-feldspar (I-J) Rhyolite with 15-25 vol% phenocrysts of plagioclase (0.25-1.5mm), quartz (0.15-2mm), biotite (0.1-1.25mm), and K-feldspar (0.1-1.25mm). Abbreviations: Bt = biotite, Chl = chlorite, Hbl = hornblende, Ms = muscovite, Pl = plagioclase, Qz = quartz, Ser = sericite

described petrographically or geochemically in this study. The diorite is mafic rich, medium to dark gray, fine-medium grained (0.05-4 mm) rock with twinned hornblende 0.2-4 mm and abundant plagioclase 50-60 vol%. The diorite is distinguished by its texture, dark color, and lack of quartz phenocrysts. Primary ilmenite within the diorite has been observed optically with the complete absence of magnetite. Dacitic dikes at Robertson exhibit porphyritic textures containing 30-40 vol% phenocrysts in an aphanitic microcrystalline biotite rich groundmass. Here, subrounded quartz phenocrysts up to 15 mm have been observed with plagioclase, often with mottled rims. Polyphase granodiorite is largely medium-coarse grained, equigranular with porphyritic end members, and distinguished from the diorite by volumetrically characteristic quartz (30-40 vol%), feldspar phenocrysts, and lack of amphiboles. Both medium and coarse-grained phases of the granodiorite have been observed to contain primary ilmenite. Coarse grained phases of the granodiorite exhibit crystals typically >5 mm and can occasionally display pegmatitic end members (Table 1). Optically the granodiorite presents granular textures with occasional aplitic zones and trace myrmekitic phases. Granitic porphyry dikes (formerly feldspar porphyry) with an aphanitic groundmass and phenocrysts (50-60 vol%) of subrounded quartz, biotite, k-feldspar, and distinct plagioclase cut the granodiorite and earlier intrusive phases (Fig. 4). These dikes are commonly are altered to sericite and or chlorite and are crosscut by later polymetallic base metal veining. Feldspar-quartz-biotite porphyritic rhyolite dikes display fresh phenocrysts (15-25 vol%) in a cryptocrystalline groundmass. Where unaltered, the dike margins

Table 1. Petrographic Characteristics of Robertson Igneous Rocks

		Phenocryst vol % and grain size (mm)						
Rock Type	Rock Texture	K-Feldspar	Plagioclase	Hornblende	Biotite	Quartz	Pheno Vol %	GM vol % and grain size
Diorite	Eq	1-3% 0.05-0.3mm	50-60% 0.2-2.5mm	15-20% 0.2-4mm	13-15% 0.1-0.75mm	5-7% 0.05-0.2mm	N/A	N/A
Dacite	Ppy	1-2% 0.2-1mm	30-35% 0.1-4mm	Trc	3-5% 0.2-1mm	10-13% 0.5-15mm	30-40%	60-70% 0.05-.15mm
Granodiorite (medium grained)	Eq	15-25% 0.25-1.75mm	35-40% 0.25-2mm	Trc	5-13% 0.1-1.75mm	40-50% 0.05-2.5mm	N/A	N/A
Granodiorite (coarse grained)	Eq	10-15% 0.05-3mm	30-45% 0.2-6mm	Trc	5-10% 0.1-4mm	40-50% 0.1-4mm	N/A	N/A
Granitic Porphyry Dikes	Ppy	5-10% 0.2-1.1mm	25-30% 1-9mm	Trc	5-7% 0.15-1mm	25-30% 0.1-6mm	50-60%	40-50% 0.25-0.075mm
Rhyolite	Ppy	15-20% 0.1-1.25	3-5% 0.25-1.5	Trc	5-10% 0.1-1.25mm	30-40% 0.15-2mm	15-25%	75-85% <0.025-0.05mm

Mineral abundances were determined using visual percentage charts in both hand samples and polished thin section
Abbreviations: Eq = equigranular, Ppy = porphyritic, Trc = Trace

exhibit a black vitrophyre that reaches up to 0.5 m thick. The classification terminology regarding the dacite and rhyolite dikes imply an extrusive nature; however, field relations and observations from detailed core logging would suggest that these units are not extrusive or subaerial in nature, but rather are subvolcanic. Because of this, the terms hypabyssal rhyolite and hypabyssal dacitic dikes are used to describe these units and will be referred to as such in the remainder of this thesis.

5.1.b Lithogeochemistry

As a result of multi-element geochemical analysis four of the five previously described intrusive rocks have been classified into distinct populations. Due to limited drill intercepts and geochemical analysis the hypabyssal rhyolite dikes have not been included in this geochemical suite. Using a total alkali silica diagram after Middlemost (1994) the least altered samples from the four intrusive units define a cluster within the granodiorite field straddling the boundary of the granite field (Fig. 5B). Total SiO_2 ranges from 63-79.5 wt. %, with the granodiorite falling on the higher end and the diorite representing the lower granodiorite SiO_2 field. These relatively high SiO_2 values may in part be explained by how SiO_2 was calculated, where major oxides were normalized to 100% and SiO_2 representing the subtracted field which also includes the LOI elements. These values may also be explained by alteration, specifically silicification, that may have not been filtered out when cleaning the data.

Alumina saturation molar ratios in a majority of samples indicate granitoids of metaluminous nature with granitic porphyry dikes and some diorite samples tailing into the peraluminous field (Fig. 5A). In the B-A diagram (see Bonin et al., 2020) the differentiation index indicates that all rocks plot into the metaluminous field, again with a few granitic porphyry dikes and some diorite

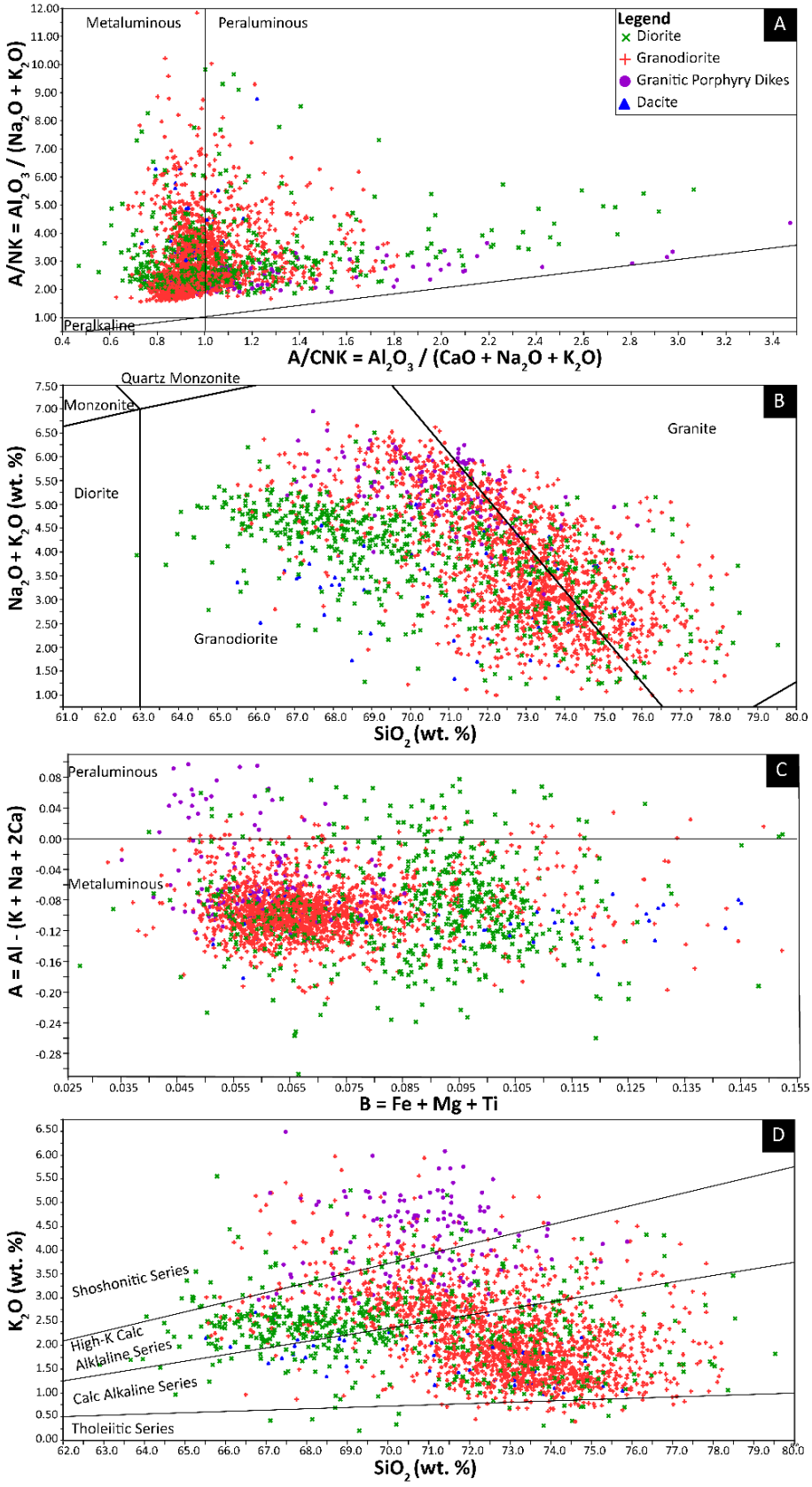
A
Legend
Diorite
Granodiorite
Granitic Porphyry Dikes
Dacite
Metaluminous
Peraluminous
Peralkaline
A/NK = Al2O3 / (Na2O + K2O)
A/CNK = Al2O3 / (CaO + Na2O + K2O)
B
Quartz Monzonite
Monzonite
Granite
Diorite
Granodiorite
Na2O + K2O (wt. %)
SiO2 (wt. %)
C
Peraluminous
Metaluminous
A = Al - (K + Na + 2Ca)
B = Fe + Mg + Ti
D
Shoshonitic Series
High-K Calc Alkaline Series
Calc Alkaline Series
Tholeiitic Series
K2O (wt. %)
SiO2 (wt. %)

Fig. 5. Representative geochemical plots of Robertson intrusive rocks. (A) Shand's peraluminosity index representing the molar ratio A/NK = $Al_2O_3/(Na_2O + K_2O)$ as function of the molar ratio A/CNK = $Al_2O_3/(CaO + Na_2O + K_2O)$ (B) Total Alkali Silica diagram after Middlemost (1994) (C) Differentiation index B = Fe + Mg + Ti as function of the peraluminous index A = Al-(Na + K + $_2$Ca) after Debon & Le Fort (1988) (D) K_2O vs. SiO_2 diagram showing the main magmatic series. Note that SiO_2 in these diagrams was estimated assuming zero LOI elements (see methods for details).

samples within the peraluminous domain (Fig. 5C). These rocks plot throughout the calc-alkaline series, high-K calc alkaline series, and into the shoshonitic series (Fig. 5D). Again, variations within these diagrams may be explained in part by hydrothermal alteration which is present in many of these units. Harker variation diagrams illustrate the negative correlation of these intrusive units with respect to Fe_2O_3, TiO_2, and CaO, indicating crystal fractionation (Fig. 6 and Appendix E). Granitic porphyry dikes express elevated values of Zr and Rb and depressed values of compatible elements MgO, CaO, Na_2O compared to the rest of the suite. Trace element analysis would be needed in order to properly explain these differences.

Based on this geochemical analysis the diorite would appear to be of granodiorite composition; however, our petrographic observations suggest quartz contents (<20 wt. %) are too low to be a granitic rock (Table 1). Here it is inferred that the geochemistry is an over interpretation of this unit that may be representing altered end members. This, along with the compatible element concentrations in Figure 6 would suggest that this unit is less evolved compared to the granodiorite. Granitic porphyry dikes plot in both the granodiorite and granite field; however, when combined with major oxide plots, observed CaO and Na_2O values are lower and K_2O values are higher compared to other intrusive phases. These findings, along with petrographic observations lead to the classification of formerly named feldspar porphyry dikes to granitic porphyry dikes. Now while this geochemical variation may also be explained by increased alteration, it is believed that the statistical confidence of the 436 samples analyzed accurately reflects the classification.

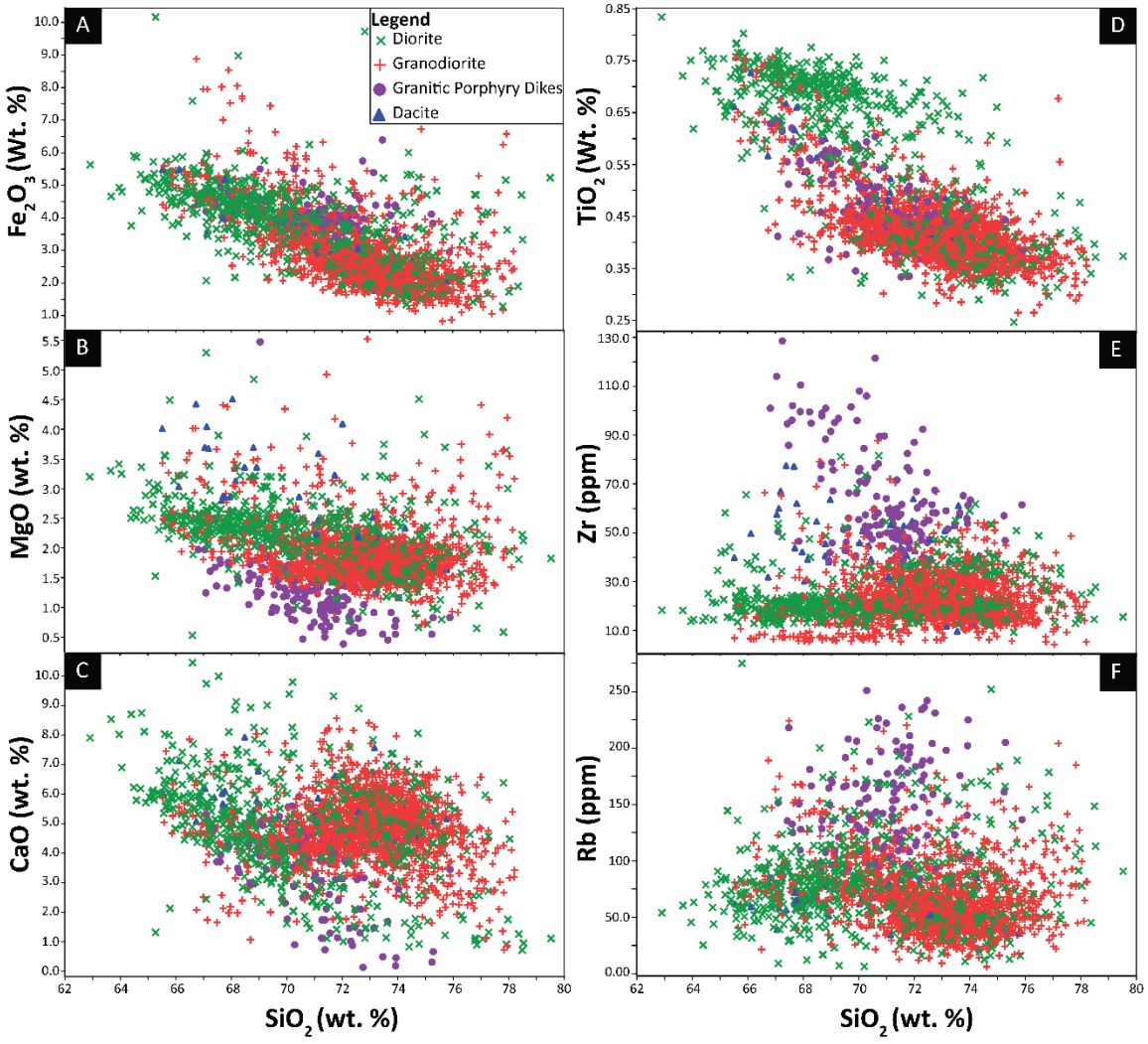

Fig. 6. Major element compositions of intrusive rocks from Robertson. Multi element data from this study (n = 3,973). Note that SiO_2 in these diagrams was estimated assuming zero LOI elements (see methods for details).

5.2. Contact Metamorphism and Hydrothermal Alteration

5.2a Contact Metamorphism

The emplacement of the Tenabo stock produced an aureole of contact metamorphism affecting the local siliciclastic lithologies yielding the formation of quartz, biotite, and calc-silicate hornfels that can be observed up to 1 km away from the Tenabo stock (Table 2). Due to the

Table 2. Metamorphic and Metasomatic Assemblages at Robertson

	Style	Gangue	Sulfides	Morphology	Description
Contact Metamorphism	Quartz Hornfels	Qz	N/A	Massive, fine grained, conchoidal fractures	Occurs within the hornfels aureole of the Tenabo stock. Recrystallization of host, overprints depositional textures Often gradational with biotite hornfels
	Biotite Hornfels	Bt - qz	N/A	Fine grained bands of layered interstitial brown biotite & quartz	Occurs within the hornfels aureole of the Tenabo stock and takes on irregular shape/forms as a result of deformed host rocks
	Calc-Silicate Hornfels	Act - qz	N/A	Fine grained pale green calc-silicates & quartz	Occurs within the hornfels aureole of the Tenabo stock within impure calcareous strata eg. Elder Formation
Hydrothermal Alteration	Endoskarn	Act - qz ± vrm - chl - ep - ves - ttn - non - ap - pl (?)	± Po - ccp	Fracture/ vein controlled, appears forest green and milky white	Destroys igneous textures where strongest (primarily granodiorite & diorite)
	Potassic Alteration	Bt - kfs ± chl - zo - zeo	± Mol - ccp	Strongest zones are seen as vein stockworks destroying igneous textures	Flooding of pink potassium feldspar and black secondary biotite, hosted both within intrusive and siliciclastic units, commonly as vein selvages
	Exoskarn	Act - chl - ep ± cal - ttn - zo - ap	± Po - ccp - py - mrc	Massive replacement where strongest, fracture controlled where weaker, sulfide rich	Controlled along fractures, lithologic contacts or bedding planes, proximal to intrusive centers or focused along major structures
	Sericitic	Qz - ser ± clay - chl - rt	Py ± apy - gn - sb - sp - ccp - ttr	Friable, weak, pale white rock that overprints igneous textures	Strong base metal signatures (Pb-Zn-Sb-Ag-Sn), commonly along dikes and as selvages to veins
	Chloritic	Chl - cal - clay ± ant	Py ± gn - sp	Fracture controlled chlorite often replacing mafic minerals	Commonly proximal to sericitic alteration in igneous units but is seen along fractures in siliciclastic host rocks

Mineral abbreviations: Act = actinolite, Ant = Anatase, Ap = apatite, Apy = Arsenopyrite, Bt = biotite, Cal = calcite, Chl = chlorite, Ccp = chalcopyrite, Ep = Epidote, Gn = Galena, Kfs = potassium feldspar, Mrc = marcasite, Mol = molybdenite, Non = Nontronite, Pl = Plagioclase, Py = pyrite, Qz = quartz, Rt = rutile, Ser = sericite, Sp = sphalerite, Sb = Stibnite, Ttn = Titanite, Ttr = tetrahedrite, Vrm = vermiculite, Ves = vesuvianite, Zeo = Zeolite, Zo = zoisite

complex thin bedded nature and internal deformation within the siliciclastic units the resulting thermal metamorphism shares this complex nature. Original protolith composition exerts significant primary control on the resulting alteration assemblage and consequently forms differing mineral assemblages. Quartz hornfels appears as fine-grained, massive, typically milky quartz aggregates that break conchoidally and overprints previous sedimentary structures such as cross-bedding. In thin section, quartz hornfels can be seen as static quartz recrystallization involving grain boundary migration (GBM). Here grain boundaries of quartz have been reduced and exhibit lobate textures. If recrystallization is indeed GBM then this metamorphism likely occurred at temperatures above 500°C based on experimental quartz recrystallization tests by Stipp et al., (2002). Quartz hornfels often grades into both biotite and calc-silicate hornfels and commonly forms crackle breccias when deformed. Biotite hornfels consists of medium to dark brown to black fine-grained layers of interstitial biotite that can often take on irregular shapes and forms, due to the complex bedding nature and deformation of the host. In thin section, biotite hornfels displays microstructures of dynamic bulging recrystallization within biotite grains, where grain boundaries display irregular protrusions. Biotite hornfels typically occur in muddy/ silty protoliths with variable amounts of quartz. Calc-silicate hornfels are developed in weakly calcareous rocks and impure strata, forming a dense pale green rock with fine actinolite and quartz, most often observed within the Elder Formation. Here fine calc silicates are commonly overprinted by later hydrothermal alteration events.

5.2b Hydrothermal Alteration

Hydrothermal alteration at Robertson includes a sequence that ranges from early endoskarn, potassic, and exoskarn to later sericitic and chloritic alteration. The alteration types discussed here are classified based on distinct mineral assemblages and/or visible physical changes in the

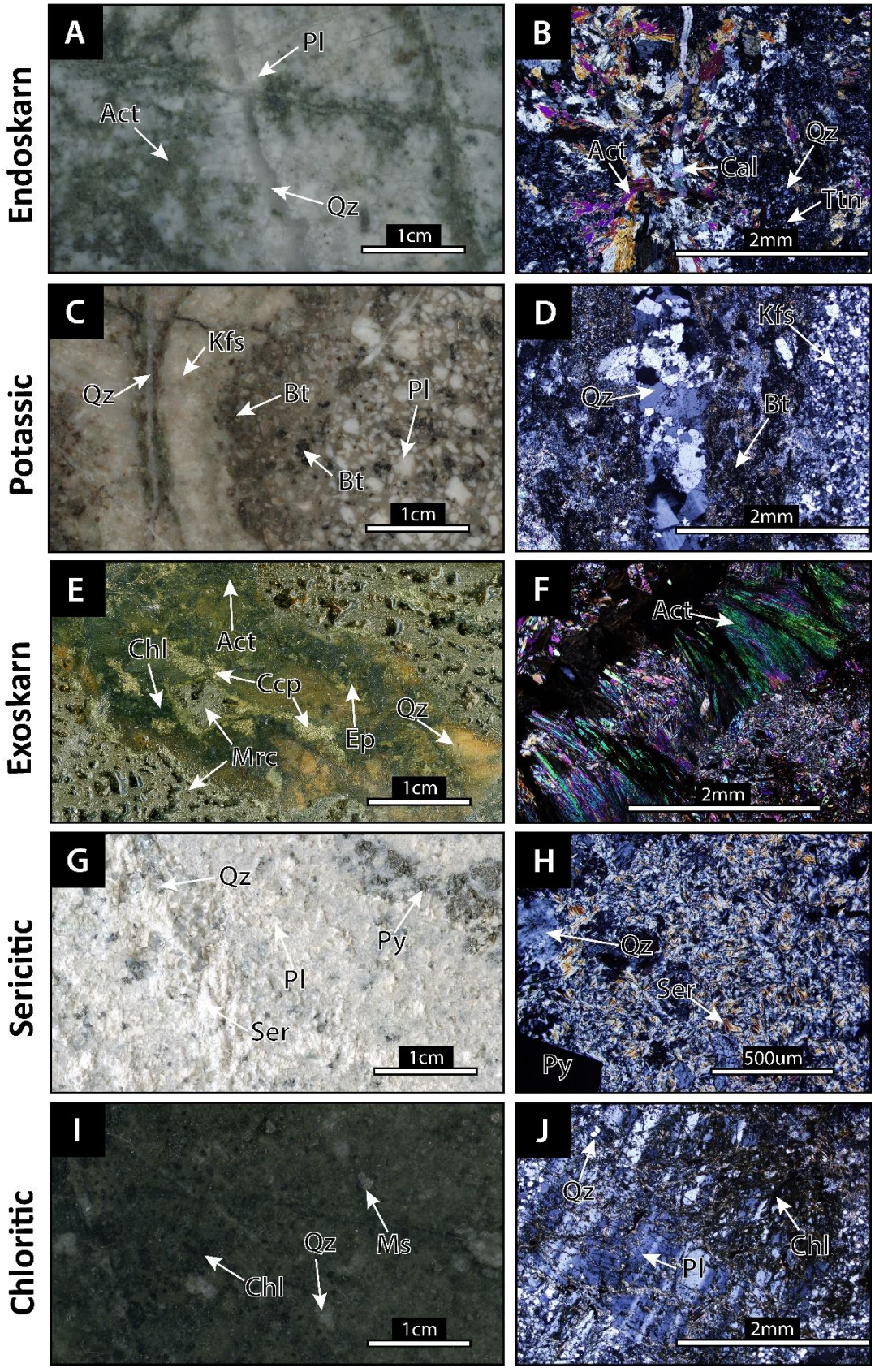
Endoskarn
A
Pl
Act
Qz
1cm
B
Act
Cal
Qz
Tth
2mm
Potassic
C
Kfs
Qz
Bt
Pl
Bt
1cm
D
Kfs
Qz
Bt
2mm
Exoskarn
E
Act
Chl
Ccp
Qz
Ep
Mrc
1cm
F
Act
2mm
Sericitic
G
Qz
Py
Pl
Ser
1cm
H
Qz
Ser
Py
500um
Chloritic
I
Qz
Ms
Chl
1cm
J
Qz
Chl
Pl
2mm

Fig. 7. Hydrothermal alteration styles of the Robertson Deposit represented by the rock slab photos on the left and cross-polarized photomicrographs on the right. (A-B) Endoskarn alteration within granodiorite, seen as actinolite and quartz overprinting igneous textures (C-D) Potassic alteration within diorite, seen as a vein selvage with secondary biotite and K-feldspar replacing primary igneous minerals (E-F) Exoskarn alteration within the Silurian Elder formation, pervasive replacement by actinolite and lesser quartz, chlorite, and epidote with abundant sulfides including pyrite, chalcopyrite, and marcasite (G-H) Sericitic alteration within granodiorite, seen as strong quartz, sericite, and sulfides. In this sample primary mafic minerals here have been altered out (I-J) Fracture controlled chloritic alteration of granodiorite. Abbreviations: Act = actinolite, Bt = biotite, Ccp = chalcopyrite, Chl = chlorite, Ep = epidote, Hbl = hornblende, Ksp = K-feldspar, Mrc = marcasite, Ms = muscovite, Pl = plagioclase, Py = pyrite, Qz = quartz, Ser = sericite

host lithology and are summarized in Table 2 and Figure 7. Intensity is used here to describe the degree of hydrothermal alteration from weak (primarily fracture controlled), through moderate (fracture controlled and disseminated), to strong (pervasive). Note that all minerals described may have not precipitated at the same time but rather reflect summation of all events until the present. Thus, the term assemblage is used to describe minerals thought to be cogenetic and the term associated is used to describe minerals thought to simply coexist. In separating these events, cross-cutting and off-setting relationships in conjunction with age dating was used in order to accurately determine relative timing

Endoskarn

Endoskarn alteration consists primarily of an actinolite-quartz assemblage with lesser, variable amounts of associated chlorite, epidote, vesuvianite, titanite, and nontronite. This assemblage is typically fracture or vein controlled and appears as dark green patches or lenses, most commonly disseminated within igneous dikes on the margins of the Tenabo stock. This alteration type is seen within all proximal mineralized zones including the Porphyry, Gold Pan, and Altenburg Hill zones. The sulfides frequently associated with endoskarn alteration include pyrrhotite, chalcopyrite, and pyrite. In previous studies light brown, fine grained garnet has been observed with this mineral assemblage (McCusker, 1996). Strong endoskarn alteration overprints

original igneous textures and within these zones, mafic minerals and feldspars are replaced. Within strong zones, contacts between intrusive units and hornfels can become difficult to distinguish, bordering between endoskarn and exoskarn. Here this alteration type can be associated with intense zones of mineralization and veining. In thin section, a wash of actinolite and quartz is typically seen with minerals such as apatite and titanite at higher magnification, locally in close association with the actinolite. Where more moderate or weaker degrees of alteration occur, rims of mafic minerals and feldspars become mottled, but are not completely replaced. In weak zones, alteration is constrained along small fractures and structures depending on the characteristics of the protolith. Geochemically these zones are typified by the introduction of Ca and the removal of K; however, due to later stages of alteration and veining, these patterns may become overprinted. In places, endoskarn can be observed being cut by secondary biotite, but in a few instances, the opposite has been observed. This may be the result of the emplacement of multiple intrusions and successive hydrothermal fluid phases at increased temperatures (diorite then granodiorite).

Potassic Alteration

Potassic alteration at Robertson can be observed both within Eocene igneous rocks as well as the Paleozoic siliciclastic units; however, it is best developed within intrusive rocks of the Porphyry and Altenburg Hill zones. Within intrusive rocks, this alteration assemblage consists of widespread fine-grained secondary biotite and K-feldspar selectively replacing coarse-grained magmatic biotite, hornblende, and plagioclase. Often fine-grained secondary biotite is later replaced by chlorite. Where strongest, potassic alteration destroys primary igneous textures and accompanies stockwork veining commonly infilled with later zoisites. In these strong zones, molybdenite and lesser chalcopyrite are typically observed in quartz vein stockworks, with lesser disseminated

occurrences of these sulfides. Where less intense, secondary biotite can be seen along narrow veinlets or fractures where it is often overprinted and/or offset by later calc-silicates or sericite. Outside of the intrusion, within upper plate units, fine secondary biotite can be seen along fine mm scale fractures cutting hornfels. Here, potassic alteration is viewed in more moderate and weaker styles due to the chemical nature of the protolith. Within the Slaven metabasalt, this alteration can form cm-scale selvages on quartz-sulfide veins which have been observed to overprint primary minerals such as skeletal ilmenite. The representative geochemical signature of potassic alteration in these zones includes increased K and decreased Ca-Na values. These areas also exhibit higher Rb/Sr and Zr/Hf ratios most likely due to increased K-metasomatism.

Exoskarn

The exoskarn alteration mineral assemblage observed at Robertson includes actinolite-chlorite-epidote ± calcite-titanite-zoisite, and is seen outside of the Tenabo stock within the Slaven and Elder Formations. This alteration type can be seen both proximal to intrusive centers, typically in the Elder Formation, or outboard of intrusions focused along fracture zones, lithologic contacts, or bedding planes. Where strongest, exoskarn appears as massive, dull, dark green, sulfide rich bodies that may reach 6 m thick and persist laterally for many tens of meters, such as in the Gold Pan or 39A zones. Accompanying these local replacement horizons, are associated 8-70% fine sulfides, including pyrite, marcasite, pyrrhotite, chalcopyrite, and lesser arsenopyrite (McCusker, 2004). In the strongest zones, host rocks are difficult to discern as bedding features are overprinted and usually accompanied by extensive brecciation. Where weaker, exoskarn can be seen as open space fillings along fractures, lithologic contacts, or bedding planes. Like the hornfels, protolith composition has strong influence over where exoskarn forms and how it is manifested. Due to the relative calcareous nature of the Elder Formation compared to the other

formations, exoskarns tend to form preferentially in these units where primary minerals can be easily removed. Within the Slaven metabasalt, exoskarn alteration is additionally abundant, often with patches or blebs of calc-silicate and later minerals infilling vesicles. Due to the Fe-rich nature of the metabasalt, sulfidation of this unit tends to occur, forming zones rich in pyrrhotite, chalcopyrite, pyrite, and later marcasite. Within less reactive host rocks, exoskarn alteration is tightly constrained to veinlets, fractures, and bedding planes. Locally these zones can be associated with increased gold mineralization; however, this is not consistent throughout the whole deposit.

Sericitic Alteration

Sericitic alteration is observed as selective or pervasive replacements of host lithologies, forming quartz-sericite-sulfide ± clay-chlorite-rutile rich assemblages. This alteration type is most common within dikes and along selvages of quartz-sulfide veins. The result is typically a pale, white, friable/ weak rock superimposed on earlier alteration events such as potassic alteration. Where strongest, primary igneous textures have been destroyed, mafic minerals are completely altered to sericite or clay minerals, and disseminated or vein-controlled sulfides are common. Quartz addition to the groundmass and replacement of feldspars by sericite is pervasive in these zones. ASD analysis of sericitic alteration in representative samples, confirms the presence of illite overprinting hydrothermal muscovite in igneous dikes (Appendix F). The associated disseminated sulfides in these areas typically include pyrite-arsenopyrite ± sphalerite-galena. Vein-hosted sulfides in these zones show strong Pb-Zn-Sb-Ag-Sn signatures and consist typically of pyrite, arsenopyrite, sphalerite, galena, and stibnite with lesser amounts of tetrahedrite, freibergite, and stannite. In weaker zones quartz-sericite-sulfides are fracture-controlled, preferentially alter mafic minerals, and are constrained closer to fracture margins. Within

siliciclastic units, sericite is strongly fracture controlled and typically accompanies polymetallic veins. Here quartz and sulfide assemblages dominate, and disseminated styles are less common. Locally this alteration type can be seen superimposed on earlier alteration styles and in thin section, sericite can be observed overprinting earlier actinolite or secondary biotite alteration. Geochemically these zones broadly see increases in K, Hg, Sb, As, Pb, Zn.

Chloritic Alteration

Chloritic alteration is the latest type of alteration observed at Robertson and is characterized by the mineral assemblage chlorite-calcite-clay ± anatase. Similar to other styles of alteration, chloritic alteration is strongly controlled by protolith composition. This alteration type is most common within igneous units as partial or complete replacements of mafic minerals; however, it can also occur along fractures cutting siliciclastic rocks. Sulfides in these areas are frequently pyrite with lesser galena and sphalerite. The strongest zones show disseminated assemblages away from fractures and form pervasive replacements seen in Figure 7. In weaker zones, chlorite is constrained to the fracture envelopes and calcite is more common. Typically, chloritic alteration is observed proximal to sericitic alteration and can occasionally be observed grading into it.

5.3. Gold Mineralization

Gold mineralization at Robertson, has previously been recognized in 5 main mineralized zones including Porphyry, Altenburg Hill, Gold Pan, 39A, and Distal (Fig. 1B). All of these zones occur within or near the Tenabo stock, with the 39A and Distal zones being the furthest from intrusive rocks. Here, previously defined mineralization outlined in past reports along with new insights from this study are presented. Characteristics of gold mineralization within the different zones can be seen in Table 3 and Figures 8 and 9. Within these 5 zones, gold occurs as native particles

Table 3. Ore Resource Zone Characteristics

Resource Zone	Host Rock	Mineralization Style	Gold Association	Dominant Alteration	Description
Altenburg Hill	Hornfels and intrusive rocks	Sheeted veins with Au alone or within apy grains	Galena-Native Bismuth-Hedleyite	Potassic	Potassic alteration is best developed here. Galena, freibergite, and boulangerite clearly post date apy
Porphyry	Hornfels and intrusive rocks	Structurally controlled disseminations of Au and in veins with minor bi sulfosalts (no apy)	Electrum-Native Bismuth-Bismuthinite-Babkinite-Kawazulite-Naumannite	Potassic & exoskarn	All Au found within intrusive units was alone. Electrum & Bi sulfosalts were only observed in siliciclastic units. Lesser Te & As signature. Cu best developed here. Bi clearly postdates ccp
Gold Pan	Hornfels and basalt	Au disseminated alone and/or in veins within apy	Loellingite-Galena-Native Bismuth-Pilsenite-Tellurobismuthite-Hedleyite-Tetradymite-Ikunolite-Kawazulite-Hessite-Cosalite-Canfieldite-Tsumoite	Exoskarn	Basalt commonly sulfidized and exoskarn altered with act-po-ccp. Strong sulfosalts. Loellingite within apy. Ccp & gn clearly postdate apy
39A	Hornfels	Structurally controlled disseminations of Au within massive sulfide layers alone or within apy grains	Loellingite-Native Bismuth-Tellurobismuthite-Hedleyite-Tetradymite-Ikunolite	Exoskarn	Massive sulfide layers up to 9 m thick. Loellingite within apy, Au clearly postdates apy, abundant marcasite postdates apy
Distal	Hornfels	Structurally controlled disseminations of Au and in veins commonly inside apy grains	Electrum-Native Bismuth-Hedleyite-Pilsenite-Protojoseite-Bismuthinite-Tetradymite-Ikunolite-Cosalite-Babkinite-Canfieldite	Exoskarn	Strong increase in apy, po commonly within apy, ccp clearly postdates apy, abundant marcasite postdates apy

Mineral abbreviations: Actinolite = Act Arsenopyrite = Apy Chalcopyrite = Ccp Galena = Gn Pyrrhotite = Po
Chemical Formulas: Babkinite = $Pb_2Bi_2(Se,S)_3$ Bismuthinite = Bi_2S_3 Boulangerite = $Pb_5Sb_4S_{11}$ Canfieldite = Ag_8SnS_6 Cosalite = $Pb_2Bi_2S_5$ Electrum = AuAg Freibergite = $(Ag, Cu, Fe)_{12}(Sb, As)_4S_{13}$ Hedleyite = Bi_7Te_3 Hessite = Ag_2Te Ikunolite = $Bi_4(Se,S)_3$ Kawazulite = $Pb_2Bi_2S_5$ Loellingite = FeAs Native Bismuth = Bi Naumannite = Ag_2Se Pilsenite = Bi_4Te_3 Protojoseite (Bi_7TeS_5) Tellurobismuthite = Bi_2Te_3 Tetradymite = Bi_2Te_2S Tsumoite BiTe

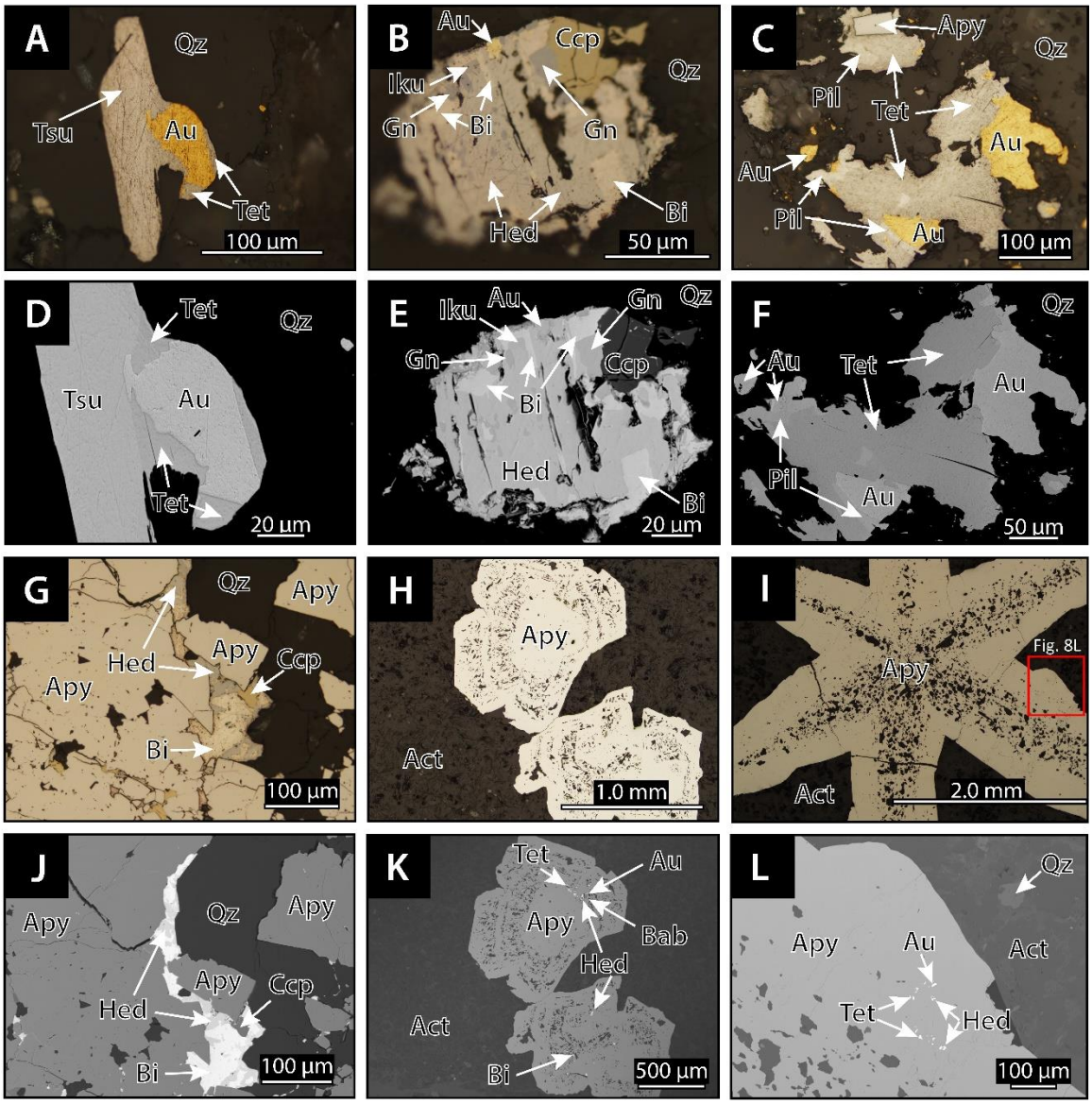

Fig. 8. Reflected light and backscatter electron photomicrographs of gold mineralization and associated hydrothermal minerals. Each reflected light photomicrograph has the associated backscatter electron image below it (A & D) Gold in close association with tsumoite and tetradymite (B & E) Gold with native bismuth, galena, hedleyite, ikunolite, and chalcopyrite. Chalcopyrite here is seen cut by bi-bearing minerals (C & F) Gold in association with tetradymite and pilsenite. These bi-bearing minerals surround nearby arsenopyrite grains (G & J) Native bismuth, hedleyite, and chalcopyrite infill cracks within earlier arsenopyrite (H & K) Mottled arsenopyrite with apparent zoning infilled with gold, hedleyite, babkinite, tetradymite, and native bismuth. EDS analysis shows no chemical differences in growth zones (I & L) Arsenopyrite grain with mottled interior infilled with gold, tetradymite, and hedleyite. L is zoomed in view of I annotated with the red square. Abbreviations: Act = actinolite, Apy = arsenopyrite, Au = gold, Bab = Babkinite ($Pb_2Bi_2(Se,S)_3$) Bi = native bismuth, Ccp = chalcopyrite, Gn = galena, Hed = Hedleyite (Bi_7Te_3) Iku = Ikunolite ($Bi_4(S,Se)_3$, Pil = Pilsenite (Bi_4Te_3) Py = pyrite, Qz = quartz, Tet = Tetradymite (Bi_2Te_2S), Tsu = Tsumoite (BiTe)

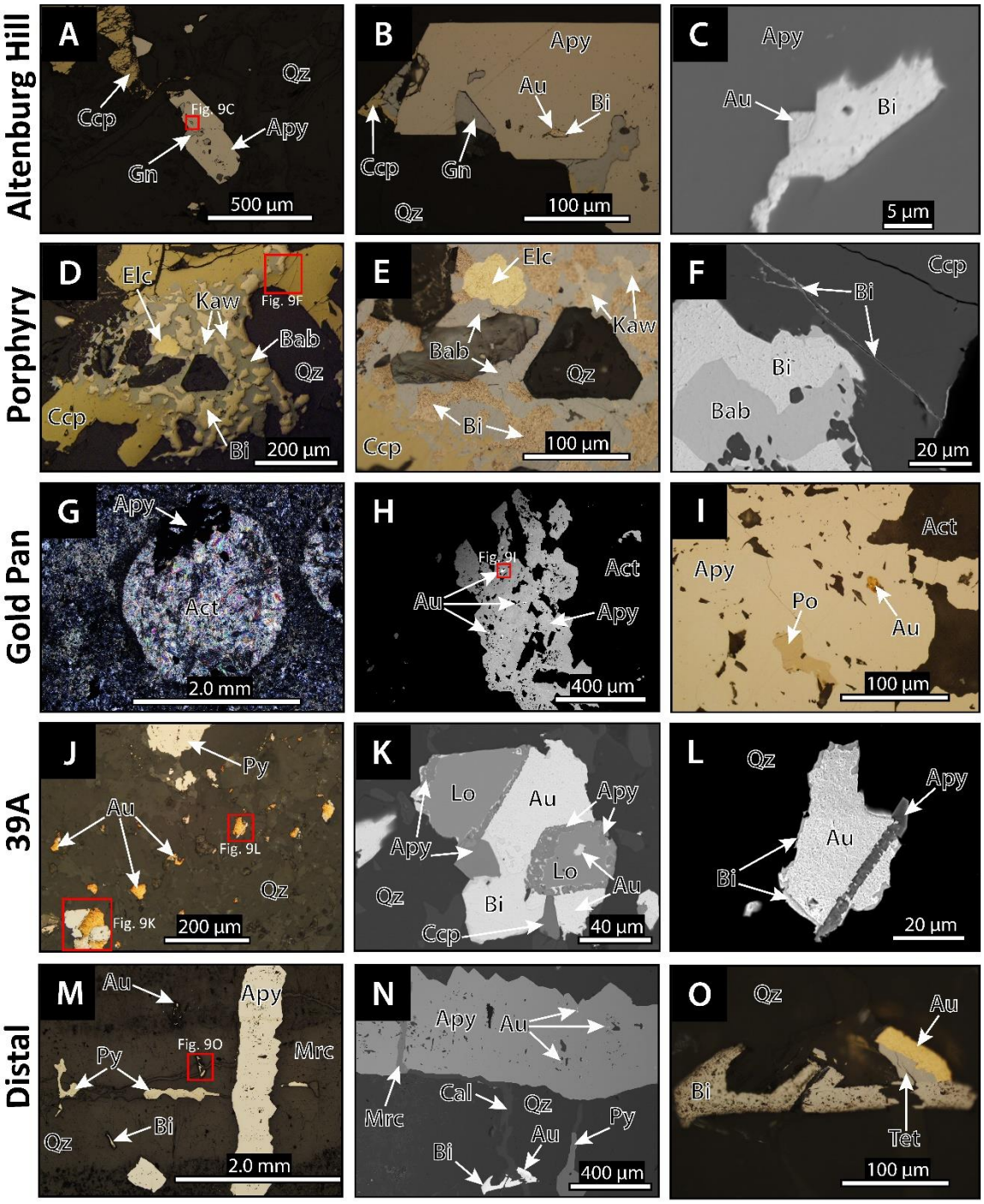

Fig. 9. Reflected light, transmitted cross-polarized light, backscatter electron and secondary electron photomicrographs of gold mineralization in the different resource zones at Robertson including Altenburg Hill (A-C), Porphyry (D-F), Gold Pan (G-I), 39A (J-L), and Distal (M-O). (A) Quartz - gold vein cutting granodiorite, sample can be seen in fig. 9k (B) Zoom in view of image A of au in apy (C) Au and native bismuth within apy (D) Gold and bi sulfosalts on ccp grain precipitated in sheeted veins (core scan in Fig. 9H) (E) Zoomed in view of image D with gold and bi sulfosalts with ccp (F) Native bi cutting ccp along fracture

(G) Amygdule in basalt with act and apy (H) Apy grain from image G with au inside (I) Zoom in on au and po within apy (J) Massive sulfide zone in 39A with native au in quartz gangue (K) Zoom in on left au grain from image J with associated minerals (L) Zoom on right grain from image J with au infilling apy (M) Quartz - gold vein cutting quartz hornfels (N) Zoom in on image M with au grains seen within apy and outside in quartz vein (O) Zoom in on image N, au associated with native bismuth and tetradymite. Abbreviations: Act = actinolite, Apy = arsenopyrite, Au = gold, Bab = Babkinite ($Pb_2Bi_2(Se,S)_3$) Bi = native bismuth, Cal = calcite, Ccp = chalcopyrite, Gn = galena, Kaw = Kawazulite ($Pb_2Bi_2S_5$) Lo = loellingite, Mrc = marcasite, Ms = muscovite, Pl = plagioclase, Po = pyrrhotite, Py = pyrite, Qz = quartz, Ser = sericite, Tet = Tetradymite (Bi_2Te_2S)

of generally high fineness that range in size from 2 to 200 µm and with an average of 40 µm (McCusker, 1996). This free, visible gold can be found both within intrusive and siliciclastic rocks as disseminations or in veins, commonly associated with tellurides and Bi-Te-Se-Pb-Ag-S bearing minerals, most commonly including native bismuth, hedleyite, and tetradymite. Frequently, native gold particles can be observed encapsulated within arsenopyrite grains and quartz gangue and/or on the surface of pyrrhotite, arsenopyrite, chalcopyrite, and loellingite grains. For all samples analyzed for multi-element geochemistry at Robertson, gold correlates moderately with Bi (0.41) Te (0.52) Cu (0.44), using a spearman correlation matrix.

5.3.a Altenburg Hill Zone

The Altenburg Hill zone is located along the southeast contact of the granodiorite, where lesser diorite intrudes highly fractured and folded biotite and quartz hornfels of the Elder Formation at depth, and shallows to the north where the intrusion is exposed at surface. Here, the Tenabo stock cuts the thrusted contact between Elder and Slaven Formations, which are exposed on surface (Fig. 1B). Within the Slaven Formation, an east dipping package of metabasalt is exposed, and based on drilling, is currently estimated to be ~122 m thick (Fig. 3). Potassic alteration is best developed within the Altenburg Hill zone, with pervasive replacement of igneous rocks by secondary K-feldspar and biotite (Fig. 7C). On the west side of this zone, potassic alteration can also be seen cutting Slaven metabasalt in the form of biotite veinlets (Fig. 10B).

The Altenburg Hill zone is confined primarily to the Elder Formation; however, gold mineralization has also been observed within the Tenabo stock. Here, gold is distributed along high angle, NW-striking, SW-dipping faults within hornfels of the Elder Formation. The Elder here is exposed at surface and is in contact with granodiorite to the north and extends to depth to the south. Within the hornfels, gold can be seen in veins commonly associated with tellurides and Bi-bearing sulfosalts. In Figure 10J, gold is associated with clear narrow veins cutting and offsetting earlier milky quartz molybdenite veins. Some of the highest Mo values occur at Altenburg Hill and are hosted in the granodiorite, with values up to 890 ppm but average ~15 ppm. Within the granodiorite, gold has been observed within arsenopyrite grains as free disseminations associated with native bismuth (Fig. 9A-C). The Altenburg Hill zone is cut by a series of porphyritic dacitic dikes ~0.5-1.5 m. These dikes are most voluminous within this zone and constitute a dike swarm, cutting both diorite and hornfels, locally concentrating gold mineralization. Post gold hypabyssal rhyolite dikes are also seen on the west side of this zone cutting both the granodiorite and Slaven Formation. These NW-striking SW-dipping dikes disrupt the continuity of gold mineralization within the Slaven.

5.3.b Porphyry Zone

The Porphyry zone includes the NE margin of the Tenabo stock which intrudes the Elder Formation near surface, and the Slaven Formation at depth (Fig. 3). Within the center of the mineralized zone, the lower east-dipping thrusted contact between the Elder and Slaven Formation occurs ~152-182 m below the surface, with the Tenabo stock intruding this contact to the south (Fig. 3). This contact is exposed at surface to the west and extends at depth to the east, similar to the Altenburg Hill zone. Here, the structural nappe of Elder Formation is highly deformed, faulted, and metamorphosed to quartz, biotite, and calc-silicate hornfels. Diorite in

this zone forms a thick >121 m sill-like body along the north and east margins of the stock that dips west ~35° and is locally converted to endoskarn near the contacts with calc-silicate hornfels (McCusker, 1996). EW-striking south-dipping post gold granitic porphyry dikes cut the diorite, granodiorite, dacitic dikes and upper plate siliciclastic lithologies in this zone and disrupt the continuity of gold mineralization.

The majority of the gold mineralization in the Porphyry zone is hosted within the Elder Formation; however, there is extensive mineralization in both the diorite and granodiorite here. The highest grades of gold are found in this zone, with one five-foot interval within granodiorite returning over 89ppm gold; however, most of the gold grade here is closer to 0.05 ppm. The overall distribution of gold in the porphyry zone is concentrated along the contact of diorite and granodiorite in overlying hornfels of the Elder Formation. Here, a series of NS-striking, moderately west-dipping faults called the Endoskarn fault series, are associated with intrusion emplacement and strongly control higher grade gold mineralization. Auriferous veins cut earlier styles of alteration and are seen in Figures 10H and 10I. Within intrusive units here, these veins cut earlier potassic alteration and on the microscopic scale (~10-50µm) gold is seen alone in quartz gangue. Cutting hornfels, within the upper plate siliciclastic units these veins may come in sheeted sets or may use earlier veins as preferred fluid pathways. Under reflected light, the close association of gold, native bismuth, and sulfosalts such as babkinite and kawazulite can be seen (Fig. 9E). Further SEM-EDS analysis highlights the chemical composition of these Bi-bearing minerals along with cross-cutting relationships with other sulfides (Fig. 9F). Interestingly, gold in this zone has not been found in association with arsenopyrite in any samples as in the other zones, and specifically, gold has not been observed with any Bi-bearing minerals within intrusive units. Within the intrusive units in the porphyry zone, gold has been found to be alone in quartz vein gangue as an

alloy with ~4-6 wt. % Ag. Outside of the intrusion within siliciclastic units, this study along with previous studies have found gold as electrum (>20 wt. % Ag). Geochemical correlations with gold in this zone include Bi (0.53), Te (0.67) and Cu (0.6) using spearman correlation matrices.

Copper is best developed in the Porphyry zone, with the highest Cu values being >3% over a 1.5 m interval. However, the overall Cu grade (<0.02%) is not high enough to be considered ore (Amax Gold Inc. 1994 Feasibility Study). Hypogene copper sulfide mineralization consists primarily of chalcopyrite, which is commonly affected by supergene processes resulting in digenite, covellite, cuprite, and malachite. Supergene native copper can also be observed, and is commonly associated with gossan zones. Previous studies indicate the presence of chalcocite in some of these zones.

5.3.c Gold Pan

The Gold Pan zone is located along the northwest contact of the Tenabo stock in the highly folded Devonian Slaven Formation, including hornfelsed chert/argillite and metabasalt (Fig. 1B). In the SE portion of this zone, the Tenabo stock is exposed at surface where it steeply drops off to the NW. Similar to western Altenburg Hill, the package of east-dipping metabasalt at Gold Pan is estimated to be ~122 m thick. Continuing from the Porphyry zone, a series of EW-striking, south-dipping, post-gold granitic porphyry dikes cut both the Tenabo stock and upper plate siliciclastic lithologies.

Gold mineralization here is found within veins and disseminated throughout the hornfels and metabasalt. A majority of the gold mineralization is hosted by the metabasalt, along a series of high and low-angle faults, forming a number of lenticular zones of strong exoskarn alteration which are generally oriented to the northwest. The metabasalt here has undergone significant exoskarn alteration with intense sulfidation in the form of pyrite, marcasite, pyrrhotite,

chalcopyrite, and lesser arsenopyrite. Gold mineralization within the metabasalt is commonly observed as free disseminations or enclosed in arsenopyrite grains (Fig. 9I). In thin section, these arsenopyrite grains typically contain loellingite and pyrrhotite and are cut by later chalcopyrite. Detailed SEM-EDS analysis of these samples has confirmed the presence of native bismuth, hedleyite, and ikunolite in close association with gold mineralization.

Outside of the metabasalt and within the hornfels, gold is observed disseminated fault breccias or within mm-scale quartz veins. Here, the hornfels has not undergone strong exoskarn alteration and sulfidation, compared to the metabasalt; likely due to protolith composition. In thin section, free disseminated gold can be observed with quartz gangue as breccia infill or along small veins cutting hornfels. Within the quartz veins that cut the hornfels, gold can be seen alone in quartz gangue, with native bismuth and Bi-bearing sulfosalts, or within or around arsenopyrite grains which typically contain loellingite in the center. These veins can be seen cutting hornfels in crackle breccias or following biotite hornfels lenses. Visible gold in these veins is closely associated with various types of Bi-bearing sulfosalts including, babkinite, kawazulite, hedleyite, pilsenite, tellurobismuthinite, hessite, and cosalite (Table 3). Later stages of mineralization, including galena and marcasite, are seen cutting these earlier events.

5.3.d 39A Zone

The 39A zone is a shallow, 20-35° E-NE dipping, structurally controlled stratiform body of semi-massive sulfide, located 243-308 m outboard of the Tenabo stock, hosted entirely in hornfels of the Slaven Formation (Fig. 3). Locally, the replacement body forms (1.5-8 m), persistent layers that can extend along strike up to 75 m, with the highest gold values generally encountered at or near the base of these sulfide layers (McCusker, 2004). Sulfide layers encompass 8-70% fine

sulfides, including pyrite, marcasite, pyrrhotite, chalcopyrite, lesser arsenopyrite and trace molybdenite. Below this zone, auriferous quartz veins control much of the gold mineralization. Strong exoskarn is typically present with the sulfides in this zone, dominated by actinolite and chlorite with lesser epidote, titanite, zoisite and trace tourmaline. Similar to the Gold Pan zone structurally above, south-dipping post mineral granitic porphyry dikes cut the 39A stratiform body. High angle east-dipping post mineral faults including the Gylding fault additionally cut the 39A structure.

Gold mineralization at 39A is present as disseminations of native particles alone or associated with Bi-bearing sulfosalts. In hand samples of these massive sulfide horizons, visible gold can be seen disseminated throughout the pervasive exoskarn. Below these horizons gold tends to be vein hosted. Within thin section, coarse gold up to 200µm is observed in quartz gangue or associated with arsenopyrite grains (Fig. 9J-L). More detailed SEM-EDS analysis in this study, along with previous observations, indicate the presence of native bismuth, loellingite, tetradymite, tellurobismuthinite, hedleyite, and ikunolite in close association with gold particles, either in quartz gangue or hosted within arsenopyrite grains. At the micron scale, gold can be seen cutting and infilling arsenopyrite grains and grain boundaries between arsenopyrite and loellingite (Fig. 9K). Within the 39A zone, the highest tungsten values are encountered, with one five-foot interval returning over 7,100 ppm, but averaging ~12 ppm within the zone. Previous studies indicate the presences of scheelite in some of these areas (Johnson, 1973). Later stages of mineralization in the 39A zone include marcasite replacing pyrrhotite and cutting arsenopyrite. Discontinuous pyrite veinlets are common in this zone and where strongest, appear as dull sooty masses or lenses.

5.3.e Distal Zone

The Distal zone is the furthest from the Tenabo stock ~520 m NW and is hosted by a thick sequence (>300 m) of biotite, quartz, and calc-silicate hornfels in the Slaven Formation (Fig. 1B). The favorable mineralized horizon at the Distal zone appears to be similar in nature to the mineralized horizon in the 39A zone, but down stratigraphy and in a more distal position with respect to the Tenabo stock contact (Fig. 3). This area consists of a series of persistent, but narrow flat-lying mineralized zones controlled by an east-dipping fault series called the distal fault series. Here a major fault, called the quartz fault, is exposed at surface returning multi-gram gold assays from rock chips. These mineralized zones consist of strong exoskarn alteration (Fig. 7E) with pervasive actinolite-tremolite and abundant sulfides including pyrite, pyrrhotite, marcasite, chalcopyrite, arsenopyrite, sphalerite, galena, tetrahedrite, boulangerite, and stannite. Cutting these zones are sheeted quartz – chalcopyrite veins, quartz – gold veins, and later polymetallic veins.

Gold at Distal is primarily hosted in quartz veins or as disseminations within arsenopyrite grains with native bismuth and Bi-bearing sulfosalts. In hand sample, visible gold can be seen within these quartz veins cutting calc-silicate altered hornfels (Fig. 10G). Under reflected light, the close association of gold with Bi-bearing minerals is apparent and can be seen both in quartz gangue and within arsenopyrite grains (Fig. 9M-O). SEM-EDS analysis confirms the presence of these minerals including native bismuth, hedleyite, pilsenite, protojoseite, bismuthinite, and tetradymite, ikunolite, cosalite, babkinite, and canfieldite (Table 3). Minor electrum has been observed in this area enclosed within arsenopyrite grains. Arsenopyrite is best developed in this zone and can often be seen disseminated throughout the hornfels or focused along fractures. Optically, this arsenopyrite often looks mottled and can be infilled or crosscut by later mineralization including chalcopyrite and later Bi-bearing sulfosalts (Fig. 8G-L). Locally, massive

fine-grained arsenopyrite forms narrow discontinuous replacement horizons. Later polymetallic base metal veins are common here, which typically carry stibnite, sphalerite, galena, with lesser tetrahedrite, boulangerite, and pavonite. Geochemically, the Distal zone has significantly higher concentrations of As and Sb compared to the other zones, ranging from 1.60-29,300 ppm As and 1.17-840 ppm Sb, with the highest Hg interval recorded here at 2.77 ppm. Geochemical correlations with gold in this zone include Bi (0.61), Te (0.69), As (0.66) and Cu (0.51). It has been noted that Distal has mineralogical and geochemical characteristics of distal gold skarns, as described by Myers (1988), Meinert (1989), and Ray et al (1990). Previous work has indicated that a later stage of mineralization cuts the stratiform zones and fills moderately-high angle faults and fractures including adularia.

5.4 Veining and Paragenetic Sequence

Based on detailed core logging, petrographic observations, SEM-EDS, and SEM-CL analysis, a paragenetic sequence of vein events at Robertson has been established. In order to determine the sequence of vein formation, a vein relationship matrix was created and implemented during the core logging process (Fig. 11). As a result of this work, vein cross-cutting relationships and associated hydrothermal alteration and mineralization indicate the succession of three main paragenetic stages referred as 1) pre-gold, 2) syn-gold, and 3) post-gold. The details of each of these stages can be found in Table 4 and are described below. More detailed SEM-CL imaging of these quartz veins reveals evidence for multiple crack-and-seal events and reactivation of earlier veins (Fig. 12). This highlights the importance of off-setting vein relationships when trying to understand sequence of events. The terms selvage and halo are used here to describe minerals precipitated next to a vein, where a selvage describes minerals at the vein-wallrock interface and halo described minerals extending outside of the vein into wallrock.

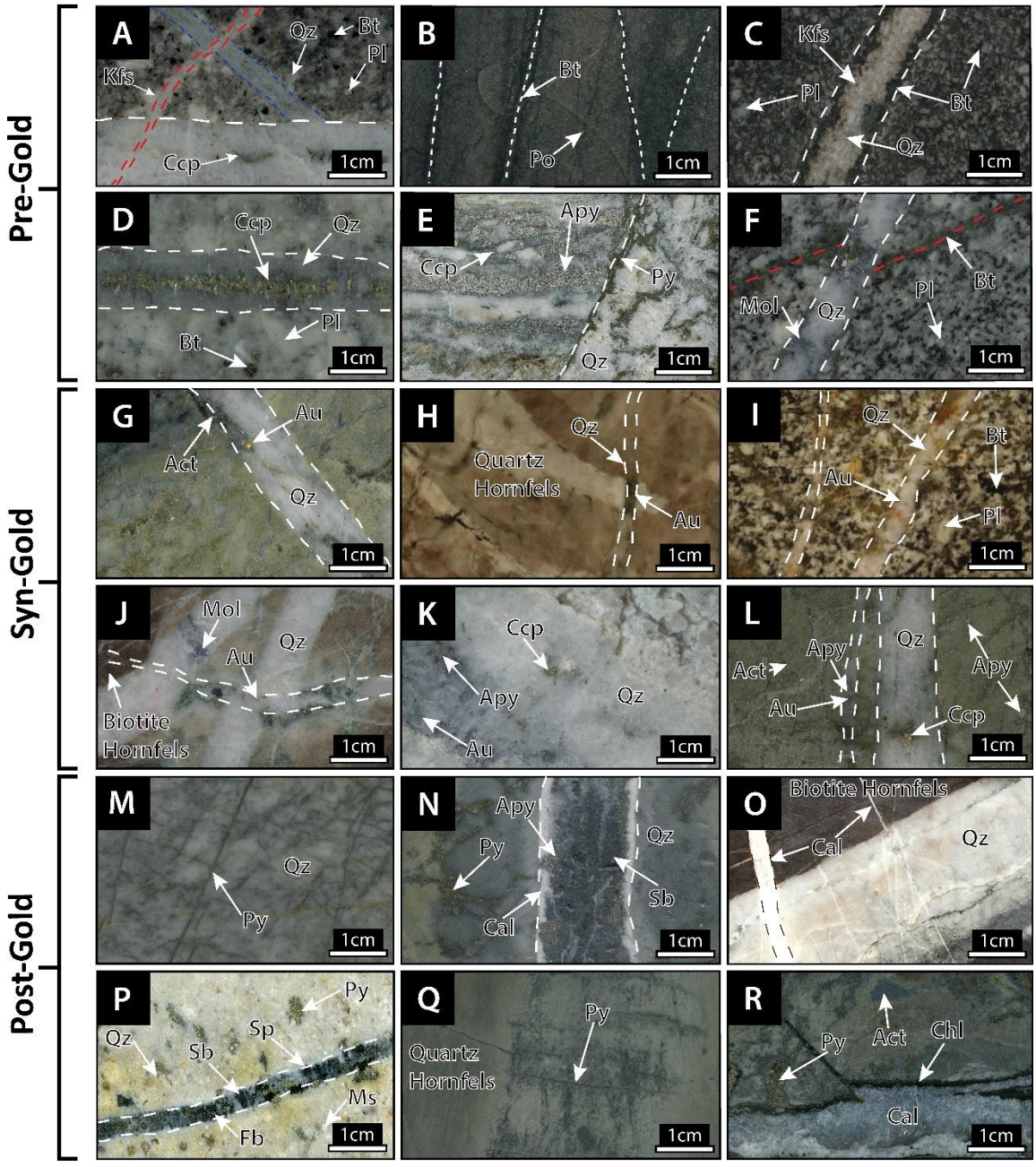

Fig. 10. Core scans of veins separated into pre-gold, syn-gold, and post-gold stages. Mineral abbreviations and detailed vein descriptions are listed in table 4. (A) Barren quartz vein cutting granodiorite cut and offset by a quart-K-feldspar vein and cut by a quartz-chalcopyrite vein (B) Biotite veinlets cutting basalt (C) Quartz – Kfs vein with biotite selvage cutting diorite (D) Quartz – chalcopyrite vein cutting granodiorite (E) Quartz – arsenopyrite vein cut by pyrite veinlets (F) Quartz – molybdenite vein cutting and offsetting earlier biotite veinlet (G) Quartz – gold vein cutting calc silicate hornfels (H) Quartz – gold vein cutting quartz hornfels (I) Quartz – gold vein cutting diorite (J) Quartz – gold vein cutting and offsetting quartz – molybdenite vein in biotite hornfels (K) Quartz – gold vein and several other vein types cutting granodiorite (L) Quartz – gold vein within quartz -arsenopyrite vein parallel to quartz – chalcopyrite vein (M) Pyrite veinlets cutting quartz

hornfels (N) Polymetallic vein cutting quartz hornfels (O) Bull quartz vein cutting biotite hornfels, cut by calcite vein (P) Polymetallic vein cutting sericitically altered granitic porphyry dike (Q) Thin discontinuous pyrite veinlets as “cleats” within bedded Elder formation (R) Calcite vein with euhedral calcite vug cutting basalt. Abbreviations: Act = actinolite, Apy = arsenopyrite, Au = gold, Bt = biotite, Cal = calcite, Chl = chlorite, Ccp = chalcopyrite, Fb = freibergite, Gn = galena, Ksp = K-feldspar, Mol = molybdenite, Ms = muscovite, Pl = plagioclase, Po = pyrrhotite, Py = pyrite, Qz = quartz, Ser = sericite, Sp = sphalerite, Sb = Stibnite

		Offsetting Vein (Younger)									
	Vein Type	Aplite	Barren Quartz Veins	Potassic Veins	Quartz - Chalcopyrite	Quartz - Molybdenite	Quartz - Pyrite	Bull Quartz Veins	Pyrite Veinlets	Polymetallic Veins	Calcite Veins
Vein That Was Offset (Older)	Aplite				1			1	2		2
	Barren Quartz Veins		14	5	10	5		1	2		8
	Potassic Veins		2	4	19	10	2	7			13
	Quartz - Chalcopyrite			1	16	6	5	4	3	1	16
	Quartz - Molybdenite			1	3	1	3	2	5		4
	Quartz - Pyrite					1		2	1		1
	Bull Quartz Veins			1	1	2			4	1	2
	Pyrite Veinlets							2		2	1
	Polymetallic Veins										2
	Calcite Veins										

Fig. 11. Vein crosscutting relationship matrix after Seedorff and Einaudi (2004). Vein descriptions are presented in table 3. Offsetting vein observations made during core logging, binoc descriptions, and in thin section were input into this matrix to establish a vein chronology. Each cell contains a number of observed off setting relationships with the shaded diagonal region separating normal from anomalous crosscutting relationships. A normal relationship (above the diagonal) is defined where a vein is cut by a vein from a later stage, and an anomalous relationship (red) is defined as a reversal in the typical sequence where a normally younger vein type is crosscut by a normally older vein. Blank cells represent no observed cross cutting relationships.

Cross-cutting and off-setting vein relations were captured to create a vein chronology (Fig. 11). Here each cell contains a number of observed off setting relationships with the shaded diagonal region separating normal from anomalous cross-cutting relationships. As stated by Seedorff and Einaudi (2004), a normal relationship (above the diagonal) is defined where a vein is cut by a vein from a later stage, and an anomalous relationship is defined as a reversal in the typical sequence where a normally younger vein type is crosscut by a normally older vein. Such anomalous relationships are not uncommon for early, high-temperature veins and may indicate multiple high-temperature magmatic-hydrothermal fluid pulses forming stockwork vein systems (Sepp and Dilles, 2018). Blank cells in this figure represent no observed cross-cutting relationships. Not shown in the matrix, are other cross-cutting relationships between intrusive units, other vein types, and observations between different minerals; however, the results of the findings are discussed in the following section and presented in a paragenetic sequence in Figure 17.

5.4.a Pre-gold stage

The pre-gold stage includes a sequence of barren quartz veins, biotite veinlets, quartz-K-feldspar early dark micaceous (EDM) veins, quartz-arsenopyrite, quartz-chalcopyrite, and quartz-molybdenite veins.

Barren quartz veins: Barren quartz veins are the earliest veins observed and are characterized as thin (0.5-3mm), with wavy wall geometries and filled with clear quartz. These veins typically are not continuous, have no vein selvages or halos, and do not usually contain sulfides. In figure 10A an early barren quartz vein is cut and offset by a quartz vein with a k-feldspar selvage is also cut by a quartz-chalcopyrite vein. The quartz-k-feldspar vein here cuts quartz-chalcopyrite vein and represents an anomalous relationship as previously discussed.

Table 4. Petrographic Characteristics of Vein Types at Robertson

				Vein Fill			Vein Halo		
	Vein Type	Wall Geometry	Description	Width (mm)	Gangue	Sulfides	Width (mm)	Gangue	Sulfides
Pre-Gold	Barren Quartz	Wavy	Thin, clear, sometimes smokey due to fluid inclusions	0.5-3	Qz	± Ccp - po - py	N/A	N/A	N/A
	Biotite	Wavy	Thin wavy brown veinlets of biotite with biotite halos occasionally with kspar often alt to chl	0.5-2	Bt	± Ccp - po	0-5	Bt ± kfs	± Ccp - po
	Quartz - Kfs	Wavy	Light pink veins often with biotite "EDM veins" forming stockworks where strongest	1-4	Qz - kfs ± bt	N/A	3-7	Kfs ± bt	N/A
	Quartz - Arsenopyrite	Straight	Clear syntaxial veins with medium grained, zoned arsenopyrite commonly cut by later ccp and py	1-7	Qz	Apy ± lo - po	N/A	N/A	N/A
	Quartz - Chalcopyrite	Straight	Clear quartz, commonly sheeted sets, sulfide mid-centers, open space veins	1-6	Qz	Ccp ± po - py - mol	1-2	± Act - chl	± Ccp - po - py
	Quartz - Molybdenite	Straight	Commonly granular milky quartz, tend to be larger veins, often re-opened by later vein stages	2-15	Qz	Mol ± ccp - po	N/A	N/A	N/A
Syn-Gold	Quartz - Gold	Straight	Clear-milky quartz with variable amounts of sulfides cutting both intrusive and sedimentary units commonly associated with Bi-Te-Se-Pb-Ag-S sulfosalts	1-10	Qz - au	± Apy - sulfosalts	N/A	N/A	N/A
Post-Gold	Pyrite Veins	Irregular	Thin, discontinuous, fine sooty sulfide veins filling dilational fractures at random orientations	0.5-2	± qz	Py	1-4	Ser	± Py
	Polymetallic Veins	Straight	Commonly associated with sericitic alteration, strong Pb-Zn-Sb-Ag-Sn base metal signatures, minerals include freibergite, stannite, boulangerite	2-19	Qz - cal	Py - apy - sp - gn - sb - ccp - ttr	1-5	Ser	Py - apy - ccp -
	Bull Quartz	Straight	Milky quartz veins with no sulfides that typically tend to be larger than other vein types	5-40	Qz	N/A	N/A	N/A	N/A
	Calcite Veins	Irregular	Thin, wispy, calcite stringers that often form networks or crackles in fractured rocks	0.5	Cal	± Py	N/A	N/A	N/A

Mineral abbreviations: Act = Actinolite, Apy = Arsenopyrite, Au = Gold, Bt = biotite, Cal = calcite, Ccp = chalcopyrite, Chl = chlorite, Gn = Galena, Kfs = potassium feldspar, Lo = Loellingite, Mol = molybdenite, Po = Pyrrhotite, Py = pyrite, Qz = quartz, Sb = Stibnite, Ser = sericite, Sp = sphalerite, Ttr = tetrahedrite

Biotite veinlets: Biotite veinlets are composed of fine brown secondary biotite, 0.5-2 mm wide, with narrow secondary biotite selvages typically 0-5 mm (Fig. 10B). These veins can be observed cutting both sedimentary and igneous units and earlier stages of hydrothermal alteration including endoskarn. Depending on the host lithology, vein halos can extend out replacing primary minerals. In the diorite or granodiorite fine "shreddy" biotite is observed to replace primary mafic minerals. In quartz hornfels; however, these veins display no haloes and are constrained to the fractures they fill. Chlorite can typically be observed overprinting these early veins.

Quartz K-feldspar veins: Quartz-potassium feldspar "EDM" following the terminology of Meyer (1965), are characterized by unfilled fractures with alteration halos in which plagioclase phenocrysts are replaced by andalusite (10–15%), biotite (15–20%), sericite (30–40%), and K-feldspar (25–45%) (Redmond & Einaudi, 2010). At Robertson, these veins are characteristically quartz-K-feldspar-biotite assemblage with lesser sericite and no andalusite (Fig. 10A and 10C). These veins commonly occur in areas of strongest potassic alteration, where these veins can form stockworks and sometimes pervasively replace the host lithology. In thin section, fine secondary potassium feldspar and biotite in vein halos can be seen replacing primary igneous minerals (Fig. 7D). Depending on the host rock, vein halos may extend away from the vein wall up to 7 mm away, however, where veins contact other veins these halos may disappear such as in Figure 10A. Quartz-K-feldspar veins are most common within the Tenabo stock at Porphyry and Altenburg Hill where potassic alteration is strongest (Fig. 1B).

Quartz-Arsenopyrite veins: Quartz-arsenopyrite veins contain medium grained (1-5 mm) subhedral to-euhedral arsenopyrite grains in quartz gangue that cut both the Tenabo stock and

upper plate units (Fig. 10E). These veins commonly have straight wall geometries and no associated selvages. In thin section, arsenopyrite within these veins commonly appears zoned and mottled; however, SEM-EDS analysis of these zones reveals no apparent geochemical variation in major elements (Appendix A). Within the center of these grains, pyrrhotite and lesser loellingite are typically observed and most likely reflect a change in sulfidation state, from lower to higher, as described in Einaudi (2003). Arsenopyrite here, can regularly be seen cut by later stages of mineralization including chalcopyrite, pyrite, galena, stibnite, and marcasite. Although few cross-cutting relationships of these veins have been observed in core, these veins likely come early in the paragenetic sequence and pre-date gold mineralization as gold can typically be seen infilling voids within arsenopyrite grains (Fig. 9 and 10). These veins are most common at Distal, reflected by the increased arsenic values in multi-element geochemistry.

Quartz-Chalcopyrite veins: Quartz-chalcopyrite veins often occur as sheeted sets of 1-6 mm clear quartz with sulfide mid-centers and sharp wall rock contacts (Fig. 10D & 10A). These veins are observed cutting the Tenabo stock and upper plate units. These veins cut previous types of hydrothermal alteration, including endoskarn, potassic alteration, and exoskarn. It is noted however, that the exoskarn and these veins may have been synchronous in their development. Disseminated within vein halos, chalcopyrite ± pyrrhotite ± pyrite ± actinolite can sometimes be observed. Where oxidized, chalcopyrite in these veins undergoes supergene processes to digenite and covellite often forming rims or oxidation fronts seen in thin section. These veins are most common within the Porphyry zone, where increased copper grades can be seen. Along the center of these veins, it has been observed that later native bismuth and Bi-bearing sulfosalts have precipitated. Further SEM-CL analysis confirms the presence of multiple hydrothermal veining

events where earlier quartz-chalcopyrite veins are reopened and used by later hydrothermal events.

Quartz-Molybdenite veins: Quartz-molybdenite veins are observed to have straight wall geometries, tend to be larger veins (2-15 mm), and are composed of granular milky quartz. These veins can be seen cutting the Tenabo stock, siliciclastic host rocks, and earlier related hydrothermal events. These veins also cut endoskarn, potassic alteration, and exoskarn. Molybdenite is predominantly observed in veins; however, it is disseminated in areas of strong potassic alteration within the Porphyry and Altenburg Hill zones. Figure 10F shows an example of an earlier biotite veinlet and associated potassic alteration cut and offset by a quartz-molybdenite vein within granodiorite. Anomalous cross-cutting relationships have been observed in these veins (Fig. 11), which may be the result of limited observations of cross-cutting or may indicate multiple hydrothermal fluid pulses. Due to these uncertainties and limited cross-cutting relations, it is possible that these veins precede quartz–chalcopyrite precipitation, or reflect multiple episodes of hydrothermal events. Based on existing observations it is thought that these veins precede gold mineralization and one example of this can be seen in Figure 10J where an earlier quartz – molybdenite vein is cut and offset by a thin quartz vein containing gold.

Scheelite veins: Previous studies have indicated the presence of scheelite veins within the diorite and granodiorite phases at Robertson (AMAX feasibility). Historic mining reports mention that scheelite was recovered along with gold during dredging operations in the early 20th century. Results of this study however, did not encounter such mineralization in hand sample or in thin section and thus were not included within the vein matrix. The lack of these observations does not rule out the possibility of such mineralization; however, conclusions on mineral associations and cross-cutting relationships cannot be made. Geochemical indicators suggest increased

tungsten mineralization within the Altenburg Hill and 39A zones (0.1-7,120 ppm W). Principle component analysis plots indicate weak W correlations with Ag, and within the Distal zone tungsten shows moderate correlations with, As (0.58), and Bi (0.52) (Appendix D).

5.4.b Syn-gold stage

The syn-gold stage is composed of quartz – gold ± As-Bi-Te-Se-Pb-Ag-S sulfosalt veins. These veins tend to be the least common vein type observed, likely due to difficulties seeing visible gold while logging and thus are not included in the vein matrix. However, detailed observations at the microscopic scale show that these veins occur in all five mineralized zones at Robertson and appear to be straight walled, 1-10 mm wide, with clear-milky quartz, commonly associated with sulfosalts. Previous studies by Tarnoci (1998) indicate that within intrusive rocks these veins are 5-30 mm wide, massive-comb textured quartz, spaced 20 cm to 2 m apart, dip steeply, and have narrow silicified and arsenic oxide stained wallrock envelopes. Auriferous veins can be seen in Figure 10G-L cutting a variety of host units and associated alteration types including endoskarn, potassic alteration, and exoskarn.

Inside these veins, gold can be seen as single grains disseminated in quartz gangue or associated with bismuth-bearing sulfosalts within or on the surface of arsenopyrite, chalcopyrite, and pyrrhotite grains. Reflected light petrography highlights these associations and can be seen in Figure 9E. Galena has been observed to be associated with bismuth-bearing sulfosalts and gold at Altenburg Hill; and in previous studies at Gold Pan. SEM-CL imaging of these auriferous veins reveals multiple generations of hydrothermal quartz, most notably an earlier highly luminescent quartz and later low luminescent quartz that is associated with deposition of Au mineralization (Fig. 12). Au-bearing veins commonly use earlier veins as fluid pathways as shown by quartz

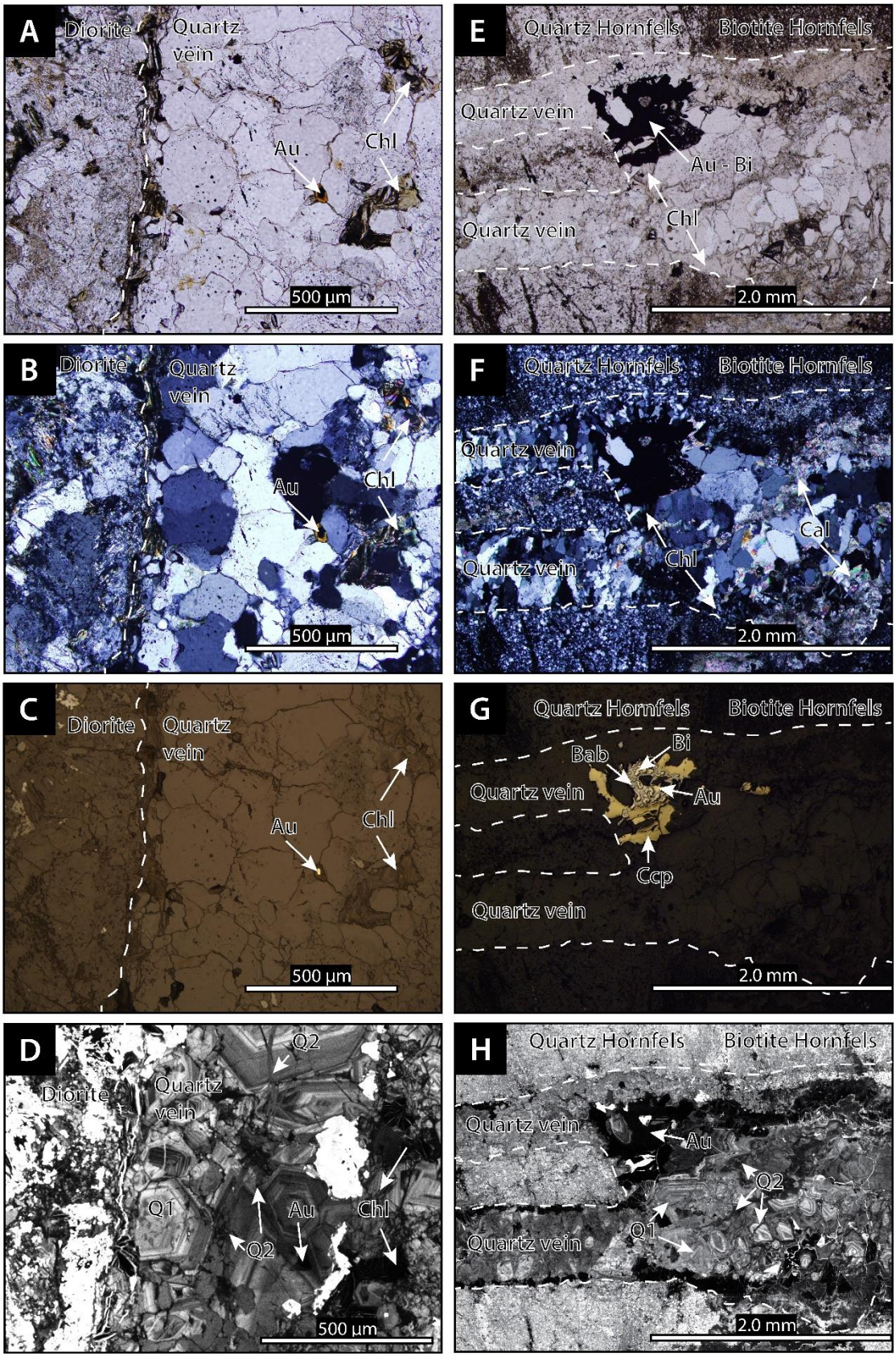
A
Diorite
Quartz vein
Au
Chl
500 µm
B
Diorite
Quartz vein
Au
Chl
500 µm
C
Diorite
Quartz vein
Au
Chl
500 µm
D
Q2
Diorite
Quartz vein
Q1
Au
Chl
Q2
500 µm
E
Quartz Hornfels
Biotite Hornfels
Quartz vein
Au - Bi
Chl
Quartz vein
2.0 mm
F
Quartz Hornfels
Biotite Hornfels
Quartz vein
Cal
Chl
Quartz vein
2.0 mm
G
Quartz Hornfels
Biotite Hornfels
Bab
Bi
Quartz vein
Au
Ccp
Quartz vein
2.0 mm
H
Quartz Hornfels
Biotite Hornfels
Quartz vein
Au
Q2
Q1
Quartz vein
2.0 mm

Fig. 12. Transmitted plane polarized light (A & E), transmitted cross polarized light (B & F), reflected plane polarized light (C & G), and cathodoluminescence images (D & H) from two veins, one cutting diorite (A-D) and one cutting hornfels within the Elder formation (E-H). These veins can be seen in core scans in figure 9H (hornfels) and 9I (diorite) respectively. Note that all images of each vein (A-D) & (E-H) are the same view. Within the CL images of each vein in (D & H), the close association of gold and Q2 can be seen, often cutting Q1.

dissolution textures of earlier quartz, such as quartz-chalcopyrite veins, that can be observed by SEM-CL. Results of this analysis indicate that gold alloy within these veins is typically ~4-6 wt. % Ag with a few observations of electrum >20 wt. % Ag. Based on the systematic association of Au with As-Bi-Te-Se-Pb-Ag-S sulfosalts and lack of evidence for multiple events or cross-cutting relationships, there is likely a single gold mineralization stage representing a unidirectional cooling path of hydrothermal fluids.

5.4.c Post-gold stage

The post-gold veins encompass pyrite ± quartz, quartz-calcite-sulfide (polymetallic veins), bull quartz, and calcite veins (Fig. 10M-R). These veins types are the only observed veins to cut granitic porphyry dikes including the older intrusive units.

Pyrite veins: Pyrite veins are commonly seen as discontinuous fine sooty sulfide veins with irregular wall geometries filling dilational fractures at random orientations. Like previous alteration types discussed, host rock composition exerts a primary control on whether a vein forms a halo or not. Within the Tenabo stock, these veins are accompanied by vein halos of sericite and pyrite, which can be seen disseminated away from the vein fill. Within metasedimentary units, these veins are constrained to the fractures in which they form and do not typically develop halos. In well bedded siliciclastic lithologies, these veins can form cleated layers where the rheologic contrast between two differing sedimentary beds leads to focused mineralization of discontinuous subparallel pyrite. These veins are most commonly observed near the 39A

structure, in quartz hornfels, where these veins form within hornfels crackle breccias and can appear as massive sulfide lenses.

Polymetallic veins: Quartz-calcite-sulfide or polymetallic base metal sulfide veins, are the most variable vein type at Robertson, hosting a dynamic suite of sulfides. These veins have strong Pb-Zn-Sb-Ag-Sn metal associations, and include sulfides such as pyrite, arsenopyrite, chalcopyrite, sphalerite, galena, stibnite and lesser tetrahedrite, freibergite, stannite, and boulangerite. Depending on the host lithology, these veins can be associated with sericitic alteration. When cutting intrusive units, these veins can have broadened vein haloes of sericite and sulfides as seen in Figure 10P. Where they cut siliciclastic host rocks, vein halos are diminished and sulfides are constrained to the vein fill (Fig. 10N). Here, the fill can be of quartz and calcite that often represents multiple episodes of hydrothermal flow. Commonly, multiple generations of calcite and associated sulfides can be seen within these veins.

Bull quartz veins: Bull quartz veins tend to be larger than other vein types, 5-40 mm wide, and filled with massive milky quartz and no sulfides. These veins tend to have no preferred orientation and appear to fill late fractures. The only other vein type observed to cut these veins are calcite veins as seen in Figure 10O.

Calcite Veins: Calcite veins crosscut all observed vein types, commonly infill irregular fractures, and fill the matrices of crackle breccias. Commonly these veins contain open space mineralization in the form of vugs, where euhedral calcite crystals can be observed. Calcite veins are common with chloritic alteration which can be seen cutting all rock types except rhyolite dikes at Robertson (Fig. 10R).

Adularia veinlets: Veinlets of adularia have been observed in previous work (Honea, written communication), (McCusker, 2004), (Henry, written communication); however, they were not observed during this study and are thus not included in the vein matrix. In the past, these veins were described cutting the hornfels and basalt of the Slaven Formation and in several localities were found to be coarse-grained (> 5mm) fracture fillings and as cement in several pebble dikes.

5.5. Geochronology

Geochronological methods were applied at Robertson in order to understand the relative timing of intrusions and associated hydrothermal events. As a result of this work, six new U/Pb LA-ICP-MS dates of intrusive phases, one molybdenite Re/Os date, and one hydrothermal orthoclase $^{40}Ar/^{39}Ar$ date were obtained. U/Pb zircon chronometers were used in this study in lieu of other analytical methods because of their ability to resist resetting due to hydrothermal overprinting, in order to build upon different chronometers used in the past. Re/Os and $^{40}Ar/^{39}Ar$ methods were used in order to determine the relationships between molybdenite veins, potassic alteration, and host rocks. Results from U/Pb and $^{40}Ar/^{39}Ar$ analysis are shown in figures 13 and 14 respectively, and a summary of all geochronologic data is reported in Table 5.

5.5.a U/Pb Zircon Dating

Six representative samples of diorite, dacitic dikes, medium-grained granodiorite, coarse-grained granodiorite, granitic porphyry dikes, and hypabyssal rhyolite were selected for U/Pb zircon dating. Zircons in all of these samples generally show euhedral elongate prismatic shapes with lesser grains being subhedral-anhedral and or fragmented. SEM-CL analysis shows oscillatory zoning in some grains parallel to core growth zones and differences in brightness within grains may reflect inherited zircon grains. The diorite (GS474027) may contain some of these inherited

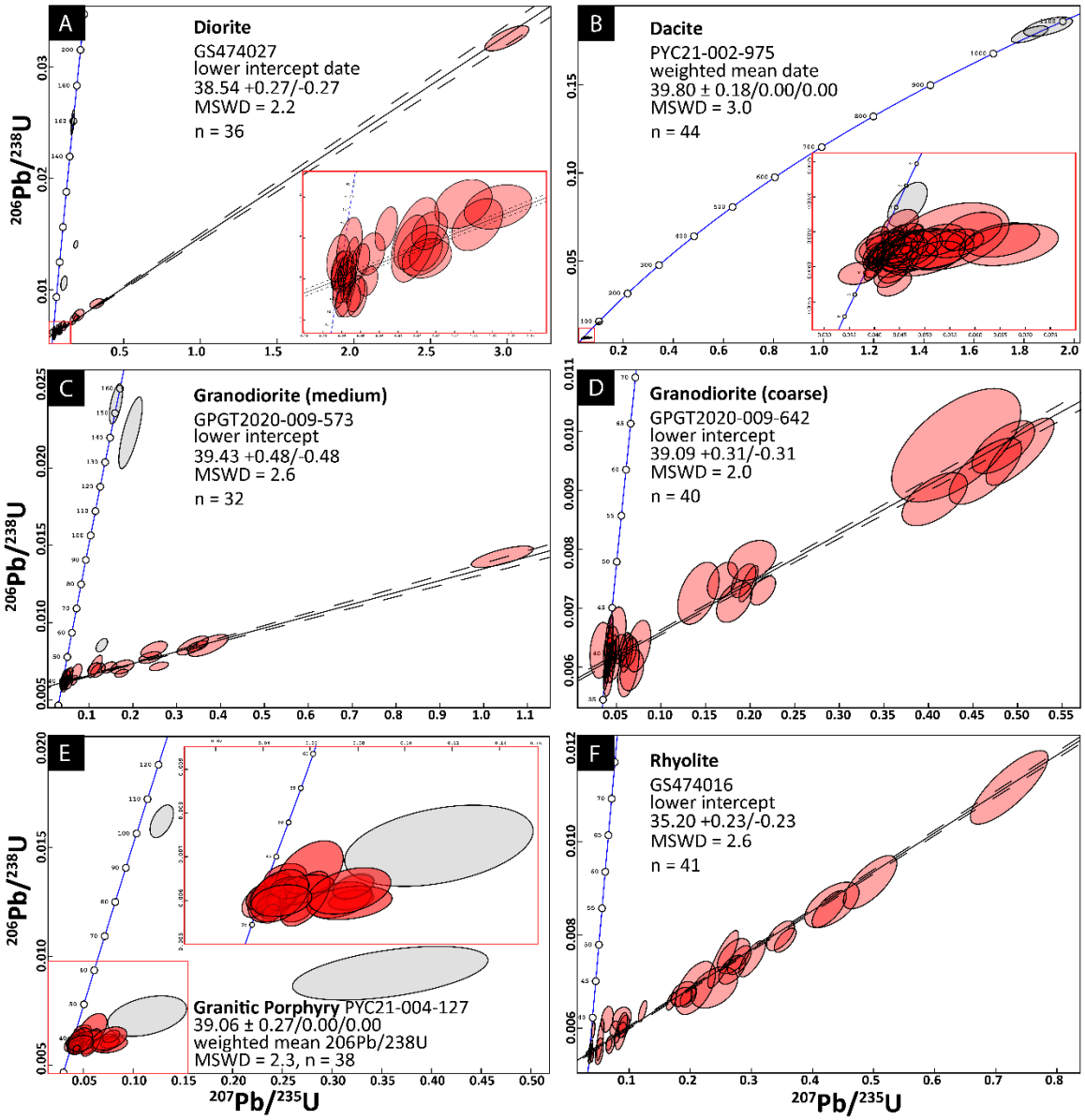

Fig. 13. Concordia diagrams of U-Pb zircon analysis of intrusive phases at Robertson. Weighted mean or lower intercept ages are shown. (A) Diorite GS474027 (B) Dacite PYC21-002-975 (C) Granodiorite (medium) GPGT2020-009-573 (D) Granodiorite (coarse) GPGT2020-009-642 (E) Granitic Porphyry PYC21-004-127 (F) Rhyolite GS474016

zircon grains as some of the 40-analysis plot off Concordia. Of the 40-analysis, 36 yielded a lower intercept date of 38.54 ± 1.16 Ma (2σ; MSWD = 2.2; n/nt = 36/40), with the lower intercept shown on the inset within figure 13a. Zircons within the dacitic dike (PYC21-002-975) may also reflected

some inherited grains (Fig. 13b) with 44 of the 49-analysis used to calculate a weighted mean date of 39.80 ± 1.19 Ma (2σ; MSWD = 3.0; n/nt = 44/49). Two phases of the granodiorite, medium and coarse-grained, were selected based on crosscutting relationships in core, both yielding lower intercept dates. Medium-grained granodiorite (GPGT2020-009-573) yielded 39.43 ± 1.18 Ma (2σ; MSWD = 2.6; n/nt = 32/35) (Fig. 13c), with the coarse-grained granodiorite (GPGT2020-009-642) yielding 39.09 ± 1.17 Ma (2σ; MSWD = 2.0; n/nt = 40/40), (Fig. 13d). Forty-one U/Pb analysis were performed on the granitic porphyry dike sample (PYC21-004-127), thirty-eight used to calculated a weighted mean date of 39.06 ± 1.17 Ma (2σ; MSWD = 2.3; n/nt = 38/41) (Fig. 13e). Hypabyssal rhyolite (GS474016) shows less possible inherited grains and yield a distinctly younger lower intercept date at 35.20 ± 1.06 Ma; (2σ; MSWD = 2.6; n = 41) (Fig. 13f).

5.5.b Re/Os Molybdenite Dating

In this study, one Re/Os date for vein controlled molybdenite (PYC21-5-690) cutting medium-grained granodiorite was obtained. Vein controlled molybdenite is common at Robertson cutting igneous rocks similar to what is seen in figure 10F. Molybdenite here yields 39.55 ± 0.17 Ma (2σ), including a 0.31% uncertainty in the decay constant of ^{187}Re. This date is in accordance with previously obtained values in past studies and is presented in Table 5.

5.5.c ^{40}Ar/^{39}Ar K-feldspar Dating

Hydrothermal orthoclase (PYC21-4-452) within a vein with secondary biotite cutting diorite was selected for ^{40}Ar/^{39}Ar determinations and can be seen in figure 10C. Orthoclase in this sample along with secondary biotite reflects potassic alteration similar to what is seen in Figure 7C and 7D. ^{40}Ar/^{39}Ar analysis yielded a composite date of 38.99 ± 0.02 Ma (2σ). Step heating over 12 steps yielded no concise plateau; thus, an integrated date was calculated by summing the isotopic measurements of all the steps (Fig. 14).

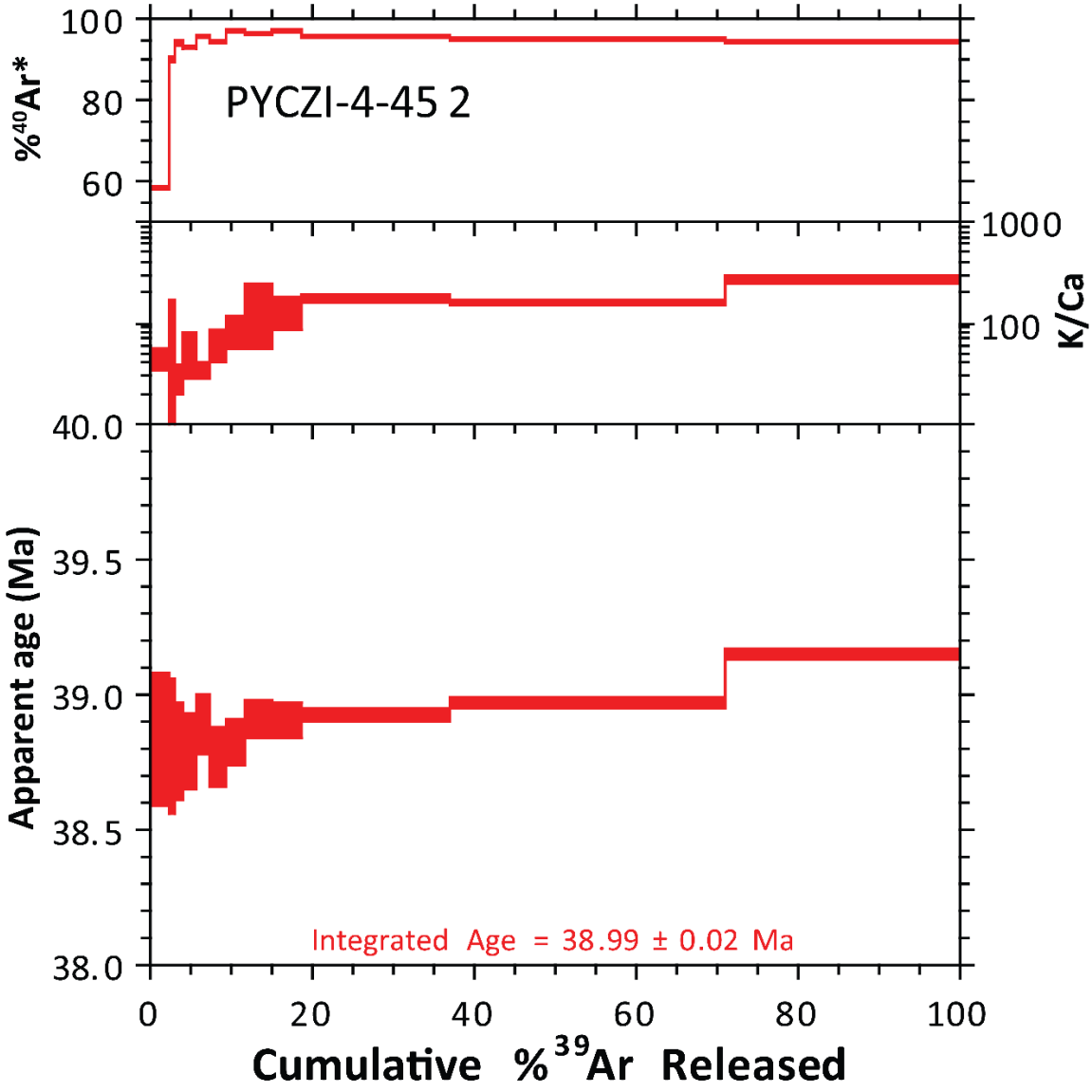

Fig. 14. $^{40}Ar/^{39}Ar$ step heating spectrum of hydrothermal orthoclase (PYC21-4-452) with integrated age over 12 steps

6. DISCUSSION

6.1. Timing of Magmatic and Hydrothermal Events at Robertson

The timing of magmatic and hydrothermal events at Robertson was determined from field relationships, drill core logging, petrography, geochemistry, and geochronology. Hydrothermal alteration includes a sequence that ranges from early endoskarn, potassic, and exoskarn to later

Table 5. Summary of geochronological data for the Robertson Deposit

Sample	Rock type	Material							Reference
$^{40}Ar/^{39}Ar$			Age (Ma) plateau	±2s	Plateau Steps	Plateau % ^{39}Ar	Isochron	±2s	
T99413-570	Granodiorite	Biotite	39.55	0.10	8	85.60	NA	NA	Kelson et al. 2005
PYC21-4-452	Vein cutting Diorite	Orthoclase	38.99	0.02	12	No Plateau	NA	NA	This Study
H10-42	Andesite Dike	Sericite	39.5	0.30	NA	96.9	38.2	1.6	Henry pers. comm.
H10-39	Vein cutting Slaven	Adularia	39.07	0.08	NA	57.1	39.02	0.11	Henry pers. comm.
$^{40}Ar/^{39}Ar$			Age (Ma) wtd mean	±2s	n/nt	K/Ca	±1s		
H10-21	High-SiO2 rhyolite dike, non-mineralized	Sanidine	35.83	0.08	12/23	93.1	11.4		Henry pers. comm.
H10-22	High-SiO2 rhyolite dike, non-mineralized	Sanidine	35.84	0.07	15/16	96.2	54.5		Henry pers. comm.
Re-Os			Age (Ma)	±2s	Re (ppm)	±2s	^{187}Os (ppb)	±2s	
PYC21-5-690	Quartz - mol vein cutting granodiorite	Molybdenite	39.55	0.17	23.94	0.07	9.917	0.005	This Study
T99413-560	Quartz - mol vein cutting granodiorite	Molybdenite	39.00	1.40	58	NA	23.82	NA	Kelson et al. 2005
K-Ar			Age (Ma) Apparent Age	±2s	% K_2O	Ar^{40} rad mol/gm $X10^{-10}$	Ar^{40} rad / Ar^{40} total		
M-123	Porphyritic biotite-hornblende granodiorite	Hornblende	39.13	0.80	1.07	0.613	71.31		Silberman and McKee 1975
M-123	Porphyritic biotite-hornblende granodiorite	Biotite	38.31	0.80	7.99	4.454	81.42		Silberman and McKee 1975
M-124	Porphyritic biotite-hornblende granodiorite	Biotite	38.18	0.80	8.79	4.883	78.29		Silberman and McKee 1975
M-125	Rhyolite	Biotite	35.68	0.70	8.24	4.275	80.34		Silberman and McKee 1975
M-125	Rhyolite	Sanidine	35.59	0.70	11.6	6.003	80.73		Silberman and McKee 1975
U-Pb			Age (Ma)	±2s	n	n/nt	MSWD		
GS474027	Diorite	Zircon	38.54	1.16	36	36/40	2.2		This Study
PYC21-002-975	Hypabyssal Dacite Dike	Zircon	39.80	1.19	44	44/49	3.0		This Study
GPGT2020-009-573	Granodiorite (medium)	Zircon	39.43	1.18	32	32/35	2.6		This Study
GPGT2020-009-642	Granodiorite (coarse)	Zircon	39.09	1.17	40	40/40	2.0		This Study
PYC21-004-127	Granitic Porphyry Dike	Zircon	39.06	1.17	38	38/41	2.3		This Study
GS474016	Subvolcanic Rhyolite Dike	Zircon	35.20	1.06	41	41/41	2.6		This Study

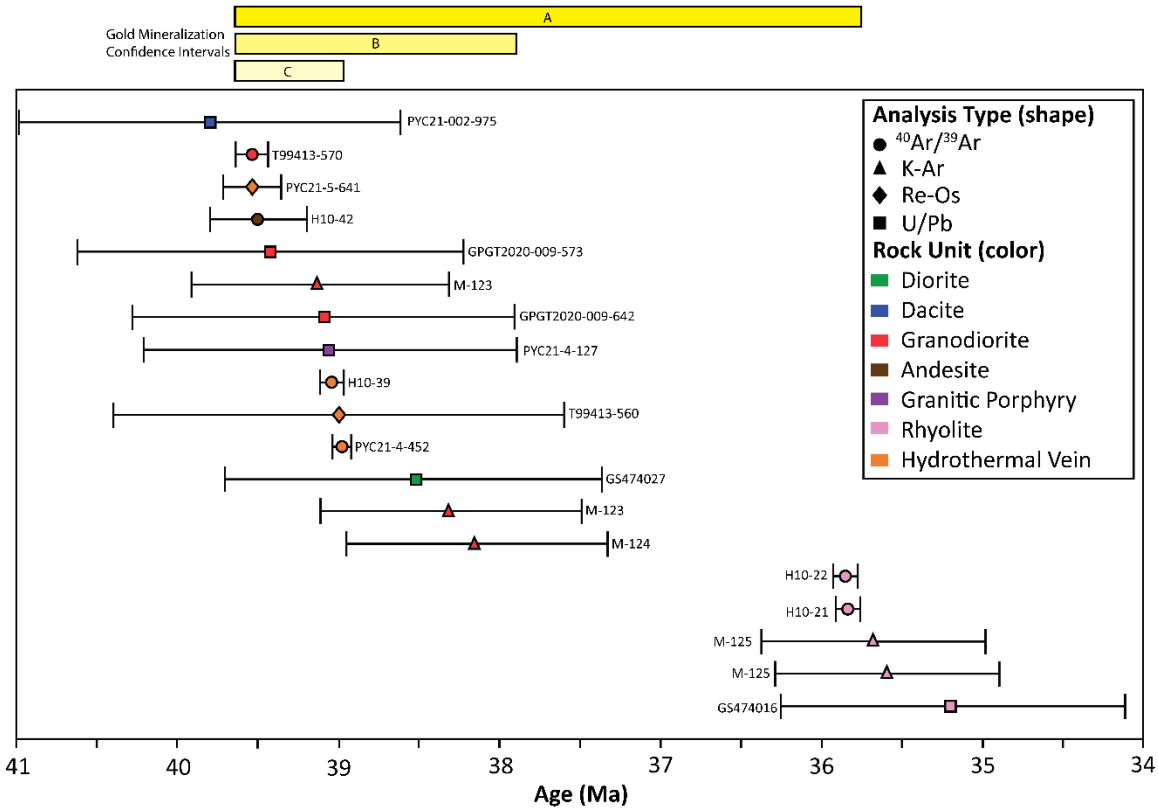

Fig. 15. Compilation summary of historic and current geochronologic data for igneous rocks and hydrothermal minerals at Robertson. Different point shapes represent analysis type. Compilation of geochronologic data in Table 5. Gold confidence intervals give time constraints on gold mineralization using different cross cutting relationships with 2σ included. (A) pre-gold granodiorite and post-gold rhyolite 39.65-35.77 Ma (B) Pre-gold granodiorite and post-gold granitic porphyry dikes 39.65-37.89 Ma (C) Pre-gold granodiorite and post-gold? adularia 39.65 - 38.99 Ma

sericitic and chloritic alteration and were classified based on distinct mineral assemblages and/or visible physical changes in the host lithology (Fig. 7 & Table 2). Mineralization has been characterized over the 5 zones at Robertson including Porphyry, Altenburg Hill, Gold Pan, 39A, and Distal (Fig. 9 & Table 3). Vein relationships were characterized using a vein relationship matrix, and subsequent stages were separated into pre-gold, syn-gold, and post-gold (Fig. 10 & Table 4). Geochronologic data from this study and previous work, along with cross cutting relationships, help to constrain the timing of these events and is summarized in Figure 15 and Table 5. Previous geochronologic data includes five K-Ar ages, one molybdenite Re/Os age, and four $^{40}Ar/^{39}Ar$ ages

of intrusive phases and subsequent hydrothermal events. Previous geochronologic data have been re-calculated with modern Ar/Ar decay constants and are described in detail in the methods section.

The emplacement of the Tenabo stock resulted in early hornfelsing/ thermal metamorphism of Paleozoic siliciclastic lithologies developing quartz, biotite, and calc-silicate hornfels depending on the original protolith composition. Cross-cutting relationships along with geochemical, and geochronologic data indicate a sequential succession of intrusive phases including, an early ilmenite-bearing diorite, hypabyssal dacitic dikes, composite ilmenite-bearing granodiorite, granitic porphyry dikes, and subvolcanic rhyolite dikes (Fig. 2). Five of the six U/Pb LA-ICP-MS dates of intrusive phases from this study, show a tight clustering from 40.99-37.38 Ma with ± 2 sigma included (Fig. 15). With this tight clustering, the sequence of intrusion emplacement is not resolvable at the resolution provided by LA-ICP-MS, thus cross-cutting relationships and previous geochronologic data are needed, however, an Eocene age assessment for these intrusive phases is apparent. Based on age dates and cross-cutting relationships the emplacement of the diorite stock is thought to be the earliest phase of the Tenabo stock, pre 39.55 ± 0.10 Ma, which is the most precise date of the granodiorite, via $^{40}Ar/^{39}Ar$ biotite dating methods, with vein controlled molybdenite cutting the granodiorite dated to 39.55 ± 0.17 Ma. It must be noted that $^{40}Ar/^{39}Ar$ biotite and U/Pb zircon dates do not record the same events in the evolution of igneous magmas and rocks, because different minerals become closed to loss of radiogenic daughter isotopes at different temperatures (Simon et al., 2008; Chiaradia et al., 2014). Cross-cutting relationships, show that the dacitic dikes post-date the diorite but precedes the granodiorite, which based on geochronology, puts it older than 39.55 ± 0.10 Ma, but younger than 39.70 Ma; which is the oldest possible age of the diorite given a 2-sigma error. Geochemical data indicates that the most

evolved phase of this intrusive suite discussed includes the granitic porphyry dikes, which overlap in error with these earlier intrusive phases (39.06 ± 1.17 Ma), but based on cross cutting relations and geochemical data appear to come late in the paragenetic sequence.

Following emplacement of earlier intrusive phases but before intrusion of rhyolite dikes, are sequential hydrothermal alteration, mineralization, and veining stages (Fig. 15). Veining at Robertson appears to closely follow the emplacement of the Tenabo stock and associated hydrothermal alteration, as seen by veins cut by later igneous phases and overprinted by hydrothermal alteration. Pre-gold and syn-gold veins cut all intrusive phases except the granitic porphyry dikes and rhyolite dikes. Included in the pre-gold vein stage, are veins associated with potassic alteration, and as a result of this study, hydrothermal orthoclase from this stage has been dated to 38.99 ± 0.02 Ma; however, this date represents cooling and closure of the Ar/Ar isotopic system which occurred later than the crystallization of the orthoclase. Hydrothermal orthoclase is thought to crystallize at higher temperatures (>400-500˚C) associated with potassic alteration where the closure of the Ar/Ar isotopic system in K-feldspar occurs at lower temperatures (180-400˚C). Based on cross-cutting relationships, pre-gold quartz-molybdenite veins are observed to crosscut earlier hydrothermal orthoclase and biotite veins, thus potassic alteration is thought to occur before 39.55 ± 0.17 Ma, but after emplacement of the diorite and granodiorite stocks. Previous work by Henry (written communication), obtained an ^{40}Ar-^{39}Ar plateau age on vein-controlled adularia cutting the Slaven Formation which came back at 39.07 ± 0.08 Ma. Now while this date closely reflects the date of the hydrothermal orthoclase, it is interpretated that these dates reflect the closure age of the Ar/Ar system and not necessarily the timing of crystallization where adularia is thought to crystallize at lower temperatures (~250˚C) compared to hydrothermal orthoclase. Post-gold veins cut the granitic porphyry dikes, and earlier intrusive

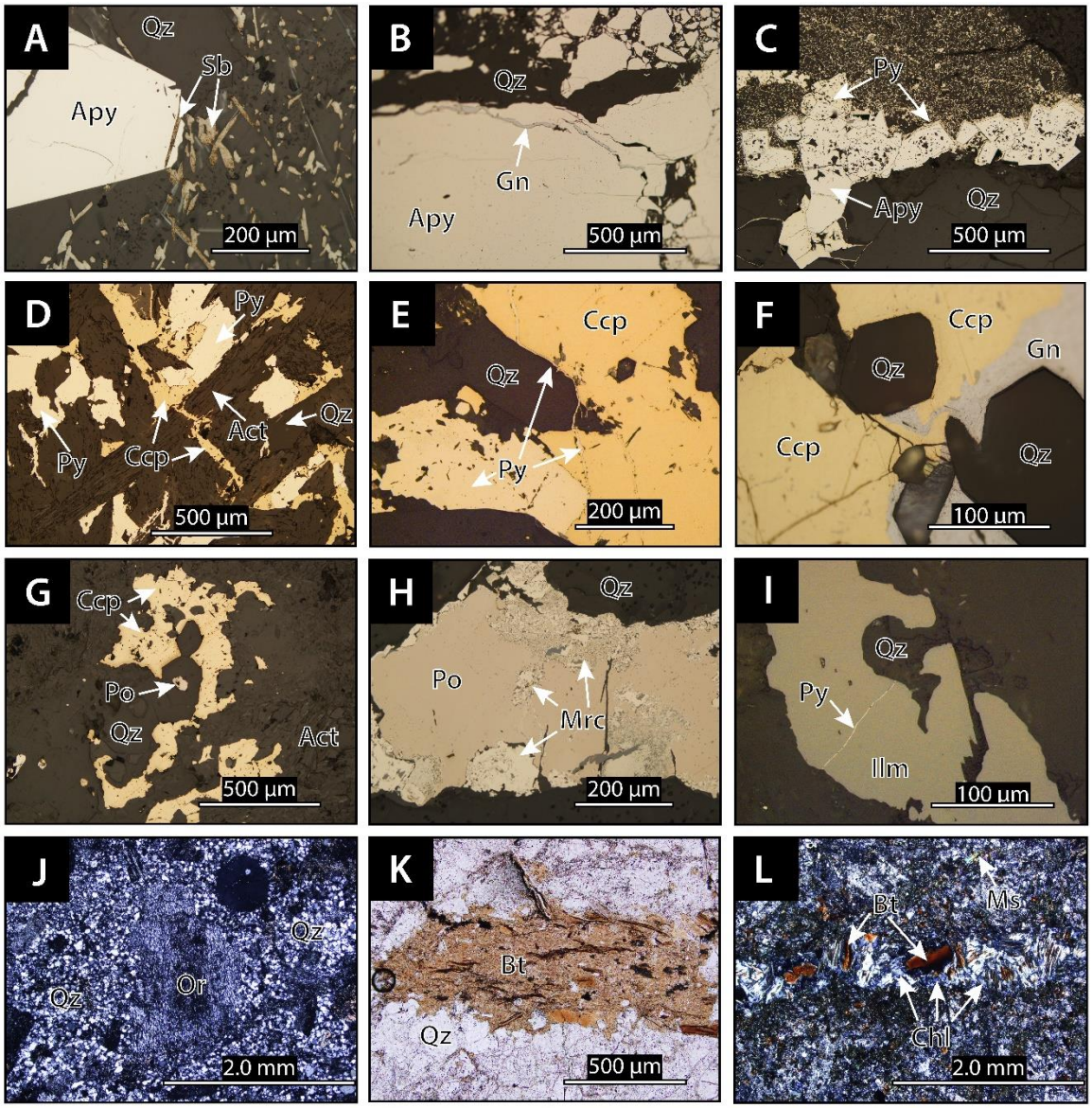

Fig. 16. Reflected light and transmitted cross polarized and plane polarized light photomicrographs of sulfide relations and key hydrothermal alteration phases (A) Reflected light photomicrograph of stibnite cutting arsenopyrite (B) Reflected light photomicrograph of galena cutting arsenopyrite (C) Reflected light photomicrograph of pyrite surrounding arsenopyrite (D) Reflected light photomicrograph of chalcopyrite cutting actinolite (E) Reflected light photomicrograph of pyrite cutting chalcopyrite (F) Reflected light photomicrograph of galena cutting chalcopyrite (G) Reflected light photomicrograph of chalcopyrite surrounding and infilling between quartz and pyrrhotite (H) Reflected light photomicrograph of marcasite after pyrrhotite (I) Reflected light photomicrograph of pyrite cutting ilmenite (J) Transmitted cross polarized photomicrograph of secondary hydrothermal orthoclase replacing earlier primary plagioclase (K) Transmitted plane polarized photomicrograph of secondary hydrothermal “shreddy” biotite replacing primary mafic mineral (L) Transmitted cross polarized photomicrograph of chlorite after secondary biotite in biotite veinlet. Abbreviations: Act = actinolite, Apy = arsenopyrite, Bt = biotite, Ccp = chalcopyrite, Chl =

Chlorite, Gn = galena, Mrc = marcasite, Ms = muscovite, Or = orthoclase, Po = pyrrhotite, Py = pyrite, Sb = stibnite, Qz = quartz

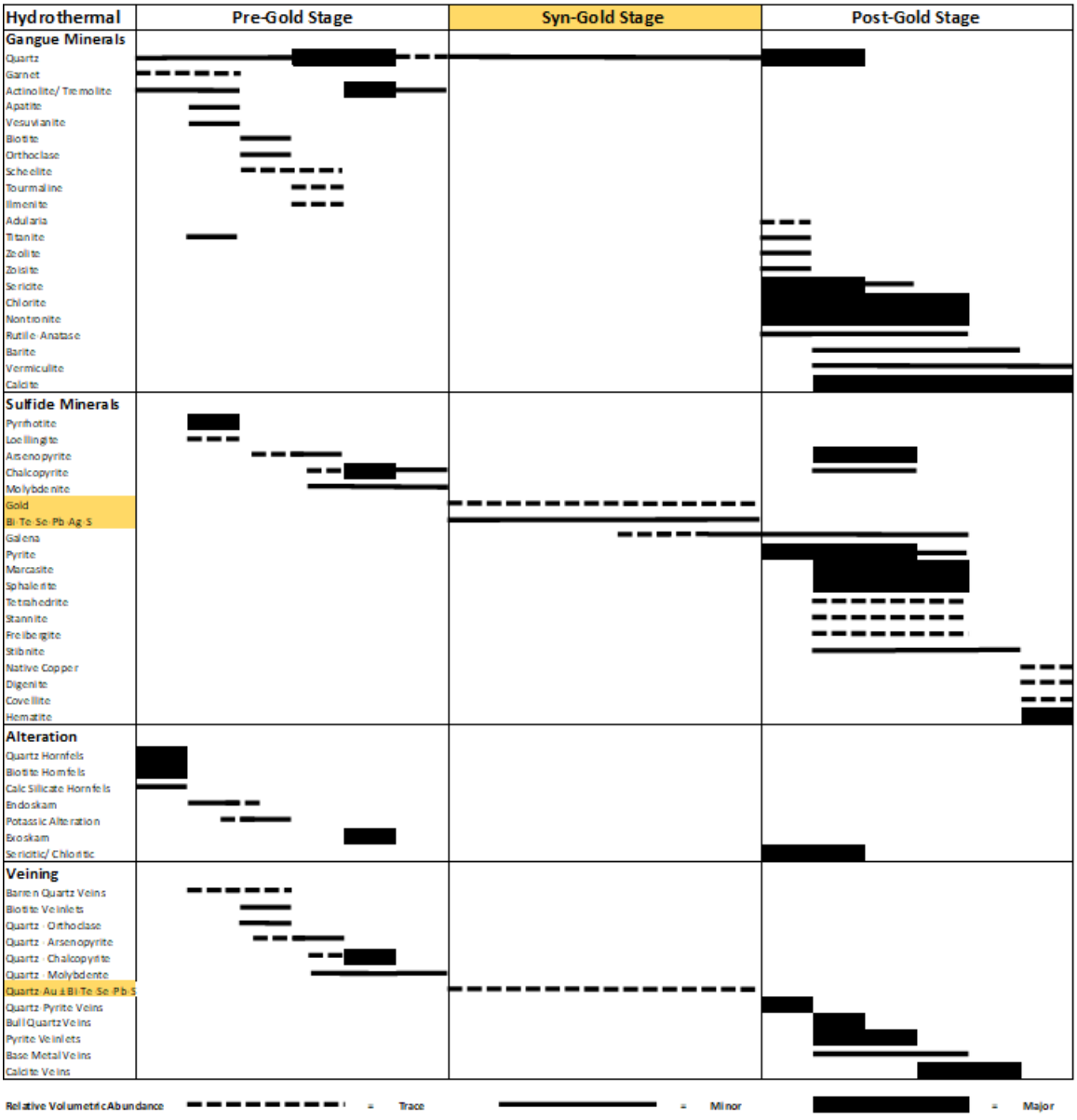

Fig. 17. Paragenetic sequence table separating minerology, alteration, and veining types by pre, syn, and post-gold events. Note that all cells are represented by relative volumetric abundances and are shown with respect to gold mineralization. All minerals, alteration assemblages, and vein types are hydrothermal in origin and do not represent primary minerals. This generalized sequence expresses the overall relationships of these events in a unidirectional manner and does not take into account the possibility of multiple hydrothermal pulses

phases, but not rhyolite dikes which constrains the ages of these veins between (39.06 ± 1.17-35.84 ± 0.07 Ma). $^{40}Ar/^{39}Ar$ dates of sanidine from rhyolite dikes record the time of dike

emplacement, when the dikes cooled geologically instantaneously from magmatic to host rock temperatures (Mercer, 2021). Based on all of these observations it is concluded that the U/Pb zircon ages reflect emplacement age signatures at elevated temperatures where Ar/Ar hornblende, Re/Os molybdenite, Ar/Ar biotite, and Ar/Ar K-feldspar represent cooler closing systems (in order from higher to lower temperatures) (Berger and York, 1981).

To constrain the age of gold mineralization at Robertson, cross-cutting relationships, geochemistry, and geochronology can be used. Using the pre-gold granodiorite $^{40}Ar/^{39}Ar$ biotite date and post-gold adularia date, gold mineralization in constrained between 39.65 - 38.99 Ma, with 2 sigma included. However, this is based on the assumption that adularia truly post-dates gold mineralization as no direct cross-cutting relationships were found in this study. Looking at geochemistry, the Au-rich granodiorite and Au-poor granitic porphyry dikes can place an upper and lower bound of gold mineralization from 39.65-37.89 Ma with 2-sigma error included. Using a more conservative age bracket, pre-gold granodiorite and post-gold rhyolite constrains gold 39.65-35.77 Ma with 2-sigma included, originally reported by Tarnocai (1998). Looking at these relationships regardless of exact timing, there is an apparent relationship between upper Eocene intrusive stocks and gold mineralization at Robertson. Key cross-cutting relationships can be seen in photomicrographs in Figures 8, 9, and 10 with sulfide relations and hydrothermal alteration seen in Figure 16. Gangue minerals, sulfide minerals, alteration, and veining have been separated into pre, syn, and post-gold stages and a summation of this paragenesis can be seen in (Fig. 17).

6.2. Metallogenic Implications of the Robertson Deposit

Cross-cutting relationships, geochronological data, and geochemistry indicate that gold mineralization at Robertson resulted from the emplacement of upper Eocene reduced ilmenite-

bearing intrusive stocks into Paleozoic siliciclastic sedimentary lithologies forming a high-tonnage, low-grade gold deposit characterized by a Au-As-Bi-Te-Se-Pb-Ag-S metal association. It has been identified that a majority of the gold mineralization at Robertson occurs in proximal hornfels to the Tenabo stock; however, substantial gold mineralization is intrusion hosted. These intrusions are classified, by our new geochemical data, as metaluminous granitoids exhibiting several phases and appear to become more evolved over time as represented by elevated values of incompatible elements including Rb and depressed values of compatible MgO, CaO, Na_2O (Fig. 6). Based on petrographic evidence, it is inferred that mineralizing conditions for gold precipitation were under relatively low sulfur fugacity and oxidation state, leading to deposition of a native Bi, arsenopyrite, pyrrhotite, and loellingite assemblage, which is typical of low-sulfidation conditions (Einaudi et al., 2003). Here the close association between gold with tellurides and Bi-Te-Se-Pb-Ag-S sulfosalts, including hedleyite, bismuthinite, and tetradymite is present.

These conditions are typical for intrusion-related gold systems (IRGS) described by Sillitoe (1991), Thompson et al., (1999), Thompson and Newberry, (2000), Lang et al., (2000), Baker et al., (2005), Hart, (2005), and Hart (2007). These types of deposits are typified by (1) metaluminous subalkalic intrusions of intermediate to felsic composition, (2) low primary oxidation states “reduced ilmenite-series” (Ishihara, 1981), (3) well developed hornfelsed thermal aureoles, (4) volumetrically restricted hydrothermal systems compared to the footprint of porphyry systems (5) intrusion hosted sheeted vein arrays of low sulfide quartz veins (<5 vol %) with a Au-As-Bi-Sb-Te-W signatures, (6) comprise bulk tonnage, low-grade Au resources lacking anomalous Cu grades, and (7) generate fluids which are low salinity and CO_2 rich. Major deposit examples of this class include Fort Knox (Alaska), Dublin Gulch (Yukon), Shotgun (Alaska), True North (Alaska), Brewery Creek (Yukon), Mokrsko (Czech Republic), Vasilkovskoe (Central Asia), Timbarra (New

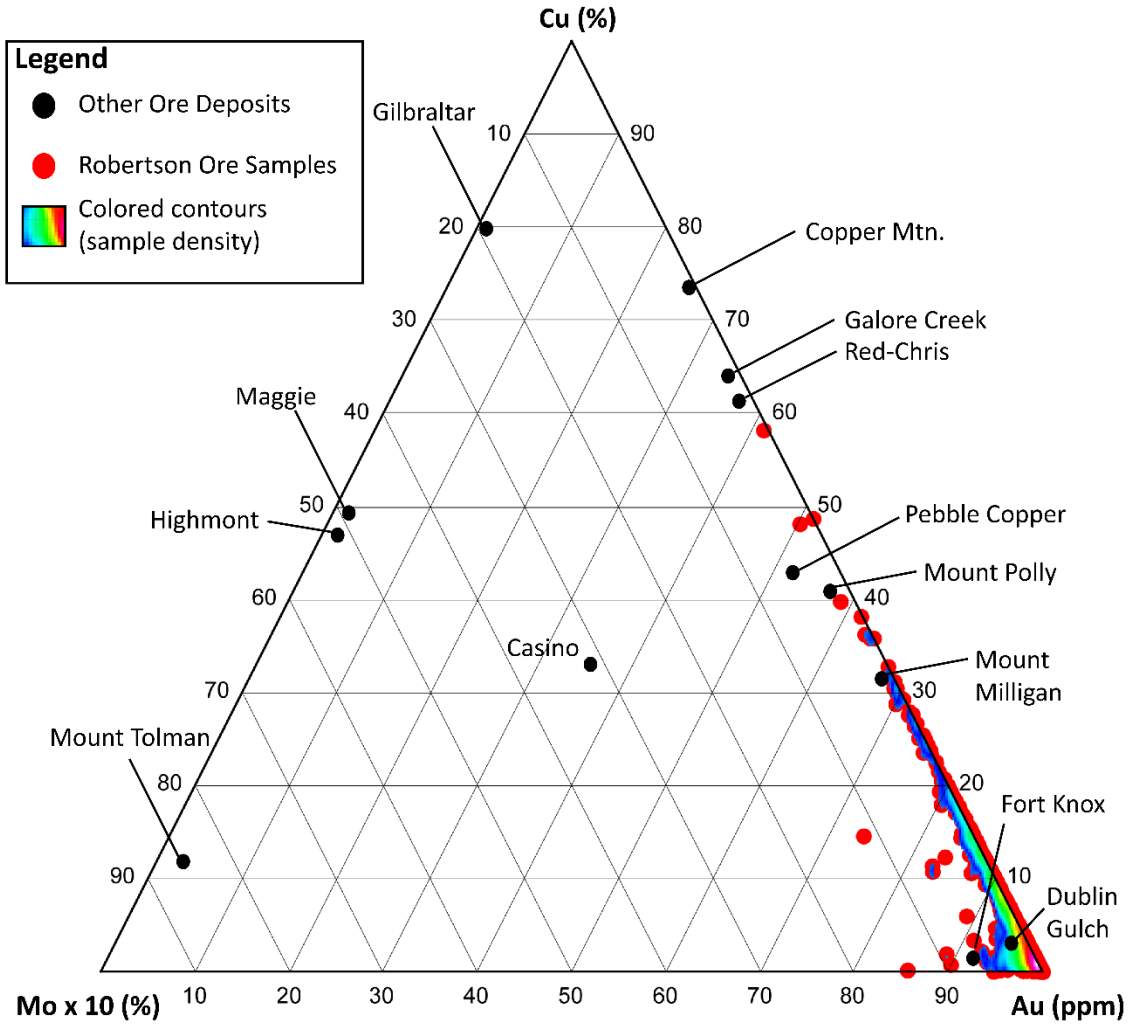

Fig. 18. Plot of relative abundances of copper (%), molybdenum (% x 10), and gold (ppm) for selected cordilleran deposits (black) and Robertson samples (red) with colored contours (sample density). Modelled after McMillan (1995), Cox and Singer (1988), and Sillitoe (1993). Robertson ore samples sorted by grades > 0.685 g/t

South Wales, Australia), Kidston (Queensland, Australia), and Kori Kollo (Bolivia). Intrusion-hosted ores are dominated by a Au-W-Bi-Te signature, with Au correlating closely with Bi and Te, but not at all with W (Hart 2007). The correlation between Au and Bi in some of these major deposits is presented in Table 1 of Baker et al., (2005). Striking similarities are present between these deposits and intrusion hosted gold at Robertson. This contrasts with porphyry copper an

Table 6. Selected Characteristics of Intrusion Related Gold Deposits

Region	Deposit	Deposit Type	Associated Intrusion	Age (Ma)	Size (Mt)	Au Grade (g/t)	Au Total (Moz.)	Metal Suite	Reference
Battle Mountain -Eureka Trend, Nevada, USA	***Robertson***	Au Skarn	Granodiorite	39	54	0.63	1.94	Au-Ag-As-Bi-Te-Se-Pb-S	This Study
	Phoenix Fortitude	Au Skarn	Granodiorite Porphyry	40.7	N/A	0.70	10.2	Au-As-Bi-Te-Sb	Johnson & Ressel 2020
	McCoy Creek	Au Skarn	Granodiorite	38.9	1	10.9	3.3	Au-Ag-As-Pb-Zn	Bonner & Muntean 2019
	Buffalo Valley	Au Skarn	Granodiorite	36.9	27	0.66	0.63	Au-Ag-Bi-Te-Se-Pb-Zn	Reid et al., 2010
Bida Trend, Nevada, USA	***Bald Mountain***	Disseminated	Quartz Monzonite Porphyry	159	7.6	N/A	2	Au-Ag-As-Bi-Mo-Cu-W-Sb-Pb-Zn	Nutt & Hofstra 2007
Tintina Gold Belt, Alaska/ Yukon, USA/ Canada	***Fort Knox***	Sheeted Veins	Granite Porphyry	92	210	0.90	7	As-Bi-Te-Mo-Sb-W	Hart 2007
	True North	Disseminated	Granite	90	14.6	1.69	N/A	Au-As-Sb-Hg	Hart 2004
	Dublin Gulch	Sheeted Veins	Granodiorite	92	50.3	0.93	1.5	Au-As-Bi-Te-Mo-Sb-W-Pb	Maloof et al. 2001
	Brewery Creek	Disseminated	Monzonite	91.4	17.2	1.44	0.285	Au-As-Sb-Hg	Hart 2007
Kuskokwim Mineral Belt, Alaska, USA	***Donlin Creek***	Sheeted veins	Rhyodacite	70	541	2.24	39	Au-As-Bi-Te-Mo-Sb-W-Pb	Goldfarb et al. 2004
	Shotgun	Stockwork	Granite	70	32.8	0.93	1.0	Au-Ag-Bi-Te-Mo-Cu	Hart 2004
Tasman Fold Belt, Eastern Australia	***Kidston***	Breccia Hosted	Rhyolite Porphyry	332	94	1.48	4.5	Au-As-Bi-Te-Mo-Cu-Pb-Zn-W-Sn	Baker & Andrew 1991
	Timbarra	Disseminated	Granite	245-238	13	1.00	0.4	Au-Ag-As-Bi-Mo-Sb	Mustard 2001
Altaid Orogenic Belt, Central Asia	***Jilau***	Au Skarn	Granodiorite	299	54	1.10	1.9	N/A	Cole et al. 2000
	Vasilkovskoe	Sheeted Veins	Granodiorite	443	80	3.70	N/A	Au-As-Bi-Te-Cu-Pb-Sb-W	Burshtein 1996
Yana Kolyma Metallogenic Belt, NE Russia	***Myakit***	Sheeted veins	Granite	141	15	6.30	N/A	Au-As-Bi-Zn	Vikenteva et al. 2018
	Chepak	Sheeted veins	Granitoid	149	70	7.00	N/A	Au-As-Bi-Te-W	
	Dubach	Stockwork	Granite	141	35	2.60	N/A	Au-As-Bi	
	Christoe	Stockwork	Granodiorite	140	140	10.0	N/A	Au-As-Bi-W	
Central Bohemian metallogenic zone, Czech Republic	***Mokrsko***	Sheeted Veins	Granodiorite	349	66	1.5	N/A	Au-As-Bi-Te-Mo-W-Sb-Cu	Moravek 1995

porphyry gold deposits, which exhibit episodic fluid pulses of volatiles and banded quartz veinlets with magnetite (Muntean & Einaudi, 2000). A ternary diagram plotting the relative abundances of copper (in %), molybdenite (%x10), and gold (ppm) modified from Cox and Singer (1988), Sillitoe (1993), and McMillan (1995) of select porphyry type and intrusion related gold systems, illustrates these differences and can be seen in Figure 18.

Deposits associated with intrusion-related gold deposits may include gold skarns described by Meinert (1989), Theodore et al., (1991), and Ettlinger et al., (1992). Gold skarns are typified by (1) clastic or volcaniclastic host rocks proximal to an igneous intrusion (2) zoned deposits in relation to an igneous stock with proximal garnet and distal pyroxene (3) proximal zones tend to be more Cu rich where distal zones are commonly elevated in Au, As, Bi, Te, sometimes with Pb-Zn-Ag halos beyond the skarn limits (4) Bi-dominant minerals including native bismuth, maldonite, hedleyite, and joseite (5) arsenopyrite and pyrrhotite dominant sulfide assemblages with lesser and usually later pyrite and marcasite (6) low-grade high-tonnage deposits. Major deposit examples of this class include Hedley (British Columbia, Canada), Bau (Malaysia), Beal (Montana, USA), La Luz (Nicaragua), Stormont (Tasmania, Australia), and Red Dome (Queensland, Australia). In northern Nevada, a number of Au-Ag (Cu) skarn systems with similar geologic settings include McCoy Creek, Fortitude, Minnie-Tomboy, and Buffalo Valley, all of which are on the Battle Mountain Eureka trend. These deposits have been discussed to fit the reduced intrusion related gold deposit model; where hornfelsed, variably calcareous, clastic host rocks are host to auriferous arsenopyrite-rich mineralization, either as replacements, or with diopside ± chlorite ± actinolite skarns that can be widespread, occurring several kilometers away from the causative pluton (Hart et al., 2000; Mair et al., 2006). Compared to deposits globally and locally, it appears Robertson fits in a class of reduced intrusion related gold deposits and associated gold skarns. As a result of these findings a compilation of intrusion-related gold deposits is compared in Table 6.

Gold mineralization and Robertson is interpretated to be the result of a cooling magmatic hydrothermal fluid representing unidirectional cooling path from the Tenabo stock. Given the systematic association of Au with Bi-bearing minerals, possible gold transport mechanisms to lower temperatures <300°C, such as the liquid bismuth collector model first proposed by Douglas et al., (2000); Tooth et al., (2008); Tooth et al., (2013); and built upon by Cave et al., (2019) may be important. Here it is proposed that under certain conditions (low

sulfur fugacity) liquid bismuth may exsolve from a hydrothermal fluid (>271.4°C), scavenging gold, and transporting it as an immiscible liquid to lower temperatures. This explains the complex intergrowths of native gold with native bismuth, bismuthinite, tetradymite, tellurobismuthinite, and even Pb-Bi mineral phases. At lower temperatures (~141-219°C) gold lacks a suitable remobilization process and remains within the pyrite lattice as invisible gold thus not forming visible gold (Cave et al., 2019).

6.3. Regional Implications and Relations with Carlin-style Gold Deposits

Emplacement of the Tenabo stock and subsequent gold mineralization has implications beyond the limits of the Robertson area. Looking at regional pre-Eocene geologic frameworks, characteristics of the Robertson intrusive suite with regards to other deposits, and what is known about post emplacement structures and geologic constraints, the paleodepth of emplacement for the Tenabo stock can be estimated. Before discussing this, it is currently unknown at which depth the Tenabo stock was emplaced and any comment on such in this thesis is merely an interpretation.

The pre-Eocene tectonic framework of the region is defined by a series of compressional events, spanning from the Antler Orogeny (late Devonian early Mississippian), Sonoma Orogeny (Permian-Triassic), and potential Cretaceous east directed thrusting event, defined by the Abyss fault in the Gold Acres and Pipeline area by Leonardson et al., (2011). Culminating from these thrusting events, it is known that the upper plate in the northern Shoshone Range has been regionally thickened by a series of thrust duplexes which form large structural nappes (Kelson et al., 2008). Gilluly and Gates (1965) estimated that the upper plate thickness in the northern Shoshone Range is on the order of five times its original depositional thickness. Based on modern drilling, it is estimated that the upper plate near Robertson is on the order of 900 m thick.

The Eocene marks the transition between compressional to extensional tectonics (~45 Ma), as a result of the Farallon plate decoupling from the North American plate, accompanying slab rollback and lithospheric delamination initiated along a slab tear (Humphreys, 1995), (Ressel and Henry, 2006). During this time, the Tenabo stock was emplaced into thickened upper plate siliciclastic lithologies and based on recent geochronological data it is inferred that the upper portion of the stock was cooled to ~373 ± 21°C by 39.55 ± 0.10 Ma based on Ar/Ar thermochronometry (Berger & York 1981). Nearby Eocene intrusions, including Hilltop

and Granite Mountain, have been previously dated via ^{40}Ar-^{39}Ar methods and indicate similar cooling ages of 39.6-38.3 Ma (Kelson, 2008). Both biotite and hornblende separates were analyzed from the Granite Mountain stock (samples GM-6 and GM-15: Kelson et al., 2005) and their respective plateau ages (GM-6, biotite, 39.25 ± 0.1 Ma; GM-6, hornblende, 39.45 ± 0.2 Ma; GM-15, biotite, 39.55 ± 0.1 Ma; GM-15, hornblende, 39.25 ± 0.1 Ma) represent the time of closure to Ar loss associated with cooling of the pluton below 550°C (hornblende) and 350°C (biotite; McDougall and Harrison, 1999). The similar plateau ages of biotite and hornblende from both samples may indicate that the Granite Mountain stock cooled quickly, thus implying a relatively shallow level of emplacement ≤2 km (Kelson et al., 2005). Similarity in mineralogy, composition, and age suggest that the three main intrusions (Hilltop, Granite Mtn, and Tenabo) to be apophyses of one larger body that underlies ~55 km^2 (Henry, written communication).

Since the Eocene magmatism ceased ~33 Ma, it is noted that the area remained relatively tectonically quiescent until the onset of basin and range extension and northern Nevada rift (Colgan et al., 2014). New observations from Colgan et al., (2014) found 35.8 Ma densely welded ash flow tuffs (informally named, Tuff of Mount Lewis) interbedded with volcaniclastic deposits atop of Paleozoic rocks in the Mt. Lewis area, 17 km northwest of Tenabo in the northern Shoshone Range. If indeed truly an ash flow tuff, this unit would mark the paleosurface at this time. Colgan et al., (2014) additionally noted the 25.4 Ma Nine Hill Tuff, 3 km north of Tenabo, which would have also marked the paleosurface. Following 25 Ma, major Middle Miocene extension (>100%) related to the northern Nevada Rift cut the 34 Ma Caetano caldera and extended north through the Shoshone Range (Colgan et al 2008). This event tilted intracaldera tuffs ~40° east by west dipping normal faults (John et al., 2008) and along with younger high angle normal faulting is thought to have tilted the Tenabo area 20-30° east. Given the discussed past observations along with new insights from this study it is estimated that the Tenabo stock was emplaced at shallow-moderate levels (~2-5 km) (Fig. 19). This is in accordance with observations from similar Eocene intrusion stocks within the northern Shoshone Range, including Hilltop and Granite Mountain, along with findings of volcanic units marking the paleosurface shortly after.

Considering the relatively shallow level of emplacement discussed, the presence of an Eocene intrusion-related gold deposit at Tenabo within 5 km of the 20 Moz plus Pipeline Carlin-type deposit begs the question of whether the two deposits are genetically related. Similar

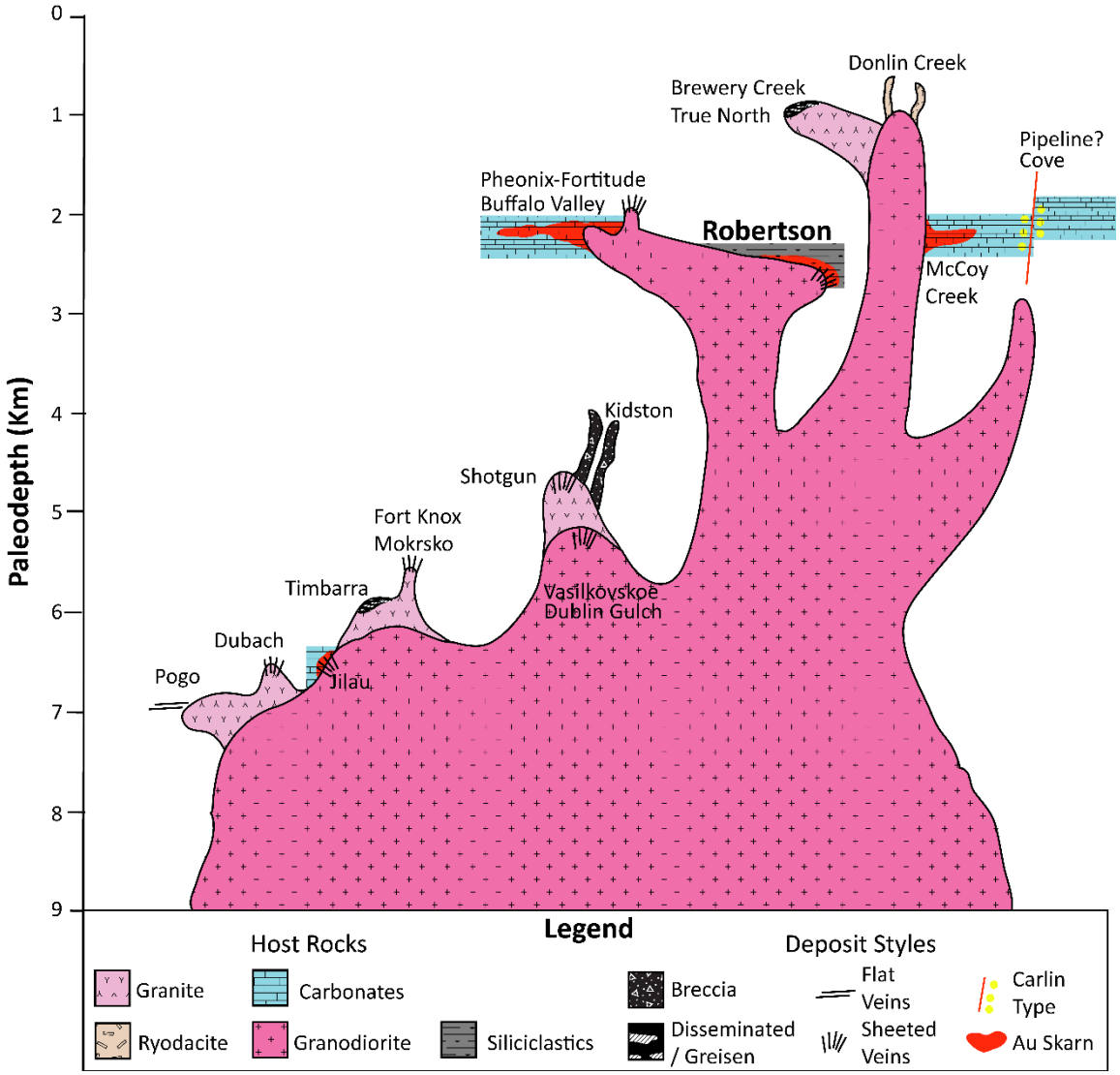

Fig. 19. Schematic diagram illustrating different mineralization styles and their relationships to different intrusion related gold deposits at varying depths of emplacement. Modified after Thompson (1999); Yakubchuk (2002); Baker (2002); Muntean (2004); Baker (2005); Friedland (2007); Reid (2010); Hart (2007), Sillitoe (2010). Note that overlain intrusive rock types do not reflect proper cross cutting relationships. Many of the deposits here exhibit more than one style of mineralization (eg. intrusion hosted veins and gold skarns) but for simplicity the dominating style is shown

relationships are described at Cove/McCoy (Lander County, Nevada) (Johnston et al., 2008; Muntean et al., 2017), Kinsley (Elko County, Nevada) (Hill, 2016; Muntean et al., 2017), Archimedes (Eureka County, Nevada) (Dilles et al., 1996), and the Carlin Trend (Ressel and Henry, 2006; Hollingsworth et al., 2017; Holley et al., 2022), where Carlin-style mineralization is both spatially and temporally related to intrusive stocks (typically Eocene). Carlin-type deposits are generally interpretated to have formed at shallow depths (~1-3 km), at moderate temperatures (~160°-220°C), and to be spatially and temporally associated with deep-seated intrusions, lending magmatic-hydrothermal fluids which lead to carbonate replacement and silicification, containing gold in arsenian pyrite lattices with Au-Hg-Sb-Tl-As-S metal associations (Cline et al., 2001; Arehart

et al., 2003; Cline et al., 2005; Muntean et al., 2011; Muntean and Cline, 2018; Muntean, 2020). The timing for auriferous mineralization at Robertson is synchronous with the emplacement of the Tenabo stock, and is compatible with the initial stages of extensional tectonics and the estimated timing for gold mineralization (~35.7 Ma) in Carlin type gold deposits within the Cortez mining district just to the south (Arbonies et al., 2011; Henry et al., 2020; Mercer, 2021). Arehart and Donelick (2006) present thermochronologic data at the Pipeline deposit, where it is clear that there was a significant hydrothermal event at approximately 38.7 ± 2.0 Ma and while the Tenabo stock may not be the causative intrusion it is possible that there are other, presently unexposed, plutons of that age that contributed at least thermal energy to drive the Pipeline system.

7. CONCLUSION AND RESEARCH OUTLOOKS

Results of this study document the presence of a low-grade high tonnage gold deposit with low oxidation and sulfidation state mineral assemblages proceeding the emplacement of an upper Eocene reduced ilmenite-bearing intrusive stock that intruded into Ordovician-Devonian siliciclastic sedimentary lithologies. Subsequent magmatic hydrothermal alteration, mineralization, and veining stages have been characterized and separated into pre, syn, and post-gold events. Based on these observations Robertson is considered within the class of reduced intrusion related gold deposits and associated gold skarns. The link between Robertson or other intrusion related gold systems and proximal Carlin-style gold deposits may be assessed and this work may serve as a foundation for future studies.

Further observations of cross-cutting relationships, igneous phases, and major structures will aid future field descriptions and core logging. Continued use of vein offsetting matrices, will lend statistically significant relationships between differing vein types. Mineralogical descriptions of garnet and pyroxene phases permit the opportunity to describe chemical zonations and hydrothermal fluid evolution. More detailed work may aim to describe fluid inclusions in order to determine conditions of formation for gold in quartz veins, emplacement depths of the Tenabo stock, trace element compositions of ore forming fluids, and CO_2 concentrations under these conditions. Alternatively, apatite fission tracks or U-Th/He geochronology may yield a clear indication of exhumation rates in the northern Shoshone Range and thus refine emplacement depths for intrusions at Robertson. Whole rock and trace element geochemistry can further classify intrusive

units at Robertson and may prove useful in areas of increased hydrothermal alteration. Determining the oxidation state of the Tenabo stock via Ce X-ray absorption near-edge spectroscopy (XANES) or from zircon trace element data (Loucks et al., 2020) can facilitate the detailed classification of these units. Major and trace element analysis of sulfides at Robertson can provide insights into geothermometry and may indicate gold bearing sulfide phases in the distal settings of the deposit.

REFERENCES

Ahmed, A.D., Hickey, K.A., Barker, S.L., Steininger, R. and Pennell, B., 2010. The Elder Creek deposit: The upper plate expression of an auriferous Carlin-type hydrothermal system?. *Final Technical Report September, 2010*, p.227

Arbonies, D.G., Creel, K.D., and Jackson, M.L., 2011, Cortez Hills lower zone discovery and geologic update: Geological Society of Nevada Symposium, Reno-Sparks, Nevada, May 2010, Extended Abstracts, p. 447–462.

Arehart, G.B. and Donelick, R.A., 2006. Thermal and isotopic profiling of the Pipeline hydrothermal system: Application to exploration for Carlin-type gold deposits. *Journal of Geochemical Exploration*, *91*(1-3), pp.27-40.

Arehart, G.B., Chakurian, A.M., Tretbar, D.R., Christensen, J.N., McInnes, B.A. and Donelick, R.A., 2003. Evaluation of radioisotope dating of Carlin-type deposits in the Great Basin, western North America, and implications for deposit genesis. *Economic Geology*, *98*(2), pp.235-248.

Baker, T., Pollard, P.J., Mustard, R., Mark, G. and Graham, J.L., 2005. A comparison of granite-related tin, tungsten, and gold-bismuth deposits: Implications for exploration. *SEG Discovery*, (61), pp.5-17.

Berger, G.W. and York, D., 1981. Geothermometry from 40Ar39Ar dating experiments. *Geochimica et Cosmochimica Acta*, *45*(6), pp.795-811.

Black, L.P., Kamo, S.L., Allen, C.M., Davis, D.W., Aleinikoff, J.N., Valley, J.W., Mundil, R., Campbell, I.H., Korsch, R.J., Williams, I.S. and Foudoulis, C., 2004. Improved 206Pb/238U microprobe geochronology by the monitoring of a trace-element-related matrix effect; SHRIMP, ID–TIMS, ELA–ICP–MS and oxygen isotope documentation for a series of zircon standards. *Chemical Geology*, *205*(1-2), pp.115-140.

Bonin, B., Janoušek, V. and Moyen, J.F., 2020. Chemical variation, modal composition and classification of granitoids. *Geological Society, London, Special Publications*, *491*(1), pp.9-51.

Bowring, J.F., McLean, N.M. and Bowring, S.A., 2011. Engineering cyber infrastructure for U-Pb geochronology: Tripoli and U-Pb_Redux. *Geochemistry, Geophysics, Geosystems*, *12*(6).

Brooks, J.W., 1994. *Petrology and geochemistry of the McCoy gold skarn, Lander County, Nevada* (Doctoral dissertation, Washington State University).

Cave, B.J., Barnes, S.J., Pitcairn, I.K., Sack, P.J., Kuikka, H., Johnson, S.C. and Duran, C.J., 2019. Multi-stage precipitation and redistribution of gold, and its collection by lead-bismuth and lead immiscible liquids in a reduced-intrusion related gold system (RIRGS); Dublin Gulch, western Canada. *Ore Geology Reviews*, *106*, pp.28-55.

Christiansen, R.L., Yeats, R.S., Graham, S.A., Niem, W.A., Niem, A.R. and Snavely, P.D., 1992. Post-Laramide geology of the US Cordilleran region. The Cordilleran Orogen, B.C. Burchfiel, P.W. Lipman, M.L. Zoback

Cline, J.S., 2001. Timing of gold and arsenic sulfide mineral deposition at the Getchell Carlin-type gold deposit, north-central Nevada. *Economic Geology*, *96*(1), pp.75-89.

Cline, J.S., Hofstra, A.H., Muntean, J.L., Tosdal, R.M. and Hickey, K.A., 2005. Carlin-type gold deposits in Nevada: Critical geologic characteristics and viable models.

Cockerton, A.B. and Tomkins, A.G., 2012. Insights into the liquid bismuth collector model through analysis of the Bi-Au Stormont skarn prospect, northwest Tasmania. *Economic Geology*, *107*(4), pp.667-682.

Colgan, J.P. and Henry, C.D., 2009. Rapid middle Miocene collapse of the Mesozoic orogenic plateau in north-central Nevada. *International Geology Review*, *51*(9-11), pp.920-961.

Colgan, J.P., John, D.A., Henry, C.D. and Fleck, R.J., 2008. Large-magnitude Miocene extension of the Eocene Caetano caldera, Shoshone and Toiyabe Ranges, Nevada. *Geosphere*, *4*(1), pp.107-130.

Colgan, J.P., Henry, C.D. and John, D.A., 2011. Geologic map of the Caetano caldera, Lander and Eureka counties, Nevada. *Nevada Bureau of Mines and Geology Map 174*.

Colgan, J.P., Henry, C.D. and John, D.A., 2014. Evidence for large-magnitude, post-Eocene extension in the northern Shoshone Range, Nevada, and its implications for the structural setting of Carlin-type gold deposits in the lower plate of the Roberts Mountains allochthon. *Economic Geology*, *109*(7), pp.1843-1862.

Debon, F. and Le Fort, P., 1988. A cationic classification of common plutonic rocks and their magmatic associations: principles, method, applications. *Bulletin de Minéralogie*, *111*(5), pp.493-510.

Dickinson, W.R., 2002. The Basin and Range Province as a composite extensional domain. *International Geology Review*, *44*(1), pp.1-38.

Dilles, P.A., Wright, W.A., Monteleone, S.E., Russell, K.D., Marlowe, K.E., Wood, R.A., Margolis, J., Coyner, A.R. and Fahey, P.L., 1996, April. The geology of the West Archimedes deposit: A new gold discovery in the Eureka mining district, Eureka County, Nevada. In *Geology and Ore Deposits of the American Cordillera: Geological Society of Nevada Symposium, Reno, 1995, Proceedings* (pp. 159-171).

Douglas, N., 2000. The liquid bismuth collector model: an alternative gold deposition mechanism. In *Geological Society of Australia Abstracts* (Vol. 59, pp. p-135). Geological Society of Australia; 1999.

Eddy, M.P., Ibañez-Mejia, M., Burgess, S.D., Coble, M.A., Cordani, U.G., DesOrmeau, J., Gehrels, G.E., Li, X., MacLennan, S., Pecha, M. and Sato, K., 2019. GHR 1 Zircon–A New Eocene Natural Reference Material for Microbeam U-Pb Geochronology and Hf Isotopic Analysis of Zircon. *Geostandards and Geoanalytical Research*, *43*(1), pp.113-132.

Einaudi, M. T., Hedenquist, J. W., & Inan, E. E. (2003). Sulfidation state of fluids in active and extinct hydrothermal systems: Transitions from porphyry to epithermal environments. *Special Publication-Society of Economic Geologists*, *10*, 285-314.

Emmons, W.H., 1910, A reconnaissance of some mining camps in Elko, Lander, and Eureka Counties, Nevada: U. S. Geological Survey Bulletin 408, 130 p.

Ettlinger, A.D., Meinert, L.D. and Ray, G.E., 1992. Gold skarn mineralization and fluid evolution in the Nickel Plate Deposit, British Columbia. *Economic Geology*, *87*(6), pp.1541-1565.

Fithian, M.T., Holley, E.A. and Kelly, N.M., 2018. Geology of gold deposits at the Marigold mine, Battle Mountain district, Nevada.

Gilluly, James and Gates, Olcott, 1965, Tectonic and igneous geology of the northern Shoshone Range, Nevada: U.S. Geol. Survey Prof. Paper 465, 153 p.

Hart, C.J., 2007. Reduced intrusion-related gold systems. *Geological Association of Canada, Mineral Deposits Division*, *5*, pp.95-112.

Hart, C.J., Baker, T. and Burke, M., 2000. New exploration concepts for country-rock-hosted, intrusion-related gold systems: Tintina gold belt in Yukon. *The Tintina gold belt: concepts, exploration and discoveries. British Columbia and Yukon Chamber of Mines, Special*, *2*, pp.145-172.

Henry, C.D. and John, D.A., 2013. Magmatism, ash-flow tuffs, and calderas of the ignimbrite flareup in the western Nevada volcanic field, Great Basin, USA. *Geosphere*, *9*(4), pp.951-1008.

Henry, C.D., John, D.A., Heizler, M.T., Leonardson, R.W., Colgan, J.P., Watts, K.E., Ressel, M.W. and Cousens, B.L., 2020. Why did Great Basin Eocene magmatism generate Carlin-type gold deposits when extensive Jurassic to middle Miocene magmatism did not? Lessons from the Cortez region, northern Nevada, USA. In *8th Symposium of Geological Society of Nevada*.

Holley, E.A., Fulton, A., Jilly-Rehak, C., Johnson, C. and Pribil, M., 2022. Nanoscale isotopic evidence resolves origins of giant Carlin-type ore deposits. *Geology*.

Reid, R.F., Nicholes, J., Kofoed, R., McComb, M. and Sechrist, K.J., 2010, May. Buffalo Valley gold mine: Porphyry copper, gold skarn or distal disseminated precious-metal deposit. In *Great Basin evolution and metallogeny, Geological Society of Nevada, Symposium, Reno/Sparks* (pp. 637-656).

Hollingsworth, E.R., Ressel, M.W. and Henry, C.D., 2017. Age and Depth of Carlin-type Gold Deposits in the Southern Carlin Trend: Eocene Mountain Lakes, Big Volcanoes, and Widespread, Shallow Hydrothermal Circulation. *Special Publication*, *64*, pp.149-173.

Humphrey, F. L., 1945, Report on Gold Quartz and Phoenix mines, Lander County,
Nevada: Nevada Bureau of Mines Report (unpublished), 11 p.

Humphreys, E.D., 1995. Post-Laramide removal of the Farallon slab, western United States. *Geology*, *23*(11), pp.987-990.

John, D.A., Wallace, A.R., Ponce, D.A., Fleck, R.B., Conrad, J.E., Cluer, J.K., Price, J.G., Struhsacker, E.M., Hardyman, R.F. and Morris, C.L., 2000. New perspectives on the geology and origin of the northern Nevada rift. *Geology and ore deposits*, pp.127-154.

Johnson, C.L., Ressel, M.W. and Ruprecht, P., 2020. Toward a global Carlin-type exploration model: The relationship between Eocene magmatism and diverse gold-rich deposits in the Great Basin, USA. *Vision for discovery. Geology and ore deposits of the Basin and Range*, *1*, pp.355-382.

Johnson, M. G.,1973, Placer gold deposits of Nevada: U.S. Geol. Survey Bull. 1356, pp. 39-41.

Johnston, M.K., Thompson, T.B., Emmons, D.L. and Jones, K., 2008. Geology of the Cove mine, Lander county, Nevada, and a genetic model for the McCoy-Cove hydrothermal system. *Economic Geology*, *103*(4), pp.759-782.

Hickey, K.A., Ahmed, A.D., Barker, S.L. and Leonardson, R., 2014. Fault-controlled lateral fluid flow underneath and into a Carlin-type gold deposit: Isotopic and geochemical footprints. *Economic Geology*, *109*(5), pp.1431-1460.

Hill, T.J., 2016. *Time-space relationships between sediment-hosted gold mineralization and intrusion-related polymetallic mineralization at Kinsley Mountain, NV*. University of Nevada, Reno.

Kelson, C.R., Keith, J.D., Christiansen, E.H., and Meyer, P.E., 2000, Mineral paragenesis and depositional model of the Hilltop gold deposit, Lander County, NV: Geology and ore Deposits 2000: The Great Basin and Beyond: Geological Society of Nevada Symposium, Reno/Sparks, May 2000, Proceedings, p. 1107–1132.

Kelson, C.R., Crowe, D.E. and Stein, H.J., 2008. Geochemical and geochronological constraints on mineralization within the Hilltop, Lewis, and Bullion mining districts, Battle Mountain-Eureka trend, Nevada. *Economic Geology*, *103*(7), pp.1483-1506.

Kelson, C.R., Crowe, D.E. and Stein, H.J., 2005. Geochronology and geochemical study of part of the Battle Mountain-Eureka trend, Nevada. *Geochimica et Cosmochimica Acta Supplement*, *69*(10), p.A567.

Ketner, K.B., 2012. *An alternative hypothesis for the mid-Paleozoic Antler orogeny in Nevada*. US Department of the Interior, US Geological Survey.

King, C., Bien, J., and Humphreys, A.A., 1876, Geological and topographical atlas accompanying the report of the geological exploration of the fortieth parallel, made by authority of the Hon. Secretary of War under the direction of Brig. and Brvt. Major-General A.A. Humphreys: U.S. Army Engineer's Department Professional Paper 18, 25 plates.

Kuiper, K.F., Deino, A., Hilgen, F.J., Krijgsman, W., Renne, P.R. and Wijbrans, A.J., 2008. Synchronizing rock clocks of Earth history. *science*, *320*(5875), pp.500-504.

Lang, J.R., Baker, T., HART, C.J. and Mortensen, J.K., 2000. An exploration model for intrusion-related gold systems. *SEG Discovery*, (40), pp.1-15.

Lee, W.T., Stone, R.W., Gale, H.S., and others, 1916, The overland route, with a side trip to Yellowstone Park, Pt. B. Guidebook of the western United States: U.S. Geological Survey Bulletin 612, 251 p.

Leonardson, R.W., Steininger, R. and Pennell, B., 2011. Barrick Cortez gold acres structure. In *Geological Society of Nevada 2010 Symposium: Great Basin Evolution and Metallogeny: Lancaster, DEStech Publications* (pp. 17-29).

Loucks, R.R., Fiorentini, M.L. and Henríquez, G.J., 2020. New magmatic oxybarometer using trace elements in zircon. *Journal of Petrology*, *61*(3), page 034.

Mair, J.L., Goldfarb, R.J., Johnson, C.A., Hart, C.J. and Marsh, E.E., 2006. Geochemical constraints on the genesis of the Scheelite Dome intrusion-related gold deposit, Tombstone gold belt, Yukon, Canada. *Economic Geology*, *101*(3), pp.523-553.

Maniar, P.D. and Piccoli, P.M., 1989. Tectonic discrimination of granitoids. *Geological society of America bulletin*, *101*(5), pp.635-643.

Markey, R., Stein, H.J., Hannah, J.L., Zimmerman, A., Selby, D. and Creaser, R.A., 2007. Standardizing Re–Os geochronology: a new molybdenite reference material (Henderson, USA) and the stoichiometry of Os salts. *Chemical Geology*, *244*(1-2), pp.74-87.

Maroun, L.R.C., Cline, J.S., Simon, A., Anderson, P. and Muntean, J., 2017. High-grade gold deposition and collapse breccia formation, Cortez Hills Carlin-type gold deposit, Nevada, USA. *Economic Geology*, *112*(4), pp.707-740.

McCusker, R.T., 1996, Geology, mineralization and alteration of the Tenabo sub-district of the Bullion Mining District, Lander County, Nevada: *in* Green, S.M. and Struhsacker, E. (eds.), Geology and Ore Deposits of the American Cordillera, Field Trip Guidebook Compendium, Geological Society of Nevada, p. 288-297.

McCusker, R. T.,2004, Geological Report on the Robertson Property, Lander County, Nevada U.S.A.: unpublished report, 74 p.

McDougall, I., Mac Dougall, I. and Harrison, T.M., 1999. *Geochronology and Thermochronology by the 40Ar/39Ar Method*. Oxford University Press on Demand. McMillan, 1995

McLean, N.M., Bowring, J.F. and Bowring, S.A., 2011. An algorithm for U-Pb isotope dilution data reduction and uncertainty propagation. *Geochemistry, Geophysics, Geosystems*, *12*(6).

Meinert, L.D., 1989. Gold skarn deposits—geology and exploration criteria.

Meinert, L.D., 1998. A review of skarns that contain gold. *Mineralogical Association of Canada Short Course Series*, *26*, pp.359-414.

Mercer, C.N., 2021. Eocene magma plumbing system beneath Cortez Hills Carlin-type gold deposit, Nevada: Is there a deep-seated pluton?. *Economic Geology*, *116*(2), pp.501-513.

Middlemost, E.A., 1994. Naming materials in the magma/igneous rock system. *Earth-science reviews*, *37*(3-4), pp.215-224.

Min, K., Mundil, R., Renne, P.R. and Ludwig, K.R., 2000. A test for systematic errors in 40Ar/39Ar geochronology through comparison with U/Pb analysis of a 1.1-Ga rhyolite. *Geochimica et Cosmochimica Acta*, *64*(1), pp.73-98.

Muntean, J.L. and Einaudi, M.T., 2000. Porphyry gold deposits of the Refugio district, Maricunga belt, northern Chile. *Economic Geology*, *95*(7), pp.1445-1472.

Muntean, J.L. ed., 2018. *Diversity of Carlin-style gold deposits*. Society of Economic Geologists, Incorporated.

Muntean, J.L., Cline, J.S., Simon, A.C. and Longo, A.A., 2011. Magmatic–hydrothermal origin of Nevada's Carlin-type gold deposits. *Nature geoscience*, *4*(2), pp.122-127.

Muntean, J.L., Bonner, W. and Hill, T., 2017, August. Carlin-style gold-silver mineralization at the Cove deposit in Nevada, USA: possible missing link between Carlin-type gold deposits and magmatic-hydrothermal systems. In *Society for Geology Applied to Mineral Deposits Conference Proceedings*.

Muntean, J.L., 2020. Carlin-type gold deposits in Nevada: Geologic characteristics, critical processes, and exploration.

Myers, G.L. and Meinert, L.D., 1988. Zonation of the Copper Canyon-Fortitude gold skarn system (abstr.). In *Geol. Soc. Amer. Abstracts with Programs* (Vol. 20, p. A93).

Oldow, J.S., Lallemant, H.G.A. and Schmidt, W.J., 1984. Kinematics of plate convergence deduced from Mesozoic structures in the western Cordillera. *Tectonics*, *3*(2), pp.201-227.

Paton, C., Woodhead, J.D., Hellstrom, J.C., Hergt, J.M., Greig, A. and Maas, R., 2010. Improved laser ablation U-Pb zircon geochronology through robust downhole fractionation correction. *Geochemistry, Geophysics, Geosystems*, *11*(3).

Radtke, S.A, Foo, S.T. and Percival, T.J. 1995. Geologic and chemical features of the Cortez gold deposit Lander County, Nevada. *In* Geological Society of Nevada, 1995 Symposium Field Trip Guidebook. Gold Deposits of the Cortez Trend: Relationships to a Regional Structural Framework – Field Trip G. pp. 319 – 325.

Ray, G.E., Jaramillo, V.A. and Ettlinger, A.D., 1990. THE McLYMONT NORTHWEST ZONE, NORTHWEST BRITISH COLUMBIA: A GOLD-RICH RETROGRADE SKARN?(104B). *BC Ministry of Energy Mines and Petroleum Resources, Geological Field Work*, pp.1991-1.

Reid, R.F., Nicholes, J., Kofoed, R., McComb, M. and Sechrist, K.J., 2010, May. Buffalo Valley gold mine: Porphyry copper, gold skarn or distal disseminated precious-metal deposit. In *Great Basin evolution and metallogeny, Geological Society of Nevada, Symposium, Reno/Sparks* (pp. 637-656).

Ressel, M.W. and Henry, C.D., 2006. Igneous geology of the Carlin trend, Nevada: Development of the Eocene plutonic complex and significance for Carlin-type gold deposits. *Economic geology*, *101*(2), pp.347-383.

Ressel Jr, M.W., 2006. *Igneous geology of the Carlin Trend, Nevada: the importance of Eocene magmatism in gold mineralization*. University of Nevada, Reno.

Roberts, R.J., 1964. *Stratigraphy and structure of the Antler Peak quadrangle, Humboldt and Lander counties, Nevada* (No. 459-A). US Government Printing Office.

Sampson, C. J., 1988, Report on the Robertson Project near Crescent Valley, Bullion mining district, Lander County, Nevada: unpublished report, 24 p.

Sampson, C.J. 1997. Summary report on the Robertson Property, Crescent Valley, South east of Battle Mountain, Lander County, Nevada, USA. Internal report, May 31, 36p.

Seedorff, E. and Einaudi, M.T., 2004. Henderson porphyry molybdenum system, Colorado: I. Sequence and abundance of hydrothermal mineral assemblages, flow paths of evolving fluids, and evolutionary style. *Economic Geology*, *99*(1), pp.3-37.

Selby, D. and Creaser, R.A., 2004. Macroscale NTIMS and microscale LA-MC-ICP-MS Re-Os isotopic analysis of molybdenite: Testing spatial restrictions for reliable Re-Os age determinations, and implications for the decoupling of Re and Os within molybdenite. *Geochimica et Cosmochimica Acta*, *68*(19), pp.3897-3908.

Sepp, M.D. and Dilles, J.H., 2018. Structural evolution, vein orientation, and paragenesis of the Botija porphyry Cu-Mo-(Au) deposit, Panama. *Economic Geology*, *113*(4), pp.857-890.

Silberman, M.L., and McKee, E.H., 1971, K-Ar ages of granitic plutons in north-central Nevada: Isochron/West, no. 71–1, p. 15–32

Sillitoe, R.H., 1991. Intrusion-related gold deposits. In *Gold metallogeny and exploration* (pp. 165-209). Springer, Boston, MA.

Sláma, J., Košler, J., Condon, D.J., Crowley, J.L., Gerdes, A., Hanchar, J.M., Horstwood, M.S., Morris, G.A., Nasdala, L., Norberg, N. and Schaltegger, U., 2008. Plešovice zircon—a new natural reference material for U–Pb and Hf isotopic microanalysis. *Chemical Geology*, *249*(1-2), pp.1-35.

Smoliar, M.I., Walker, R.J. and Morgan, J.W., 1996. Re-Os ages of group IIA, IIIA, IVA, and IVB iron meteorites. *Science*, *271*(5252), pp.1099-1102.

Spurr, J.E., 1903, Descriptive geology of Nevada south of the 40th parallel and adjacent portions of California: U.S. Geological Survey Bulletin 208, 229 p

Stager, H. K., 1977, Geology and the mineral deposits of Lander County, Nevada; Part 2, Mineral Deposits: MBMG Bull. 88, p. 74-77.

Steiger, R.H. and Jaeger, E., 1977. Subcommision on Geochronology: Convention on the use of decay constants in geo- and cosmochronology: Earth Planetary Science Letters, v. 36. *doi*, *10*, pp.90060-7.

Stewart, J.H., and McKee, E.H., 1977, Geology and mineral deposits of Lander County, Nevada: Nevada Bureau of Mines and Geology Bulletin 88, 106 p.

Stewart, J.H., 1980, Geology of Nevada: Nevada Bureau of Mines and Geology Special Publication 4, 136p.

Stipp, M., Stünitz, H., Heilbronner, R. and Schmid, S.M., 2002. Dynamic recrystallization of quartz: correlation between natural and experimental conditions. *Geological Society, London, Special Publications*, *200*(1), pp.171-190.

Tarnocai, 1998. Geology, Controls on Auriferous Mineralization, and Geologic Potential at Tenabo, Lander County, Nevada U.S.A. unpublished report

Theodore, T.G., Orris, G.J., Hammerstrom, J.M. and Bliss, J.D., 1991. *Gold-bearing skarns* (No. 1930). USGPO; For sale by the Books and Open-File Reports Section, US Geological Survey,.

Thompson, J.F.H. & Newberry, R.J., 2000. Gold deposits related to reduced granitic intrusions. Reviews in Economic Geology, v. 13, p. 377-400

Thompson, J.F.H., Sillitoe, R.H., Baker, T., Lang, J.R. and Mortensen, J.K., 1999. Intrusion-related gold deposits associated with tungsten-tin provinces. *Mineralium Deposita*, *34*(4), pp.323-334.

Tooth, B., Brugger, J., Ciobanu, C. and Liu, W., 2008. Modeling of gold scavenging by bismuth melts coexisting with hydrothermal fluids. *Geology*, *36*(10), pp.815-818.

Tooth, B., Etschmann, B., Pokrovski, G.S., Testemale, D., Hazemann, J.L., Grundler, P.V. and Brugger, J., 2013. Bismuth speciation in hydrothermal fluids: An X-ray absorption spectroscopy and solubility study. *Geochimica et Cosmochimica Acta*, *101*, pp.156-172.

Wiedenbeck, M.A.P.C., Alle, P., Corfu, F.Y., Griffin, W.L., Meier, M., Oberli, F.V., Quadt, A.V., Roddick, J.C. and Spiegel, W., 1995. Three natural zircon standards for U-Th-Pb, Lu-Hf, trace element and REE analyses. *Geostandards newsletter*, *19*(1), pp.1-23.

Wise, S.A. and Watters, R.L., 2011. Reference Material 8599 Henderson Molybdenite. *National Institute of Standards and Technology, Report of Investigation*, *30*.

APPENDIX A: Gold Mineralization

Appendix A contains Supplementary SEM-EDS data/images images in Fig. 8 (D,E,F,J,K,I,L)

SEM-EDS data for Figure 8D

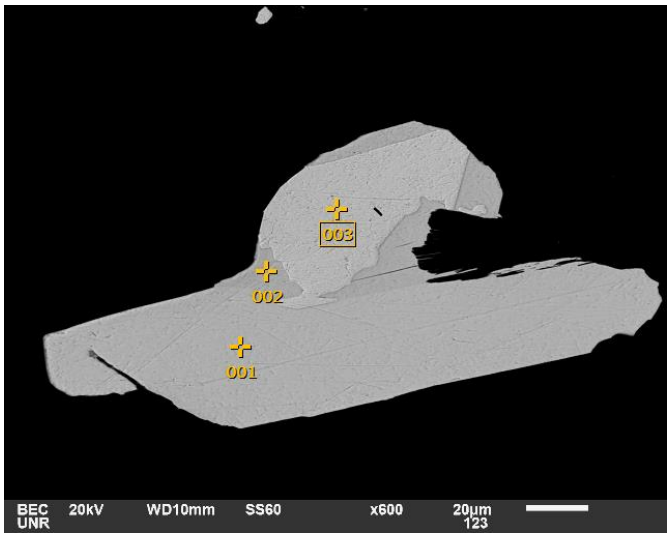

Volt : 20.00 kV

Mag. : x 600

Date : 2021/11/12

Pixel : 1280 x 960

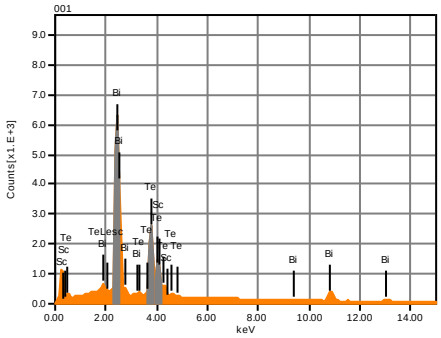

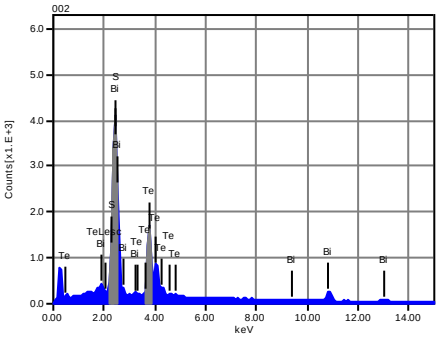

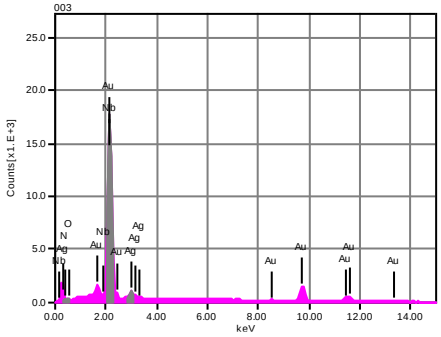

Acquisition Condition

Instrument : 6510(LA)

Volt : 20.00 kV

Current : ---

Process Time : T4

Live time : 13.17 sec.

Real Time : 34.99 sec.

DeadTime : 63.00 %

Count Rate : 57529.00 CPS

	O	Au	Ag	N	S	Sc	Nb	Te	Bi		
001						1.54		37.01	61.45		
002					4.58			35.78	59.64		
003	1.47	81.49	5.52	3.28			8.23				
Average	1.47	81.49	5.52	3.28	4.58	1.54	8.23	36.39	60.55		
Standard deviation			0.00	0.00	0.00	0.00	0.00	0.00	0.00	0.87	1.28

SEM-EDS data for Figure 8E

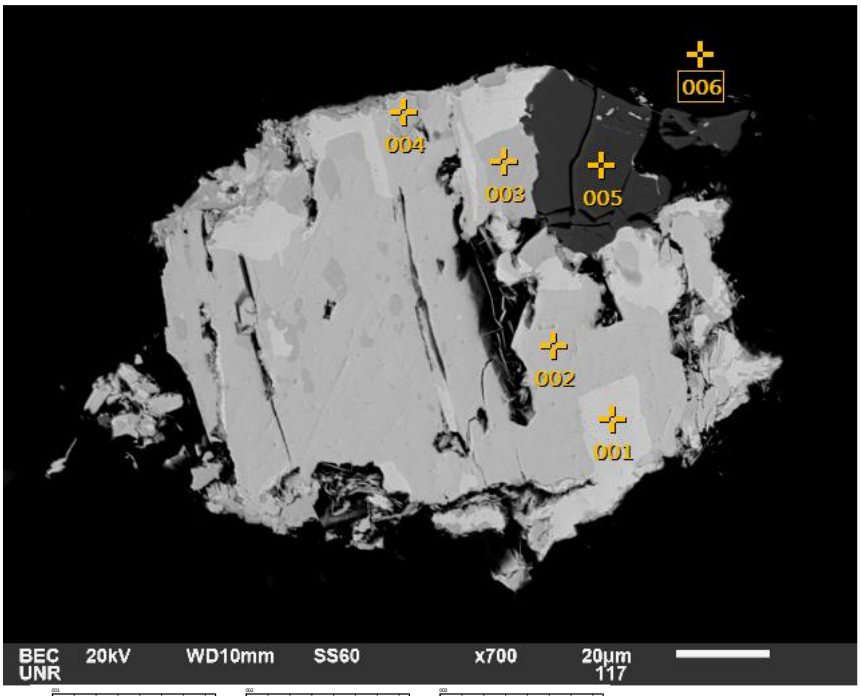

Volt : 20.00 kV

Mag. : x 700

Date : 2021/11/12

Pixel : 1280 x 960

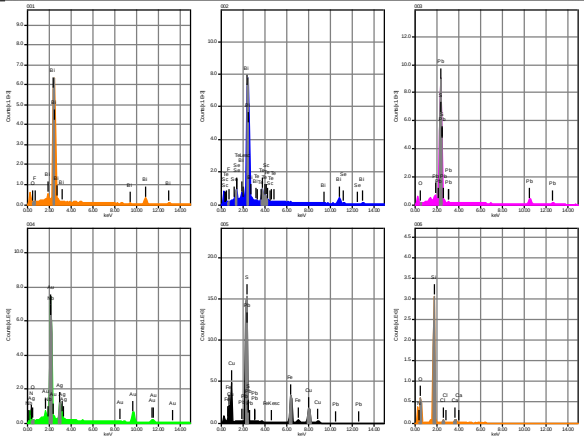

Acquisition Condition

Instrument : 6510(LA)

Volt : 20.00 kV

Current : ---

Process Time : T4

Live time : 2.35 sec.

Real Time : 3.19 sec.

DeadTime : 27.00 %

Count Rate : 19819.00 CPS

	Fe	O	Pb	Au	Ag	N	F	Si	S	Cl	Ca	Sc	Cu	Se	Nb	Te	Bi
001		0.60					0.91									98.49	
002							1.14					0.76		5.33		14.25	78.52
003		0.51	90.99						8.50								
004		1.59		72.34	15.55	3.02									7.49		
005	27.22		10.53						34.13				28.12				
006		41.35				6.82		47.68		1.80	2.35						
Average	27.22	11.01	50.76	72.34	15.55	4.92	1.03	47.68	21.31	1.80	2.35	0.76	28.12	5.33	7.49	14.25	88.51
Standard deviation	0.00	20.24	56.89	0.00	0.00	2.69	0.16	0.00	18.12	0.00	0.00	0.00	0.00	0.00	0.00	0.00	14.12

Figure 8E Detailed

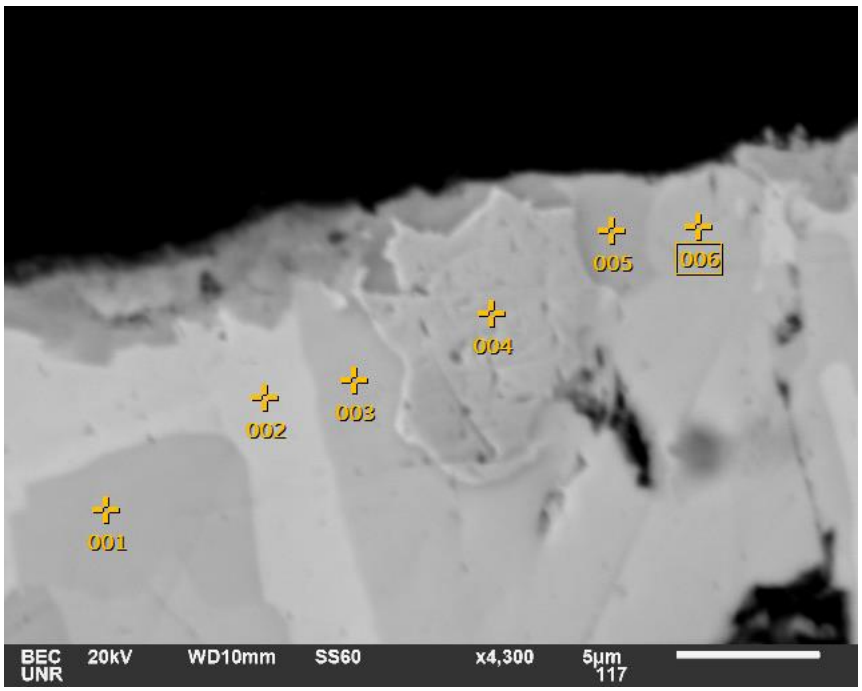

Volt : 20.00 kV

Mag. : x 4,300

Date : 2021/11/12

Pixel : 1280 x 960

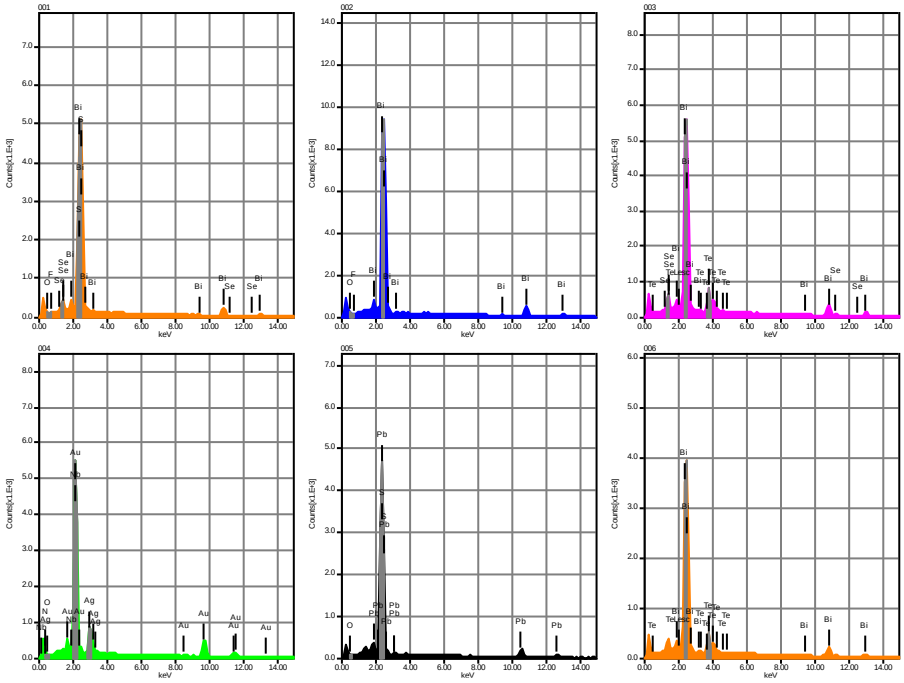

Acquisition Condition

Instrument : 6510(LA)

Volt : 20.00 kV

Current : ---

Process Time : T4

Live time : 3.97 sec.

Real Time : 9.58 sec.

DeadTime : 59.00 %

Count Rate : 51074.00 CPS

	O	Pb	Au	Ag	N	F	S	Se	Nb	Te	Bi
001	0.44					1.12	8.87	3.29			86.28
002	0.50					0.95					98.55
003								4.97		17.29	77.74
004	0.78		73.06	15.67	3.53				6.96		
005	0.60	91.28					8.12				
006										16.19	83.81
Average	0.58	91.28	73.06	15.67	3.53	1.04	8.49	4.13	6.96	16.74	86.59

SEM-EDS data for Figure 8F

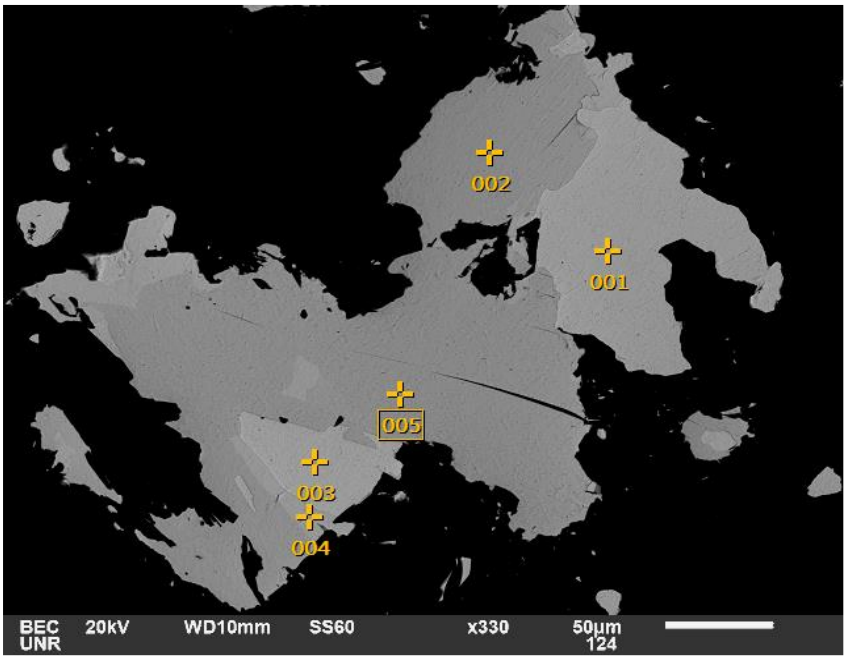

Volt : 20.00 kV

Mag. : x 330

Date : 2021/11/12

Pixel : 1280 x 960

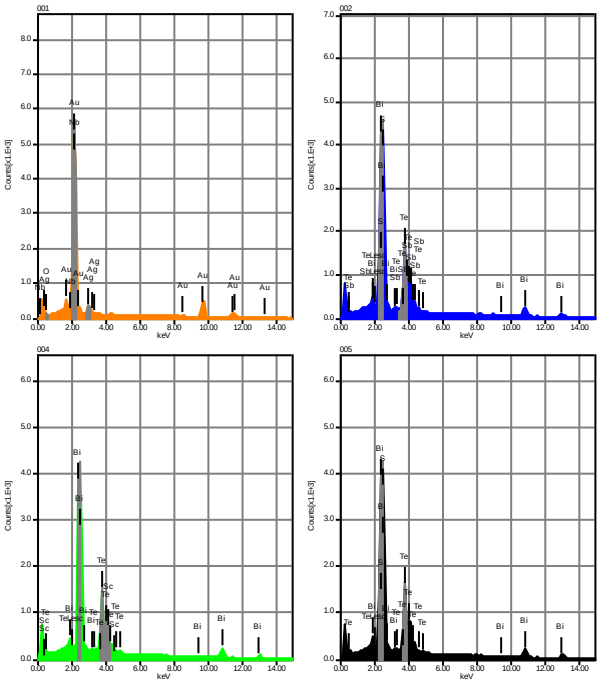

Acquisition Condition

Instrument : 6510(LA)

Volt : 20.00 kV

Current : ---

Process Time : T4

Live time : 5.58 sec.

Real Time : 13.54 sec.

DeadTime : 59.00 %

Count Rate : 51927.00 CPS

	O	Au	Ag	N	S	Sc	Nb	Sb	Te	Bi	
001	1.39	83.54	6.09				8.98				
002					4.89			4.53	33.43	57.14	
003		83.36	5.93	3.26			7.45				
004						1.25			34.05	64.70	
005					5.06				34.48	60.46	
Average	1.39	83.45	6.01	3.26	4.98	1.25	8.22	4.53	33.99	60.77	
Standard deviation		0.00	0.13	0.11	0.00	0.12	0.00	1.09	0.00	0.53	3.79

SEM-EDS data for Figure 8J

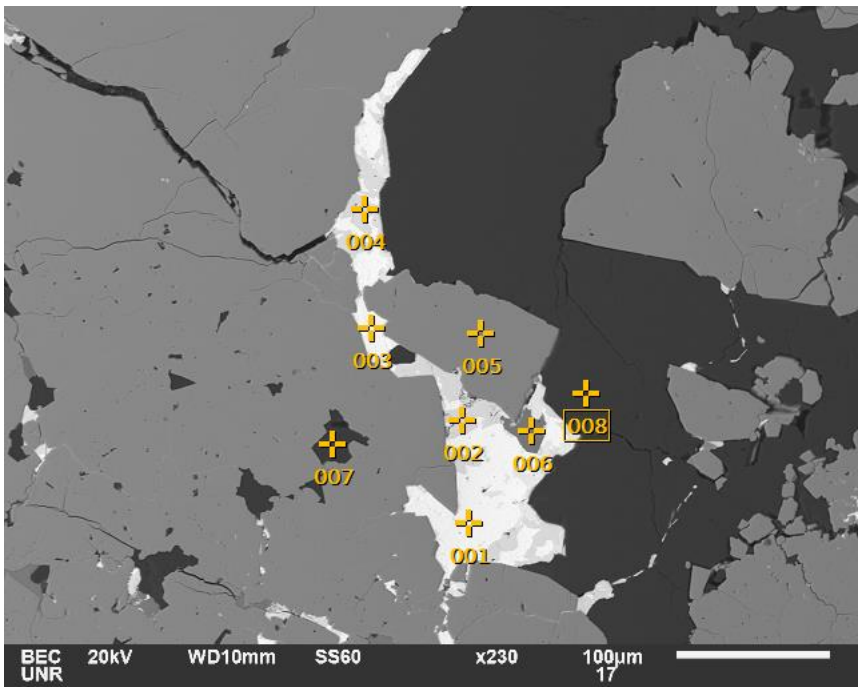

Volt : 20.00 kV
Mag. : x 230
Date : 2021/10/04
Pixel : 1280 x 960

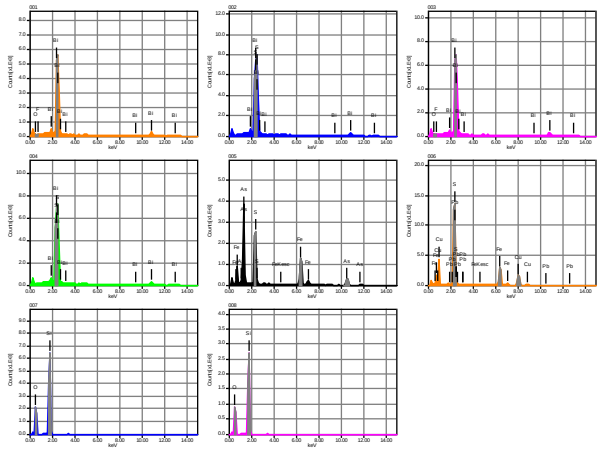

Acquisition Condition
Instrument : 6510(LA)
Volt : 20.00 kV
Current : ---
Process Time : T4
Live time : 1.36 sec.
Real Time : 2.07 sec.
DeadTime : 34.00 %
Count Rate : 27147.00 CPS

	Fe	O	Pb	F	Si	S	Cu	As	Bi		
001		0.58		1.09					98.33		
002						18.21			81.79		
003		0.86		0.86					98.28		
004						17.61			82.39		
005	37.02					22.40		40.58			
006	28.16		8.69			34.84	28.31				
007		50.53			49.47						
008		50.30			49.70						
Average	32.59	25.57	8.69	0.97	49.58	23.27	28.31	40.58	90.20		
Standard deviation			6.26	28.69	0.00	0.16	0.17	8.00	0.00	0.00	9.37

Figure 8J Detailed

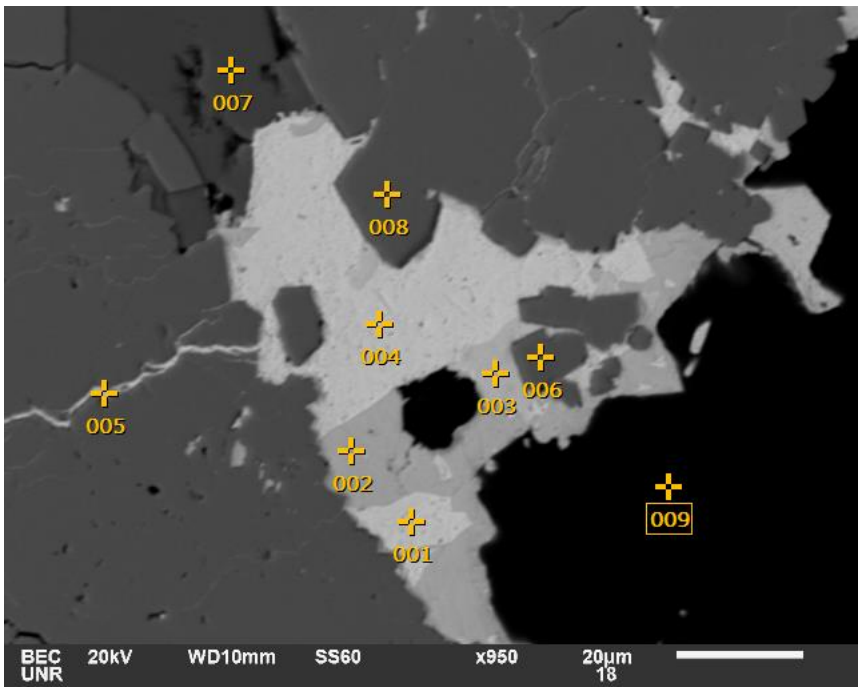

Volt : 20.00 kV

Mag. : x 950

Date : 2021/10/04

Pixel : 1280 x 960

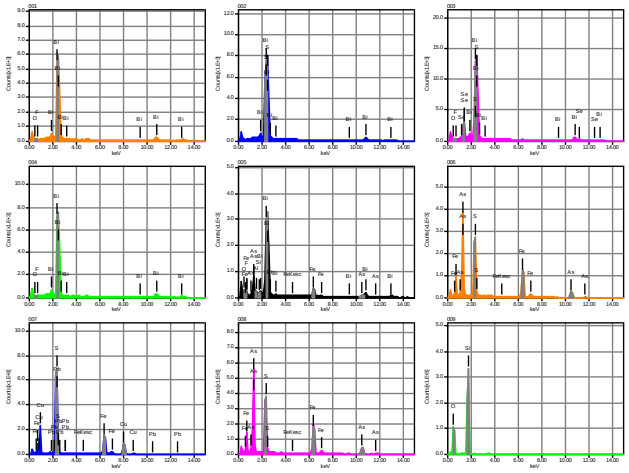

Acquisition Condition

Instrument : 6510(LA)

Volt : 20.00 kV

Current : ---

Process Time : T4

Live time : 1.66 sec.

Real Time : 2.54 sec.

DeadTime : 36.00 %

Count Rate : 27403.00 CPS

	Fe	O	Pb	F	Al	Si	S	Cu	As	Se	Bi		
001		0.67		0.82							98.50		
002							17.97				82.03		
003		0.68		0.63			5.18			11.47	82.03		
004		0.52		0.90							98.58		
005	8.06	3.15		0.63	0.89	0.73			11.81		74.74		
006	35.67						23.75		40.58				
007	27.81		9.45				34.21	28.53					
008	35.64						22.73		41.63				
009		50.55				49.45							
Average	26.79	11.12	9.45	0.75	0.89	25.09	20.77	28.53	31.34	11.47	87.18		
Standard deviation			13.03	22.07	0.00	0.14	0.00	34.45	10.54	0.00	16.92	0.00	10.7 9

SEM-EDS data for Figure 8K

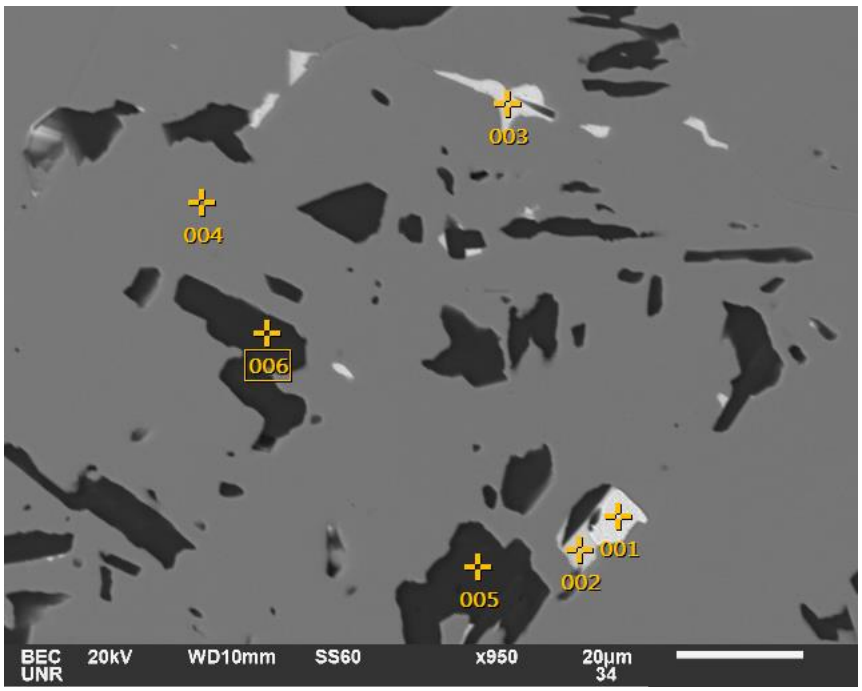

Volt : 20.00 kV
Mag. : x 950
Date : 2021/10/05
Pixel : 1280 x 960

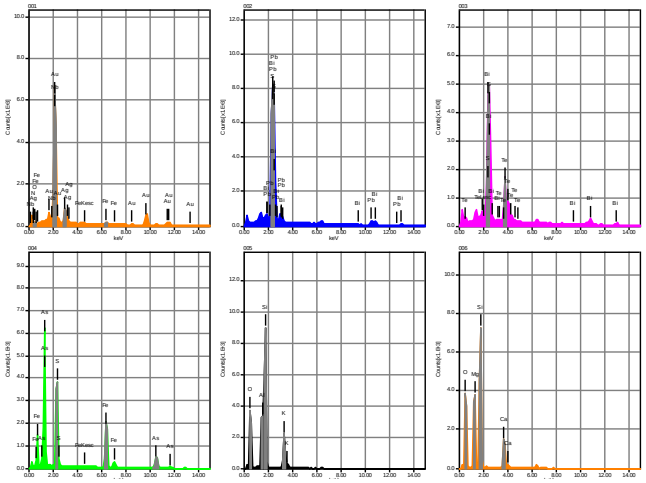

Acquisition Condition
Instrument : 6510(LA)
Volt : 20.00 kV
Current : ---
Process Time : T4
Live time : 7.49 sec.
Real Time : 11.08 sec.
DeadTime : 32.00 %
Count Rate : 24669.00 CPS

	Fe Nb	K Te	O Bi	Pb	Au	Ag	N	Mg	Al	Si	S	Ca	As
001	1.06 6.77		2.30		75.21	11.21	3.45						
002			44.13	42.60							13.27		
003		32.28	62.76								4.96		
004	35.25										21.92		42.83
005		13.01	46.13						9.39	31.47			
006			48.25					14.56		28.16		9.02	
Average	18.15 6.77	13.01 32.2	32.23	42.60	75.21	11.21	3.45	14.56	9.39	29.82	13.38	9.02	42.83
Standard deviation			24.18	0.00	25.94	0.00	0.00	0.00	0.00	0.00	0.00	2.34	8.48
	0.00	0.00	0.00	0.00									

Figure 8K Detailed

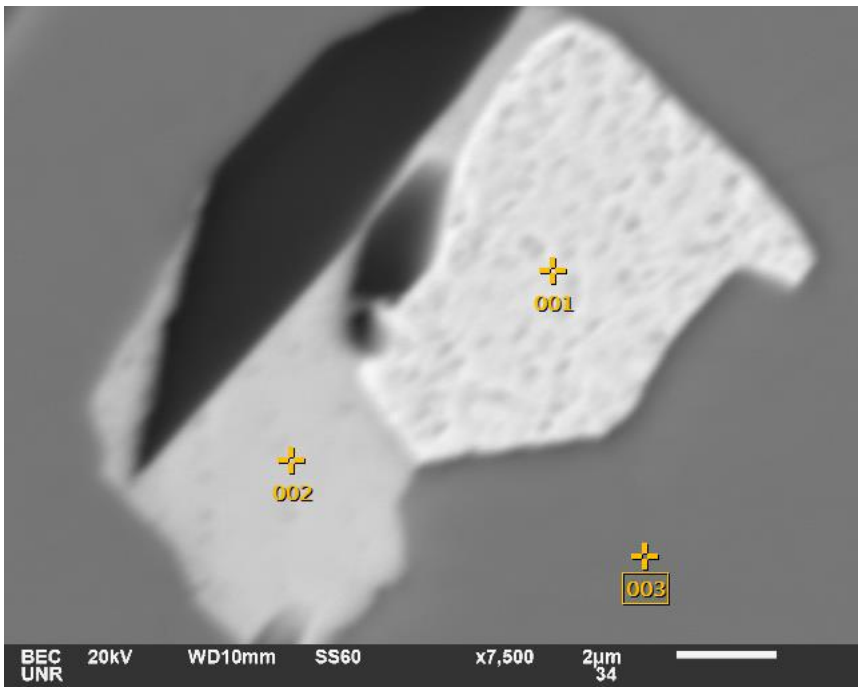

Volt : 20.00 kV

Mag. : x 7,500

Date : 2021/10/05

Pixel : 1280 x 960

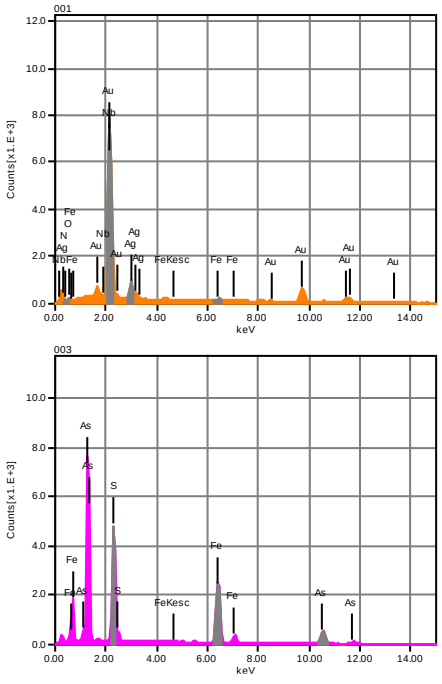

Acquisition Condition

Instrument : 6510(LA)

Volt : 20.00 kV

Current : ---

Process Time : T4

Live time : 8.25 sec.

Real Time : 15.33 sec.

DeadTime : 46.00 %

Count Rate : 38386.00 CPS

	Fe	O	Pb	Au	Ag	N	S	As	Nb	Bi		
001	0.95	1.63		76.79	11.17	3.38			6.08			
002			40.81				13.61			45.58		
003	36.43						22.67	40.90				
Average	18.69	1.63	40.81	76.79	11.17	3.38	18.14	40.90	6.08	45.58		
Standard deviation			25.09	0.00	0.00	0.00	0.00	0.00	6.41	0.00	0.00	0.00

Figure 8K Detailed

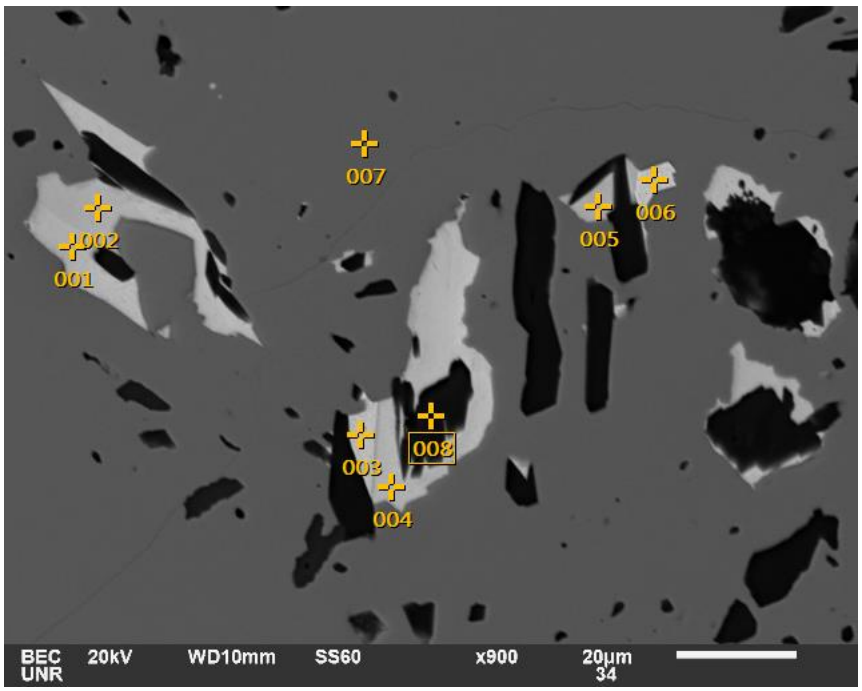

Volt : 20.00 kV

Mag. : x 900

Date : 2021/10/05

Pixel : 1280 x 960

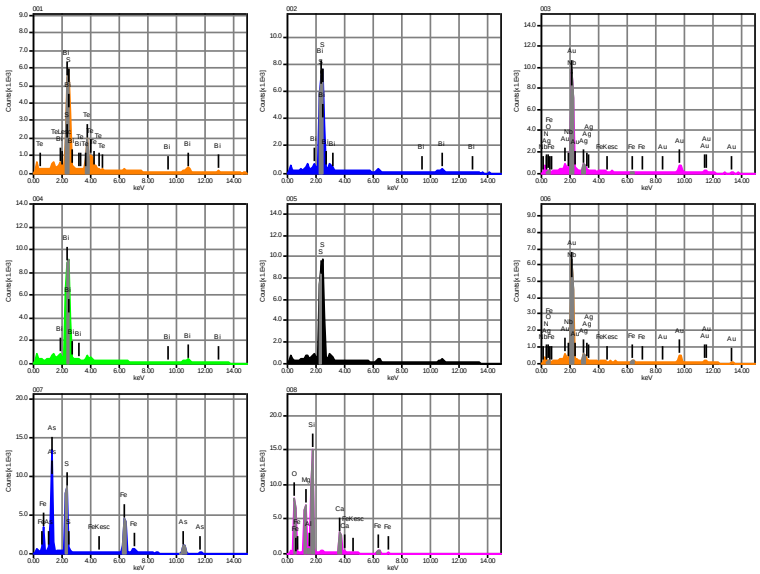

Acquisition Condition

Instrument : 6510(LA)

Volt : 20.00 kV

Current : ---

Process Time : T4

Live time : 15.00 sec.

Real Time : 22.83 sec.

DeadTime : 34.00 %

Count Rate : 34503.00 CPS

	Fe	O	Au	Ag	N	Mg	Al	Si	S	Ca	As	Nb	Te	Bi	
001									4.84				31.95	63.21	
002									20.11					79.89	
003	0.60	1.81	78.17	8.94	3.47							7.01			
004														100.00	
005									100.00						
006	1.23	1.99	77.38	8.83	2.87							7.70			
007	36.46								22.04		41.50				
008	4.23	45.49				13.15	0.89	27.79		8.44					
Average	10.63	16.43	77.77	8.89	3.17	13.15	0.89	27.79	36.75	8.44	41.50	7.36	31.95	81.03	
Standard deviation			17.29	25.17	0.56	0.07	0.43	0.00	0.00	0.00	42.87	0.00	0.00	0.49	0.

Figure 8K Detailed

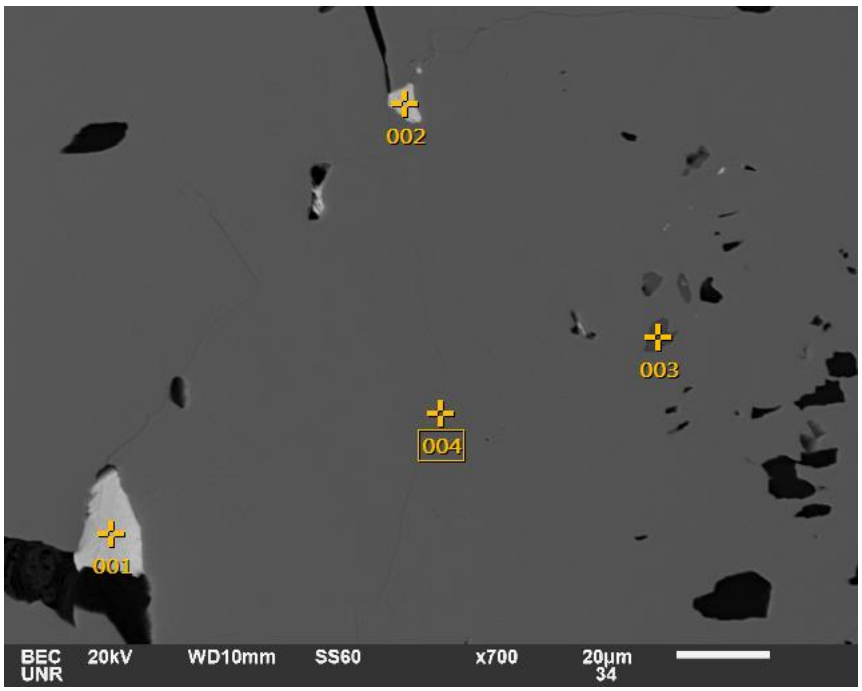

Volt : 20.00 kV

Mag. : x 700

Date : 2021/10/05

Pixel : 1280 x 960

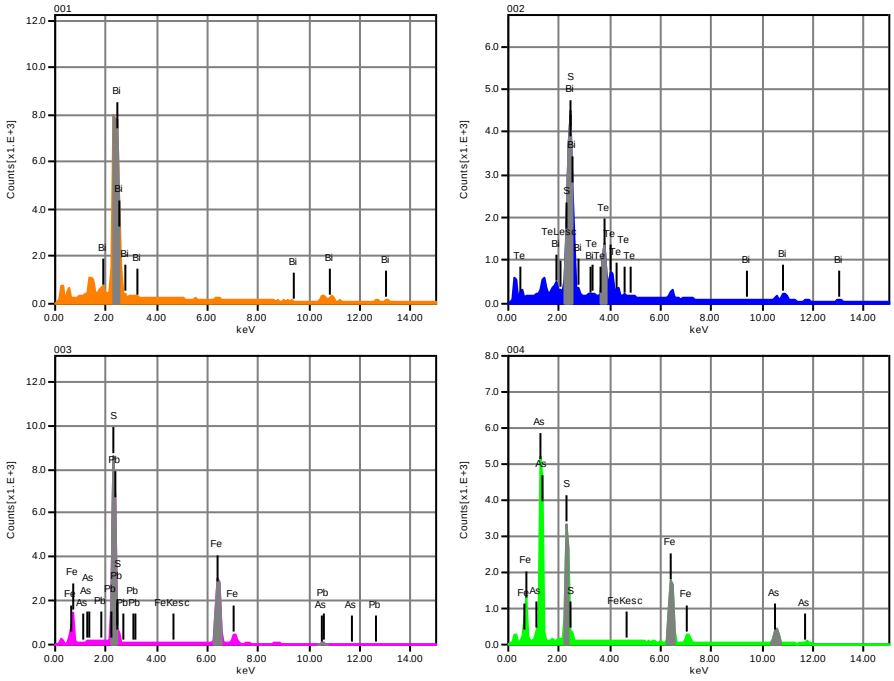

Acquisition Condition

Instrument : 6510(LA)

Volt : 20.00 kV

Current : ---

Process Time : T4

Live time : 5.77 sec.

Real Time : 10.65 sec.

DeadTime : 47.00 %

Count Rate : 37181.00 CPS

	Fe	Pb	S	As	Te	Bi		
001						100.00		
002			5.96		30.38	63.65		
003	51.70	9.43	36.74	2.14				
004	35.67		21.72	42.61				
Average	43.68	9.43	21.47	22.37	30.38	81.83		
Standard deviation			11.33	0.00	15.39	28.62	0.00	25.70

Figure 8K Detailed

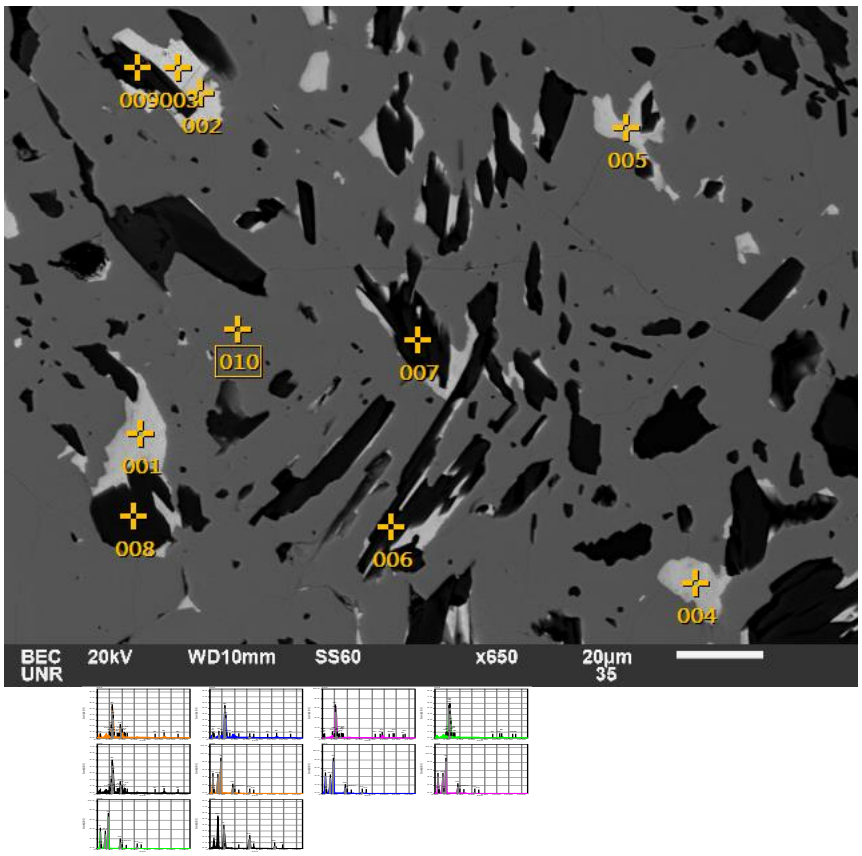

Volt : 20.00 kV

Mag. : x 650

Date : 2021/10/05

Pixel : 1280 x 960

Acquisition Condition

Instrument : 6510(LA)

Volt : 20.00 kV

Current : ---

Process Time : T4

Live time : 5.92 sec.

Real Time : 10.91 sec.

DeadTime : 46.00 %

Count Rate : 36831.00 CPS

	Fe	O	Pb	Au	Ag	N	F	Mg	Al	Si	S	Ca	As	Nb	Te	Bi
001											4.88				31.79	63.33
002	2.11	2.50					1.17		1.38							92.85
003				79.34	4.93	3.56								9.17		3.00
004			41.98								12.61					45.41
005											5.42				28.55	66.03
006	3.54	45.77						14.07		28.46		8.16				
007	3.88	46.08						13.70		28.52		7.82				
008	2.36	45.40						14.52	0.86	28.33		8.53				
009	4.66	46.25						13.15		27.69		8.24				
010	35.96										22.22		41.82			
Average	8.75	37.20	41.98	79.34	4.93	3.56	1.17	13.86	1.12	28.25	11.28	8.19	41.82	9.17	30.17	54
Standard deviation	0.00	2.29	13.37	19.40	0.00	0.00	0.00	0.00	0.00	0.58	0.37	0.38	8.10	0.29	0.00	

Figure 8K Detailed

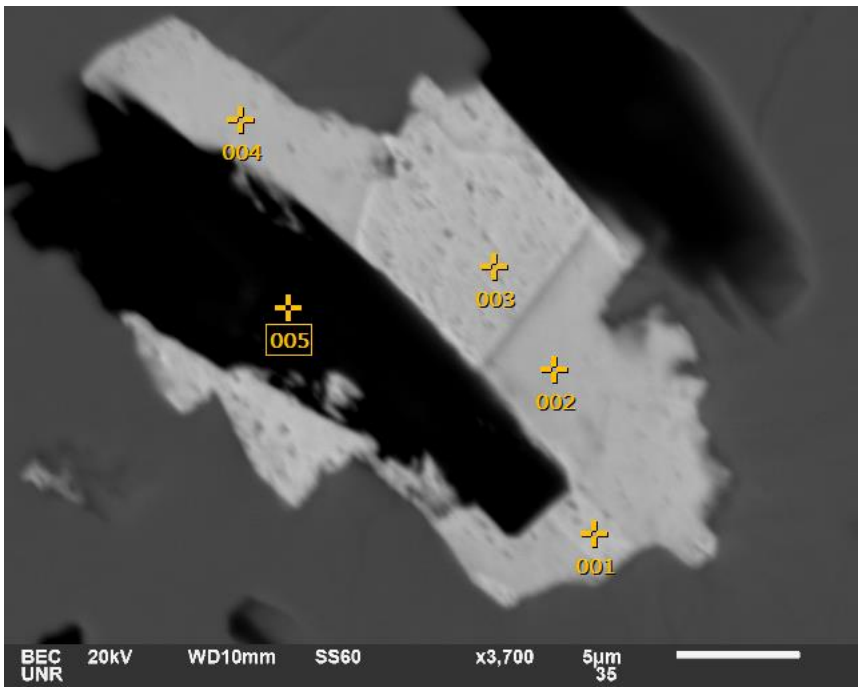

Volt : 20.00 kV

Mag. : x 3,700

Date : 2021/10/05

Pixel : 1280 x 960

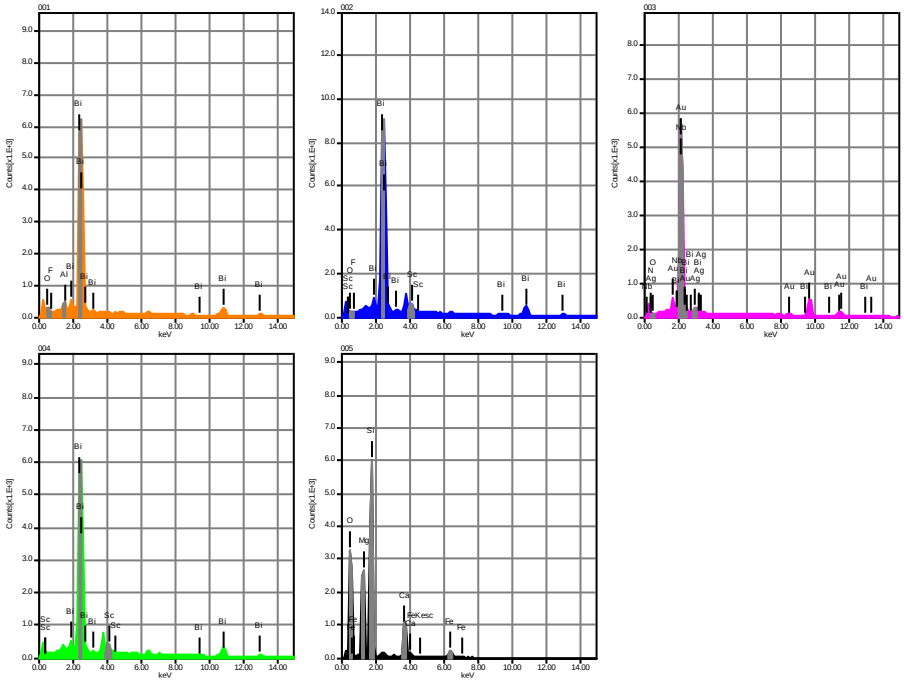

Acquisition Condition

Instrument : 6510(LA)

Volt : 20.00 kV

Current : ---

Process Time : T4

Live time : 6.17 sec.

Real Time : 9.19 sec.

DeadTime : 33.00 %

Count Rate : 25428.00 CPS

	Fe	O	Au	Ag	N	F	Mg	Al	Si	Ca	Sc	Nb	Bi	
001		1.57				1.01		0.74					96.68	
002		0.60				1.07					1.95		96.38	
003		0.85	80.16	4.18	3.38							8.87	2.56	
004											2.25		97.75	
005	5.05	45.82					13.00		28.07	8.06				
Average	5.05	12.21	80.16	4.18	3.38	1.04	13.00	0.74	28.07	8.06	2.10	8.87	73.34	
Standard deviation			0.00	22.41	0.00	0.00	0.00	0.05	0.00	0.00	0.00	0.00	0.21	0.00
	47.19													

Figure 8K Detailed

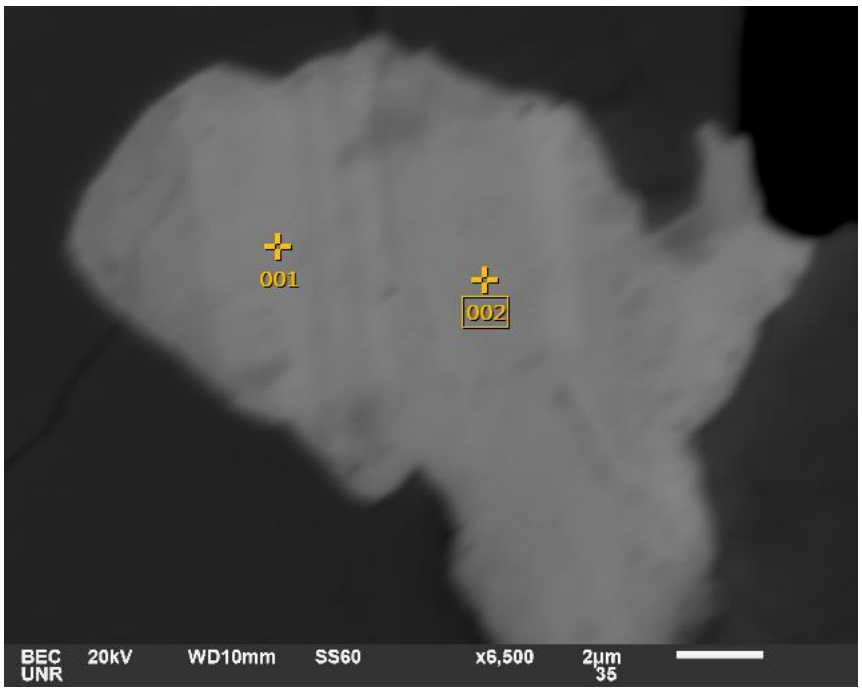

Volt : 20.00 kV

Mag. : x 6,500

Date : 2021/10/05

Pixel : 1280 x 960

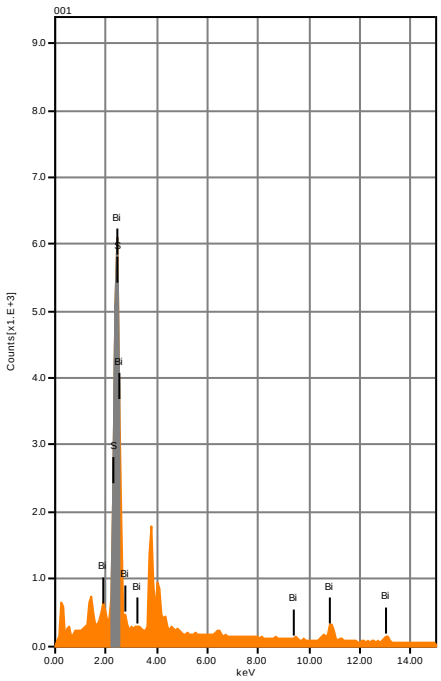

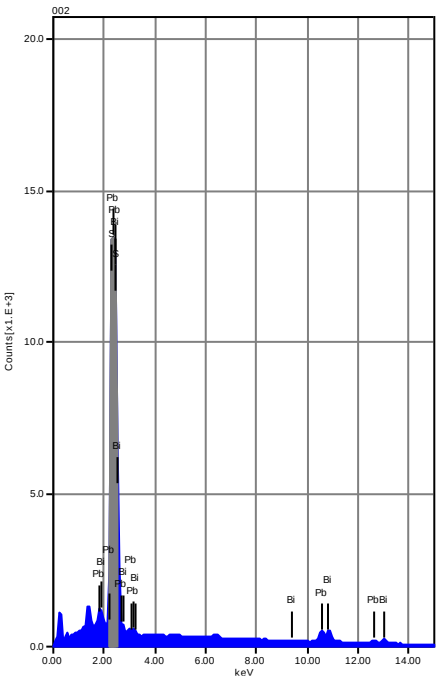

Acquisition Condition

Instrument : 6510(LA)

Volt : 20.00 kV

Current : ---

Process Time : T4

Live time : 15.00 sec.

Real Time : 35.02 sec.

DeadTime : 57.00 %

Count Rate : 50424.00 CPS

	Pb	S	Bi		
001		8.19	91.81		
002	44.14	12.24	43.62		
Average	44.14	10.21	67.72		
Standard deviation		0.00	2.86	34.08	

Arsenopyrite grain near other in figure 8K with no apparent geochemical zonation

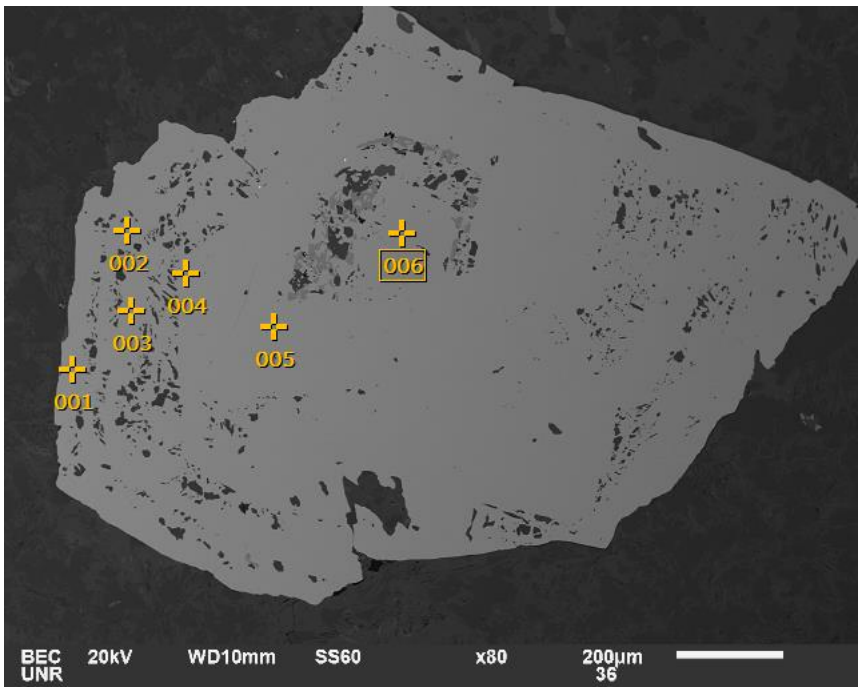

Volt : 20.00 kV

Mag. : x 80

Date : 2021/10/05

Pixel : 1280 x 960

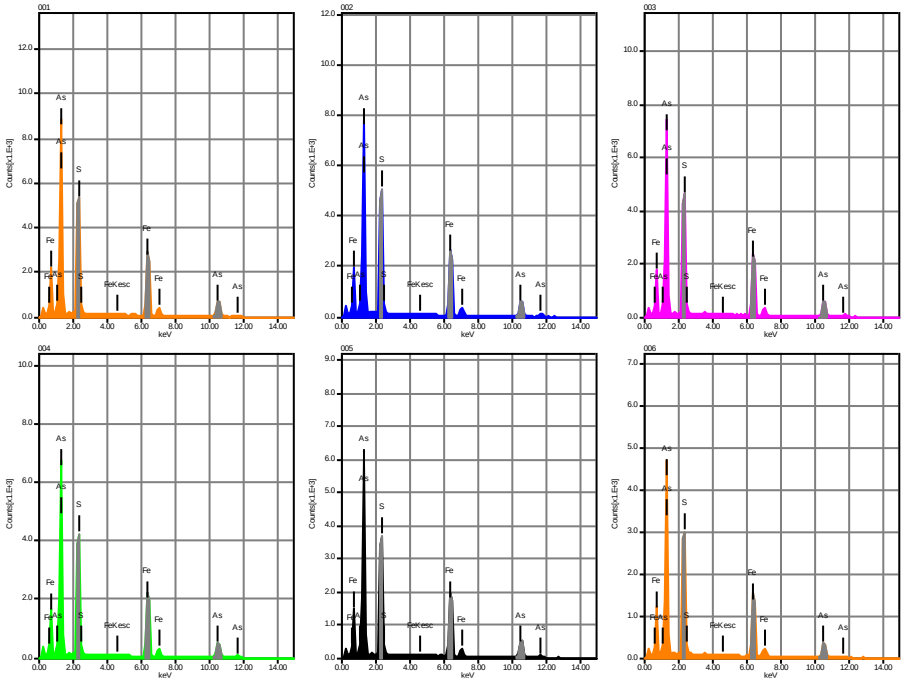

Acquisition Condition

Instrument : 6510(LA)

Volt : 20.00 kV

Current : ---

Process Time : T4

Live time : 5.10 sec.

Real Time : 9.43 sec.

DeadTime : 46.00 %

Count Rate : 37148.00 CPS

	Fe	S	As
001	35.92	21.85	42.22
002	36.27	22.33	41.39
003	35.31	22.05	42.64
004	36.38	22.02	41.60
005	34.72	21.59	43.69
006	35.94	23.12	40.94
Average	35.76	22.16	42.08
Standard deviation		0.63	0.53	0.99

Arsenopyrite grain near other in figure 8K with no apparent geochemical zonation

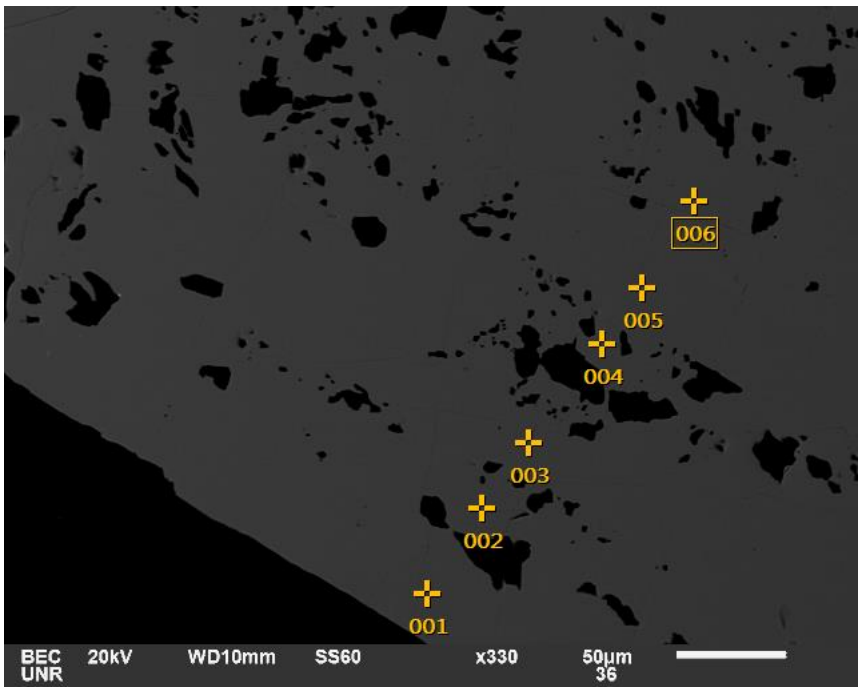

Volt : 20.00 kV

Mag. : x 330

Date : 2021/10/05

Pixel : 1280 x 960

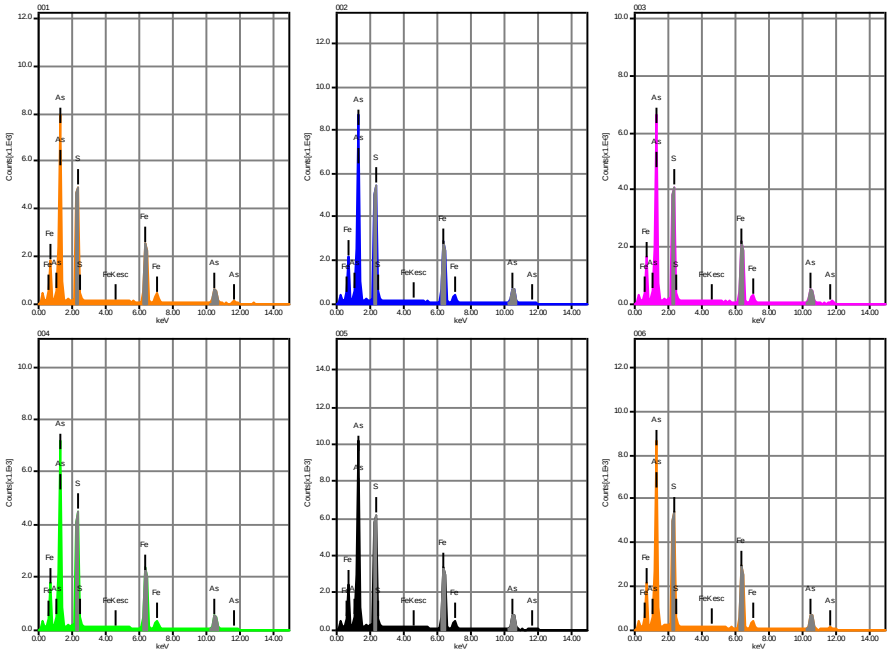

Acquisition Condition

Instrument : 6510(LA)

Volt : 20.00 kV

Current : ---

Process Time : T4

Live time : 9.43 sec.

Real Time : 17.47 sec.

DeadTime : 46.00 %

Count Rate : 37037.00 CPS

	Fe	S	As		
001	36.03	21.82	42.14		
002	35.96	22.28	41.76		
003	35.43	21.96	42.61		
004	35.07	21.84	43.09		
005	36.50	22.02	41.48		
006	36.53	21.68	41.79		
Average	35.92	21.93	42.15		
Standard deviation		0.58	0.21	0.60	

SEM-EDS data for Figure 8I

Arsenopyrite “star” showing no apparent geochemical zoning

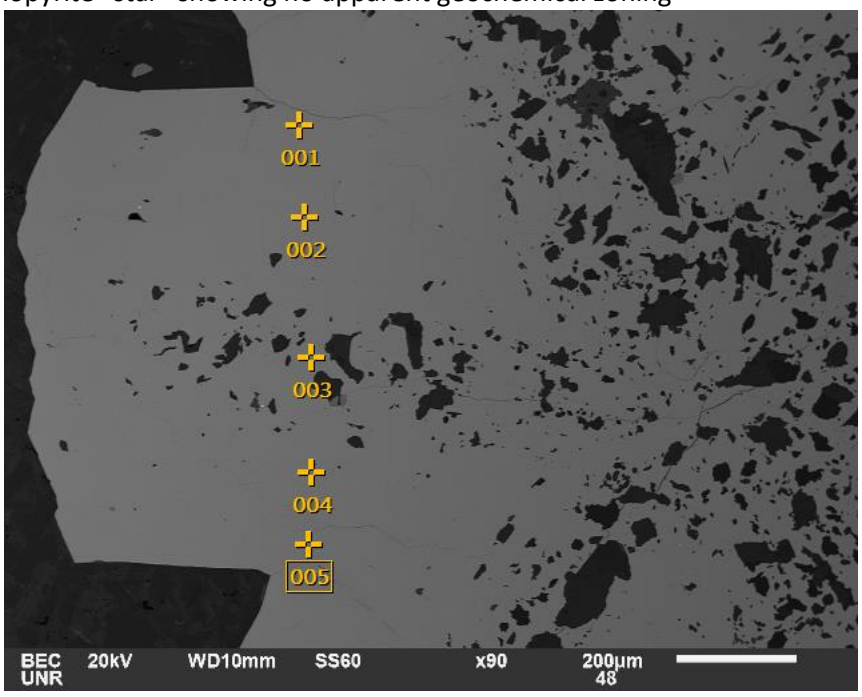

Volt : 20.00 kV

Mag. : x 90

Date : 2021/10/05

Pixel : 1280 x 960

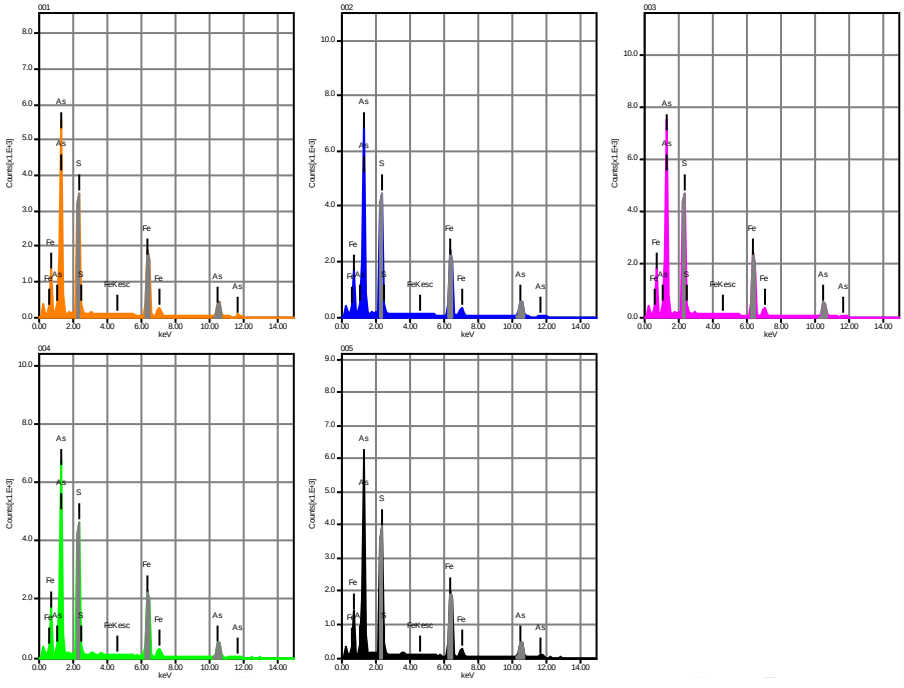

Acquisition Condition

Instrument : 6510(LA)

Volt : 20.00 kV

Current : ---

Process Time : T4

Live time : 6.81 sec.

Real Time : 12.44 sec.

DeadTime : 45.00 %

Count Rate : 35933.00 CPS

	Fe	S	As
001	36.90	22.15	40.96
002	35.67	22.50	41.83
003	36.21	22.24	41.54
004	36.14	22.82	41.04
005	36.44	22.56	41.00
Average	36.27	22.45	41.27
Standard deviation	0.45	0.27	0.39

SEM-EDS data for Figure 8L

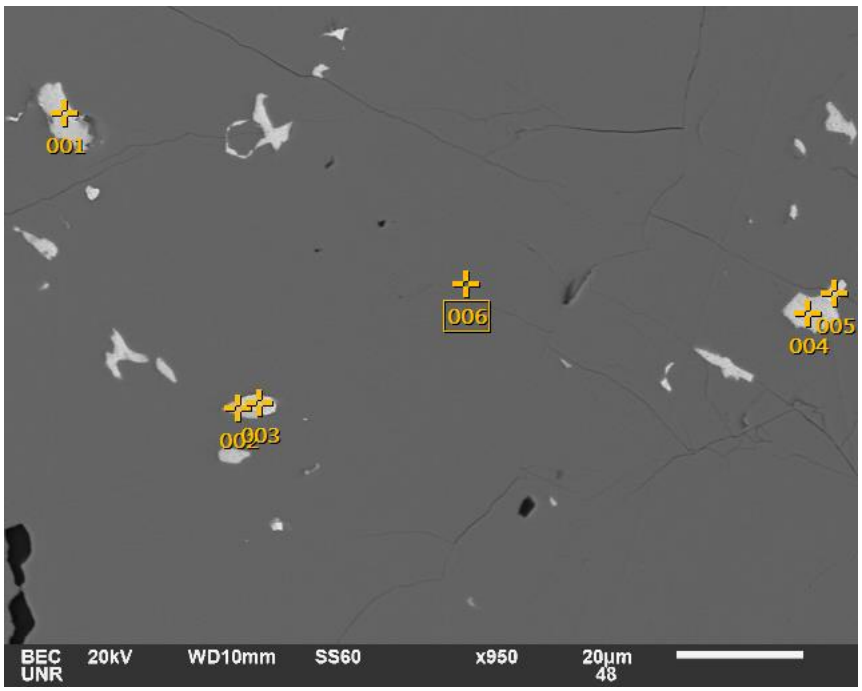

Volt : 20.00 kV

Mag. : x 950

Date : 2021/10/05

Pixel : 1280 x 960

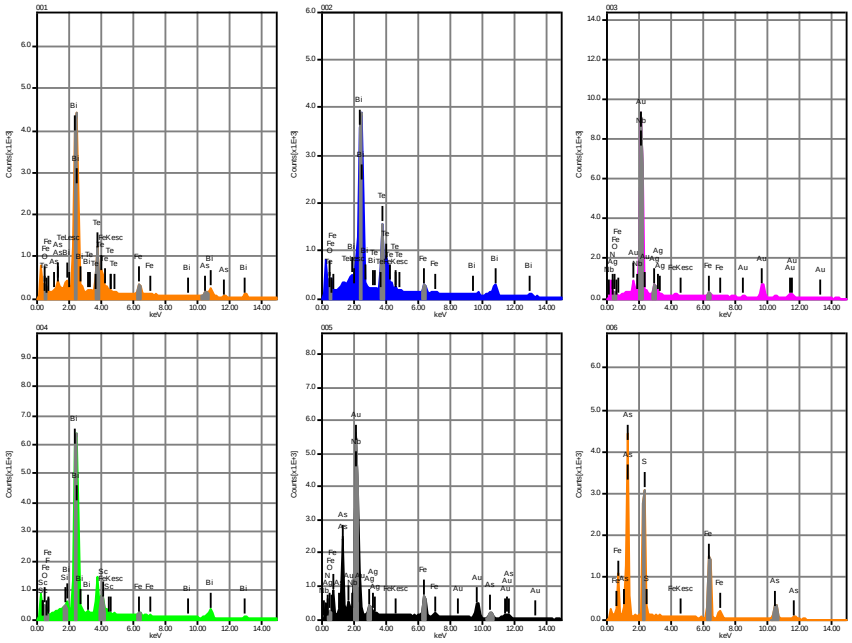

Acquisition Condition

Instrument : 6510(LA)

Volt : 20.00 kV

Current : ---

Process Time : T4

Live time : 4.99 sec.

Real Time : 9.23 sec.

DeadTime : 46.00 %

Count Rate : 36962.00 CPS

	Fe	O	Au	Ag	N	F	Si	S	Sc	As	Nb	Te	Bi	
001	4.59	1.61								8.09		28.68	57.03	
002	3.23	1.86										39.74	55.17	
003	1.82	2.96	78.64	6.45	3.10						7.03			
004	2.14	2.59				1.36	0.92		3.97				89.01	
005	8.86	2.60	58.67	5.38	2.73					10.90	10.86			
006	36.28							23.36		40.36				
Average	9.49	2.33	68.65	5.91	2.92	1.36	0.92	23.36	3.97	19.78	8.94	34.21	67.07	
Standard deviation	19.03		13.37	0.57	14.12	0.75	0.26	0.00	0.00	0.00	0.00	17.87	2.70	7.82

Figure 8L Detailed

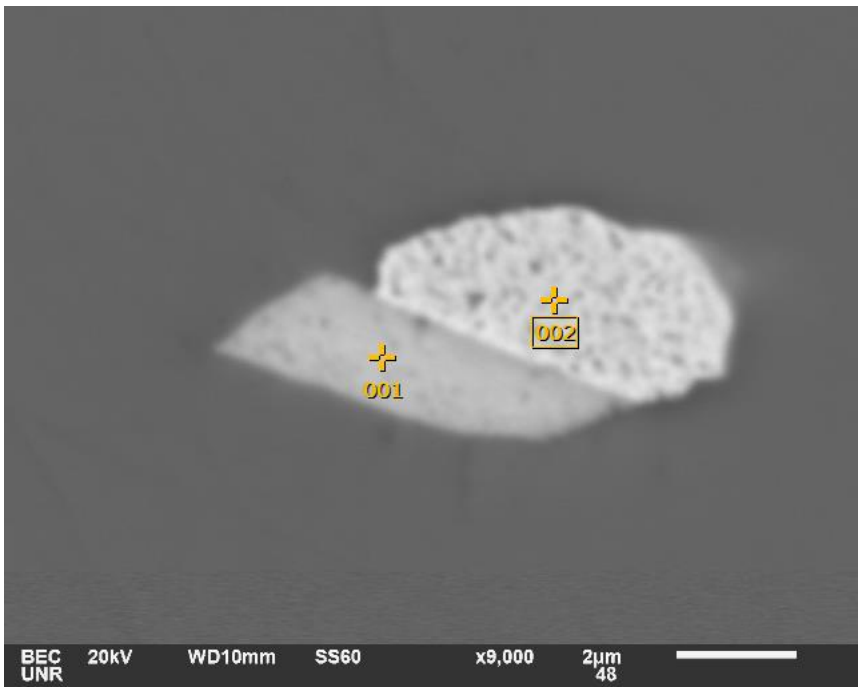

Volt : 20.00 kV

Mag. : x 9,000

Date : 2021/10/05

Pixel : 1280 x 960

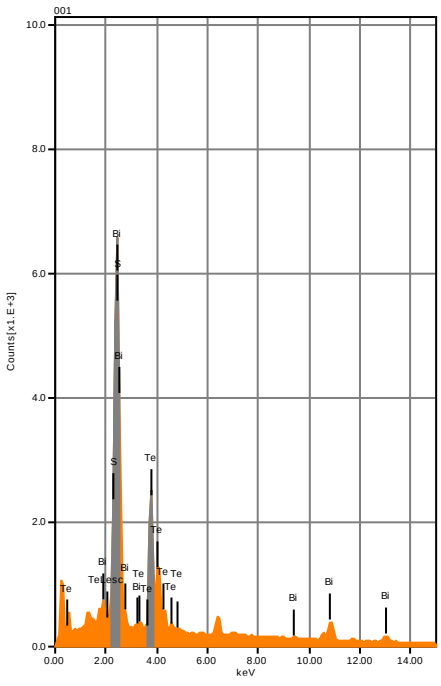

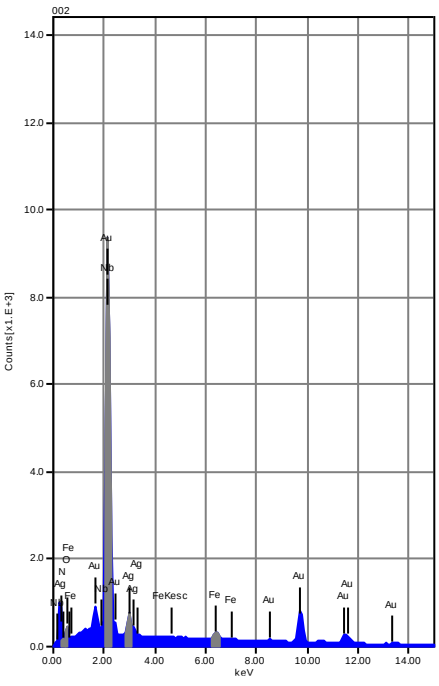

Acquisition Condition

Instrument : 6510(LA)

Volt : 20.00 kV

Current : ---

Process Time : T4

Live time : 7.45 sec.

Real Time : 18.87 sec.

DeadTime : 61.00 %

Count Rate : 54424.00 CPS

	Fe	O	Au	Ag	N	S	Nb	Te	Bi		
001						5.16		34.63	60.21		
002	1.55	3.53	77.59	7.15	2.53		7.65				
Average	1.55	3.53	77.59	7.15	2.53	5.16	7.65	34.63	60.21		
Standard deviation			0.00	0.00	0.00	0.00	0.00	0.00	0.00	0.00	0.00

Figure 8L Detailed

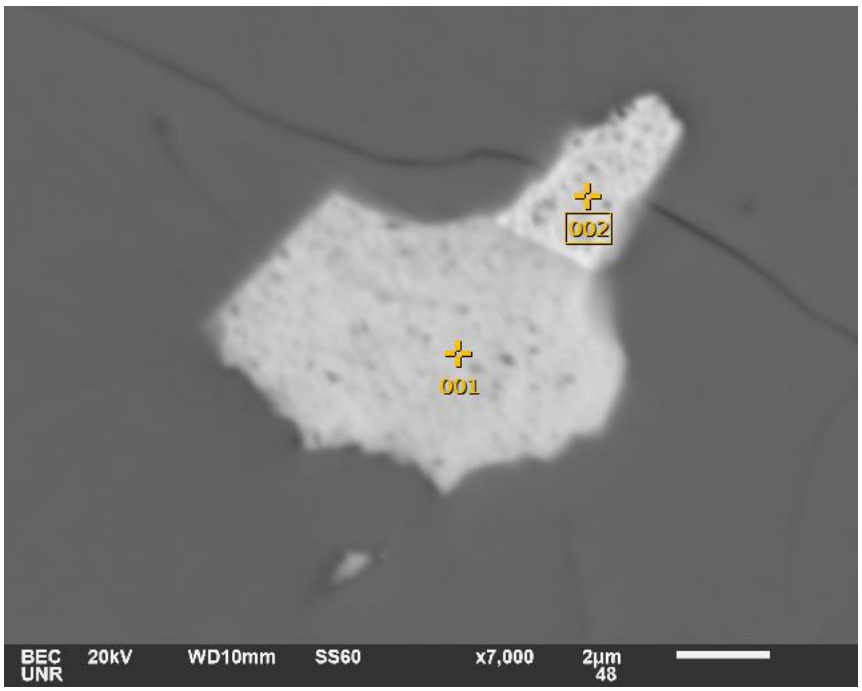

Volt : 20.00 kV

Mag. : x 7,000

Date : 2021/10/05

Pixel : 1280 x 960

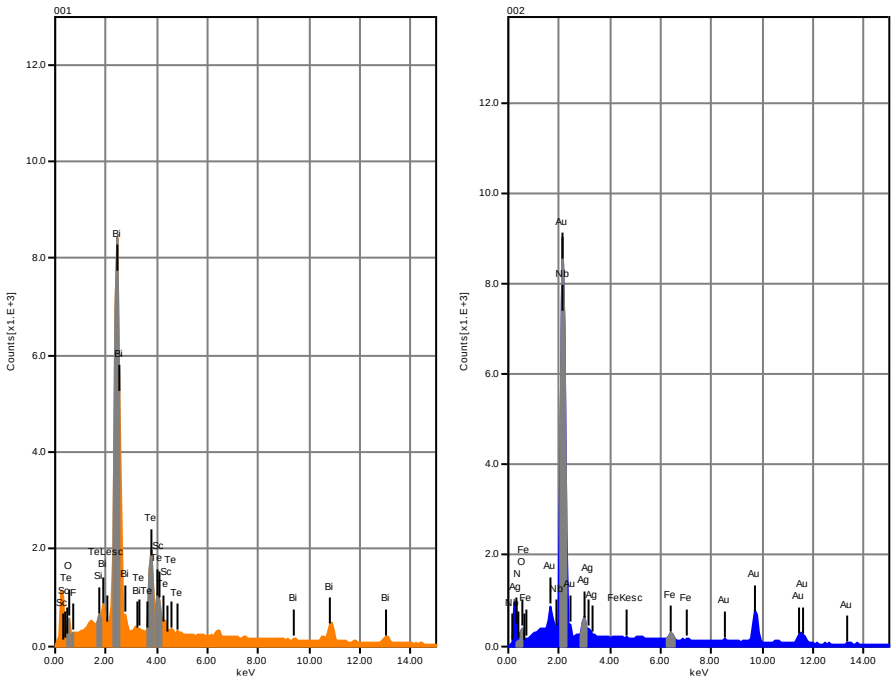

Acquisition Condition

Instrument : 6510(LA)

Volt : 20.00 kV

Current : ---

Process Time : T4

Live time : 7.15 sec.

Real Time : 17.92 sec.

DeadTime : 59.00 %

Count Rate : 53818.00 CPS

	Fe	O	Au	Ag	N	F	Si	Sc	Nb	Te	Bi		
001		1.34				1.02	0.48	1.11		26.73	69.31		
002	1.48	3.54	79.04	6.56	2.60				6.79				
Average	1.48	2.44	79.04	6.56	2.60	1.02	0.48	1.11	6.79	26.73	69.31		
Standard deviation			0.00	1.55	0.00	0.00	0.00	0.00	0.00	0.00	0.00	0.00	0.00

Supplementary SEM-EDS data for images in Fig. 9 (C,E,F,I,K,L,N,O)

Altenburg Hill Zone

SEM-EDS data for Figure 9C

Gold with native bismuth in arsenopyrite

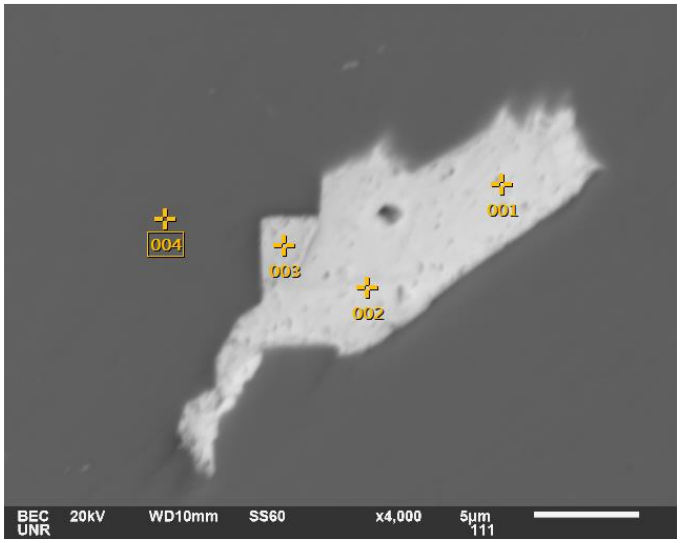

Volt : 20.00 kV

Mag. : x 4,000

Date : 2021/11/12

Pixel : 1280 x 960

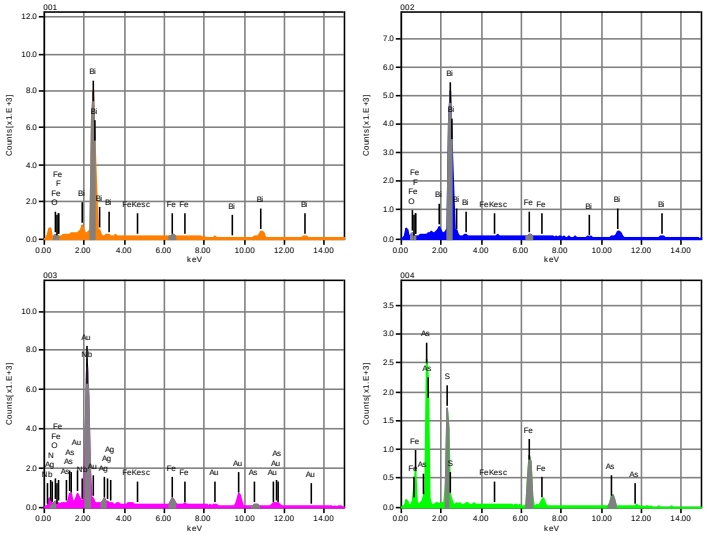

Acquisition Condition

Instrument : 6510(LA)

Volt : 20.00 kV

Current : ---

Process Time : T4

Live time : 2.81 sec.

Real Time : 5.31 sec.

DeadTime : 47.00 %

Count Rate : 37984.00 CPS

	Fe	O	Au	Ag	N	F	S	As	Nb	Bi	
001	0.94	0.67				0.85				97.53	
002	1.60	1.03				0.78				96.59	
003	3.74	2.56	73.29	4.19	3.47			4.84	7.91		
004	35.19						22.54	42.26			
Average	10.37	1.42	73.29	4.19	3.47	0.81	22.54	23.55	7.91	97.06	
Standard deviation	16.59	1.00	0.00	0.00	0.00	0.05	0.00	26.47	0.00	0.67	

Porphyry

SEM-EDS data for Figure 9E

Electrum, native bismuth, PbSeS

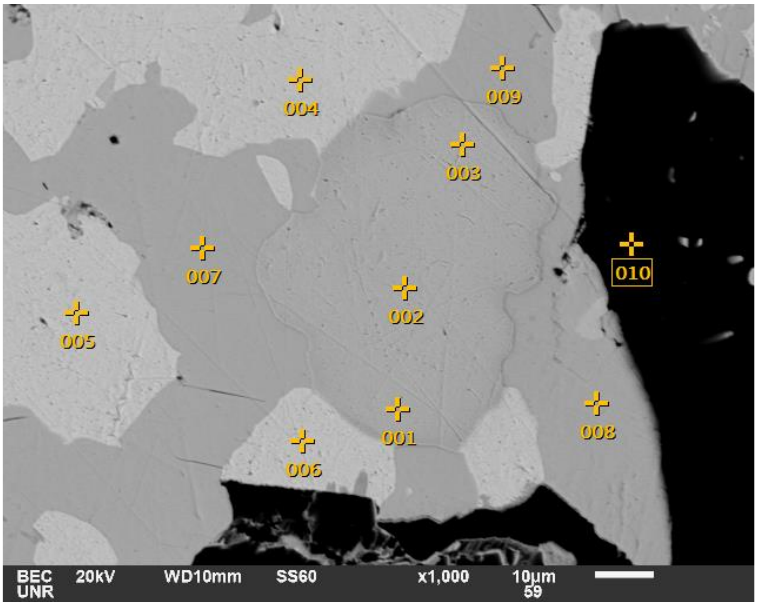

Volt : 20.00 kV

Mag. : x 1,000

Date : 2021/10/07

Pixel : 1280 x 960

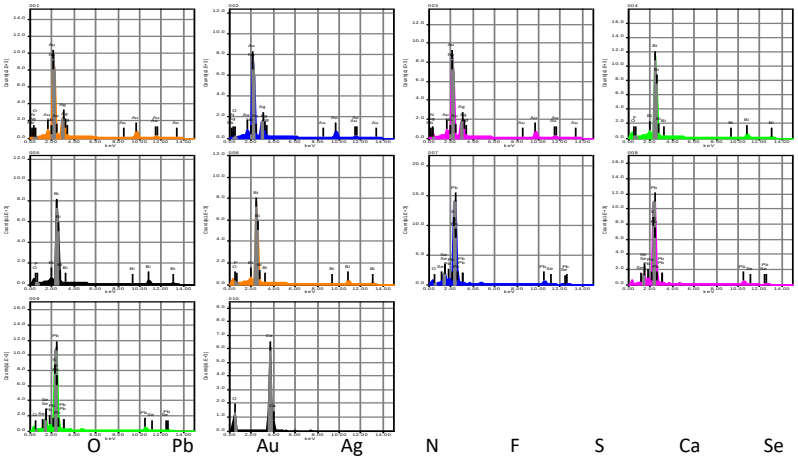

Acquisition Condition

Instrument : 6510(LA)

Volt : 20.00 kV

Current : ---

Process Time : T4

Live time : 6.79 sec.

Real Time : 9.45 sec.

DeadTime : 28.00 %

Count Rate : 19960.00 CPS

	O	Pb	Au	Ag	N	F	S	Ca	Se	Nb	Bi
001	0.93		68.76	22.01	2.51					5.79	
002	1.40		69.93	19.43	3.49					5.73	
003			70.14	19.85	4.54					5.48	
004	0.68					0.96					98.36
005	0.66					0.83					98.51
006	0.99					1.02					97.99
007	0.51	85.16					6.48		7.85		
008		86.16					6.55		7.30		
009	0.38	84.86					6.38		8.38		
010	52.36							47.64			
Average	7.24	85.39	69.61	20.43	3.51	0.94	6.47	47.64	7.84	5.67	98.29

Figure 9E

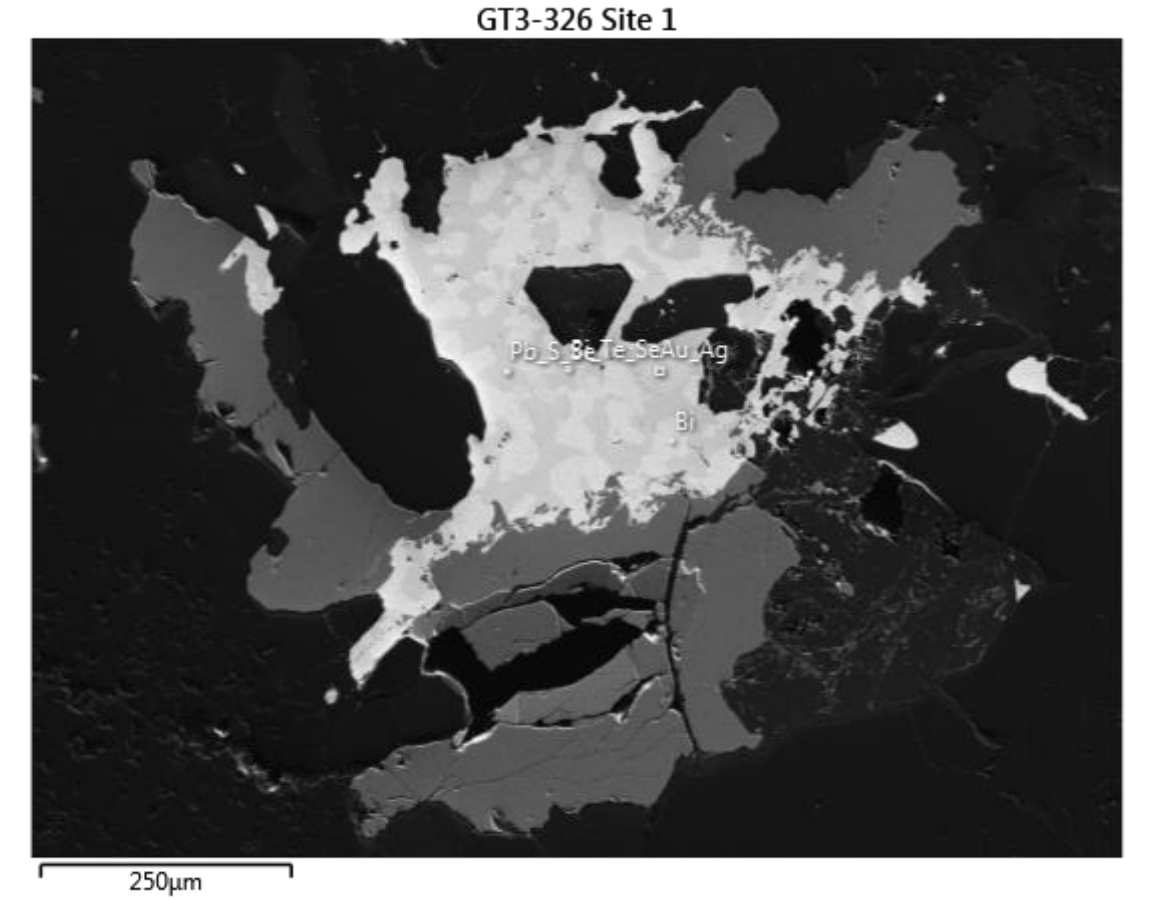
GT3-326 Site 1
Pb_S_Bi_Te_SeAu_Ag
Bi
250µm

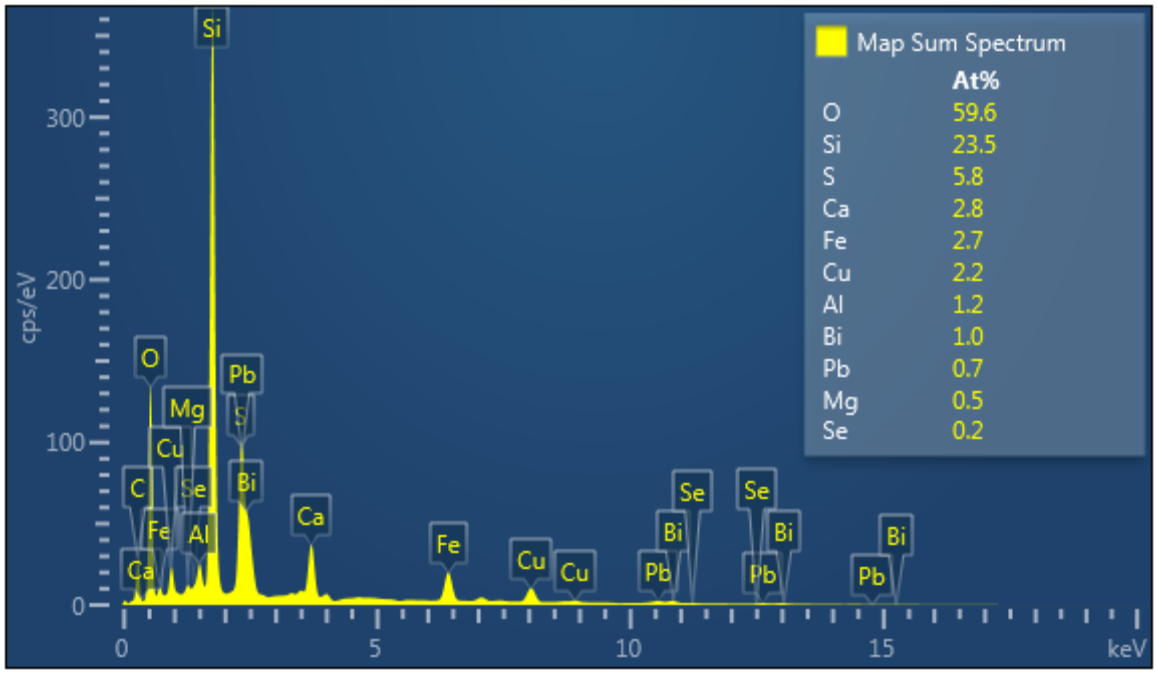
Map Sum Spectrum
At%
O 59.6
Si 23.5
S 5.8
Ca 2.8
Fe 2.7
Cu 2.2
Al 1.2
Bi 1.0
Pb 0.7
Mg 0.5
Se 0.2
cps/eV
300
200
100
0
0
5
10
15
keV
Si
O
Mg
Cu
C
Se
Fe
Al
Ca
Pb
S
Bi
Ca
Fe
Cu
Cu
Se
Bi
Pb
Se
Se
Bi
Pb
Bi
Pb

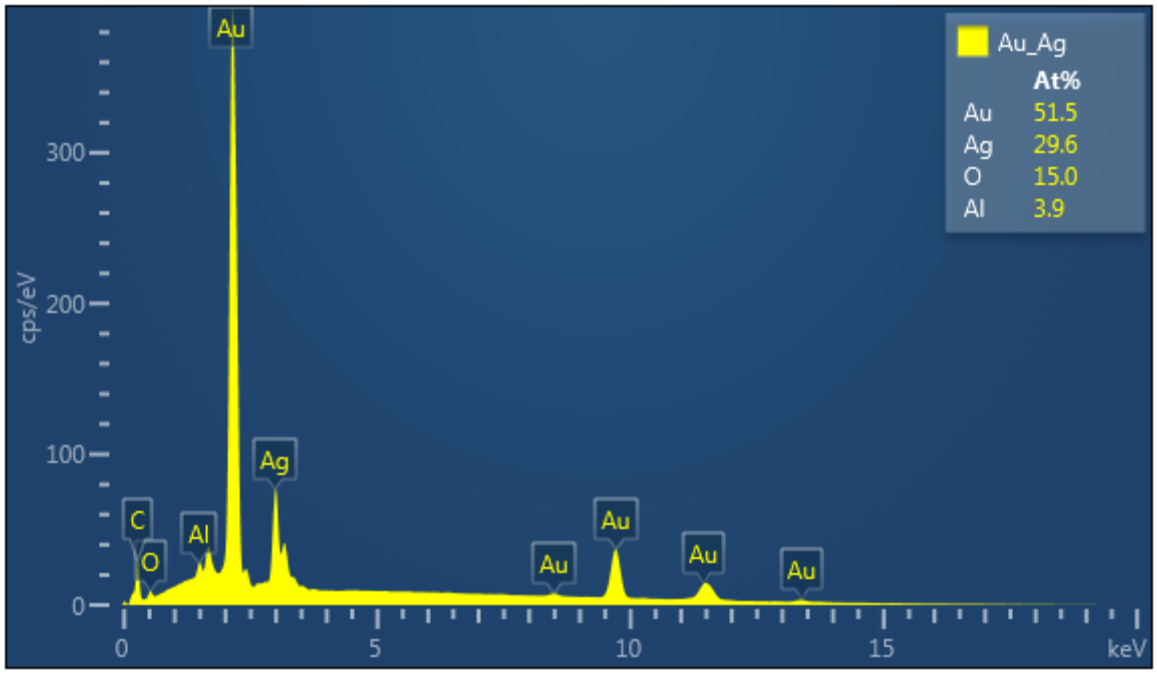
Au_Ag
At%
Au 51.5
Ag 29.6
O 15.0
Al 3.9
cps/eV
300
200
100
0
0
5
10
15
keV
Au
Ag
C
O
Al
Au
Au
Au
Au

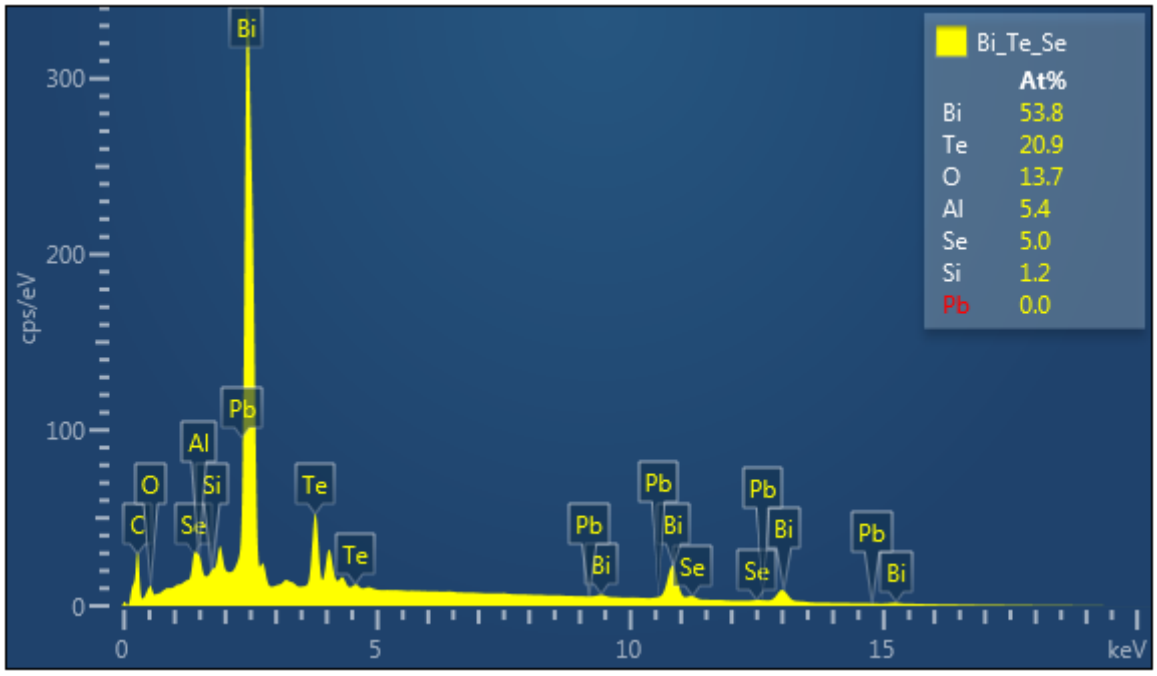
Bi_Te_Se
At%
Bi 53.8
Te 20.9
O 13.7
Al 5.4
Se 5.0
Si 1.2
Pb 0.0
cps/eV
300
200
100
0
0
5
10
15
keV
Bi
Pb
Al
O
C
Si
Se
Te
Te
Pb
Bi
Pb
Bi
Se
Pb
Se
Bi
Pb
Bi

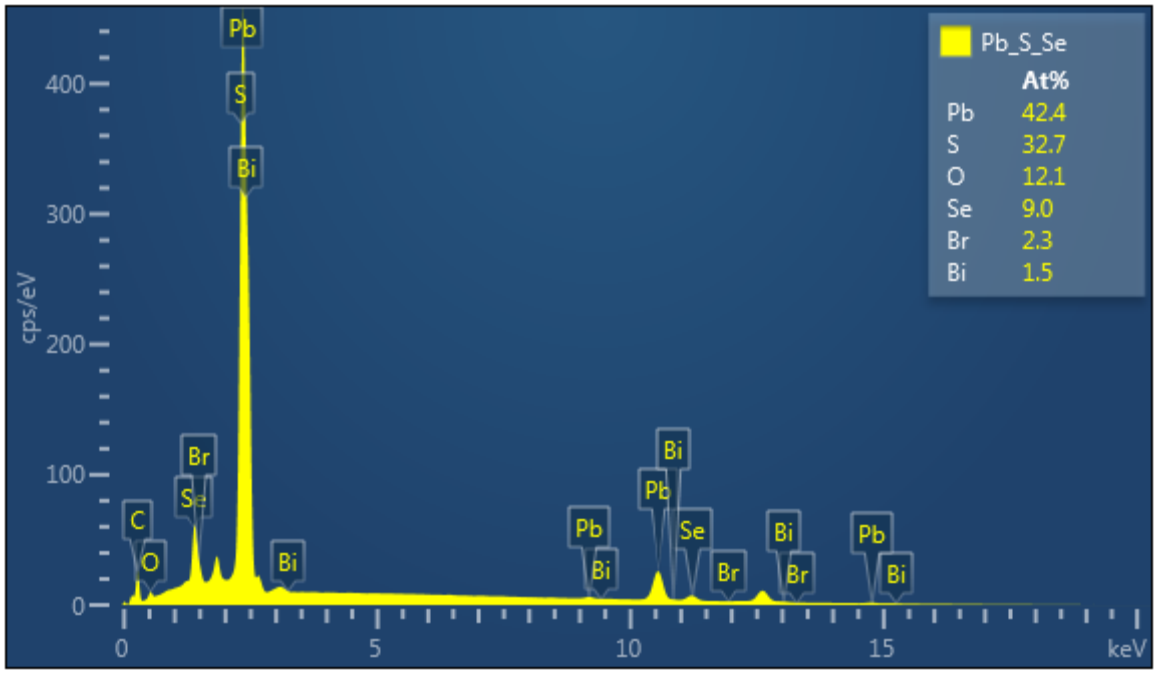
Pb_S_Se
At%
Pb 42.4
S 32.7
O 12.1
Se 9.0
Br 2.3
Bi 1.5
cps/eV
keV
Pb
S
Bi
Br
Se
C
O
Pb
Bi
Bi
Pb
Se
Br
Bi
Br
Pb
Bi

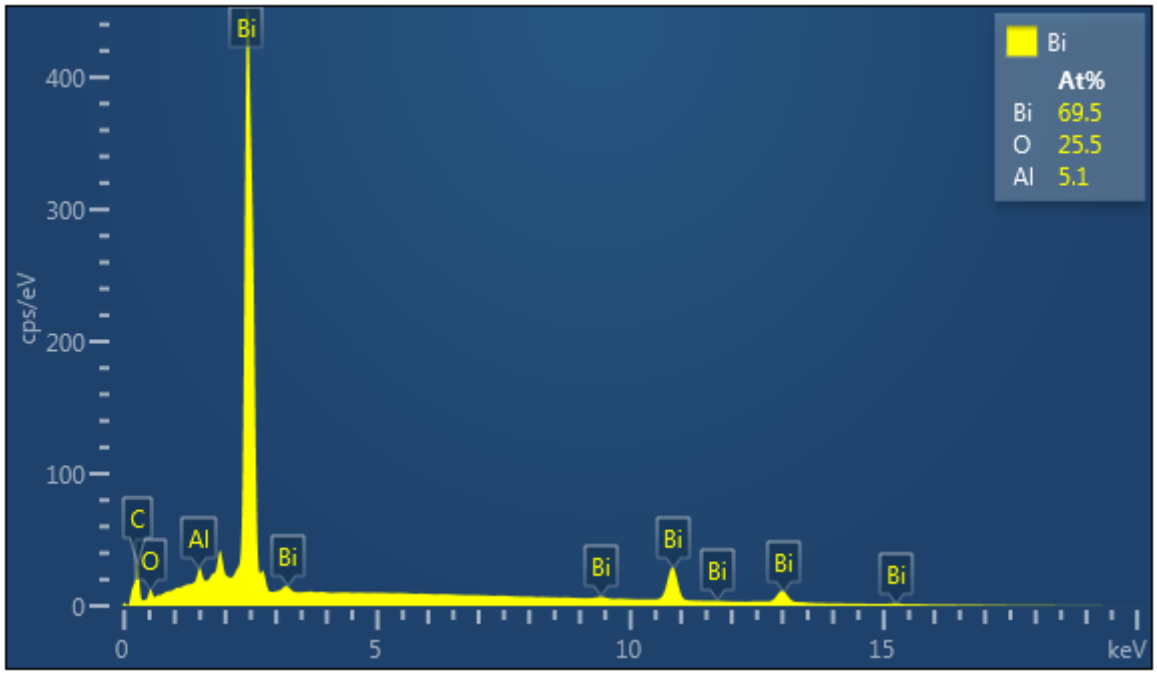
Bi
At%
Bi 69.5
O 25.5
Al 5.1
cps/eV
keV
Bi
C
O
Al
Bi
Bi
Bi
Bi
Bi
Bi

SEM-EDS data for Figure 9F

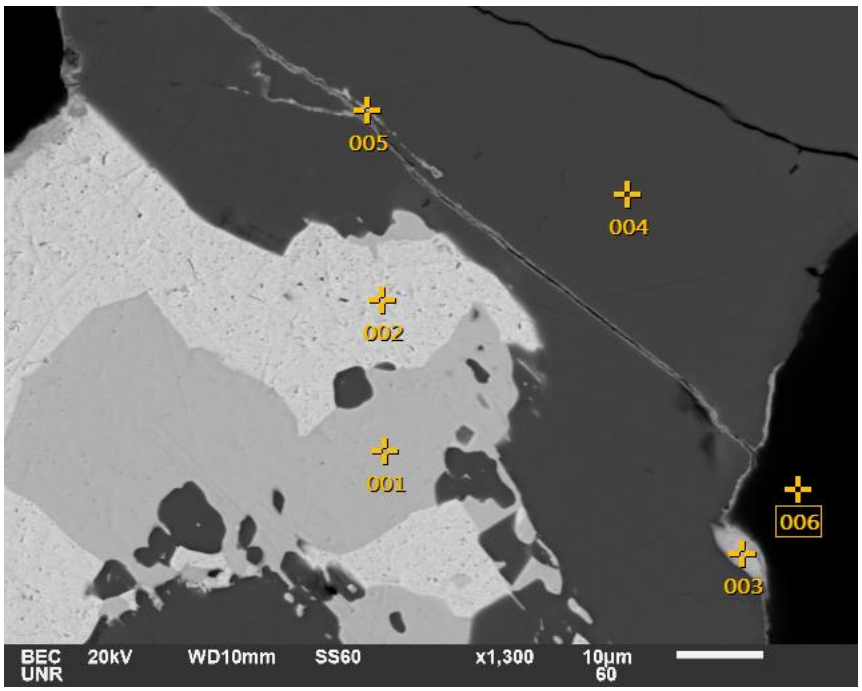

Volt : 20.00 kV

Mag. : x 1,300

Date : 2021/10/07

Pixel : 1280 x 960

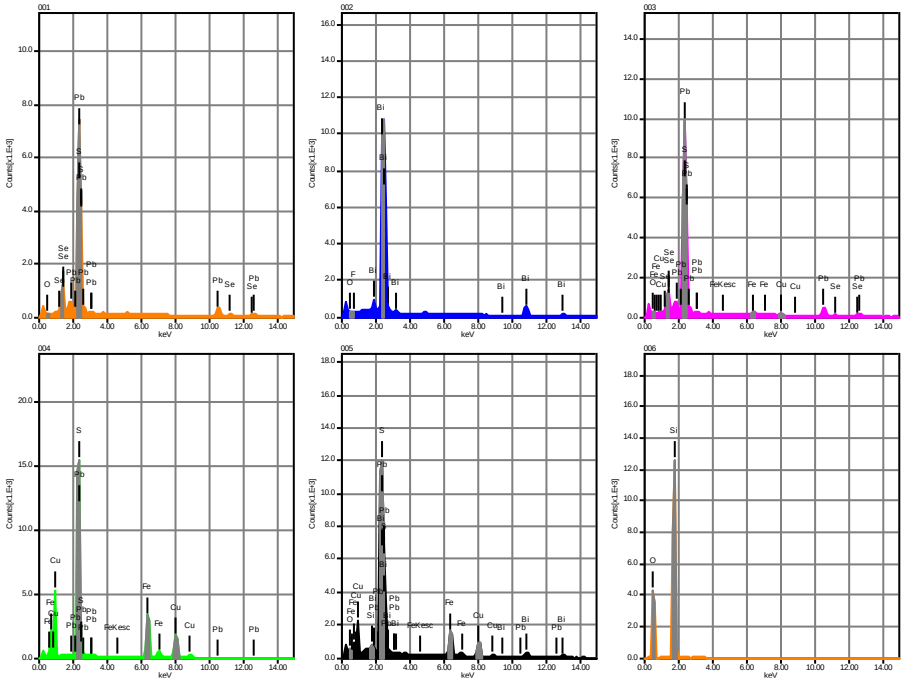

Acquisition Condition

Instrument : 6510(LA)

Volt : 20.00 kV

Current : ---

Process Time : T4

Live time : 5.76 sec.

Real Time : 9.15 sec.

DeadTime : 38.00 %

Count Rate : 29829.00 CPS

	Fe	O	Pb	F	Si	S	Cu	Se	Bi
001		0.52	83.72			6.26		9.50	
002		0.79		0.89					98.32
003	1.24	1.40	81.79			6.63	1.81	7.13	
004	27.81		9.61			34.04	28.54		
005	11.33	1.61	15.95		0.79	20.80	11.23		38.27
006		51.50			48.50				
Average	13.46	11.17	47.77	0.89	24.65	16.93	13.86	8.31	68.29

Figure 9F Detailed

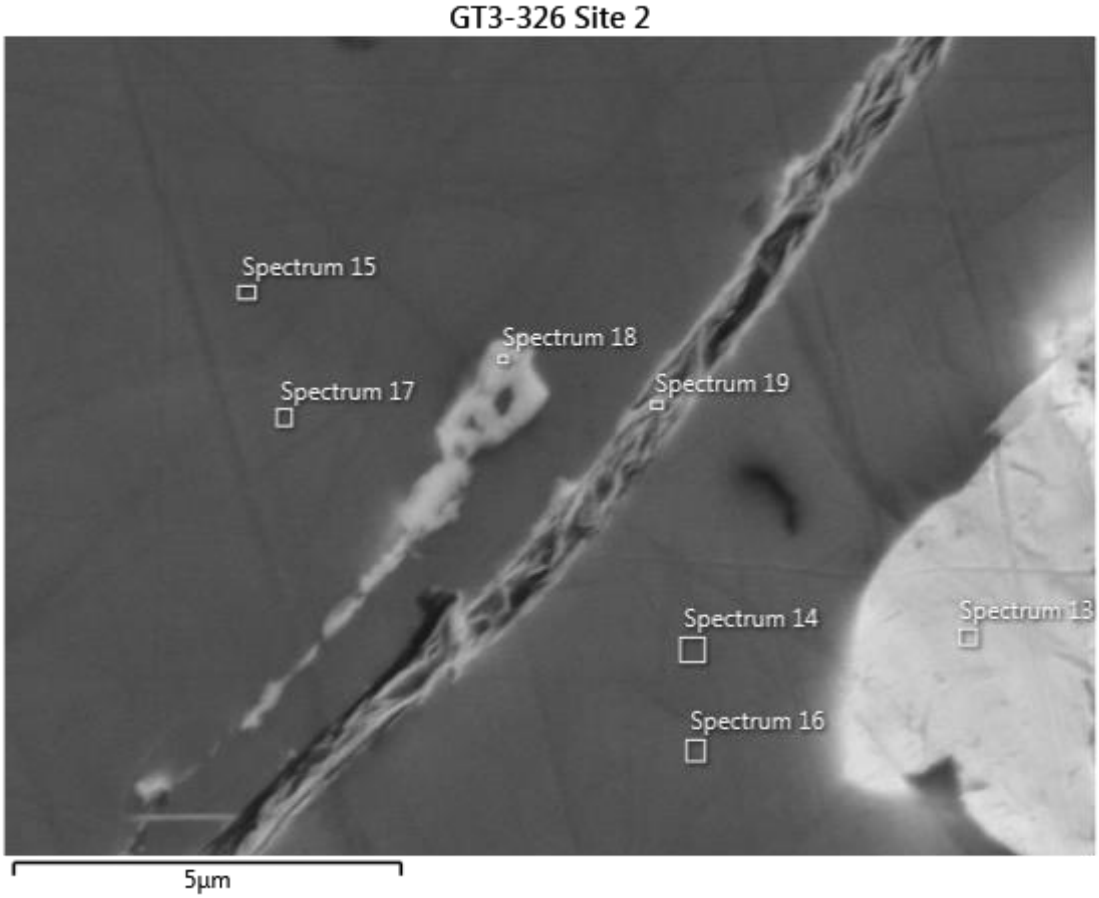

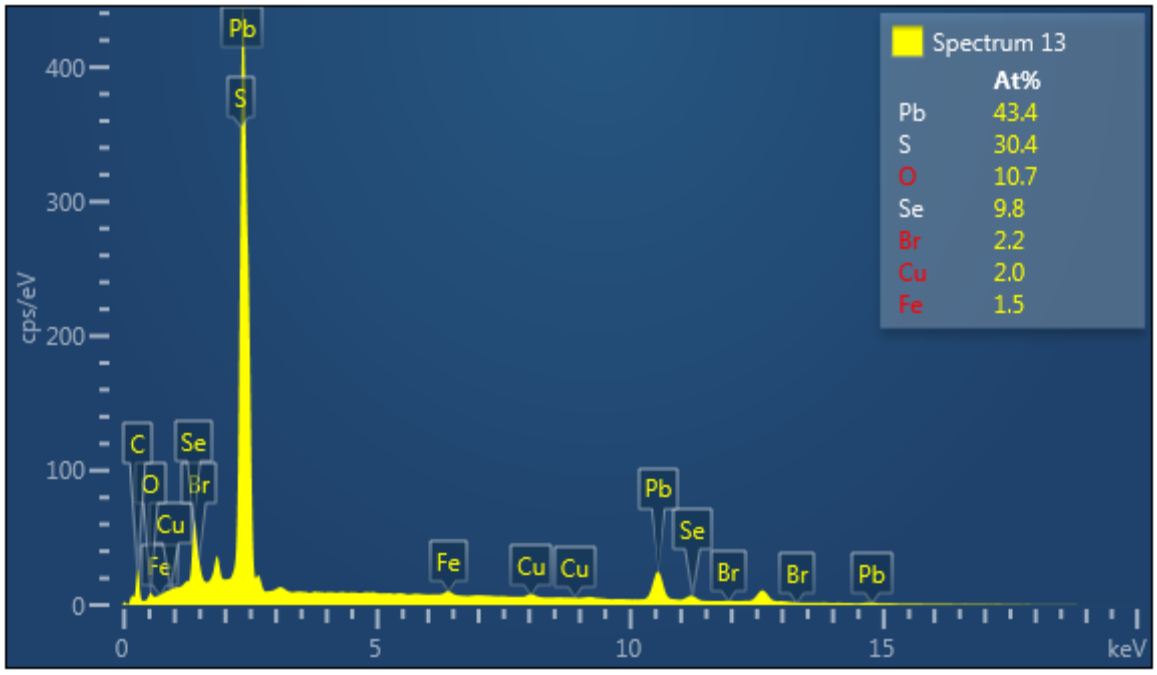

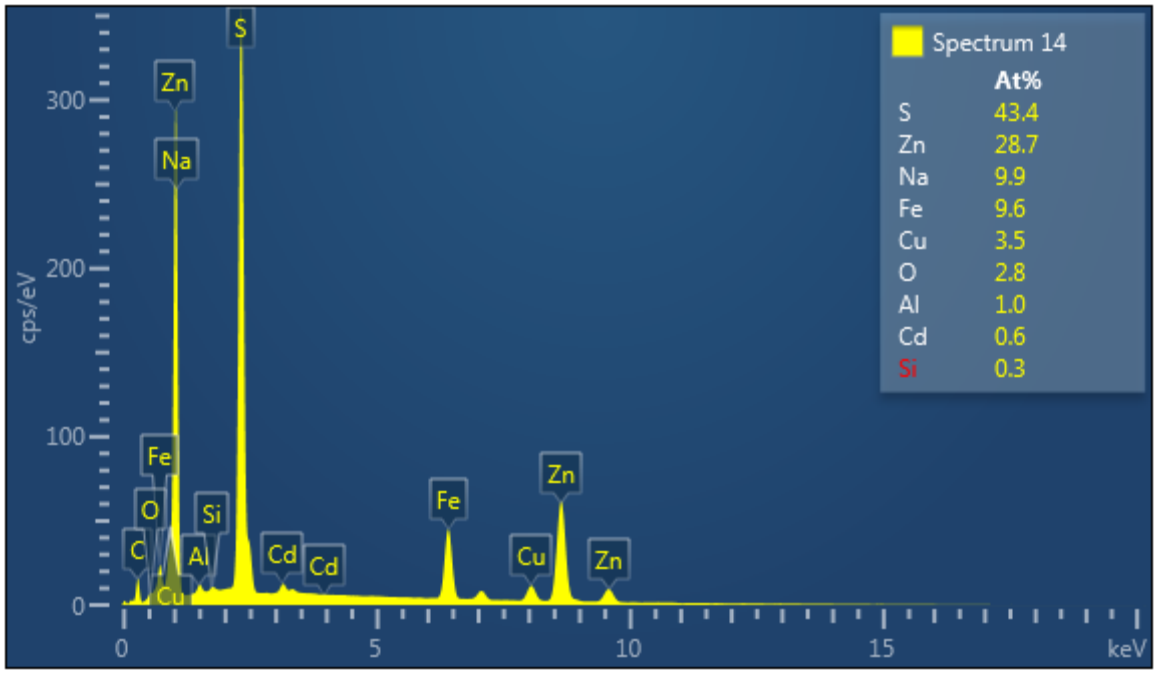
Spectrum 14
At%
S 43.4
Zn 28.7
Na 9.9
Fe 9.6
Cu 3.5
O 2.8
Al 1.0
Cd 0.6
Si 0.3
cps/eV
keV
S
Zn
Na
Fe
O
Si
C
Al
Cu
Cd
Cd
Fe
Cu
Zn
Zn

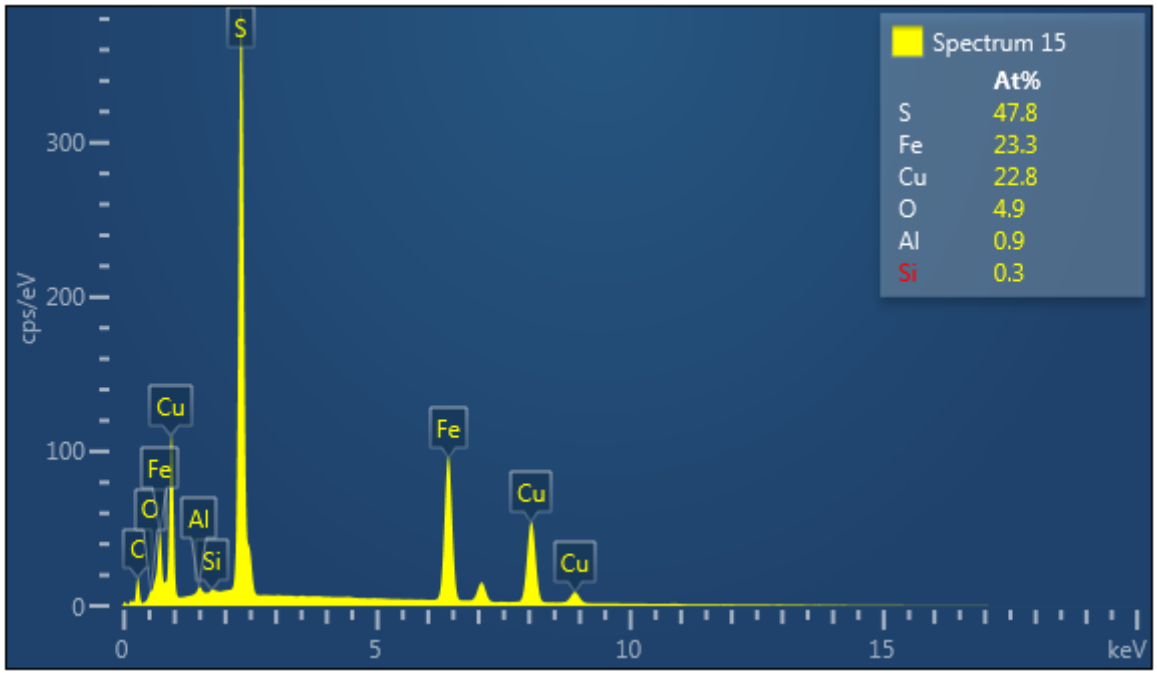
Spectrum 15
At%
S 47.8
Fe 23.3
Cu 22.8
O 4.9
Al 0.9
Si 0.3
cps/eV
keV
S
Cu
Fe
O
Al
C
Si
Fe
Cu
Cu

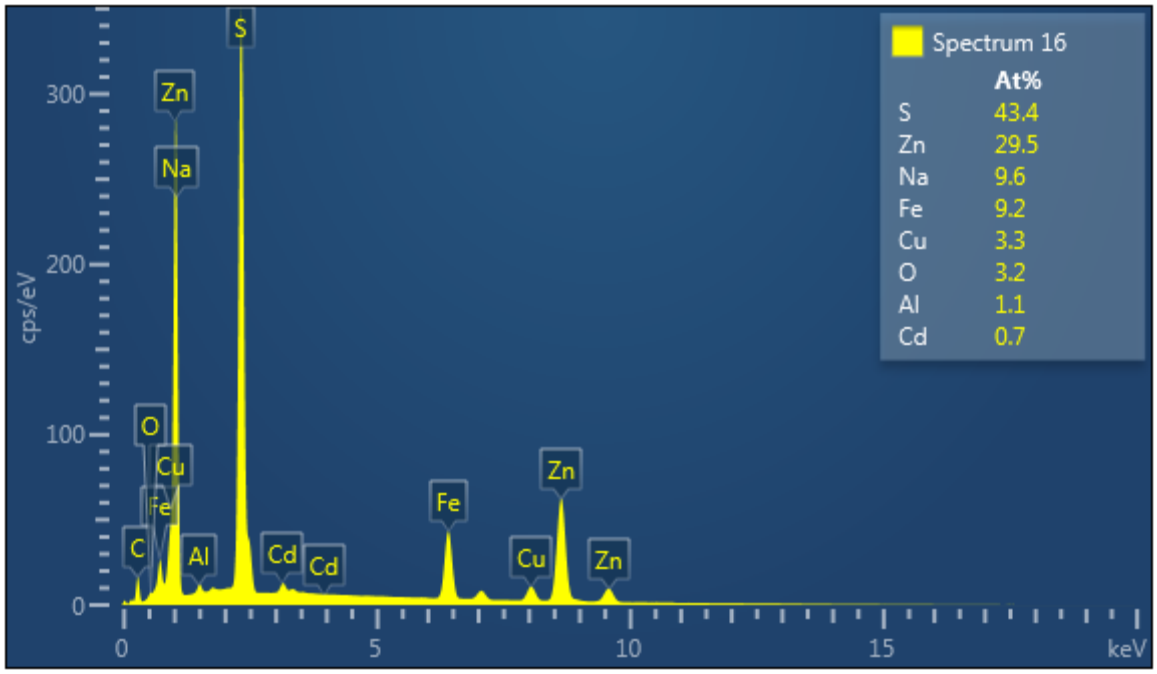
Spectrum 16
At%
S 43.4
Zn 29.5
Na 9.6
Fe 9.2
Cu 3.3
O 3.2
Al 1.1
Cd 0.7
cps/eV
keV
S
Zn
Na
O
Cu
Fe
C
Al
Cd
Cd
Fe
Zn
Cu
Zn

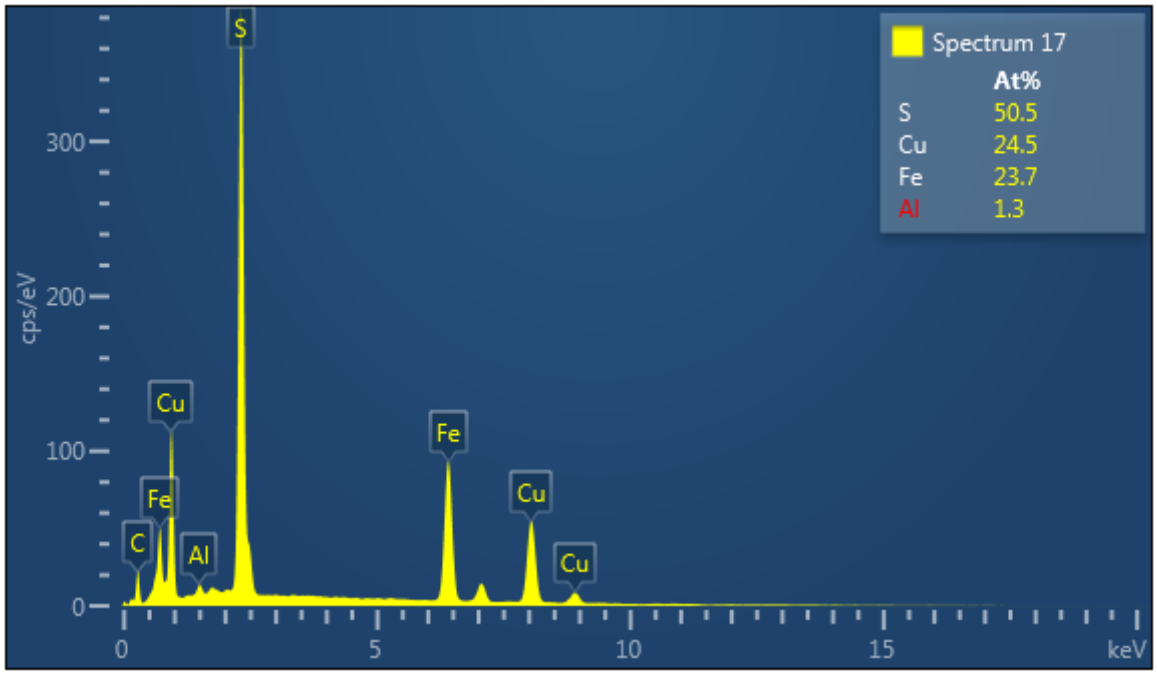
Spectrum 17
At%
S 50.5
Cu 24.5
Fe 23.7
Al 1.3
cps/eV
keV
S
Cu
Fe
C
Al
Fe
Cu
Cu

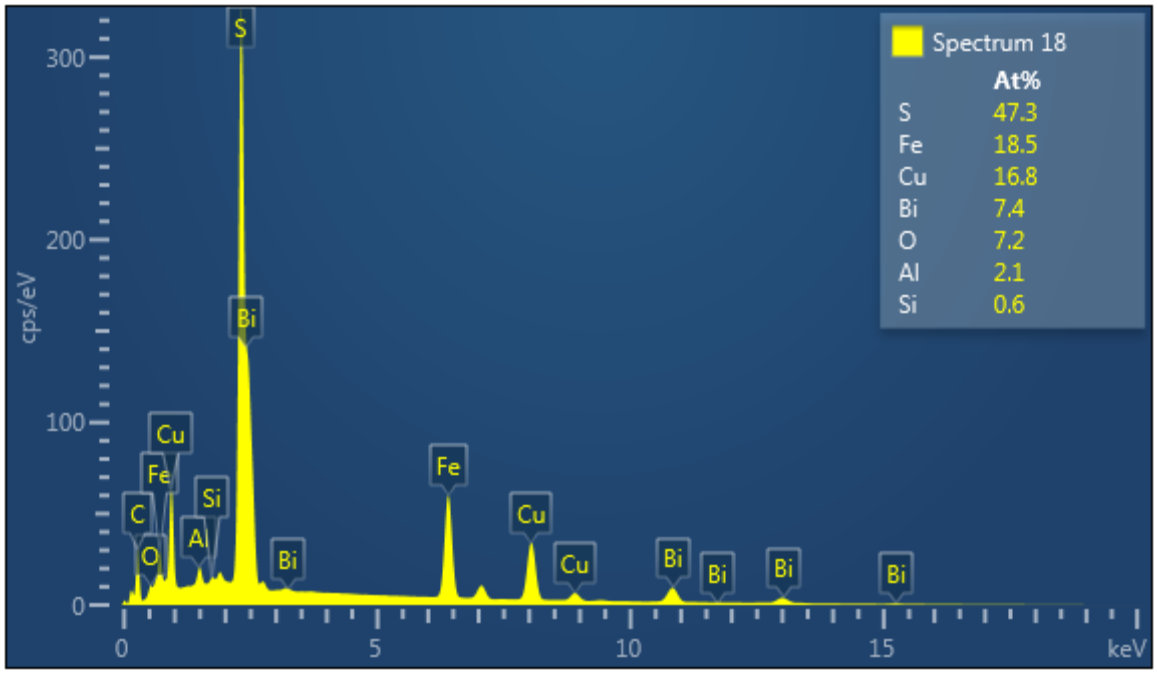
Spectrum 18
At%
S 47.3
Fe 18.5
Cu 16.8
Bi 7.4
O 7.2
Al 2.1
Si 0.6
cps/eV
keV
S
Bi
Cu
Fe
C
O
Al
Si

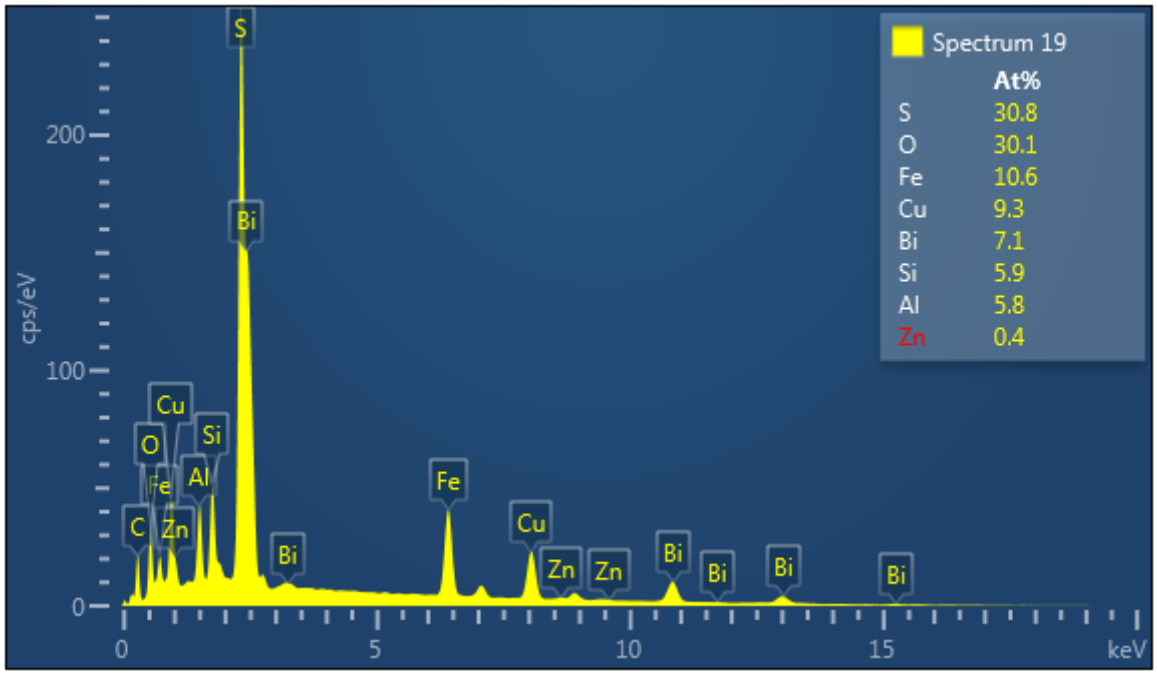
Spectrum 19
At%
S 30.8
O 30.1
Fe 10.6
Cu 9.3
Bi 7.1
Si 5.9
Al 5.8
Zn 0.4
cps/eV
keV
S
Bi
Cu
O
Si
Al
Fe
C
Zn

Gold Pan

SEM-EDS data for Figure 9I

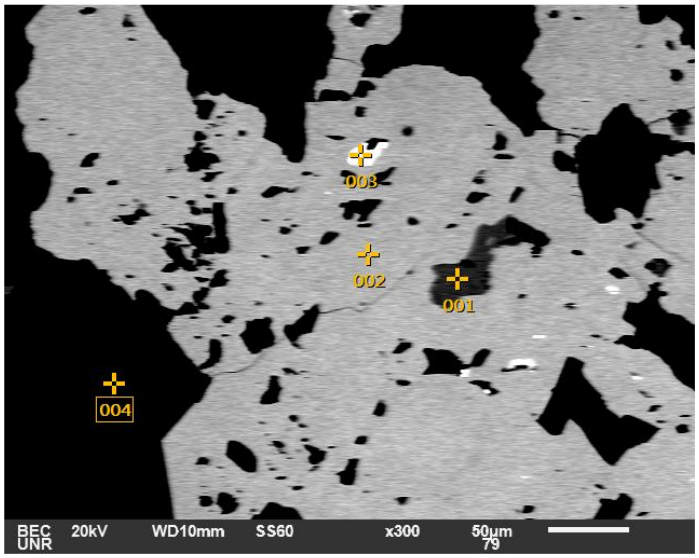

Volt : 20.00 kV

Mag. : x 300

Date : 2021/03/02

Pixel : 640 x 480

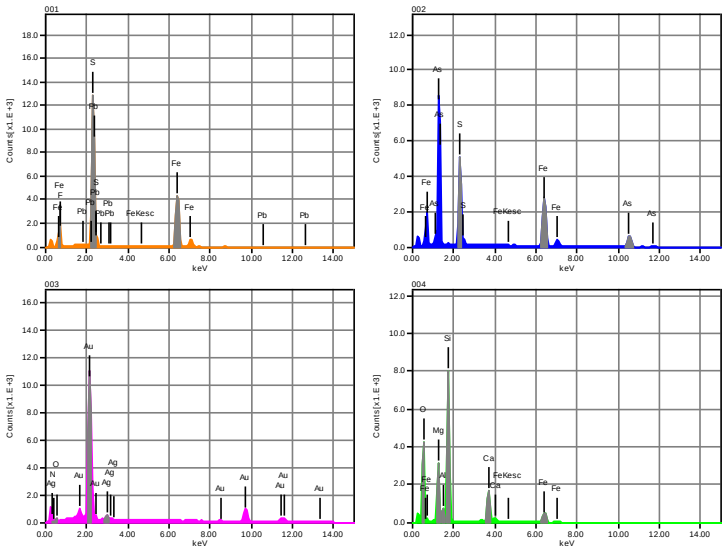

Acquisition Condition

Instrument : 6510(LA)

Volt : 20.00 kV

Current : ---

Process Time : T4

Live time : 15.00 sec.

Real Time : 18.95 sec.

DeadTime : 21.00 %

Count Rate : 14459.00 CPS

	Fe	O	Pb	Au	Ag	N	F	Mg	Al	Si	S	Ca	As	
001	55.72		4.18				1.17				38.93			
002	35.15										20.18		44.67	
003		2.08		90.26	4.62	3.04								
004	7.38	44.00						11.24	2.03	26.91		8.44		
Average	32.75	23.04	4.18	90.26	4.62	3.04	1.17	11.24	2.03	26.91	29.55	8.44	44.67	
Standard deviation	24.26	29.64	0.00	0.00	0.00	0.00	0.00	0.00	0.00	0.00	13.26	0.00	0.00	

39A

SEM-EDS data for Figure 9K

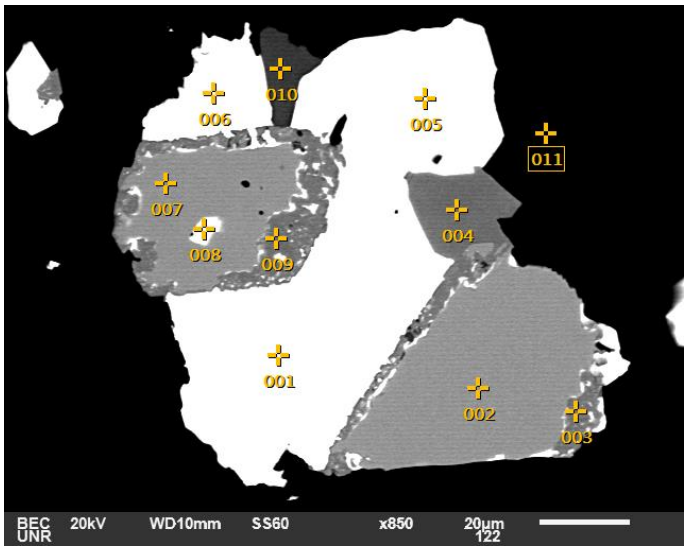

Volt : 20.00 kV

Mag. : x 850

Date : 2021/03/04

Pixel : 640 x 480

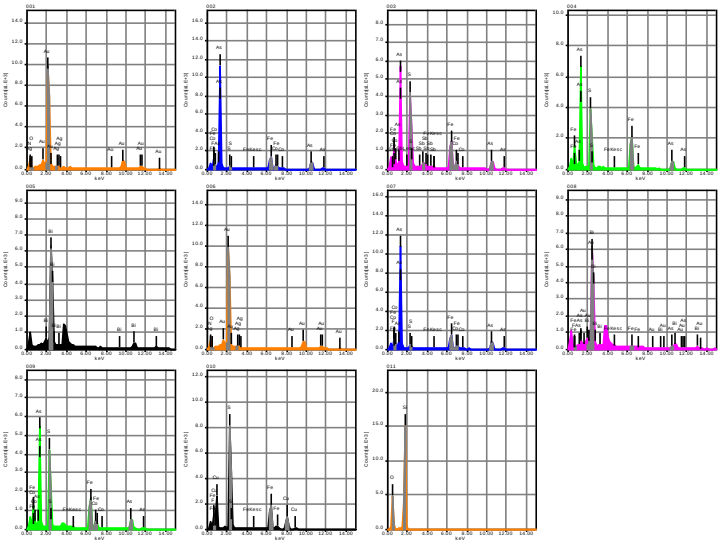

Acquisition Condition

Instrument : 6510(LA)

Volt : 20.00 kV

Current : ---

Process Time : T4

Live time : 15.00 sec.

Real Time : 18.64 sec.

DeadTime : 19.00 %

Count Rate : 16083.00 CPS

	Fe	O	Au	Ag	N	F	Si	S	Co	Cu	As	Sb	Bi
001		0.97	93.43	1.91	3.70								
002	23.63					1.55		1.15	6.23		67.45		
003	27.09							21.50	7.25		39.31	4.84	
004	35.06							20.28			44.67		
005													100.00
006		0.60	93.27	2.38	3.74								
007	24.45					1.70		1.81	5.81		66.24		
008	1.12		1.55			1.11					5.69		90.53
009	28.01							22.29	7.71		41.99		
010	30.08					1.07		36.90		31.96			
011		50.57					49.43						
Average	24.20	17.38	62.75	2.15	3.72	1.36	49.43	17.32	6.75	31.96	44.22	4.84	95.27

39A

SEM-EDS data for Figure 9L Point 3

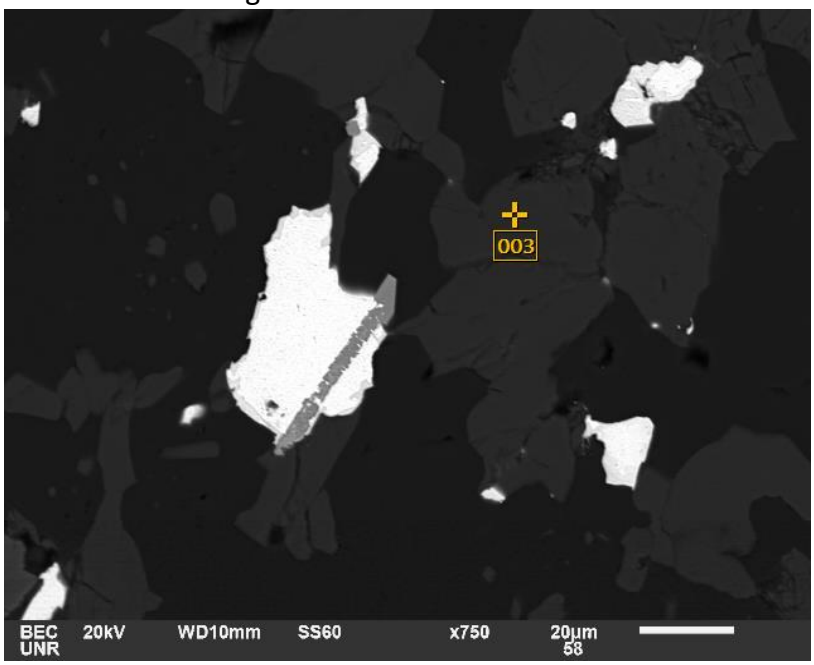

Volt : 20.00 kV

Mag. : x 750

Date : 2021/02/08

Pixel : 1280 x 960

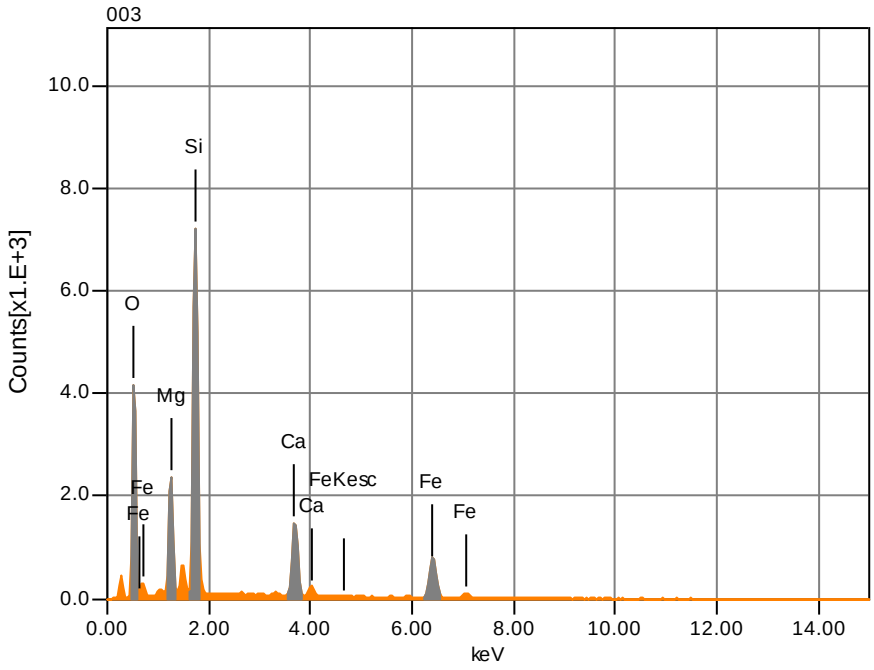

Acquisition Condition

Instrument : 6510(LA)

Volt : 20.00 kV

Current : ---

Process Time : T4

Live time : 15.00 sec.

Real Time : 18.61 sec.

DeadTime : 20.00 %

Count Rate : 13717.00 CPS

Chemical formula	mass%	Atom%	Sigma	Net	K ratio	Line
O	43.34	60.51	0.09	104481	0.5818632	K
Mg	9.81	9.01	0.05	81342	0.1482035	K
Si	26.49	21.07	0.09	280183	0.5605780	K
Ca	8.03	4.48	0.05	78905	0.2478099	K
Fe	12.33	4.93	0.07	47786	0.3408286	K
Total	100.00	100.00				

Figure 9L Point 4

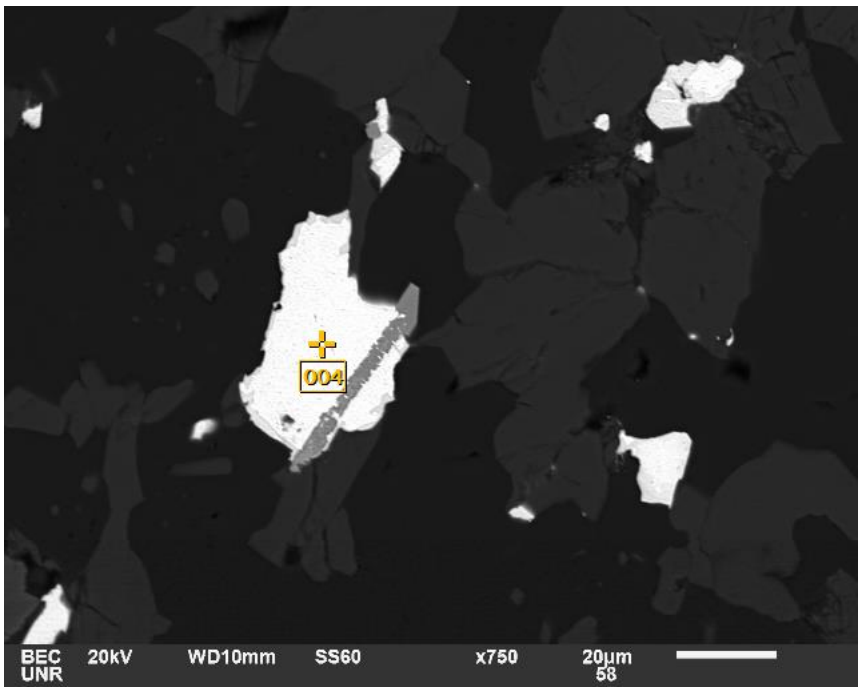

Volt : 20.00 kV

Mag. : x 750

Date : 2021/02/08

Pixel : 1280 x 960

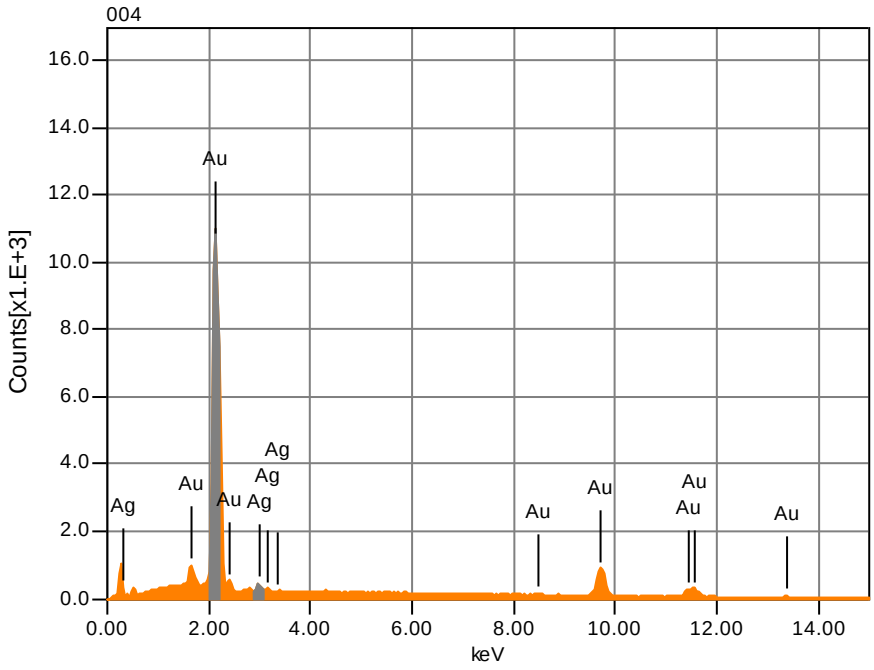

Acquisition Condition

Instrument : 6510(LA)

Volt : 20.00 kV

Current : ---

Process Time : T4

Live time : 15.00 sec.

Real Time : 24.63 sec.

DeadTime : 40.00 %

Count Rate : 27647.00 CPS

Chemical formula	mass%	Atom%	Sigma	Net	K ratio	Line
Ag	3.26	5.79	0.07	19896	0.0764092	L
Au	96.74	94.21	0.21	734441	3.1589530	M
Total	100.00	100.00				

Figure 9L Point 5

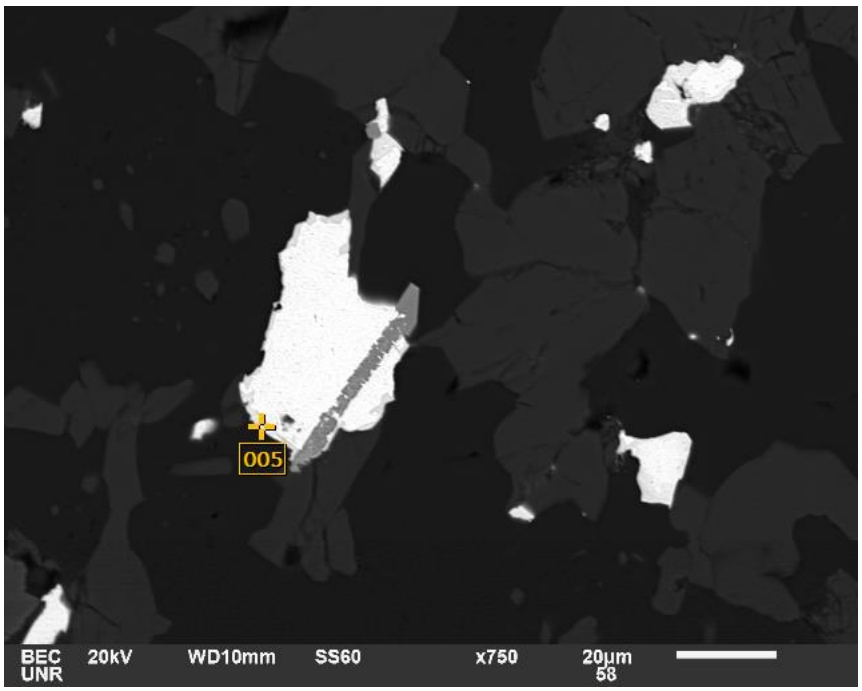

Volt : 20.00 kV

Mag. : x 750

Date : 2021/02/08

Pixel : 1280 x 960

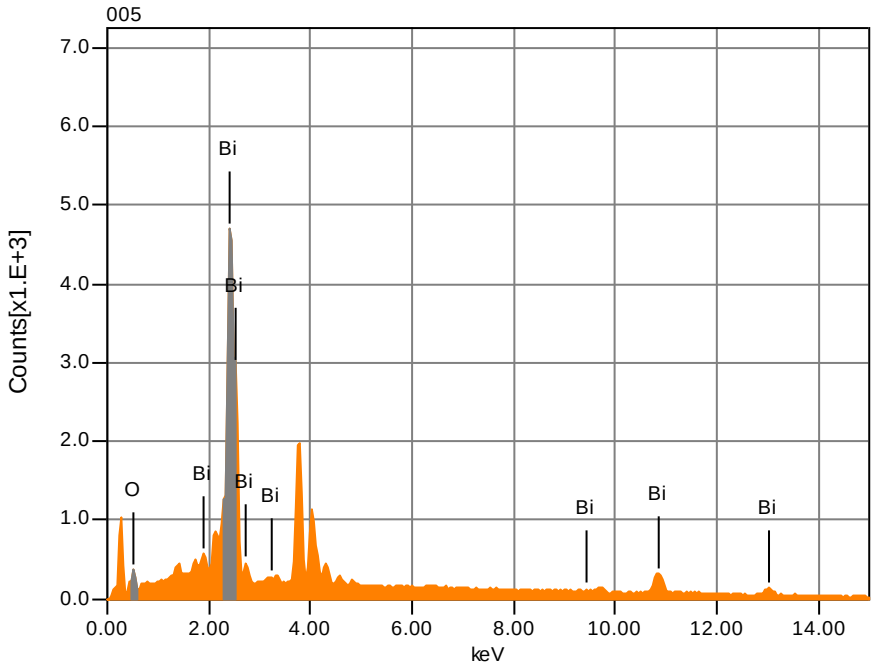

Acquisition Condition

Instrument : 6510(LA)

Volt : 20.00 kV

Current : ---

Process Time : T4

Live time : 15.00 sec.

Real Time : 22.46 sec.

DeadTime : 33.00 %

Count Rate : 23407.00 CPS

Chemical formula	mass%	Atom%	Sigma	Net	K ratio	Line
O	1.80	19.30	0.03	4888	0.0272210	K
Bi	98.20	80.70	0.43	303080	1.2958258	M
Total	100.00	100.00				

Figure 9L Point 9

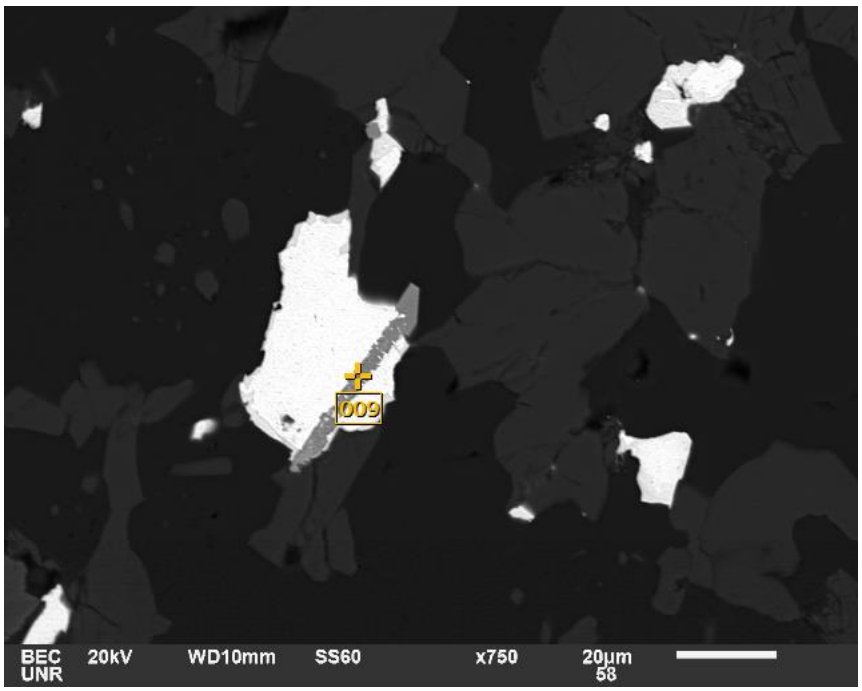

Volt : 20.00 kV

Mag. : x 750

Date : 2021/02/08

Pixel : 1280 x 960

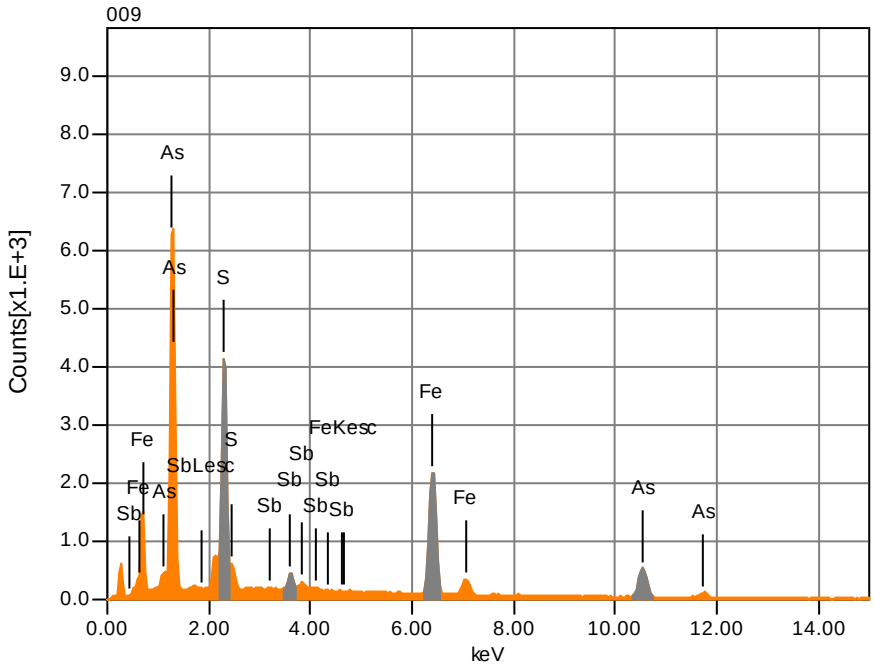

Acquisition Condition

Instrument : 6510(LA)

Volt : 20.00 kV

Current : ---

Process Time : T4

Live time : 15.00 sec.

Real Time : 21.04 sec.

DeadTime : 29.00 %

Count Rate : 20370.00 CPS

Chemical formula	mass%	Atom%	Sigma	Net	K ratio	Line
S	18.41	32.01	0.06	170450	0.4115396	K
Fe	34.01	33.95	0.10	145049	1.0345421	K
As	42.88	31.90	0.35	43184	1.1227093	K
Sb	4.69	2.15	0.09	23930	0.1077777	L
Total	100.00	100.00				

Figure 9L Point 10

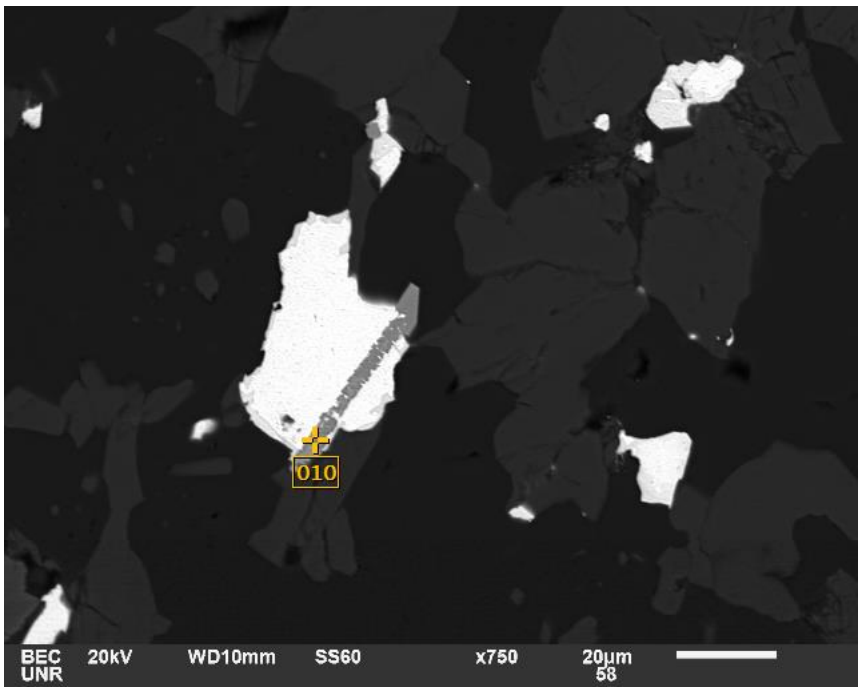

Volt : 20.00 kV

Mag. : x 750

Date : 2021/02/08

Pixel : 1280 x 960

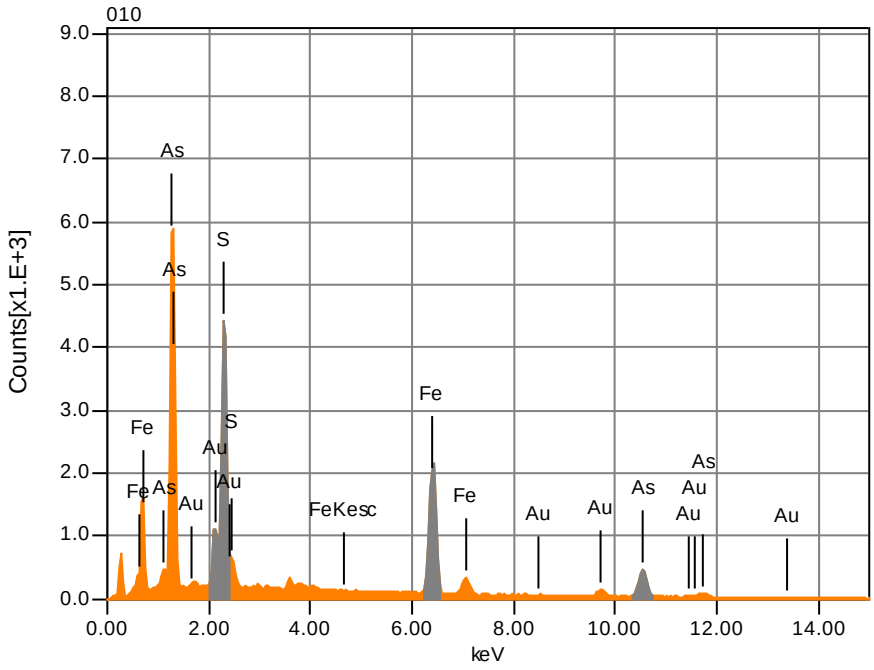

Acquisition Condition

Instrument : 6510(LA)

Volt : 20.00 kV

Current : ---

Process Time : T4

Live time : 15.00 sec.

Real Time : 21.29 sec.

DeadTime : 22.00 %

Count Rate : 15380.00 CPS

Chemical formula	mass%	Atom%	Sigma	Net	K ratio	Line
S	20.83	37.83	0.07	192381	0.4644893	K
Fe	30.60	31.90	0.10	138025	0.9844440	K
As	33.05	25.68	0.31	35755	0.9295574	K
Au	15.52	4.59	0.17	66795	0.2872945	M
Total	100.00	100.00				

Figure 9L Point 11

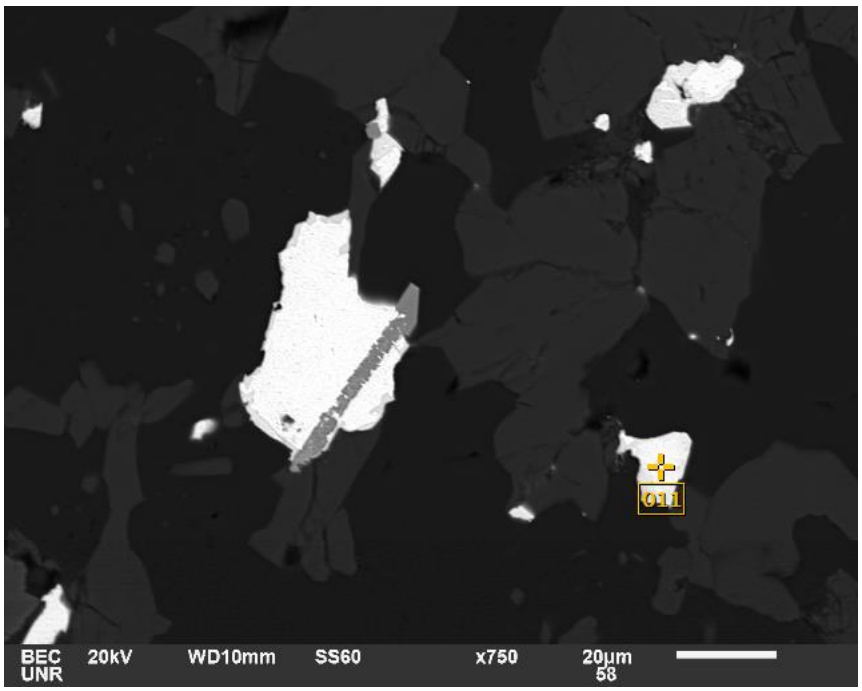

Volt : 20.00 kV

Mag. : x 750

Date : 2021/02/08

Pixel : 1280 x 960

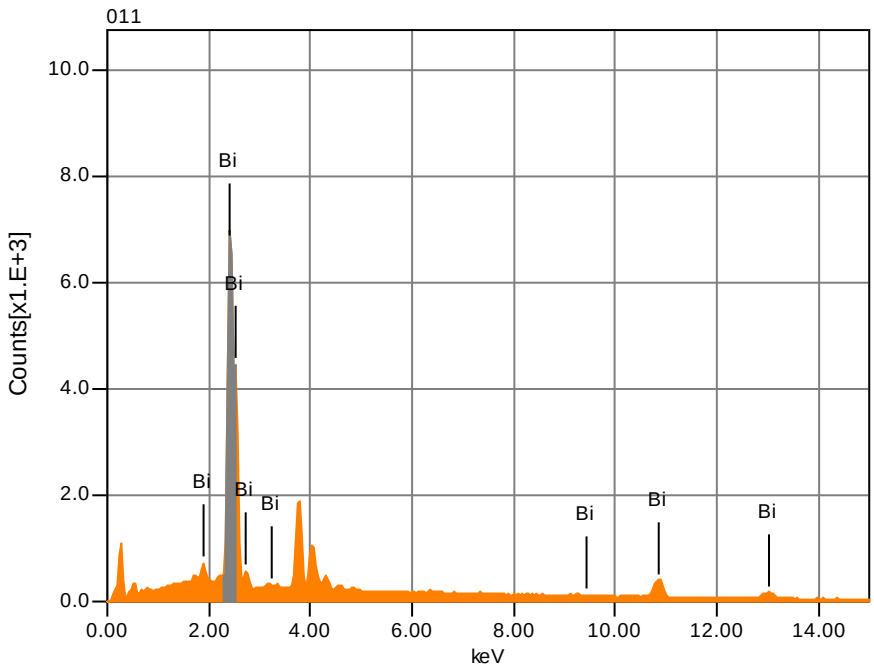

Acquisition Condition

Instrument : 6510(LA)

Volt : 20.00 kV

Current : ---

Process Time : T4

Live time : 15.00 sec.

Real Time : 23.54 sec.

DeadTime : 36.00 %

Count Rate : 26191.00 CPS

Chemical formula	mass%	Atom%	Sigma	Net	K ratio	Line
Bi	100.00	100.00	0.29	514912	2.2015231	M
Total	100.00	100.00				

Figure 9L Point 12

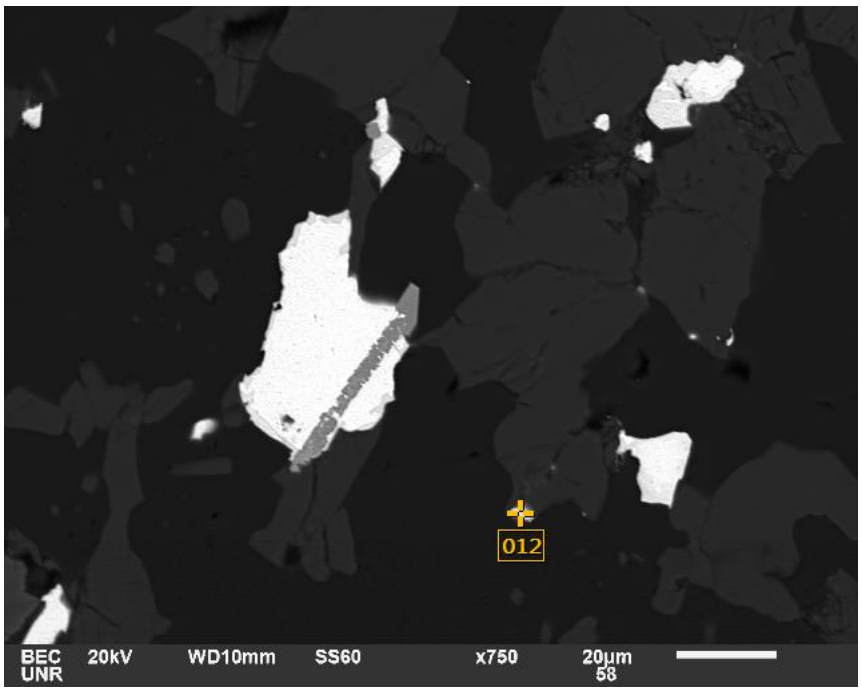

Volt : 20.00 kV

Mag. : x 750

Date : 2021/02/08

Pixel : 1280 x 960

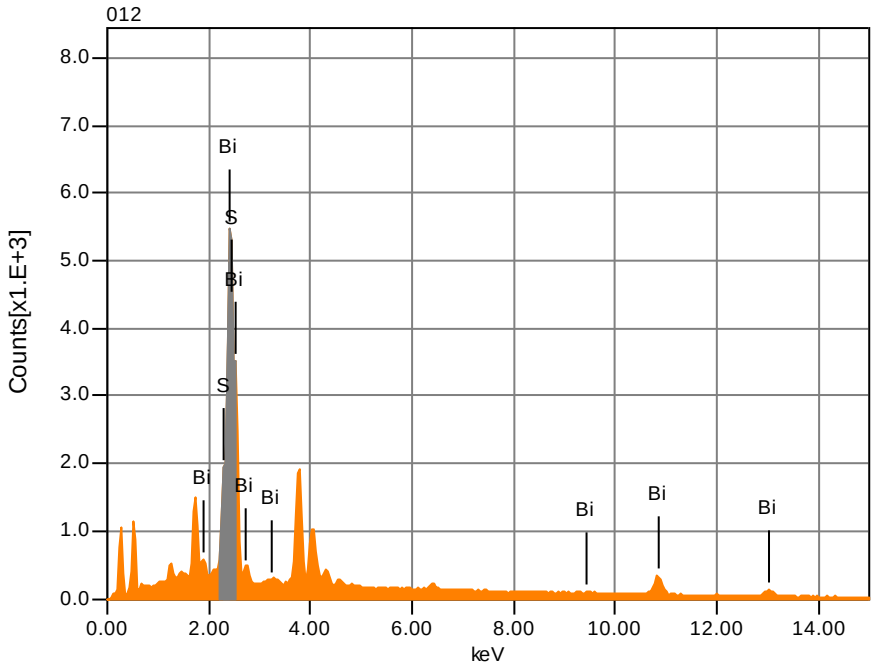

Acquisition Condition

Instrument : 6510(LA)

Volt : 20.00 kV

Current : ---

Process Time : T4

Live time : 15.00 sec.

Real Time : 22.95 sec.

DeadTime : 34.00 %

Count Rate : 25163.00 CPS

Chemical formula	mass%	Atom%	Sigma	Net	K ratio	Line
S	7.24	33.72	0.06	70344	0.1698404	K
Bi	92.76	66.28	0.37	402512	1.7209504	M
Total	100.00	100.00				

Figure 9L detailed

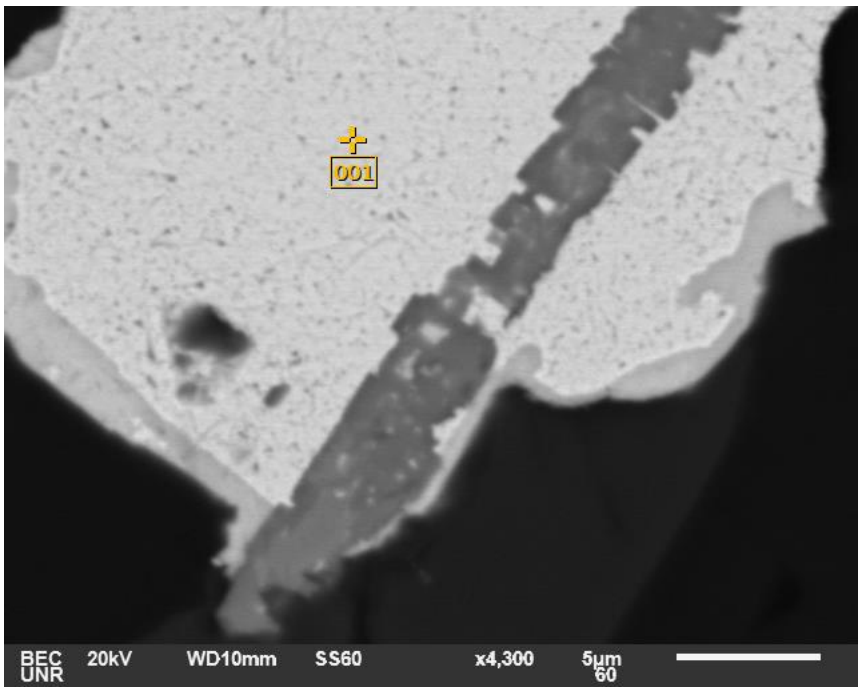

Volt : 20.00 kV

Mag. : x 4,300

Date : 2021/02/08

Pixel : 640 x 480

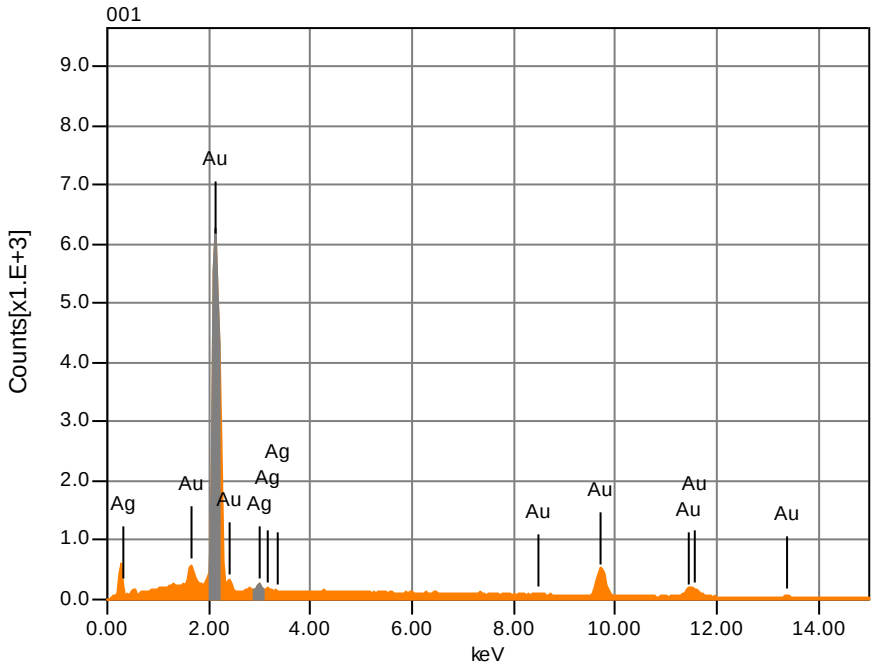

Acquisition Condition

Instrument : 6510(LA)

Volt : 20.00 kV

Current : ---

Process Time : T4

Live time : 8.32 sec.

Real Time : 13.86 sec.

DeadTime : 40.00 %

Count Rate : 29992.00 CPS

Chemical formula	mass%	Atom%	Sigma	Net	K ratio	Line
Ag	3.13	5.57	0.10	10850	0.0751278	L
Au	96.87	94.43	0.29	417818	3.2399750	M
Total	100.00	100.00				

Figure 9L detailed

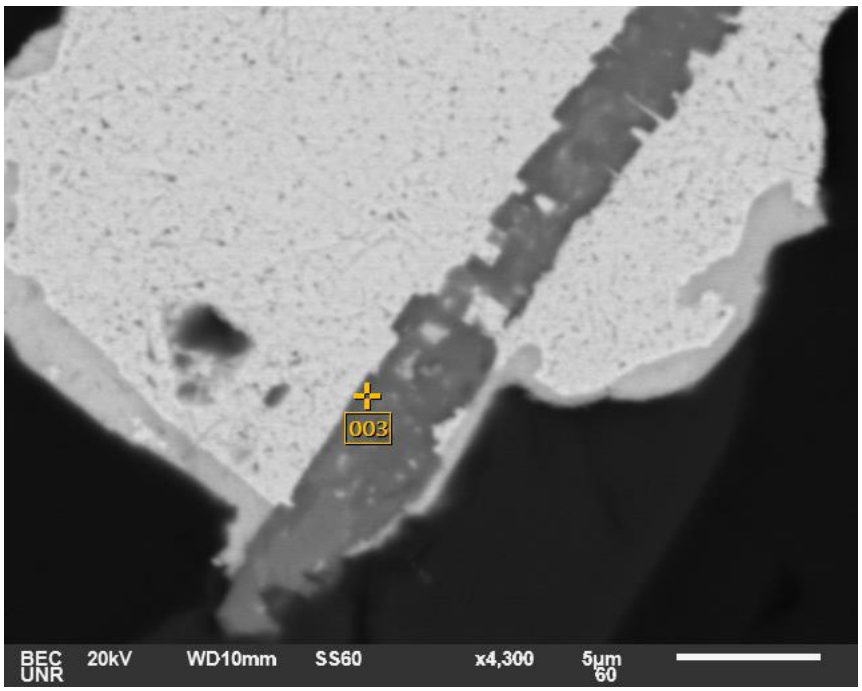

Volt : 20.00 kV

Mag. : x 4,300

Date : 2021/02/08

Pixel : 640 x 480

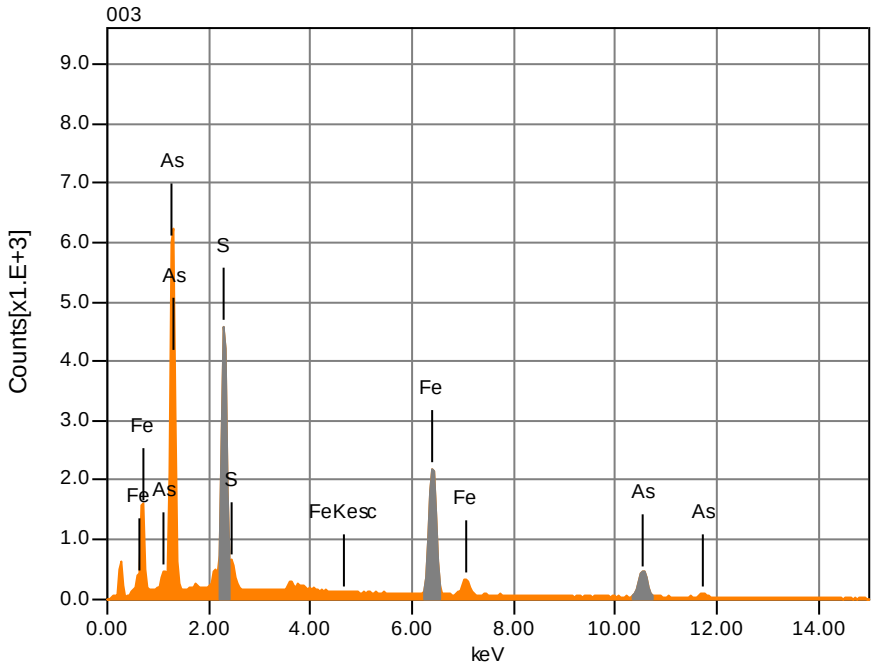

Acquisition Condition

Instrument : 6510(LA)

Volt : 20.00 kV

Current : ---

Process Time : T4

Live time : 15.00 sec.

Real Time : 20.81 sec.

DeadTime : 28.00 %

Count Rate : 19412.00 CPS

Chemical formula	mass%	Atom%	Sigma	Net	K ratio	Line
S	21.96	36.21	0.06	190257	0.4593602	K
Fe	36.26	34.32	0.11	143575	1.0240275	K
As	41.78	29.48	0.37	38726	1.0068125	K
Total	100.00	100.00				

Figure 9L detailed

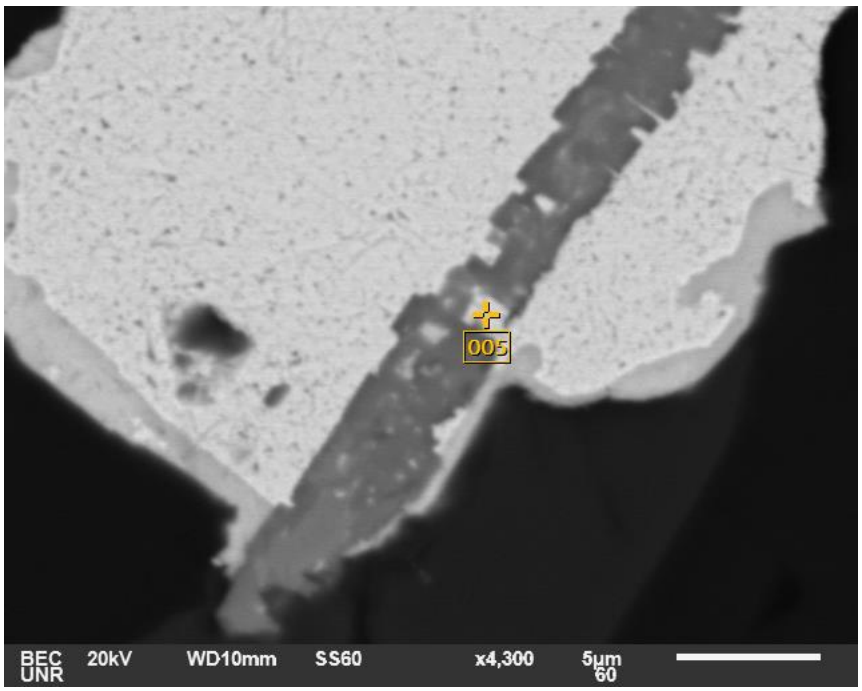

Volt : 20.00 kV

Mag. : x 4,300

Date : 2021/02/08

Pixel : 640 x 480

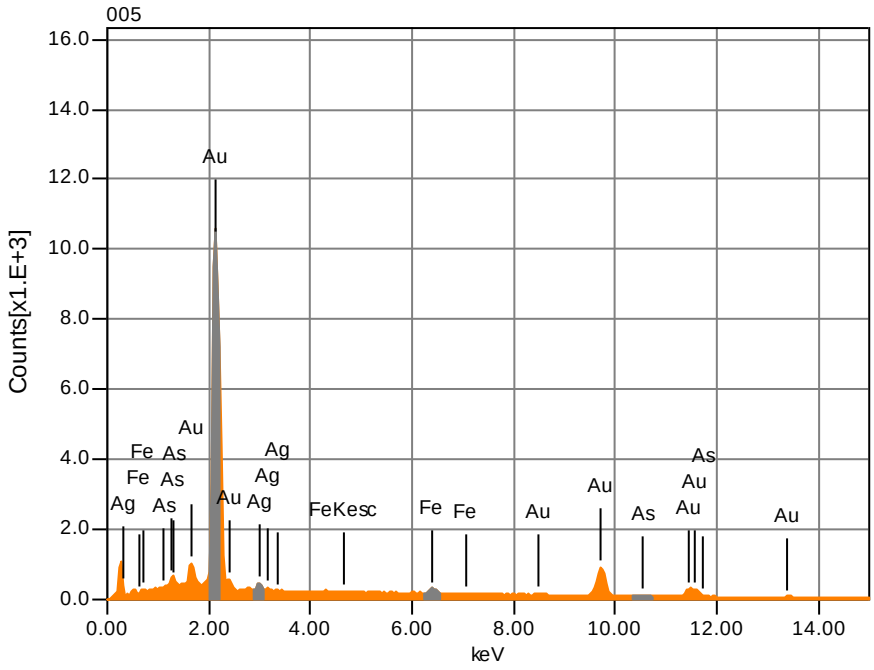

Acquisition Condition

Instrument : 6510(LA)

Volt : 20.00 kV

Current : ---

Process Time : T4

Live time : 15.00 sec.

Real Time : 24.70 sec.

DeadTime : 40.00 %

Count Rate : 29353.00 CPS

Chemical formula	mass%	Atom%	Sigma	Net	K ratio	Line
Fe	1.67	5.37	0.04	10088	0.0719505	K
As	1.87	4.47	0.15	3024	0.0786088	K
Ag	3.18	5.29	0.07	19613	0.0753249	L
Au	93.28	84.87	0.22	697034	2.9980576	M
Total	100.00	100.00				

Figure 9L detailed

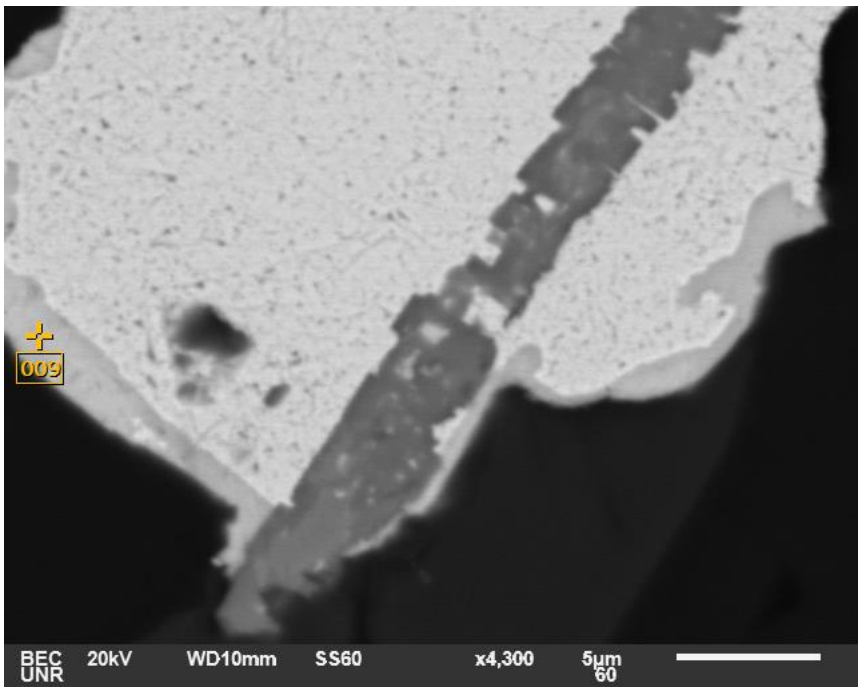

Volt : 20.00 kV

Mag. : x 4,300

Date : 2021/02/08

Pixel : 640 x 480

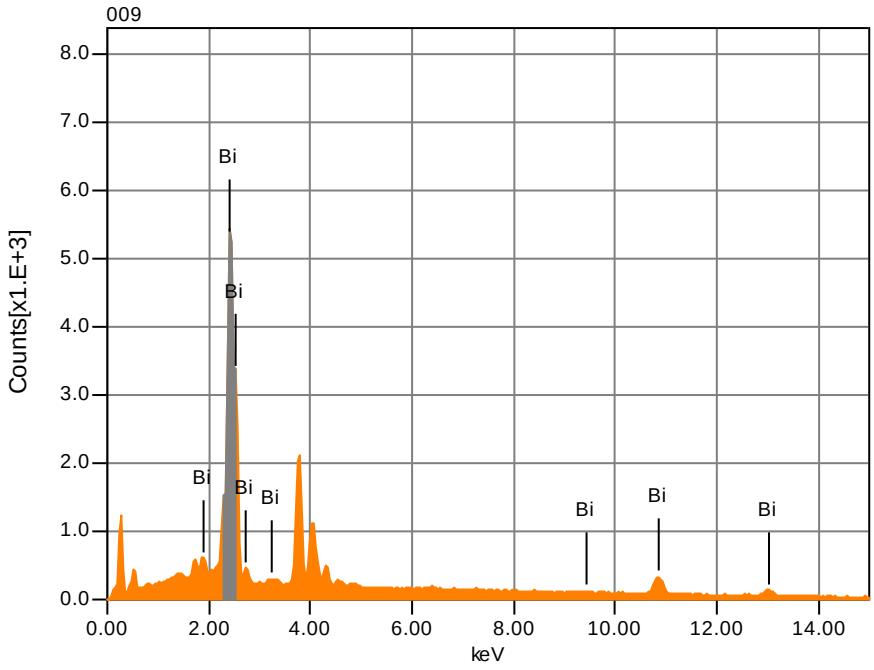

Acquisition Condition

Instrument : 6510(LA)

Volt : 20.00 kV

Current : ---

Process Time : T4

Live time : 15.00 sec.

Real Time : 22.85 sec.

DeadTime : 34.00 %

Count Rate : 24599.00 CPS

Chemical formula	mass%	Atom%	Sigma	Net	K ratio	Line
Bi	100.00	100.00	0.42	335935	1.4362996	M
Total	100.00	100.00				

Distal

SEM-EDS data for Figure 9N

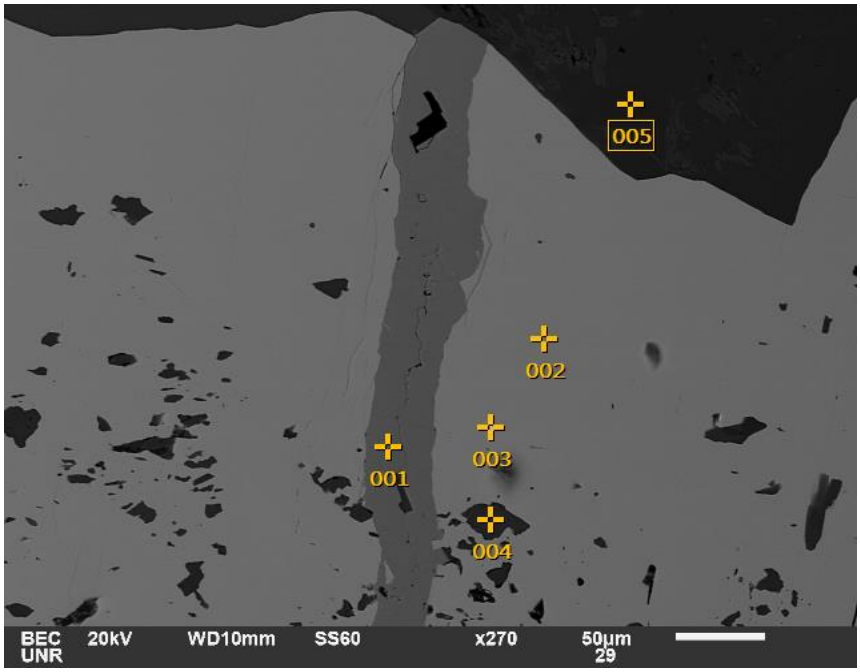

Volt : 20.00 kV

Mag. : x 270

Date : 2021/10/05

Pixel : 1280 x 960

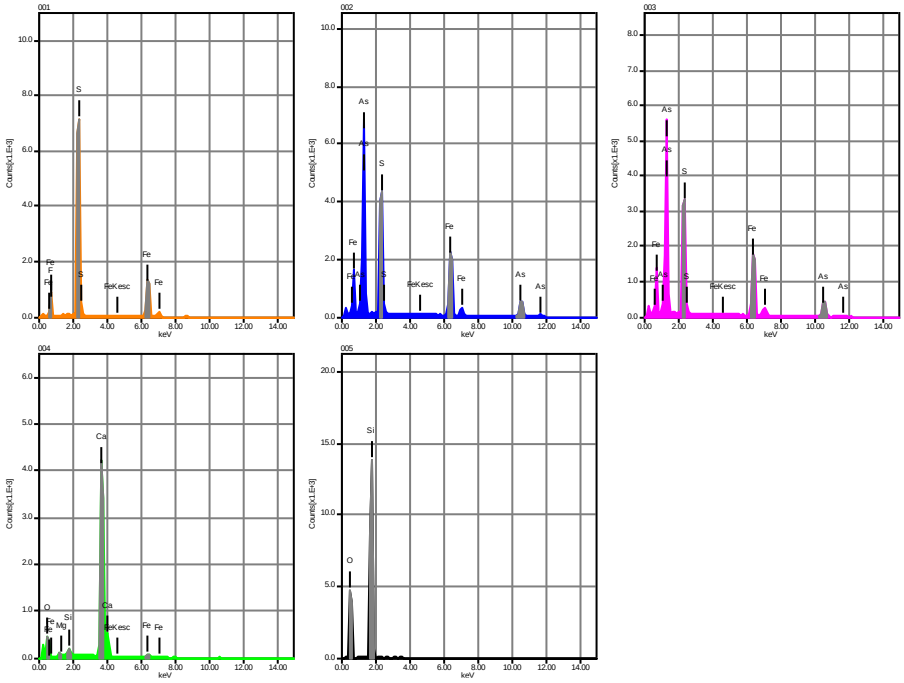

Acquisition Condition

Instrument : 6510(LA)

Volt : 20.00 kV

Current : ---

Process Time : T4

Live time : 6.33 sec.

Real Time : 10.02 sec.

DeadTime : 37.00 %

Count Rate : 29609.00 CPS

	Fe	O	F	Mg	Si	S	Ca	As		
001	42.91		1.85			55.23				
002	35.58					21.82		42.60		
003	36.24					22.09		41.67		
004	3.19	38.31		0.71	1.50		56.30			
005		51.66			48.34					
Average	29.48	44.98	1.85	0.71	24.92	33.05	56.30	42.13		
Standard deviation			17.84	9.44	0.00	0.00	33.12	19.21	0.00	0.66

Figure 9N Detailed

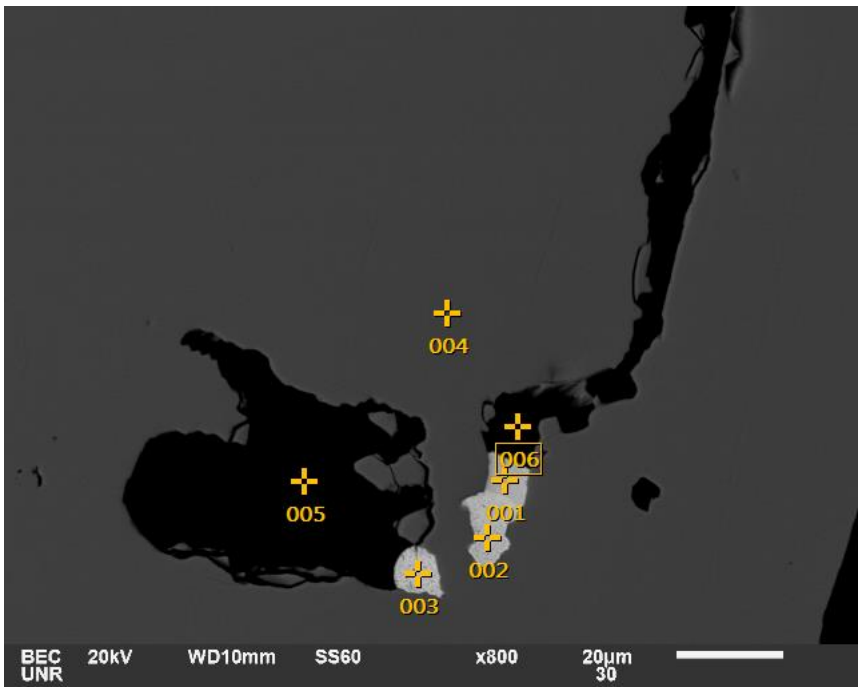

Volt : 20.00 kV

Mag. : x 800

Date : 2021/10/05

Pixel : 1280 x 960

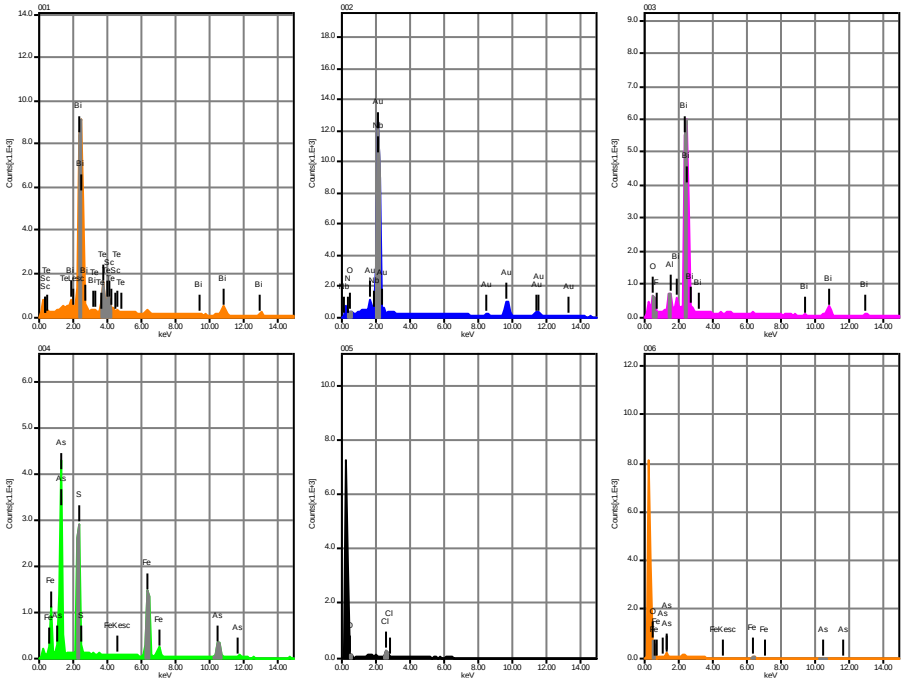

Acquisition Condition

Instrument : 6510(LA)

Volt : 20.00 kV

Current : ---

Process Time : T4

Live time : 6.99 sec.

Real Time : 8.19 sec.

DeadTime : 15.00 %

Count Rate : 10889.00 CPS

	Fe	O	Au	N	F	Al	S	Cl	Sc	As	Nb	Te	Bi
001									0.83			22.00	77.17
002		1.94	85.64	3.83							8.60		
003		3.62			1.09	1.86							93.43
004	36.66						22.33			41.00			
005		65.80						34.20					
006	14.89	72.48								12.63			
Average	25.78	35.96	85.64	3.83	1.09	1.86	22.33	34.20	0.83	26.82	8.60	22.00	85.30

Figure 9N Detailed

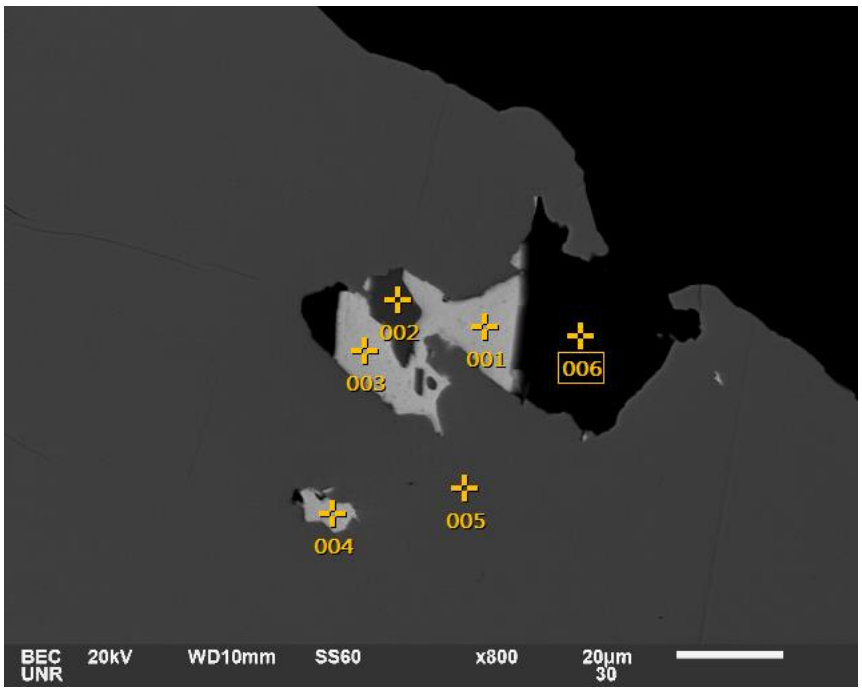

Volt : 20.00 kV

Mag. : x 800

Date : 2021/10/05

Pixel : 1280 x 960

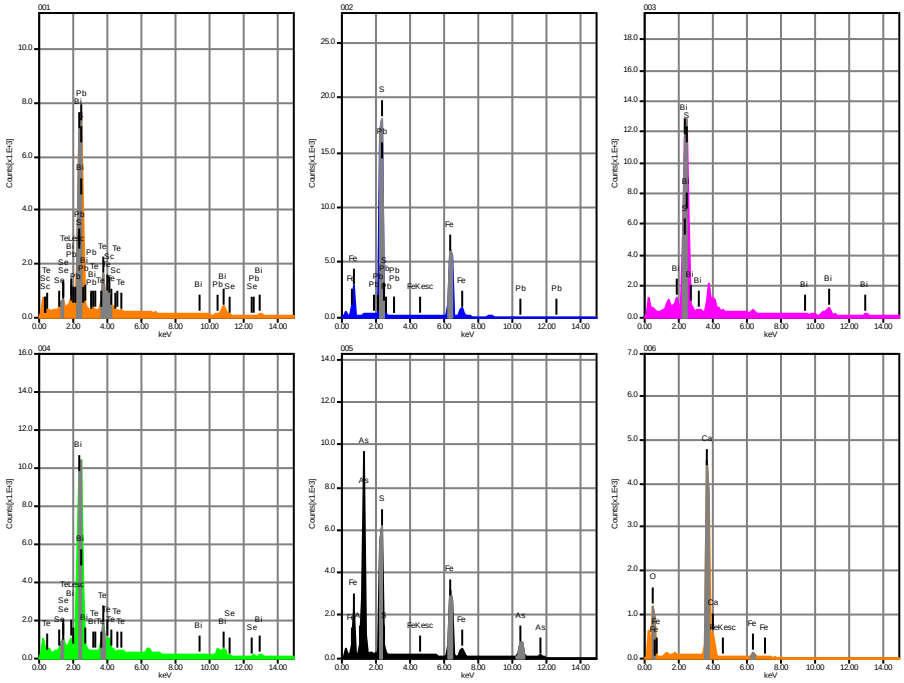

Acquisition Condition

Instrument : 6510(LA)

Volt : 20.00 kV

Current : ---

Process Time : T4

Live time : 5.34 sec.

Real Time : 7.43 sec.

DeadTime : 29.00 %

Count Rate : 20388.00 CPS

	Fe	O	Pb	S	Ca	Sc	As	Se	Te	Bi
001			6.80	4.79		1.02		2.09	20.97	64.33
002	52.18		9.62	38.20						
003				8.82						91.18
004								4.70	38.21	57.09
005	35.94			22.69			41.37			
006	3.59	53.65			42.76					
Average	30.57	53.65	8.21	18.62	42.76	1.02	41.37	3.39	29.59	70.87

Figure 9N Detailed

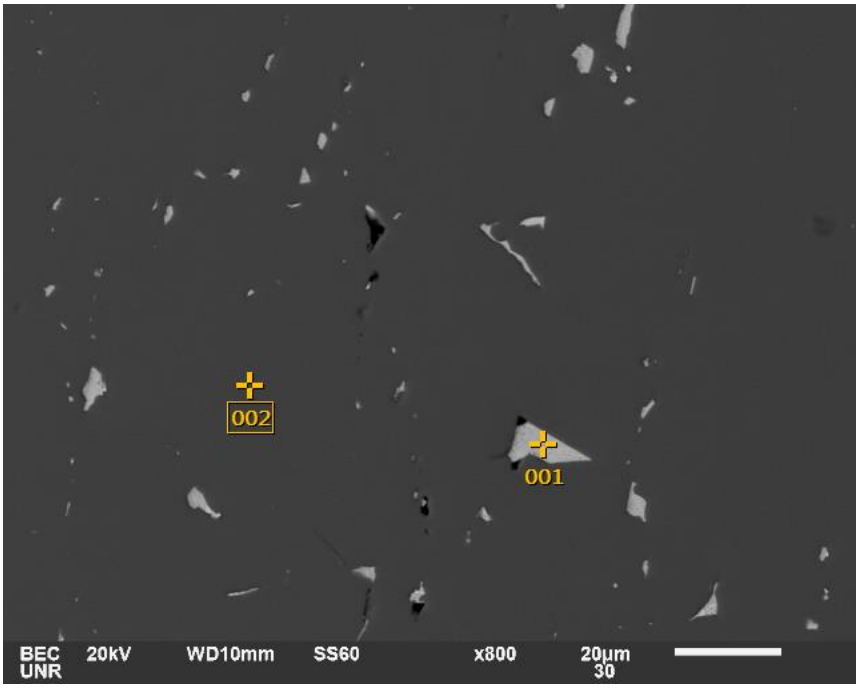

Volt : 20.00 kV

Mag. : x 800

Date : 2021/10/05

Pixel : 1280 x 960

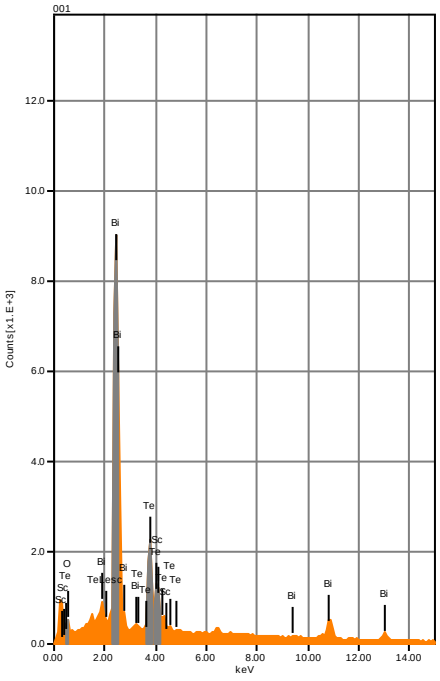

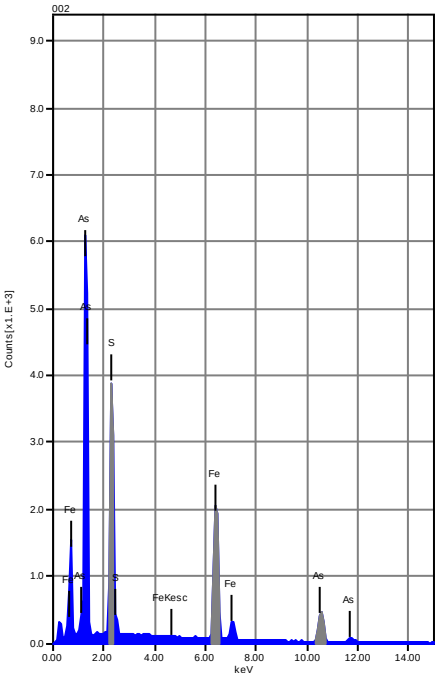

Acquisition Condition

Instrument : 6510(LA)

Volt : 20.00 kV

Current : ---

Process Time : T4

Live time : 6.69 sec.

Real Time : 12.35 sec.

DeadTime : 46.00 %

Count Rate : 36905.00 CPS

	Fe	O	S	Sc	As	Te	Bi		
001		0.96		1.01		26.25	71.78		
002	35.35		22.16		42.49				
Average	35.35	0.96	22.16	1.01	42.49	26.25	71.78		
Standard deviation			0.00	0.00	0.00	0.00	0.00	0.00	0.00

SEM-EDS data for Figure 9O

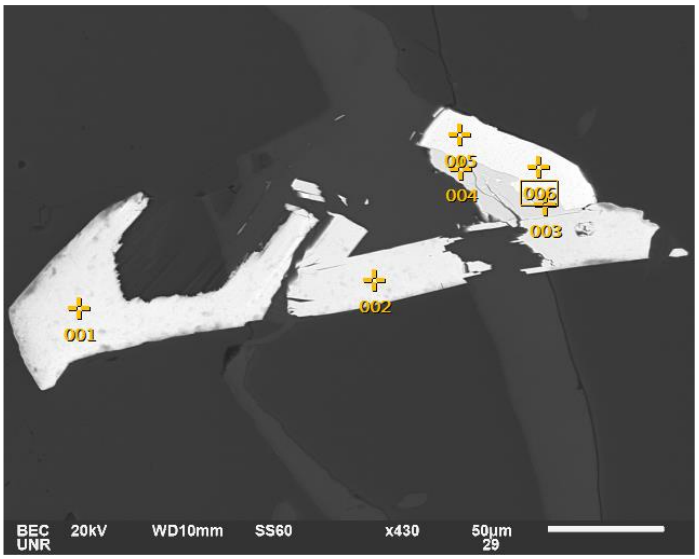

Volt : 20.00 kV

Mag. : x 430

Date : 2021/10/05

Pixel : 1280 x 960

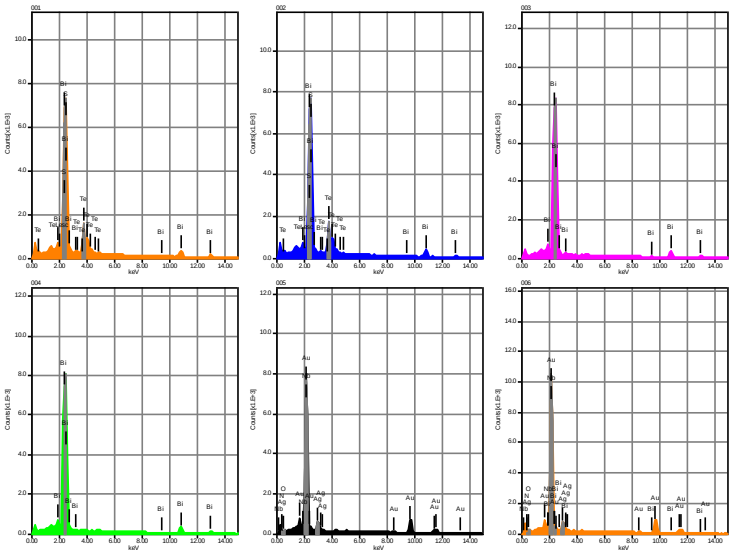

Acquisition Condition

Instrument : 6510(LA)

Volt : 20.00 kV

Current : ---

Process Time : T4

Live time : 8.68 sec.

Real Time : 20.86 sec.

DeadTime : 58.00 %

Count Rate : 50990.00 CPS

	O	Au	Ag	N	S	Nb	Te	Bi
001					6.17		24.63	69.20
002					5.96		25.71	68.33
003								100.00
004								100.00
005	1.48	80.15	6.83	4.06		7.47		
006	1.59	78.72	7.28	3.16		7.08		2.17
Average	1.54	79.44	7.06	3.61	6.06	7.27	25.17	67.94

APPENDIX B: U-Pb Geochronology

Diorite GS474027

PROJECT														
	Isotopic Ratios						Dates (Ma)							
	206Pb/		207Pb/		207Pb/		206Pb/	±2σ	207Pb/	±2σ	207Pb/	±2σ	Corr.	
Fraction	238U a	±2σ %	235U a	±2σ %	206Pb a	±2σ %	238U b	abs	235U b	abs	206Pb b	abs	coef.	% disc c
GS27::GS27														
z1	0.00625	4.6	0.0383	16	0.0444	15	40.2	1.9	38.1	6.1	-90	14	0.287	144.75
z2	0.00611	3.8	0.0390	11	0.0463	10	39.3	1.5	38.8	4.3	11.2	1.2	0.349	-249.59
z3	0.00608	4.4	0.0444	7.8	0.0529	6.5	39.1	1.7	44.1	3.4	325	21	0.557	87.97
z4	0.00633	3.7	0.0847	10	0.0971	9.5	40.7	1.5	82.6	8.5	1568	150	0.365	97.40
z5	0.00593	3.7	0.0443	7.5	0.0542	6.5	38.1	1.4	44.0	3.3	379	25	0.496	89.93
z6	0.00574	3.5	0.0409	10	0.0517	9.7	36.9	1.3	40.7	4.2	271	26	0.338	86.39
z7	0.00667	4.8	0.112	12	0.122	11	42.8	2.0	108	13	1983	220	0.394	97.84
z8	0.00594	3.9	0.0403	13	0.0492	12	38.2	1.5	40.1	5.1	155	19	0.308	75.33
z9	0.00606	3.2	0.0388	5.6	0.0465	4.6	39.0	1.2	38.7	2.2	22.0	1.0	0.564	-76.84
z10	0.00609	2.9	0.0406	5.8	0.0484	5.0	39.1	1.1	40.4	2.3	116.9	5.9	0.496	66.53
z11	0.00659	3.5	0.0867	11	0.0954	10	42.4	1.5	84.4	9.2	1536	160	0.326	97.24
z12	0.00635	4.8	0.083	16	0.095	15	40.8	2.0	81	13	1531	240	0.300	97.33
z13	0.00692	4.3	0.105	15	0.110	14	44.4	1.9	101	15	1792	250	0.296	97.52
z14	0.00625	3.8	0.085	15	0.099	15	40.2	1.5	83	13	1602	240	0.248	97.49
z15	0.00738	6.6	0.174	14	0.171	12	47.4	3.1	163	23	2565	310	0.476	98.15
z16	0.00622	3.5	0.0500	10	0.0583	9.3	40.0	1.4	49.5	4.9	541	51	0.351	92.61
z17	0.00648	8.0	0.079	16	0.089	14	41.6	3.3	77	12	1393	200	0.494	97.01
z18	0.00878	4.9	0.325	14	0.268	13	56.4	2.8	286	40	3296	430	0.349	98.29
z19	0.00609	3.5	0.0419	9.6	0.0499	8.9	39.1	1.4	41.6	4.0	190	17	0.363	79.43
z20	0.00598	3.0	0.0541	9.5	0.0656	9.0	38.4	1.2	53.5	5.1	794	71	0.322	95.16
z21	0.00604	3.1	0.0430	11	0.0516	10	38.8	1.2	42.7	4.6	269	28	0.288	85.57
z22	0.00688	3.9	0.123	15	0.130	14	44.2	1.7	118	17	2092	290	0.268	97.89
z23	0.00575	3.7	0.0437	15	0.0551	14	37.0	1.4	43.4	6.5	417	60	0.250	91.13
z24	0.00585	3.5	0.0386	8.7	0.0479	8.0	37.6	1.3	38.5	3.3	92.1	7.3	0.403	59.16
z25	0.00578	4.0	0.0484	11	0.0608	9.9	37.1	1.5	48.0	5.1	631	62	0.379	94.12
z26	0.00631	4.1	0.0553	14	0.0636	13	40.5	1.7	54.7	7.6	729	97	0.295	94.44
z27	0.0326	3.5	3.00	4.8	0.668	3.3	206.5	7.2	1407	68	4663	150	0.722	95.57
z28	0.00645	5.1	0.0765	12	0.0860	10	41.5	2.1	74.8	8.6	1338	140	0.445	96.90
z29	0.02495	3.1	0.1681	5.6	0.0489	4.7	158.8	4.9	157.8	8.9	141.6	6.6	0.554	-12.15
z30	0.01408	2.5	0.187	7.2	0.0966	6.7	90.1	2.2	174	13	1559	100	0.343	94.22
z31	0.00612	6.5	0.0443	11	0.0525	8.9	39.3	2.5	44.0	4.8	308	27	0.589	87.23
z32	0.00662	4.0	0.0637	9.4	0.0698	8.5	42.5	1.7	62.7	5.9	922	78	0.428	95.39
z33	0.00582	3.8	0.0475	10	0.0592	9.3	37.4	1.4	47.1	4.7	574	53	0.377	93.48
z34	0.00609	4.2	0.0406	15	0.0483	15	39.2	1.6	40.4	6.2	114	17	0.270	65.69
z35	0.00774	6.7	0.205	18	0.192	17	49.7	3.3	190	34	2762	460	0.372	98.20
z36	0.0250	4.5	0.166	7.0	0.0482	5.4	159.3	7.1	156	11	107.5	5.8	0.637	-48.15
z37	0.01060	6.1	0.110	19	0.075	18	68.0	4.2	106	20	1079	200	0.320	93.70
z38	0.00640	5.5	0.0442	15	0.0501	14	41.1	2.3	43.9	6.7	198	28	0.362	79.26
z39	0.00748	3.9	0.191	9.1	0.185	8.2	48.0	1.9	177	16	2698	220	0.424	98.22
z40	0.00604	2.9	0.0372	7.0	0.0446	6.4	38.8	1.1	37.1	2.6	-76.7	4.9	0.411	150.63

a <zirconPopulationChoice>

b Isotopic dates calculated using λ238 = 1.55125E-10 (Jaffey et al. 1971) and λ235 = 9.8485E-10 (Jaffey et al. 1971).

c % discordance = 100 - (100 * (206Pb/238U date) / (207Pb/206Pb date))

CL Map on zircons for Diorite GS474027

Hypabyssal Dacite Dike PYC21-002-975

PROJECT														
	Isotopic Ratios						Dates (Ma)							
	206Pb/		207Pb/		207Pb/		206Pb/	±2σ	207Pb/	±2σ	207Pb/	±2σ	Corr.	
Fraction	238U a	±2σ %	235U a	±2σ %	206Pb a	±2σ %	238U b	abs	235U b	abs	206Pb b	abs	coef.	% disc c
PYC21-2-975::PYC21-2-975														
z2	0.00594	4.0	0.0434	8.1	0.0530	7.0	38.2	1.5	43.1	3.5	-	-	0.492	-
z3	0.00591	2.7	0.0368	11	0.0451	10	38.0	1.0	36.7	3.9	-	-	0.254	-
z4	0.00638	3.8	0.0654	11	0.0744	11	41.0	1.6	64.3	7.3	-	-	0.335	-
z5	0.00628	3.0	0.0438	5.2	0.0506	4.2	40.3	1.2	43.5	2.2	-	-	0.572	-
z6	0.00618	2.6	0.0397	5.1	0.0466	4.4	39.7	1.0	39.5	2.0	-	-	0.516	-
z7	0.00613	2.4	0.0404	4.2	0.0479	3.4	39.36	0.95	40.3	1.7	-	-	0.576	-
z8	0.00689	4.6	0.0466	8.4	0.0490	7.1	44.3	2.0	46.2	3.9	-	-	0.544	-
z9	0.00631	3.3	0.0435	12	0.0500	11	40.6	1.4	43.2	5.1	-	-	0.285	-
z10	0.00614	3.6	0.0468	12	0.0553	12	39.5	1.4	46.5	5.7	-	-	0.292	-
z11	0.00617	3.2	0.0525	10	0.0617	9.6	39.7	1.3	52.0	5.3	-	-	0.318	-
z12	0.00620	2.1	0.0421	4.1	0.0492	3.5	39.86	0.86	41.8	1.7	-	-	0.522	-
z13	0.00659	3.6	0.0450	8.1	0.0496	7.3	42.3	1.5	44.7	3.6	-	-	0.439	-
z14	0.00613	5.9	0.0452	10	0.0536	8.2	39.4	2.3	44.9	4.5	-	-	0.582	-
z15	0.00627	3.6	0.0438	16	0.0507	15	40.3	1.4	43.5	6.8	-	-	0.227	-
z16	0.00634	3.2	0.0559	10	0.0641	9.8	40.7	1.3	55.3	5.7	-	-	0.315	-
z17	0.00620	5.3	0.0496	17	0.0581	16	39.8	2.1	49.2	8.4	-	-	0.306	-
z18	0.00622	2.8	0.0416	4.5	0.0485	3.6	39.9	1.1	41.3	1.9	-	-	0.614	-
z19	0.00610	2.4	0.0396	4.6	0.0471	3.9	39.22	0.94	39.5	1.8	-	-	0.524	-
z20	0.01494	4.0	0.1051	6.8	0.0510	5.5	95.6	3.8	101.5	6.9	-	-	0.585	-
z21	0.01428	2.4	0.0948	3.8	0.0482	2.9	91.4	2.2	92.0	3.5	-	-	0.641	-
z22	0.00634	3.5	0.0432	5.9	0.0495	4.7	40.8	1.4	43.0	2.5	-	-	0.598	-
z23	0.00640	2.7	0.0406	5.5	0.0460	4.8	41.2	1.1	40.4	2.2	-	-	0.482	-
z24	0.00612	2.4	0.0406	4.0	0.0481	3.2	39.34	0.96	40.4	1.6	-	-	0.605	-
z25	0.00609	2.6	0.0413	4.2	0.0492	3.3	39.1	1.0	41.1	1.7	-	-	0.622	-
z26	0.00638	3.5	0.0527	10	0.0600	9.6	41.0	1.4	52.2	5.4	-	-	0.342	-
z27	0.00625	4.7	0.050	20	0.058	20	40.2	1.9	49.3	9.9	-	-	0.233	-
z28	0.00651	4.2	0.0592	10	0.0660	9.6	41.8	1.8	58.4	6.1	-	-	0.401	-
z29	0.00643	7.5	0.055	21	0.062	19	41.3	3.1	55	11	-	-	0.359	-
z30	0.00577	3.2	0.0439	7.7	0.0553	7.1	37.1	1.2	43.7	3.4	-	-	0.411	-
z31	0.00616	2.3	0.0456	6.5	0.0537	6.1	39.58	0.91	45.3	3.0	-	-	0.354	-
z32	0.00631	3.2	0.0487	9.9	0.0560	9.4	40.5	1.3	48.3	4.8	-	-	0.325	-
z33	0.00597	2.1	0.0399	4.5	0.0485	4.0	38.36	0.80	39.7	1.8	-	-	0.462	-
z34	0.00644	2.5	0.0446	4.2	0.0503	3.4	41.4	1.1	44.3	1.9	-	-	0.600	-
z35	0.00617	2.6	0.0445	7.1	0.0523	6.6	39.6	1.0	44.2	3.1	-	-	0.360	-
z36	0.00625	4.2	0.0471	11	0.0547	11	40.2	1.7	46.8	5.3	-	-	0.370	-
z37	0.00634	4.4	0.0457	9.0	0.0523	7.8	40.7	1.8	45.3	4.1	-	-	0.495	-
z38	0.00634	2.6	0.0438	5.1	0.0501	4.3	40.7	1.1	43.5	2.2	-	-	0.519	-
z39	0.00626	3.9	0.0405	11	0.0469	10	40.2	1.6	40.3	4.3	-	-	0.363	-
z40	0.00613	4.7	0.0444	9.8	0.0525	8.6	39.4	1.8	44.1	4.3	-	-	0.477	-
z41	0.00619	2.3	0.0406	4.7	0.0476	4.1	39.77	0.93	40.4	1.9	-	-	0.494	-
z42	0.00618	4.0	0.0445	6.4	0.0522	4.9	39.7	1.6	44.2	2.8	-	-	0.633	-
z43	0.1787	2.7	1.823	4.0	0.0740	3.0	1060	28	1054	42	-	-	0.661	-
z44	0.1831	2.9	1.896	5.1	0.0751	4.2	1084	32	1080	55	-	-	0.575	-
z45	0.00640	3.2	0.0474	4.9	0.0538	3.7	41.1	1.3	47.0	2.3	-	-	0.657	-
z46	0.00615	3.3	0.0412	6.4	0.0486	5.5	39.5	1.3	41.0	2.6	-	-	0.522	-
z47	0.00612	2.5	0.0401	4.7	0.0475	4.0	39.36	0.96	39.9	1.9	-	-	0.520	-
z48	0.00632	4.8	0.0667	15	0.077	14	40.6	1.9	65.6	9.7	-	-	0.321	-
z49	0.00639	2.5	0.0570	5.1	0.0648	4.5	41.0	1.0	56.3	2.9	-	-	0.481	-
z50	0.00596	2.7	0.0397	4.3	0.0483	3.4	38.3	1.0	39.5	1.7	-	-	0.619	-

CL Map on zircons for Dacite Dike PYC21-002-975

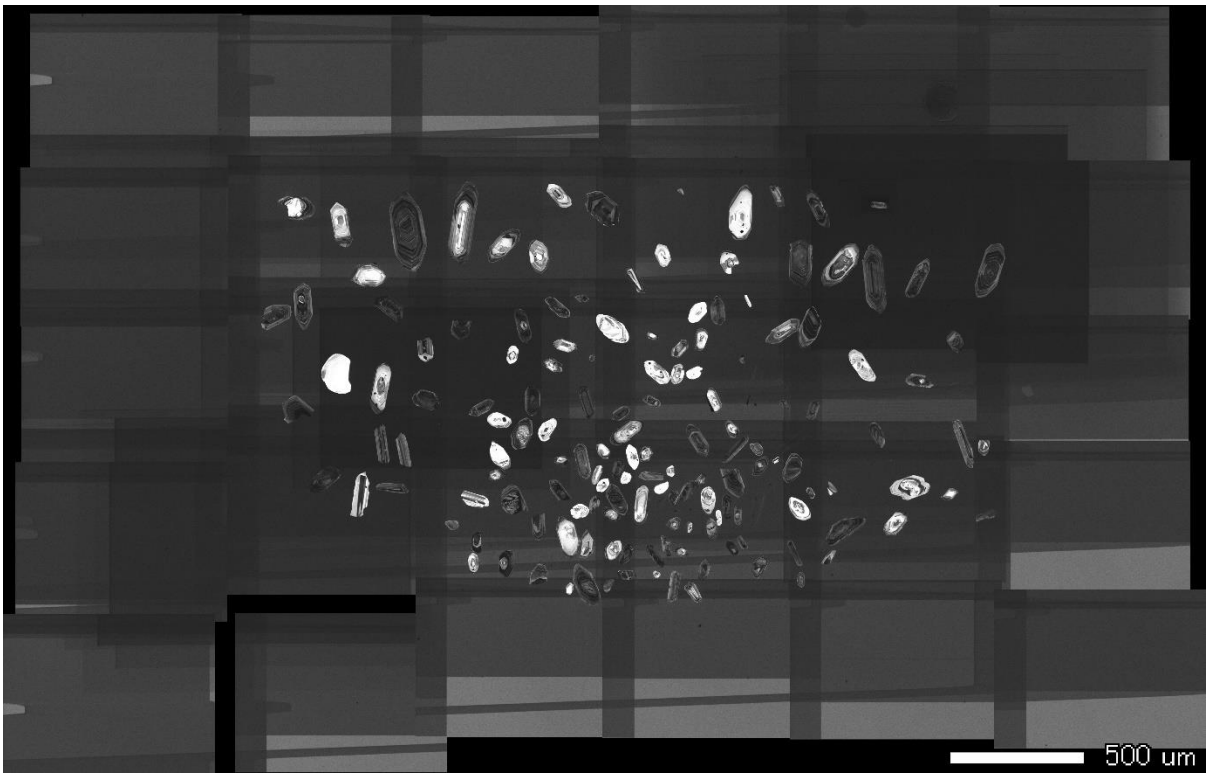

Granodiorite (medium grained) GPGT2020-009-573

PROJECT														
	Isotopic Ratios						Dates (Ma)							
	206Pb/		207Pb/		207Pb/		206Pb/	±2σ	207Pb/	±2σ	207Pb/	±2σ	Corr.	
Fraction	238U a	±2σ %	235U a	±2σ %	206Pb a	±2σ %	238U b	abs	235U b	abs	206Pb b	abs	coef.	% disc c
573::573														
z1	0.00641	7.9	0.0425	15	0.0481	13	41.2	3.2	42.2	6.4	101	13	0.517	59.34
z2	0.0223	10	0.195	14	0.0634	9.1	142	15	181	25	721	65	0.753	80.32
z3	0.01426	4.8	1.042	6.8	0.530	4.7	91.3	4.4	725	49	4327	00	0.716	97.89
z4	0.00853	7.1	0.336	11	0.286	7.9	54.7	3.9	294	31	3395	70	0.673	98.39
z5	0.00622	7.4	0.0424	17	0.0495	16	39.9	3.0	42.1	7.3	169	27	0.424	76.39
z6	0.0241	5.4	0.161	9.2	0.0485	7.5	153.8	8.2	152	14	121.2	9.1	0.583	-26.88
z7	0.00649	7.4	0.0483	17	0.0540	15	41.7	3.1	47.9	8.1	371	56	0.441	88.77
z8	0.00611	3.9	0.0388	13	0.0461	12	39.3	1.5	38.7	5.0	1.84	0.23	0.297	-2030.01
z9	0.00692	6.5	0.120	14	0.126	12	44.5	2.9	115	16	2039	50	0.465	97.82
z10	0.00629	4.9	0.0657	12	0.0757	11	40.4	2.0	64.6	7.5	1087	10	0.422	96.28
z11	0.00605	5.5	0.0482	12	0.0578	10	38.9	2.1	47.8	5.7	523	55	0.465	92.56
z12	0.00613	7.4	0.0403	16	0.0476	14	39.4	2.9	40.1	6.5	80	12	0.456	50.85
z13	0.00704	5.3	0.113	14	0.116	13	45.2	2.4	108	15	1896	50	0.379	97.61
z14	0.00614	6.7	0.0537	16	0.0635	15	39.4	2.6	53.1	8.7	726	10	0.408	94.57
z15	0.00855	5.1	0.129	10	0.1095	8.8	54.9	2.8	123	13	1789	60	0.499	96.93
z16	0.00609	5.4	0.0421	10	0.0502	8.7	39.2	2.1	41.9	4.3	201	18	0.530	80.56
z17	0.00714	6.3	0.176	15	0.179	14	45.9	2.9	165	25	2640	60	0.418	98.26
z18	0.00718	10	0.114	14	0.115	10	46.1	4.6	110	16	1885	90	0.702	97.55
z19	0.00619	5.6	0.047	22	0.055	22	39.8	2.2	46	10	396	86	0.250	89.95
z20	0.00675	5.6	0.0562	13	0.0604	12	43.4	2.4	55.5	7.3	617	73	0.427	92.97
z21	0.00853	8.3	0.372	12	0.316	9.0	54.8	4.5	321	39	3551	20	0.677	98.46
z22	0.00597	7.4	0.0440	18	0.0535	16	38.4	2.8	43.8	7.8	350	57	0.415	89.05
z23	0.00683	7.4	0.071	18	0.076	16	43.9	3.3	70	12	1088	70	0.421	95.96
z24	0.00601	5.9	0.0427	16	0.0516	15	38.6	2.3	42.5	6.8	267	40	0.369	85.53
z25	0.00848	4.1	0.346	6.9	0.296	5.5	54.4	2.3	302	21	3451	90	0.599	98.42
z26	0.00775	4.9	0.239	11	0.224	9.7	49.8	2.4	218	24	3007	90	0.450	98.34
z27	0.00718	3.9	0.259	8.4	0.262	7.4	46.1	1.8	234	20	3258	40	0.465	98.58
z28	0.00712	4.9	0.146	12	0.148	11	45.7	2.3	138	16	2326	50	0.416	98.03
z29	0.00674	3.8	0.174	8.5	0.187	7.6	43.3	1.6	163	14	2716	10	0.443	98.41
z30	0.00829	6.2	0.248	12	0.217	10	53.2	3.3	225	27	2960	10	0.511	98.20
z31	0.00647	9.0	0.051	23	0.057	21	41.6	3.7	50	12	491	00	0.389	91.52
z32	0.00614	4.6	0.0449	13	0.0530	12	39.5	1.8	44.6	5.7	329	39	0.360	87.99
z33	0.00654	6.4	0.0494	16	0.0548	15	42.0	2.7	48.9	8.0	404	61	0.389	89.60
z34	0.00631	4.9	0.0517	7.2	0.0594	5.4	40.6	2.0	51.1	3.7	579	31	0.673	92.99
z35	0.00626	5.3	0.0488	11	0.0566	9.8	40.2	2.2	48.4	5.4	475	46	0.480	91.53

a <zirconPopulationChoice>

b Isotopic dates calculated using λ238 = 1.55125E-10 (Jaffey et al. 1971) and λ235 = 9.8485E-10 (Jaffey et al. 1971).

c % discordance = 100 - (100 * (206Pb/238U date) / (207Pb/206Pb date))

CL Map for zircons in Granodiorite (medium grained) GPGT2020-009-573

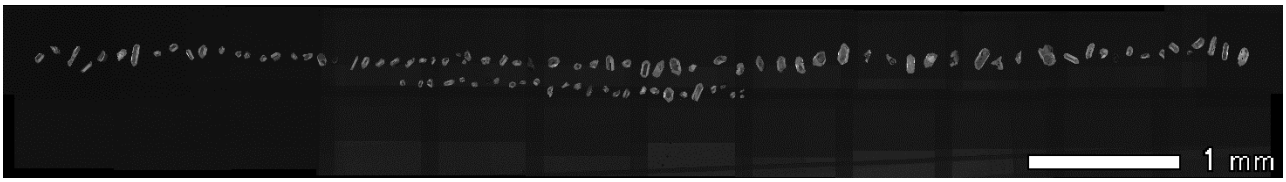

Granodiorite (coarse grained) GPGT2020-009-642

PROJECT															
	Isotopic Ratios						Dates (Ma)								
	206Pb/		207Pb/		207Pb/		206Pb/	±2σ	207Pb/	±2σ	207Pb/	±2σ	Corr.		
Fraction	238U a	±2σ %	235U a	±2σ %	206Pb a	±2σ %	238U b	abs	235U b	abs	206Pb b	abs	coef.	% disc c	
642::642															
Z1	0.0234	11	2.02	12	0.628	4.1	149	17	1124	140	4574	190	0.941	96.74	true
Z2	0.00660	6.4	0.050	23	0.055	22	42.4	2.7	49	11	396	86	0.284	89.30	true
Z3	0.01388	6.7	0.934	8.7	0.488	5.5	88.8	6.0	670	58	4206	230	0.774	97.89	true
Z4	0.00711	4.9	0.182	11	0.186	9.8	45.7	2.2	170	19	2706	260	0.449	98.31	true
Z5	0.00741	4.2	0.198	5.4	0.1942	3.5	47.6	2.0	184	10	2777	97	0.765	98.29	true
Z6	0.00626	4.2	0.0639	14	0.0740	13	40.2	1.7	62.9	8.6	1042	140	0.307	96.14	true
Z7	0.00633	6.4	0.0425	9.6	0.0487	7.1	40.7	2.6	42.2	4.0	130.1	9.3	0.669	68.73	true
Z8	0.00589	3.0	0.0402	4.9	0.0496	3.8	37.8	1.1	40.0	1.9	174.6	6.7	0.612	78.33	true
Z9	0.00885	5.1	0.407	9.0	0.334	7.4	56.8	2.9	347	31	3633	270	0.568	98.44	true
Z10	0.00617	4.0	0.0460	6.9	0.0540	5.6	39.7	1.6	45.6	3.2	370	21	0.584	89.28	true
Z11	0.00973	4.6	0.484	7.3	0.361	5.6	62.4	2.9	401	29	3753	210	0.636	98.34	true
Z12	0.00596	6.0	0.0391	8.6	0.0476	6.2	38.3	2.3	39.0	3.4	80.4	5.0	0.693	52.38	true
Z13	0.00625	3.2	0.0464	6.5	0.0538	5.7	40.2	1.3	46.0	3.0	362	21	0.497	88.91	true
Z14	0.00578	4.9	0.0410	12	0.0514	11	37.2	1.8	40.8	4.9	257	28	0.407	85.51	true
Z15	0.00747	3.8	0.193	7.2	0.187	6.1	47.9	1.8	179	13	2717	170	0.533	98.24	true
Z16	0.00977	9.9	0.431	17	0.320	14	62.6	6.2	364	61	3571	490	0.588	98.25	true
Z17	0.00649	6.1	0.0425	8.4	0.0475	5.7	41.7	2.6	42.3	3.5	73.9	4.2	0.733	43.50	true
Z18	0.00601	3.4	0.0394	5.5	0.0476	4.3	38.6	1.3	39.3	2.2	78.1	3.3	0.628	50.55	true
Z19	0.00966	5.9	0.503	7.6	0.378	4.8	62.0	3.7	413	31	3821	180	0.777	98.38	true
Z20	0.00631	3.9	0.0537	15	0.0617	14	40.5	1.6	53.1	7.8	664	95	0.267	93.90	true
Z21	0.00627	2.8	0.0458	6.4	0.0529	5.7	40.3	1.1	45.4	2.9	324	19	0.441	87.57	true
Z22	0.00725	7.3	0.142	16	0.142	15	46.6	3.4	135	22	2251	330	0.444	97.93	true
Z23	0.00636	6.9	0.075	18	0.086	17	40.8	2.8	73	14	1328	230	0.374	96.93	true
Z24	0.00730	3.4	0.214	6.6	0.213	5.7	46.9	1.6	197	13	2928	170	0.517	98.40	true
Z25	0.00594	5.8	0.067	20	0.082	19	38.2	2.2	66	13	1252	240	0.295	96.95	true
Z26	0.00594	2.8	0.0381	6.2	0.0465	5.5	38.2	1.1	38.0	2.4	24.2	1.3	0.457	-58.09	true
Z27	0.00630	6.2	0.0442	19	0.0509	18	40.5	2.5	43.9	8.5	235	43	0.319	82.81	true
Z28	0.00781	4.4	0.202	13	0.188	13	50.1	2.2	187	25	2722	340	0.326	98.16	true
Z29	0.00603	4.0	0.0483	12	0.0580	11	38.8	1.6	47.8	5.7	529	59	0.341	92.67	true
Z30	0.00599	8.3	0.064	19	0.077	17	38.5	3.2	63	12	1120	190	0.443	96.56	true
Z31	0.00624	5.3	0.0613	11	0.0713	10	40.1	2.1	60.4	6.8	964	97	0.467	95.84	true
Z32	0.00614	6.7	0.0456	10	0.0538	7.9	39.5	2.6	45.2	4.7	363	29	0.648	89.14	true
Z33	0.00614	4.3	0.0427	6.7	0.0505	5.2	39.5	1.7	42.5	2.9	216	11	0.645	81.75	true
Z34	0.00932	6.0	0.464	8.8	0.361	6.4	59.8	3.6	387	34	3753	240	0.687	98.41	true
Z35	0.00747	4.2	0.169	10	0.164	9.1	48.0	2.0	159	16	2500	230	0.419	98.08	true
Z36	0.00629	4.7	0.0593	11	0.0684	10	40.4	1.9	58.5	6.5	881	88	0.424	95.41	true
Z37	0.00619	3.4	0.0425	7.9	0.0498	7.1	39.8	1.3	42.2	3.3	183	13	0.428	78.21	true
Z38	0.00628	3.5	0.0418	12	0.0483	11	40.4	1.4	41.6	4.9	114	13	0.295	64.58	true
Z39	0.00628	7.5	0.033	38	0.038	37	40.4	3.0	33	13	-483	180	0.198	108.37	false
Z40	0.00619	3.6	0.0413	7.0	0.0483	6.0	39.8	1.4	41.1	2.9	115.2	6.9	0.510	65.45	true

a <zirconPopulationChoice>

b Isotopic dates calculated using λ238 = 1.55125E-10 (Jaffey et al. 1971) and λ235 = 9.8485E-10 (Jaffey et al. 1971).

c % discordance = 100 - (100 * (206Pb/238U date) / (207Pb/206Pb date))

CL Map for zircons in Granodiorite (coarse grained) GPGT2020-009-642

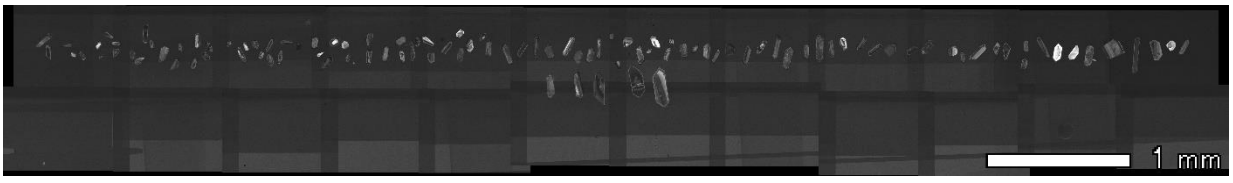

Granitic Porphyry Dike PYC21-004-127

PROJECT														
	Isotopic Ratios						Dates (Ma)							
Fraction	206Pb/ 238U a	±2σ %	207Pb/ 235U a	±2σ %	207Pb/ 206Pb a	±2σ %	206Pb/ 238U b	±2σ abs	207Pb/ 235U b	±2σ abs	207Pb/ 206Pb b	±2σ abs	Corr. coef.	% disc c
Porphry::Porphry														
z1-1	0.00597	3.6	0.0423	6.3	0.0513	5.2	38.4	1.4	42.0	2.7	-	-	0.561	-
z2-2	0.00635	2.8	0.0431	12	0.0492	11	40.8	1.1	42.8	5.0	-	-	0.240	-
z3-3	0.00601	6.9	0.072	19	0.087	18	38.7	2.7	71	14	-	-	0.359	-
z4-4	0.00604	5.8	0.0400	12	0.0480	10	38.8	2.2	39.8	4.7	-	-	0.489	-
z6-6	0.00725	13	0.114	35	0.114	33	46.6	6.0	110	38	-	-	0.366	-
z7-7	0.00653	4.9	0.0491	18	0.0546	17	41.9	2.0	48.7	8.8	-	-	0.267	-
z8-8	0.00618	3.4	0.0465	9.7	0.0545	9.1	39.7	1.3	46.1	4.5	-	-	0.350	-
z9-9	0.00606	9.2	0.044	24	0.052	22	38.9	3.6	43	10	-	-	0.392	-
z10-10	0.00587	3.8	0.0422	5.9	0.0521	4.5	37.7	1.4	41.9	2.5	-	-	0.642	-
z11-11	0.00616	2.6	0.0459	5.8	0.0540	5.2	39.6	1.0	45.5	2.6	-	-	0.442	-
z12-12	0.00574	4.0	0.0537	12	0.0680	11	36.9	1.5	53.1	6.2	-	-	0.344	-
z13-13	0.00601	3.8	0.0770	12	0.093	12	38.6	1.5	75.3	9.3	-	-	0.306	-
z14-14	0.00589	3.2	0.0427	11	0.0526	10	37.9	1.2	42.5	4.5	-	-	0.302	-
z15-15	0.00600	3.6	0.0481	11	0.0582	11	38.6	1.4	47.7	5.4	-	-	0.322	-
z16-16	0.00613	4.8	0.0479	16	0.0566	16	39.4	1.9	47.5	7.7	-	-	0.294	-
z17-17	0.00615	3.4	0.0464	11	0.0548	11	39.5	1.3	46.1	5.1	-	-	0.304	-
z18-18	0.00593	5.4	0.0367	16	0.0448	15	38.1	2.1	36.6	5.9	-	-	0.333	-
z19-19	0.00664	11	0.059	24	0.065	22	42.7	4.7	58	14	-	-	0.451	-
z20-20	0.00599	4.0	0.0423	17	0.0513	16	38.5	1.6	42.1	7.0	-	-	0.241	-
z21-21	0.00615	3.2	0.0440	9.7	0.0519	9.1	39.5	1.3	43.7	4.2	-	-	0.333	-
z22-22	0.00637	4.6	0.0464	11	0.0528	10	40.9	1.9	46.1	5.1	-	-	0.408	-
z23-23	0.00598	4.1	0.0403	7.7	0.0490	6.5	38.4	1.6	40.2	3.1	-	-	0.536	-
z24-24	0.00618	4.0	0.0466	7.5	0.0548	6.3	39.7	1.6	46.3	3.5	-	-	0.536	-
z25-25	0.00595	6.4	0.076	24	0.093	23	38.2	2.5	75	18	-	-	0.273	-
z26-26	0.01619	4.6	0.129	9.2	0.0577	7.9	103.6	4.8	123	11	-	-	0.503	-
z27-27	0.00606	4.4	0.0371	12	0.0444	11	39.0	1.7	37.0	4.5	-	-	0.362	-
z28-28	0.00628	4.3	0.0419	11	0.0484	9.8	40.4	1.8	41.7	4.5	-	-	0.405	-
z29-29	0.00611	5.0	0.0415	12	0.0493	11	39.3	2.0	41.3	4.9	-	-	0.428	-
z30-30	0.00613	5.9	0.0481	14	0.0570	13	39.4	2.3	47.7	6.7	-	-	0.422	-
z31-31	0.00604	10	0.058	18	0.069	15	38.8	4.0	57	10	-	-	0.571	-
z32-32	0.00632	4.5	0.0779	11	0.0895	10	40.6	1.8	76.2	8.5	-	-	0.401	-
z33-33	0.00637	3.5	0.059	18	0.067	18	40.9	1.4	58	11	-	-	0.192	-
z34-34	0.00629	4.0	0.0509	16	0.0587	16	40.4	1.6	50.5	8.3	-	-	0.242	-
z35-35	0.00605	5.3	0.0430	9.6	0.0516	8.0	38.9	2.0	42.8	4.1	-	-	0.551	-
z36-36	0.00622	8.5	0.076	23	0.089	21	40.0	3.4	74	17	-	-	0.370	-
z37-37	0.00585	6.4	0.0445	12	0.0552	9.7	37.6	2.4	44.2	5.2	-	-	0.550	-
z38-38	0.00589	4.1	0.0418	12	0.0515	12	37.9	1.5	41.6	5.1	-	-	0.329	-
z39-39	0.00611	9.9	0.047	27	0.055	25	39.2	3.9	46	12	-	-	0.371	-
z40-40	0.0092	13	0.359	27	0.282	24	59.1	7.9	311	85	-	-	0.488	-
z41-41	0.00600	6.0	0.048	27	0.057	26	38.6	2.3	47	13	-	-	0.224	-
z42-42	0.00575	2.9	0.0430	8.0	0.0543	7.5	36.9	1.1	42.7	3.4	-	-	0.357	-

CL Map for zircons in Granitic Porphyry Dike PYC21-004-127

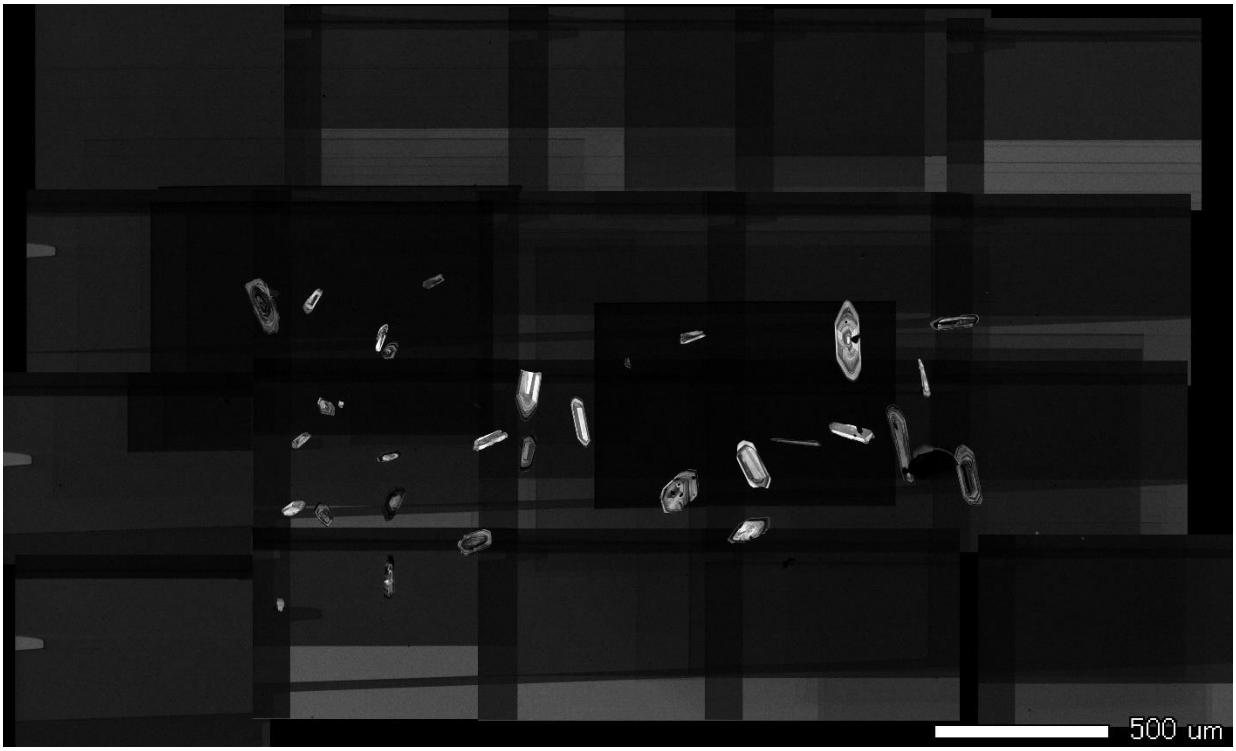

Subvolcanic Rhyolite Dike GS474016

PROJECT															
	Isotopic Ratios						Dates (Ma)								
Fraction	206Pb/ 238U a	±2σ %	207Pb/ 235U a	±2σ %	207Pb/ 206Pb a	±2σ %	206Pb/ 238U b	±2σ abs	207Pb/ 235U b	±2σ abs	207Pb/ 206Pb b	±2σ abs	Corr. coef.	% disc c	
GS16::GS16															
z1	0.00636	3.6	0.1220	5.5	0.1391	4.2	40.9	1.5	116.9	6.5	2216	94	0.644	98.15	true
z2	0.00544	2.1	0.0353	5.0	0.0471	4.6	34.96	0.75	35.2	1.8	53.6	2.4	0.425	34.75	true
z3	0.00594	6.7	0.087	12	0.106	9.7	38.2	2.6	85	10	1738	170	0.570	97.80	true
z4	0.00798	4.0	0.348	6.6	0.316	5.2	51.2	2.0	303	20	3550	190	0.606	98.56	true
z5	0.00551	2.5	0.0363	6.3	0.0478	5.8	35.42	0.87	36.2	2.3	88.9	5.2	0.390	60.17	true
z6	0.00557	3.2	0.0381	6.0	0.0496	5.1	35.8	1.2	38.0	2.3	176.3	9.0	0.532	79.69	true
z7	0.00541	2.6	0.0395	5.9	0.0530	5.3	34.79	0.90	39.4	2.3	327	17	0.440	89.36	true
z8	0.00535	2.2	0.0353	5.8	0.0478	5.4	34.38	0.75	35.2	2.0	90.1	4.8	0.379	61.86	true
z9	0.00686	8.3	0.209	16	0.221	13	44.1	3.7	192	30	2984	400	0.531	98.52	true
z10	0.00599	2.8	0.0759	9.5	0.0920	9.1	38.5	1.1	74.3	7.1	1466	130	0.294	97.37	true
z11	0.00581	2.3	0.0797	6.3	0.0995	5.9	37.36	0.85	77.9	4.9	1614	95	0.362	97.69	true
z12	0.0273	4.6	2.68	5.0	0.711	2.0	173.8	8.0	1322	66	4752	95	0.917	96.34	true
z13	0.02695	3.3	2.605	3.6	0.701	1.5	171.4	5.6	1302	47	4733	73	0.905	96.38	true
z14	0.00619	4.2	0.088	18	0.103	17	39.8	1.7	86	15	1678	290	0.234	97.63	true
z16	0.00855	4.6	0.427	6.6	0.363	4.7	54.9	2.5	361	24	3760	180	0.704	98.54	true
z17	0.00864	5.6	0.432	10	0.363	8.6	55.5	3.1	364	38	3760	320	0.548	98.52	true
z18	0.00748	8.2	0.254	9.9	0.246	5.4	48.0	4.0	230	23	3160	170	0.834	98.48	true
z19	0.00749	5.2	0.302	7.1	0.292	4.8	48.1	2.5	268	19	3429	170	0.731	98.60	true
z20	0.00596	2.8	0.0880	8.3	0.1071	7.8	38.3	1.1	85.7	7.1	1750	140	0.333	97.81	true
z21	0.00754	5.0	0.271	9.9	0.261	8.5	48.4	2.4	244	24	3250	280	0.507	98.51	true
z22	0.00667	3.1	0.186	9.3	0.203	8.8	42.8	1.3	173	16	2848	250	0.331	98.50	true
z23	0.00604	4.0	0.0914	9.8	0.1099	8.9	38.8	1.6	88.8	8.7	1796	160	0.411	97.84	true
z24	0.00658	2.9	0.1692	4.9	0.1867	3.9	42.3	1.2	158.7	7.7	2712	110	0.599	98.44	true
z25	0.00596	2.9	0.0414	6.4	0.0504	5.7	38.3	1.1	41.2	2.6	211	12	0.456	81.81	true
z26	0.00673	4.0	0.189	11	0.204	10	43.2	1.7	176	19	2856	290	0.363	98.49	true
z27	0.00687	6.4	0.239	16	0.253	15	44.1	2.8	218	35	3200	470	0.400	98.62	true
z28	0.00746	4.2	0.280	7.0	0.273	5.6	47.9	2.0	251	17	3321	180	0.602	98.56	true
z29	0.00666	3.1	0.197	6.8	0.214	6.0	42.8	1.3	182	12	2937	180	0.464	98.54	true
z30	0.00556	2.3	0.0365	5.9	0.0477	5.5	35.74	0.80	36.4	2.2	82.0	4.5	0.380	56.40	true
z31	0.01116	7.1	0.722	8.8	0.469	5.2	71.6	5.1	552	49	4147	220	0.804	98.27	true
z32	0.00788	3.3	0.355	5.0	0.327	3.8	50.6	1.7	309	16	3603	140	0.650	98.59	true
z33	0.00575	7.7	0.0526	12	0.0664	8.6	36.9	2.9	52.0	6.0	817	70	0.668	95.48	true
z34	0.0209	4.9	1.83	5.6	0.634	2.8	133.3	6.5	1055	59	4588	130	0.870	97.09	true
z35	0.00565	3.5	0.0691	9.8	0.0887	9.2	36.3	1.3	67.8	6.7	1397	130	0.357	97.40	true
z36	0.00550	5.2	0.0509	13	0.0672	12	35.4	1.8	50.4	6.8	842	100	0.388	95.80	true
z37	0.0153	6.6	1.121	8.3	0.531	5.0	97.9	6.5	763	63	4330	220	0.801	97.74	true
z38	0.00725	4.3	0.269	8.1	0.269	6.9	46.6	2.0	242	20	3298	230	0.528	98.59	true
z39	0.00567	2.5	0.0668	7.7	0.0855	7.2	36.42	0.91	65.6	5.0	1326	96	0.326	97.25	true
z40	0.00619	4.5	0.0640	15	0.075	15	39.8	1.8	63.0	9.7	1069	160	0.290	96.28	true
z41	0.00913	6.3	0.494	8.8	0.393	6.2	58.6	3.7	408	36	3882	240	0.707	98.49	true
z42	0.0295	7.0	2.86	8.0	0.704	3.9	187	13	1372	110	4738	190	0.870	96.04	true

a <zirconPopulationChoice>

b Isotopic dates calculated using λ238 = 1.55125E-10 (Jaffey et al. 1971) and λ235 = 9.8485E-10 (Jaffey et al. 1971).

c % discordance = 100 - (100 * (206Pb/238U date) / (207Pb/206Pb date))

CL Map for zircons in Subvolcanic Rhyolite Dike GS474016

APPENDIX C: ^{40}Ar-^{39}Ar Geochronology

PYC21-4-452

Table 1. $^{40}Ar/^{39}Ar$ analytical data.

	ID	Power (Watts)	$^{40}Ar/^{39}Ar$	$^{37}Ar/^{39}Ar$	$^{36}Ar/^{39}Ar$ (x 10^{-3})	$^{39}Ar_K$ (x 10^{-15} mol)	K/Ca	$^{40}Ar^*$ (%)	^{39}Ar (%)	Age (Ma)	±1σ (Ma)
	PYCZI-4-452, K-Feldspar, 0.7 mg, J=0.0054385±0.02%, IC=1.006364±0.0010576, NM-322N, Lab#=69499-01, Argus VI										
X	A	0.15	6.826	0.0117	9.747	2.30	43.4	57.8	2.4	38.83	0.12
X	E	0.22	4.410	0.0065	1.567	0.794	78.5	89.5	3.2	38.80	0.12
X	F	0.24	4.214	0.0182	0.9151	1.001	28.0	93.6	4.3	38.784	0.089
X	G	0.26	4.269	0.0095	1.097	1.38	53.7	92.4	5.7	38.786	0.070
X	H	0.28	4.154	0.0154	0.6726	1.71	33.1	95.2	7.5	38.885	0.053
X	I	0.30	4.181	0.0084	0.8063	2.04	60.6	94.3	9.6	38.764	0.054
X	J	0.32	4.081	0.0061	0.4464	2.25	83.6	96.8	12.0	38.820	0.043
X	K	0.34	4.121	0.0036	0.5528	2.95	142.4	96.0	15.0	38.904	0.034
X	L	0.36	4.099	0.0040	0.4800	3.64	126.1	96.5	18.8	38.898	0.031
X	M	0.50	4.142	0.0030	0.6171	17.6	169.7	95.6	37.1	38.919	0.012
X	N	0.75	4.184	0.0033	0.7450	32.7	152.8	94.7	71.1	38.965	0.011
X	O	3.00	4.216	0.0020	0.7897	27.8	259.5	94.5	100.0	39.145	0.011
	Integrated age ± 1σ			n=12		96.2	135.1		K2O=9.70%	38.986	0.0116
	No Plateau										

Notes:

Isotopic ratios corrected for blank, radioactive decay, and mass discrimination, not corrected for interfering reactions.
Errors quoted for individual analyses include analytical error only, without interfering reaction or J uncertainties.
Integrated age calculated by summing isotopic measurements of all steps.
Integrated age error calculated by quadratically combining errors of isotopic measurements of all steps.
Plateau age is inverse-variance-weighted mean of selected steps.
Plateau age error is inverse-variance-weighted mean error (Taylor, 1982) times root MSWD where MSWD>1.
Plateau error is weighted error of Taylor (1982).
Isotopic abundances after Steiger and Jäger (1977).
X preceding sample ID denotes analyses excluded from plateau age calculations.
Weight percent K_2O calculated from ^{39}Ar signal, sample weight, and instrument sensitivity.
Ages calculated relative to FC-2 Fish Canyon Tuff sanidine interlaboratory standard at 28.201 Ma
Decay Constant (LambdaK (total)) = 5.463e-10/a
Correction factors:

$(^{39}Ar/^{37}Ar)_{Ca}$ = 0.000697 ± 0.000002
$(^{36}Ar/^{37}Ar)_{Ca}$ = 0.0002802 ± 0.0000020
$(^{38}Ar/^{39}Ar)_{K}$ = 0.01244 ± 0.00001
$(^{40}Ar/^{39}Ar)_{K}$ = 0.00844 ± 0.00017

APPENDIX D: Geochemistry (multi-element geochemical suite, see methods)

Correlation Matrices

Altenburg Hill Spearman (27 Holes)

[Visible]

Spearman - 2193 ro...	Au_ppm	Ag_ppm	As_ppm	Bi_ppm	Cu_ppm	Hg_ppm	Mo_ppm	Pb_ppm	Sb_ppm	Se_ppm	Sn_ppm	Te_ppm	W_ppm	Zn_ppm
Au_ppm	1	0.14	0.035	0.27	0.34	0.063	-0.019	-0.17	0.011	0.15	-0.08	0.4	0.38	-0.13
Ag_ppm	0.14	1	0.56	0.51	0.54	0.073	0.031	0.34	0.51	0.28	0.43	0.35	0.16	0.56
As_ppm	0.035	0.56	1	0.64	0.41	0.14	-0.025	0.35	0.77	0.32	0.54	0.43	0.22	0.52
Bi_ppm	0.27	0.51	0.64	1	0.57	0.2	0.033	0.11	0.6	0.36	0.43	0.84	0.31	0.26
Cu_ppm	0.34	0.54	0.41	0.57	1	0.24	0.22	-0.11	0.31	0.4	0.11	0.61	0.091	0.12
Hg_ppm	0.063	0.073	0.14	0.2	0.24	1	0.34	-0.099	0.085	0.26	-0.08	0.18	0.028	0.0059
Mo_ppm	-0.019	0.031	-0.025	0.033	0.22	0.34	1	-0.072	-0.055	0.43	-0.15	0.022	-0.19	-0.048
Pb_ppm	-0.17	0.34	0.35	0.11	-0.11	-0.099	-0.072	1	0.37	0.044	0.47	-0.081	-0.019	0.8
Sb_ppm	0.011	0.51	0.77	0.6	0.31	0.085	-0.055	0.37	1	0.22	0.63	0.44	0.24	0.52
Se_ppm	0.15	0.28	0.32	0.36	0.4	0.26	0.43	0.044	0.22	1	0.017	0.3	0.11	0.13
Sn_ppm	-0.08	0.43	0.54	0.43	0.11	-0.08	-0.15	0.47	0.63	0.017	1	0.23	0.073	0.57
Te_ppm	0.4	0.35	0.43	0.84	0.61	0.18	0.022	-0.081	0.44	0.3	0.23	1	0.33	0.043
W_ppm	0.38	0.16	0.22	0.31	0.091	0.028	-0.19	-0.019	0.24	0.11	0.073	0.33	1	-0.053
Zn_ppm	-0.13	0.56	0.52	0.26	0.12	0.0059	-0.048	0.8	0.52	0.13	0.57	0.043	-0.053	1

Porphyry Spearman (44 Holes)

[Visible]

Spearman - 4995 ro...	Au_ppm	Ag_ppm	As_ppm	Bi_ppm	Cu_ppm	Hg_ppm	Mo_ppm	Pb_ppm	Sb_ppm	Se_ppm	Sn_ppm	Te_ppm	W_ppm	Zn_ppm
Au_ppm	1	0.34	0.055	0.53	0.6	0.13	0.046	0.0065	0.028	0.054	0.24	0.67	0.36	-0.011
Ag_ppm	0.34	1	0.38	0.43	0.52	0.3	0.14	0.4	0.37	0.25	0.42	0.42	0.38	0.49
As_ppm	0.055	0.38	1	0.31	0.28	0.45	0.3	0.11	0.58	0.33	0.17	0.19	0.35	0.29
Bi_ppm	0.53	0.43	0.31	1	0.7	0.1	0.034	-0.071	0.23	0.26	0.44	0.84	0.29	0.037
Cu_ppm	0.6	0.52	0.28	0.7	1	0.1	0.088	-0.17	0.17	0.3	0.47	0.71	0.29	0.067
Hg_ppm	0.13	0.3	0.45	0.1	0.1	1	0.24	0.2	0.47	0.16	0.14	0.073	0.41	0.28
Mo_ppm	0.046	0.14	0.3	0.034	0.088	0.24	1	0.073	0.23	0.48	-0.089	-0.037	0.11	0.068
Pb_ppm	0.0065	0.4	0.11	-0.071	-0.17	0.2	0.073	1	0.2	-0.067	0.099	-0.046	0.15	0.57
Sb_ppm	0.028	0.37	0.58	0.23	0.17	0.47	0.23	0.2	1	0.31	0.4	0.097	0.15	0.43
Se_ppm	0.054	0.25	0.33	0.26	0.3	0.16	0.48	-0.067	0.31	1	0.17	0.14	0.12	0.15
Sn_ppm	0.24	0.42	0.17	0.44	0.47	0.14	-0.089	0.099	0.4	0.17	1	0.37	0.019	0.35
Te_ppm	0.67	0.42	0.19	0.84	0.71	0.073	-0.037	-0.046	0.097	0.14	0.37	1	0.35	-0.0043
W_ppm	0.36	0.38	0.35	0.29	0.29	0.41	0.11	0.15	0.15	0.12	0.019	0.35	1	0.11
Zn_ppm	-0.011	0.49	0.29	0.037	0.067	0.28	0.068	0.57	0.43	0.15	0.35	-0.0043	0.11	1

GoldPan Spearman (72 holes)

[Visible]

Spearman - 11704 r...	Au_ppm	Ag_ppm	As_ppm	Bi_ppm	Cu_ppm	Hg_ppm	Mo_ppm	Pb_ppm	Sb_ppm	Se_ppm	Sn_ppm	Te_ppm	W_ppm	Zn_ppm
Au_ppm	1	0.27	0.25	0.39	0.36	0.065	-0.011	0.034	0.16	0.2	0.099	0.46	0.21	0.0093
Ag_ppm	0.27	1	0.48	0.47	0.53	0.28	0.092	0.45	0.52	0.25	0.43	0.35	0.43	0.42
As_ppm	0.25	0.48	1	0.27	0.17	0.18	0.046	0.47	0.49	0.14	0.38	0.23	0.23	0.36
Bi_ppm	0.39	0.47	0.27	1	0.53	0.027	-0.049	0.14	0.11	0.37	0.42	0.8	0.17	0.25
Cu_ppm	0.36	0.53	0.17	0.53	1	0.034	-0.032	-0.056	0.18	0.6	0.29	0.59	0.22	0.15
Hg_ppm	0.065	0.28	0.18	0.027	0.034	1	0.13	0.16	0.51	0.1	0.14	-0.012	0.36	0.12
Mo_ppm	-0.011	0.092	0.046	-0.049	-0.032	0.13	1	0.13	0.21	0.12	-0.16	-0.053	0.2	0.031
Pb_ppm	0.034	0.45	0.47	0.14	-0.056	0.16	0.13	1	0.33	-0.19	0.46	-0.078	0.15	0.51
Sb_ppm	0.16	0.52	0.49	0.11	0.18	0.51	0.21	0.33	1	0.2	0.19	0.056	0.29	0.26
Se_ppm	0.2	0.25	0.14	0.37	0.6	0.1	0.12	-0.19	0.2	1	0.19	0.53	0.11	0.17
Sn_ppm	0.099	0.43	0.38	0.42	0.29	0.14	-0.16	0.46	0.19	0.19	1	0.25	0.15	0.58
Te_ppm	0.46	0.35	0.23	0.8	0.59	-0.012	-0.053	-0.078	0.056	0.53	0.25	1	0.15	0.11
W_ppm	0.21	0.43	0.23	0.17	0.22	0.36	0.2	0.15	0.29	0.11	0.15	0.15	1	0.09
Zn_ppm	0.0093	0.42	0.36	0.25	0.15	0.12	0.031	0.51	0.26	0.17	0.58	0.11	0.09	1

Distal Spearman (4 holes)

[Visible]

Spearman - 1125 ro...	Au_ppm	Ag_ppm	As_ppm	Bi_ppm	Cu_ppm	Hg_ppm	Mo_ppm	Pb_ppm	Sb_ppm	Se_ppm	Sn_ppm	Te_ppm	W_ppm	Zn_ppm
Au_ppm	1	0.32	0.66	0.61	0.51	0.39	-0.046	0.24	0.43	0.41	0.17	0.69	0.35	-0.11
Ag_ppm	0.32	1	0.34	0.33	0.48	0.24	0.42	0.45	0.59	0.57	0.047	0.34	0.32	0.39
As_ppm	0.66	0.34	1	0.8	0.33	0.38	-0.083	0.14	0.41	0.41	0.28	0.74	0.58	-0.24
Bi_ppm	0.61	0.33	0.8	1	0.37	0.31	-0.047	0.13	0.31	0.46	0.27	0.78	0.52	-0.28
Cu_ppm	0.51	0.48	0.33	0.37	1	0.23	0.095	0.45	0.41	0.49	0.18	0.44	0.15	0.19
Hg_ppm	0.39	0.24	0.38	0.31	0.23	1	-0.24	-0.0046	0.42	0.13	0.14	0.27	0.5	-0.066
Mo_ppm	-0.046	0.42	-0.083	-0.047	0.095	-0.24	1	0.13	0.24	0.39	-0.47	0.091	-0.1	0.29
Pb_ppm	0.24	0.45	0.14	0.13	0.45	-0.0046	0.13	1	0.41	0.26	0.36	0.25	-0.0043	0.42
Sb_ppm	0.43	0.59	0.41	0.31	0.41	0.42	0.24	0.41	1	0.34	0.12	0.42	0.42	0.18
Se_ppm	0.41	0.57	0.41	0.46	0.49	0.13	0.39	0.26	0.34	1	-0.064	0.49	0.16	0.26
Sn_ppm	0.17	0.047	0.28	0.27	0.18	0.14	-0.47	0.36	0.12	-0.064	1	0.14	0.23	0.054
Te_ppm	0.69	0.34	0.74	0.78	0.44	0.27	0.091	0.25	0.42	0.49	0.14	1	0.37	-0.15
W_ppm	0.35	0.32	0.58	0.52	0.15	0.5	-0.1	-0.0043	0.42	0.16	0.23	0.37	1	-0.2
Zn_ppm	-0.11	0.39	-0.24	-0.28	0.19	-0.066	0.29	0.42	0.18	0.26	0.054	-0.15	-0.2	1

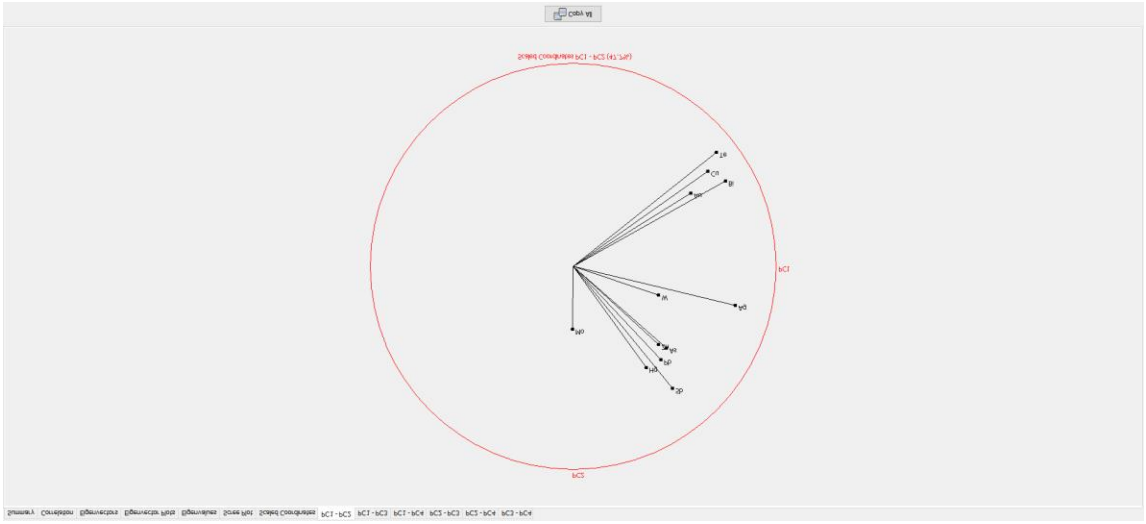

PC1-PC2 PCA Report Log 10

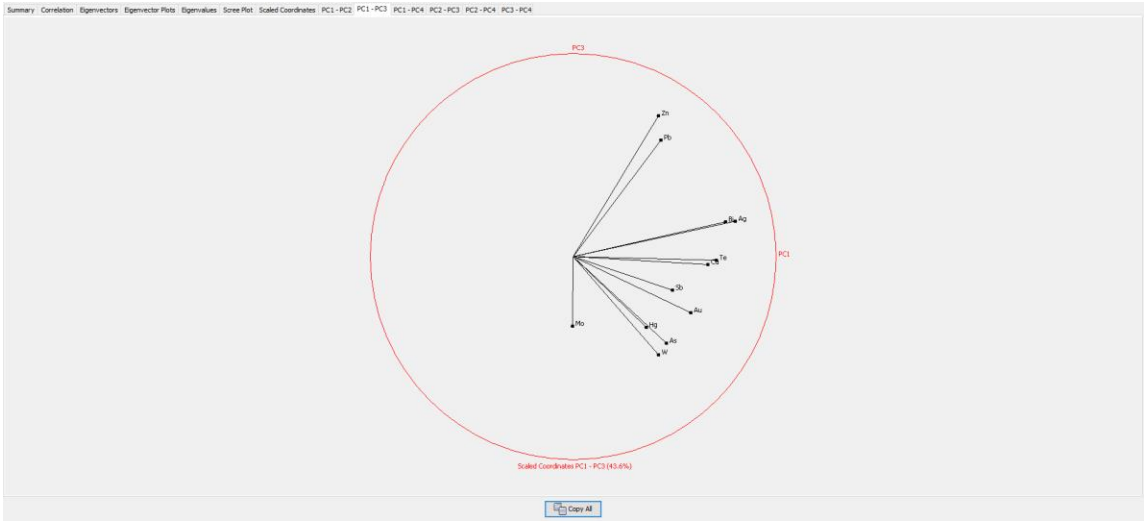

PC1-PC3 PCA Report Log 10

APPENDIX E: Linear Regressions for Harker Diagrams (Fig. 6)

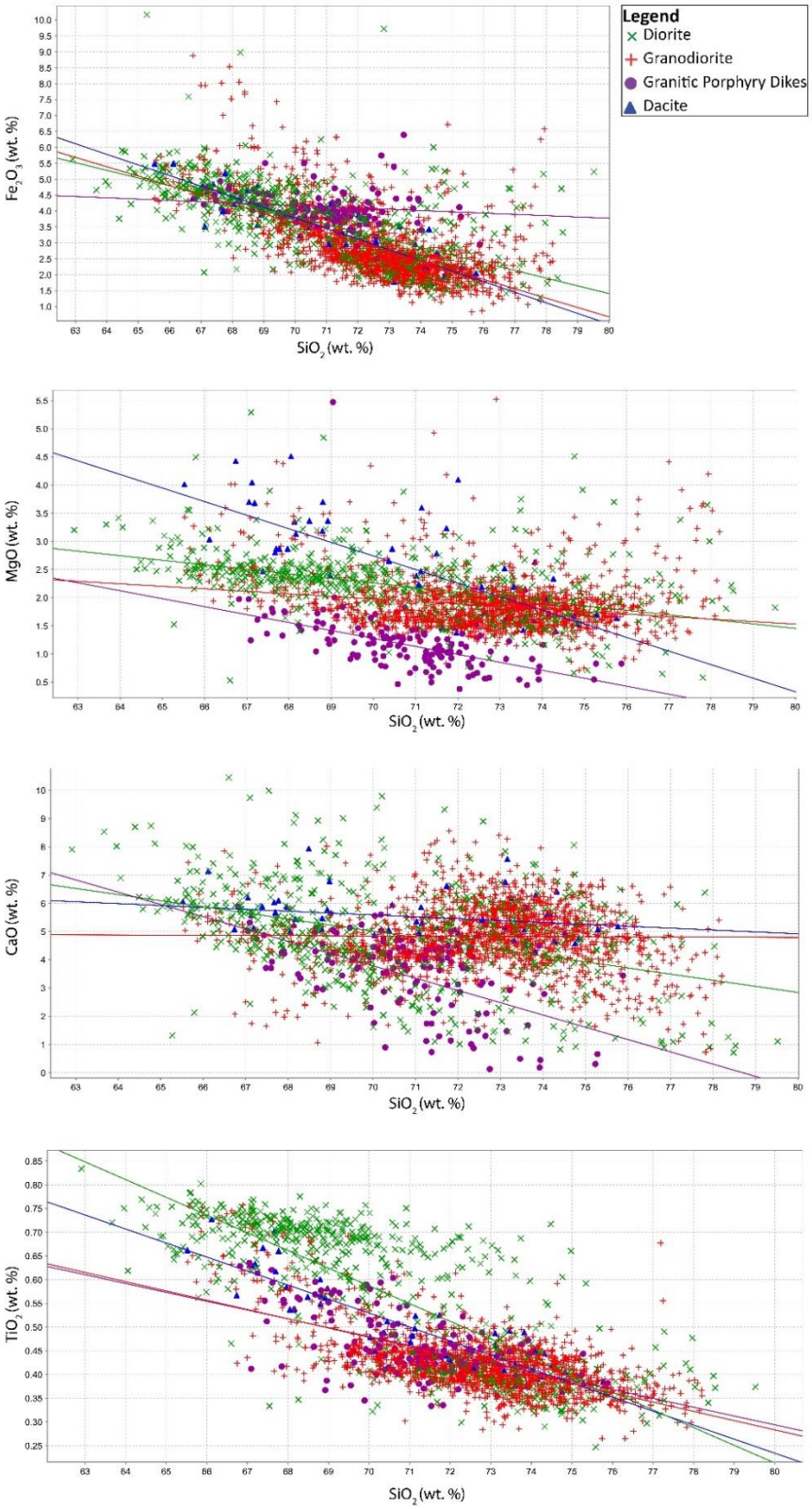

X	Y	Unit	N	Slope	Intercept	R-squared
SiO_2 (wt %)	Fe_2O_3 (wt %)	DA	64	-0.3329	27.0651	0.7781
SiO_2 (wt %)	Fe_2O_3 (wt %)	DI	721	-0.2414	20.7165	0.4142
SiO_2 (wt %)	Fe_2O_3 (wt %)	FP	406	-0.04006	6.9735	0.02025
SiO_2 (wt %)	Fe_2O_3 (wt %)	GD	2650	-0.2947	24.2512	0.4416
SiO_2 (wt %)	MgO (wt %)	DA	64	-0.2416	19.6511	0.579
SiO_2 (wt %)	MgO (wt %)	DI	721	-0.08087	7.9104	0.2211
SiO_2 (wt %)	MgO (wt %)	FP	406	-0.1417	11.1876	0.3576
SiO_2 (wt %)	MgO (wt %)	GD	2650	-0.04481	5.1119	0.04833
SiO_2 (wt %)	CaO (wt %)	DA	64	-0.06745	10.3024	0.05795
SiO_2 (wt %)	CaO (wt %)	DI	721	-0.2177	20.2336	0.1741
SiO_2 (wt %)	CaO (wt %)	FP	406	-0.4344	34.1747	0.3304
SiO_2 (wt %)	CaO (wt %)	GD	2650	-0.005583	5.2226	1.4091E-4
SiO_2 (wt %)	TiO_2 (wt %)	DA	64	-0.02959	2.5999	0.8109
SiO_2 (wt %)	TiO_2 (wt %)	DI	721	-0.03747	3.2092	0.6459
SiO_2 (wt %)	TiO_2 (wt %)	FP	406	-0.01862	1.7834	0.2519
SiO_2 (wt %)	TiO_2 (wt %)	GD	2650	-0.01953	1.8441	0.4421

APPENDIX F: ASD Spectra

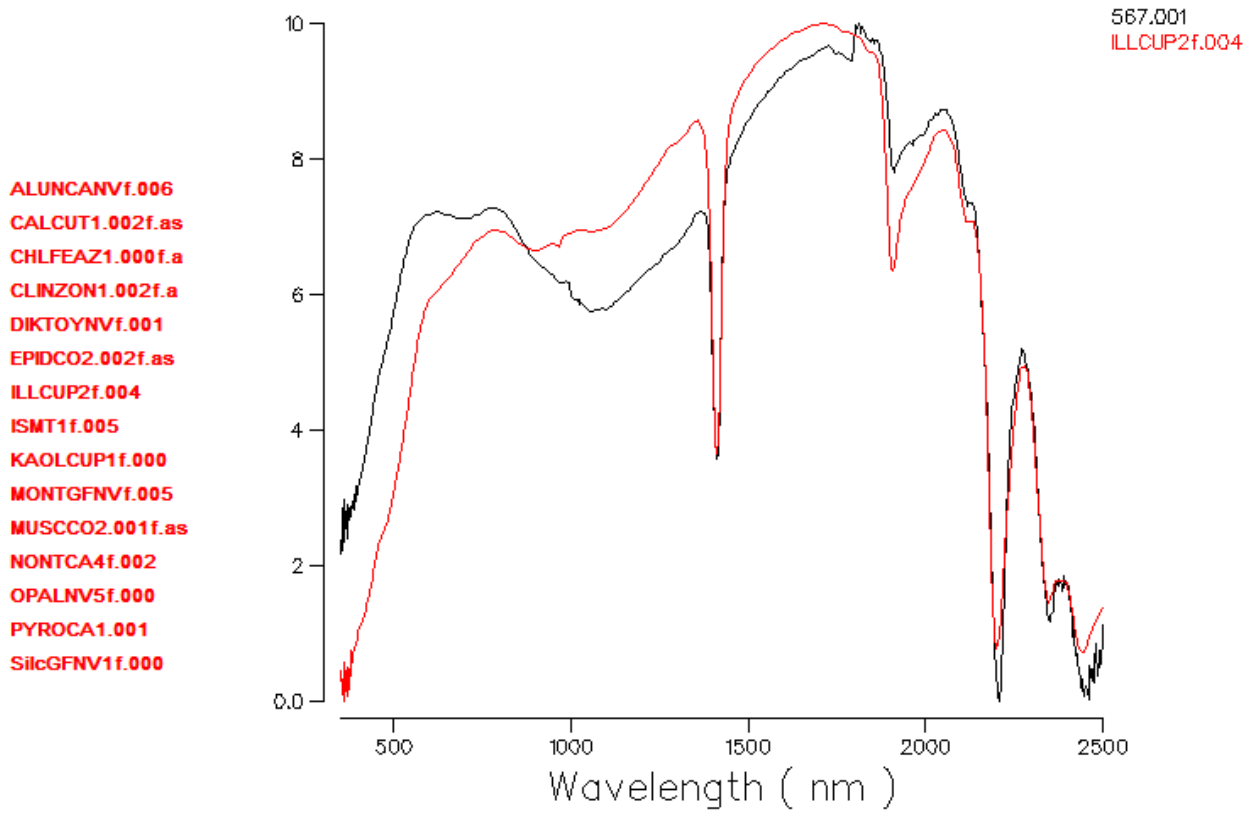

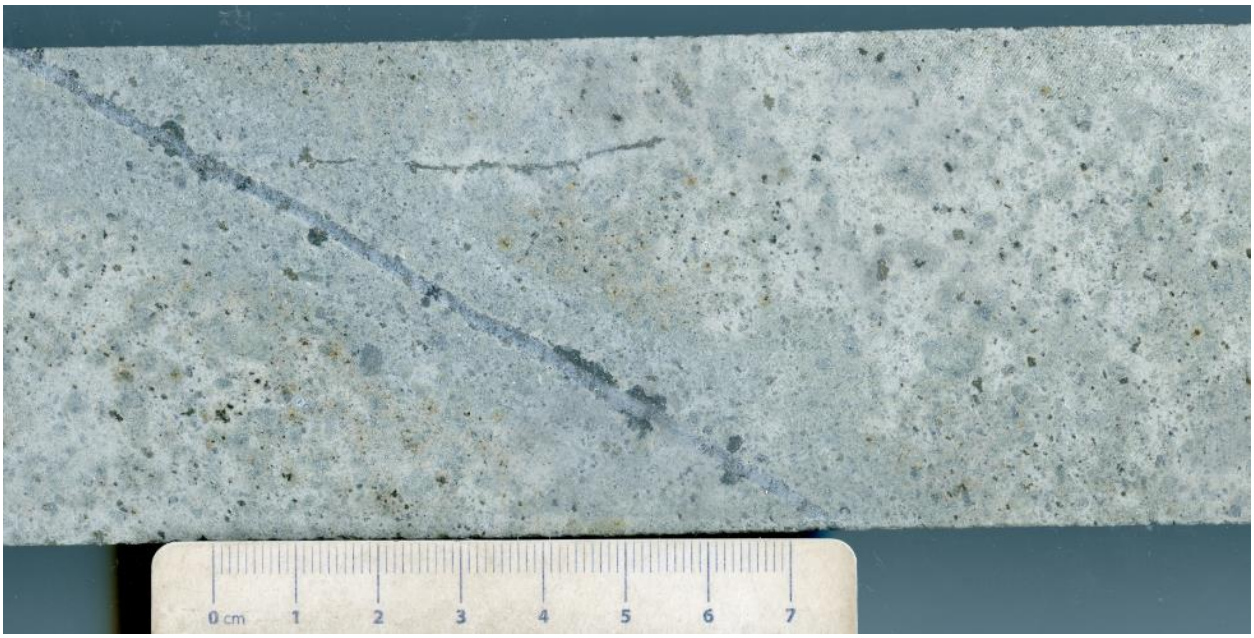

Sample GPGT2020-008-567 used in ASD analysis. Spectra matches illite standard.